# A NOVEL METHOD FOR INCORPORATING PERIODIC BOUNDARIES INTO THE FDTD METHOD AND THE APPLICATION TO THE STUDY OF STRUCTURAL COLOR OF INSECTS

A Thesis
Presented to
The Academic Faculty

by

Richard Todd Lee

In Partial Fulfillment
of the Requirements for the Degree
Doctor of Philosophy in the
School of Electrical and Computer Engineering

Georgia Institute of Technology
August 2009

# A NOVEL METHOD FOR INCORPORATING PERIODIC BOUNDARIES INTO THE FDTD METHOD AND THE APPLICATION TO THE STUDY OF STRUCTURAL COLOR OF INSECTS

Approved by:


Glenn S. Smith, Advisor
School of Electrical and Computer Engineering
*Georgia Institute of Technology*

John A. Buck
School of Electrical and Computer Engineering
*Georgia Institute of Technology*

Waymond R. Scott
School of Electrical and Computer Engineering
*Georgia Institute of Technology*

Guillermo H. Goldsztein
School of Mathematics
*Georgia Institute of Technology*

Andrew F. Peterson
School of Electrical and Computer Engineering
*Georgia Institute of Technology*



Date Approved: May 27, 2009

*To Natalie*

# ACKNOWLEDGEMENTS

This thesis is the result of eight years of graduate school. The completion is only possible due to the assistance and advice of many individuals.

First, I would like to thank my thesis advisor, Professor Glenn Smith. Working closely with such a talented and knowledgeable researcher has been an incredible experience. Dr. Smith also provides precise and accurate explanations for physical observations in his writing, and I have tried to follow his example in this work. To the extent that I have succeeded, it is due to his patient instruction and valuable advice.

I would like to thank the members of my thesis committee for evaluating this work and providing helpful advice. Professors Waymond Scott and Andrew Peterson, as well as Professor Smith, served on the reading committee. They reviewed this work in draft form and provided many helpful suggestions (and more than a few corrections!). I also would like to thank Professor Scott for significantly upgrading the computer cluster in our lab. Thanks also to Professors Buck and Goldsztein for serving on the thesis committee and for asking insightful and thought-provoking questions.

After completing this thesis, I will accept a research faculty position with the Signature Technology Laboratory at the Georgia Tech Research Institute. I first worked in this lab as an mechanical engineering undergraduate. I was exposed to interesting topics and inspired to change my major to electrical engineering. My supervisor, Brian Shirley, introduced me to Professor Smith and encouraged me to pursue a Ph.D. Several other members of the lab, specifically Jim Maloney and Eric Kuster, have been resources for developing the software described in this thesis. I especially want to thank the leadership of the lab, specifically Lon Pringle and Jim Acree, for waiting an extra year for me to finish and begin work.

My colleagues in the Electromagnetics Group have been valuable fellow travelers on this journey. I want to thank Thorsten Hertel, Rickard Petersson, Benny Venkatesan, Pelham Norville, Ilker Capoglu, Kangwook Kim, Mike Mcfadden, Tegan Counts, Ricardo Lopez,

and Mu-Hsin Wei for the interesting discussions and pleasant company in our office. I especially want to thank David Reid. David has been an incredible friend and is a great person to bounce ideas off of. Of course, the biggest thing I have to thank David, along with his Sara, for is introducing me to my wife, Natalie.

I have been blessed with a supportive family. My brother, sister-in-law, parents, and grandparents always encouraged me to pursue my academic interests. They have been there for my successes and failures and have shown me nothing but love and support through both. Over the course of this work, I have also acquired some in-laws. They welcomed me into their family and shared in my frustrations and excitements.

Most of all, I want to thank my wife, Natalie. There is absolutely no way that I would have completed this work without her constant encouragement and support. Natalie's endless confidence in me has been an inspiration and a source of strength. Natalie, I love you and thank you for everything!

This work was supported by the John Pippin Chair in Electromagnetics within the School of Electrical and Computer Engineering at Georgia Tech.

# TABLE OF CONTENTS

# LIST OF TABLES

# LIST OF FIGURES

# SUMMARY

In this research, a new technique for modeling periodic structures in the finite-difference time-domain (FDTD) method is developed, and the technique is applied to the study of structural color in insects.

First, the FDTD method is presented. The method is developed by starting with Maxwell's equations in time-domain, differential-equation form. The derivatives are replaced by central differences, and a marching-in-time algorithm is found. Various recent supplements to the FDTD method, such as a nearly-perfect plane-wave injector and convolutional perfectly matched layer absorbing boundary conditions, are used. For modeling electrically large structures, significant computer resources are required; a method for implementing the FDTD method on a parallel, distributed-memory computer cluster is given.

To model a periodic structure, a single periodic cell is terminated by periodic boundary conditions (PBCs). A new technique for incorporating PBCs into the FDTD method is presented. The simplest version of the technique is limited to two-dimensional, singly-periodic geometries, or to three-dimensional, doubly-periodic geometries when the direction of propagation for the incident plane wave is in a principle plane of the cell. The computational cost for the method is found to depend on the direction of propagation. The accuracy of the method is demonstrated by comparing to independent results calculated with a frequency-domain, mode-matching method.

The periodic FDTD method is then extended to the more general case of doubly-periodic problems in which the propagation vector of the incident plane wave is not in a principle plane. This extension requires additional steps and imposes new limitations that are not present for the simpler case. The computational cost and limitations of the method are presented. The accuracy is demonstrated by modeling the scattering from dielectric slabs and comparing to the exact solution, and by modeling a pair of complementary structures and demonstrating that the results are consistent with Babinet's principle.

Certain species of butterflies exhibit structural color, which is caused by quasi-periodic structures on the scales covering the wings. Numerical experiments are performed to develop a technique for modeling quasi-periodic structures using the periodic FDTD method. The observed structural color of butterflies is then calculated from the electromagnetic data using colorimetric theory.

Three types of butterflies are considered. The first type are from the *Morpho* genus. These are typically a brilliant, almost metallic, blue color. The second type is the *Troides magellanus*, which exhibits an interplay of structural and pigmentary color, but the structural color is only visible near grazing incidence. These two types exhibit iridescence on the dorsal side of the wings. The final type is the *Ancyluris meliboeus*, which exhibits iridescence on the ventral side. For all cases, the effects of changing the dimensions of various structural elements are considered. This type of analysis is only possible using a detailed computational model.

Finally, some earlier work on the design of TEM horn antennas is presented. This subject was considered as a possible thesis topic. The TEM horn is a simple and popular antenna, but only limited design information is available in the literature. A parametric study was performed, and the results are given. A complete derivation of the characteristic impedance of the basic antenna is also presented.

# CHAPTER I

# INTRODUCTION

In this work, a novel method for incorporating periodic boundary conditions (PBCs) into the finite-difference time-domain (FDTD) method is presented. The method is first shown for two-dimensional geometries. It is then extended to more general three-dimensional geometries, which introduces additional complexities and limitations. After demonstrating the effectiveness of the method with several example problems, a novel application in biology, structural color in butterflies, is introduced. The periodic FDTD method is used to study the effect of structural variations on the observed color for several types of butterflies.

## *1.1 FDTD Method*

### 1.1.1 Overview of the Method

This research explores problems that can be solved using the techniques of classical electromagnetism. In the 19th century, James Clerk Maxwell laid the foundation for a set of equations that are now called *Maxwell's equations* [1]. These are a set of four partial differential equations that govern the behavior of electric and magnetic fields in a macroscopic sense (i.e., outside the realm of quantum mechanics). For most geometries, the equations cannot be solved analytically, and a variety of computational techniques have been developed.

In this work, a differential equation based technique known as the finite-difference time-domain (FDTD) method is used. The FDTD method was proposed in 1966 by Kane Yee [2]. This method is discussed in much greater detail in Chapter 2, but the basic concept is that derivatives in Maxwell's equations are approximated by finite differences:

$$\left.\frac{df}{dx}\right|_{x=x_\mathrm{o}} \approx \frac{f(x_\mathrm{o}+\Delta_x/2)-f(x_\mathrm{o}-\Delta_x/2)}{\Delta_x}. \tag{1.1}$$

The resulting difference equations are then reorganized so that a "marching in time" algorithm can be used.

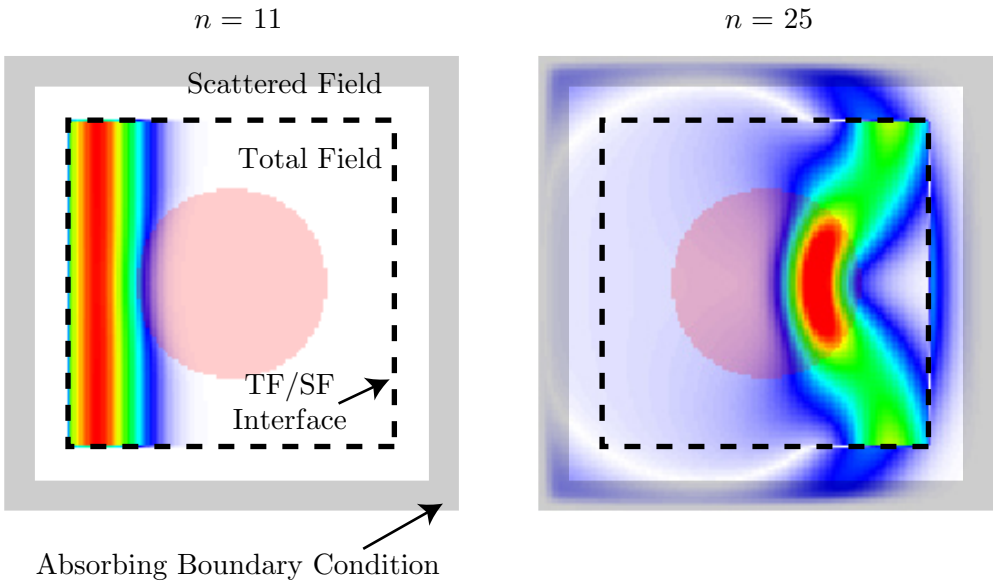


Figure 1.1: Two snapshots from a two-dimensional FDTD simulation. The total-field / scattered-field interface divides the space into a total-field region and a scattered-field region. The cylinder is modeled as being isolated in space by surrounding the entire geometry with an absorbing boundary condition.

In Figure 1.1, two snapshots in time of an FDTD simulation are shown. This simulation illustrates several important features of the method. The entire space is surrounded by an absorbing boundary condition, which is used in the solution to problems in open regions (e.g., scattering or antenna problems). The excitation is a plane wave that is launched using a total-field/scattered-field interface. This interface, which is the dotted line in Figure 1.1, creates the incident plane wave in the interior (total field) region and zero field in the exterior (scattered field) region. The scatterer is a dielectric cylinder, but any arbitrarily shaped object can be modeled just as easily. The simulation begins at time step $n = 0$ with the initial condition that all field quantities are 0. The first snapshot, Figure 1.1(a), is at time step $n = 11$, at which point the incident plane wave is just beginning to contact the scatterer. The second snapshot, Figure 1.1(b), is at $n = 25$. At this point the wave has passed through the scatterer. The difference between the scattered and total field can be seen by comparing the interior and exterior of the TF/SF interface. Calculations can be performed on the scattered field to determine typical quantities such as the scattering cross section.

In Yee's original paper, he considered the scattering by a perfect electric conductor

(PEC) infinitely long, square cylinder. He used only a crude plane-wave injector and simple PEC boundary conditions, which limited the appeal of the new algorithm. In 1975, Taflove and Brodwin used the FDTD method to calculate the scattering from a dielectric cylinder and achieved agreement to within 10% with the analytical solution. They also provided a necessary and sufficient condition for numerical stability [3].

Much of the work in subsequent decades has consisted of extending the algorithm to new types of problems and addressing sources of inaccuracy. One of largest sources of error for open region problems is the termination of the simulation space. In his original paper, Yee simply stopped the simulation before reflections from the outer boundaries returned. In 1981, Mur, building on the earlier work of Engquist and Majda, introduced the first effective absorbing boundary condition [4, 5].

The accuracy of absorbing boundary conditions was greatly improved with the introduction of the perfectly matched layer (PML) by Bérenger in 1994 [6]. This is an artificial absorbing material that is perfectly matched to free space. Therefore, a wave entering the material enters without reflection and is absorbed inside the material. Bérenger presented the PML by splitting the vector field components, which resulted in 12 field components instead of the usual 6 (as well as 12 update equations). The PML was reinterpreted as an anisotropic material by Sacks et al. [7], and implemented in the FDTD algorithm by Gedney [8]. A third interpretation of the PML is based on modifying Maxwell's equations using complex coordinate stretching [9, 10]. This interpretation is particularly useful for deriving constitutive tensors for anisotropic PML formulations in non-rectangular coordinate systems [11]. Most recently, Roden and Gedney used the complex coordinate stretching approach to derive the convolutional perfectly matched layer (CPML), which is a highly effective absorbing boundary for both propagating and evanescent waves and is straightforward to implement [12].

The use of a plane wave as excitation typically follows the approach suggested by Merewether et al. in 1980 [13]. The solution space is divided into two regions, as shown in Figure 1.1. The interior, known as the total-field (TF) region, contains the field of the incident plane wave as well as the field scattered by any objects in the solution space. The

exterior, known as the scattered-field (SF) region, contains only the scattered field. The boundary between the two regions, known as the TF/SF interface, is an "injector" surface. Ideally, the interface launches the incident field exactly into the interior region with zero field into the exterior region. In the absence of scattering objects, any field that does appear in the exterior region is referred to as "leakage". The original approach of Merewether et al. was to use an analytic expression for the incident field, along with the equivalence principle, to create equivalent currents on the interface. Although this approach is exact in the physical world, there is leakage due to the fact that the FDTD grid does not behave exactly like free space. For example, the FDTD grid is dispersive, which means that waves do not travel at exactly the speed of light.

Various methods of reducing this leakage have been proposed, and the most effective and generally applicable solution is to use the known numerical dispersive characteristics of the FDTD grid. The dispersive nature of the FDTD grid was discussed by Schneider and Wagner [14] and Schneider and Kruhlak [15], and Schneider proposed a method to use the known dispersion relationship to construct a nearly-perfect TF/SF interface [16]. An interface implemented in this way has a leakage comparable to single-precision floating-point numerical noise.

This introduction to the FDTD method has not been exhaustive; additional material is presented in Chapter 2 and in texts such as [17].

### 1.1.2 Periodic Boundary Conditions in the FDTD Method

Periodic structures are very common in engineering; examples include antenna arrays, frequency-selective surfaces, photonic band gap materials, and diffraction gratings. Periodic structures also occur in the natural world. For example, the cause of the iridescent color of certain species of butterflies is the scattering of light by the microscopic periodic structure on the surface on the wing. This particular application will be examined in detail in this thesis.

The cross-sectional view of a typical two-dimensional periodic structure is shown in Figure 1.2. The structure is finite in the $x$ direction, periodic in the $y$ direction with period

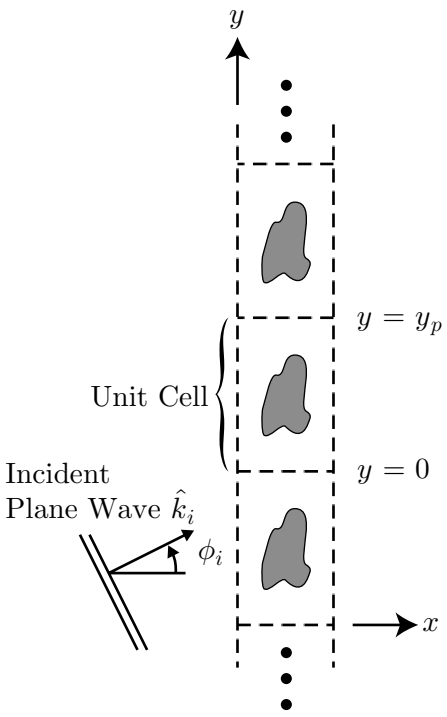


Figure 1.2: Schematic drawing for an infinite array. The period of the array is $y_p$.

$y_p$, and invariant in the $z$ direction. The figure is for a scattering problem, but the periodic techniques apply just as well to antenna problems. The structure is excited by a uniform plane wave with propagation vector $\hat{k}_i$:[1]

$$\vec{\mathcal{E}}_i(\vec{r};t) = \hat{e}\,\mathcal{G}(t - \hat{k}_i \cdot \vec{r}/c), \tag{1.2}$$

in which $\mathcal{G}$ is an arbitrary function of time. The angle between the propagation vector and the normal to the structure is $\phi_i$. Since the structure is periodic and the incident field is a plane wave, the electromagnetic field on the structure satisfies a shift property:

$$\vec{\mathcal{E}}(\vec{r} + y_p\hat{y};t) = \vec{\mathcal{E}}\left(\vec{r};t - \frac{y_p}{c}\hat{k}_i \cdot \hat{y}\right). \tag{1.3}$$

If the structure is three-dimensional and doubly-periodic (e.g., the structure is periodic along the $y$ and $z$ directions), separate shift properties apply along each direction, but the concept is the same.

[1] In this work, it will be necessary to express fields in both the time and frequency domains. To differentiate the two, time-domain quantities will be designated using a calligraphic font, for example, $\mathcal{E}$. Frequency-domain quantities will be designated using a Roman font, for example, $E$. For frequency-domain quantities, an $e^{j\omega t}$ sign convention is used.

The idea behind periodic boundary conditions is that determining the field on a single periodic cell (for example, the region $0 \leq y \leq y_p$ in Figure 1.2) is sufficient to determine the field on the entire structure. The single periodic cell is terminated by periodic boundary conditions that relate the field at $y = 0$ to $y = y_p$:

$$\vec{\mathcal{E}}(x\hat{x} + y_p\hat{y}; t) = \vec{\mathcal{E}}\left(x\hat{x}; t - \frac{y_p}{c}\hat{k}_i \cdot \hat{y}\right) \tag{1.4}$$

$$\vec{\mathcal{E}}(x\hat{x}; t) = \vec{\mathcal{E}}\left(x\hat{x} + y_p\hat{y}; t + \frac{y_p}{c}\hat{k}_i \cdot \hat{y}\right). \tag{1.5}$$

In a marching-in-time algorithm such as the FDTD method, the first of these conditions is simple to implement by storing past values in a time-delay buffer for later use. The second condition, however, requires the knowledge of *future* field values. In a straightforward implementation of the FDTD method, future field values are not available. Dealing with the future data problem is the challenge to implementing periodic boundary conditions in the FDTD method.

There have been several approaches to overcome this problem. They can be divided into two classes [18]. The first class, known as the field transformation methods, redefine the electromagnetic field in the entire solution space so that the time shift is removed. For example, a new field quantity $\vec{\mathcal{P}}$ can be defined:

$$\vec{\mathcal{P}}(x\hat{x} + y\hat{y}; t) = \vec{\mathcal{E}}\left(x\hat{x} + y\hat{y}; t + \frac{y}{c}\hat{k}_i \cdot \hat{y}\right). \tag{1.6}$$

Using this definition, the boundary condition becomes

$$\vec{\mathcal{P}}(x\hat{x}; t) = \vec{\mathcal{P}}(x\hat{x} + y_p\hat{y}; t). \tag{1.7}$$

These methods exchange one problem for another. Although the boundary condition is simple to implement, the transformation of the field quantities requires a complete re-derivation of the FDTD algorithm [19]. This new algorithm requires significantly more memory and has a stability criterion that becomes increasingly more restrictive as the angle of incidence of the excitation increases. In addition, specialized absorbing boundary conditions are required.

The second class are known as the direct field methods. In these approaches, the usual FDTD field components are used, and the algorithm is manipulated to make future field

values available. The easiest approach is to use simple wrap-around boundary conditions:

$$\vec{\mathcal{E}}(x\hat{x} + y_p\hat{y}; t) = \vec{\mathcal{E}}(x\hat{x}; t). \tag{1.8}$$

This boundary can be easily implemented without introducing any added complications. However, this approach only works for the normally incident case ($\phi_i = 0°$).

For the more general case ($\phi_i \neq 0°$), several direct-field methods exist. Two of these methods are discussed here: the angled-update method of Maloney and Kesler [18], and the sliding unit cell method of Holter and Steyskal. The angled-update method is based on the observation that all of the sampled field components in the FDTD grid do not have to be at the same time step. This is conceptually similar to the $\vec{\mathcal{P}}$ field described above, but the implementation is direct. The method requires little additional storage and has the same stability criteria as the standard FDTD algorithm. However, this method is restricted to $\phi_i < 45°$ for two-dimensional geometries, and $\phi_i \lesssim 35°$ for three-dimensional geometries.

Another approach is the sliding unit cell method [20, 21]. This method is based on the observation that the incident plane wave moves along the $y$ direction at a speed $c/(\hat{k}_i \cdot y)$, which is the phase velocity of the incident wave in the $y$ direction. However, any error caused by an imperfect boundary condition at $y = 0$ will only travel along the grid in the $y$ direction at the speed $c$. As the error travels upward, a row of cells at the bottom (minimum $y$) of the grid is removed and a new row is placed at the top (maximum $y$) using time-delayed fields. As the cells are removed, the truncation error is removed as well. This approach works for $0 < \phi_i < 90°$, but the time delay is restricted so that only certain directions are possible. This restriction is

$$\frac{y_p}{c}\hat{k}_i \cdot \hat{y} = N\frac{\Delta_y}{2c}, \quad N = \text{integer}. \tag{1.9}$$

In this thesis, a new method for incorporating periodic boundary conditions that does not suffer from these restrictions will be presented.

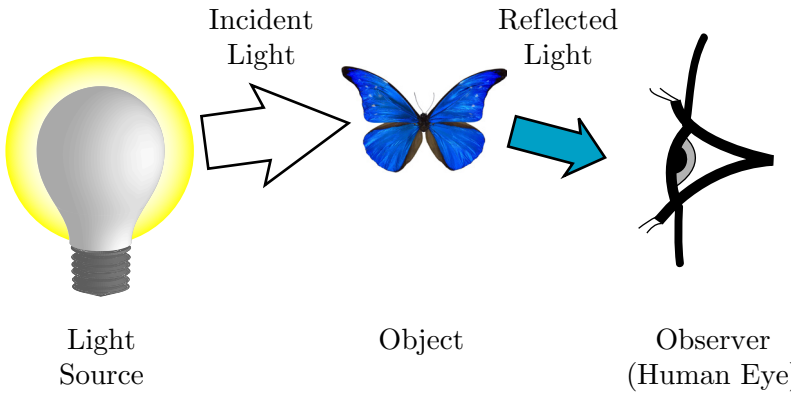


Figure 1.3: Illustration of the three main components of human color vision. The observed color is determined by the incident light from the light source, the amount of reflected light from the object, and the interpretation of the reflected light by the human eye and brain.

## *1.2 Structural Color*

### 1.2.1 Types of Color

Color is the interpretation by the human brain of light that is detected by the human eye. For determining the color of an object, there are three components: the light source, the object itself, and the observer. These components are shown in Figure 1.3. The light source radiates light with a certain power spectrum. Some portion of this light is reflected towards the observer, and this reflected light is seen as the color of the object.

Often, light in a certain range of wavelengths will be absorbed, and others will be reflected. This selective absorption can be due to dyes and pigments, and this type of color is called pigmentary color. The color of many common objects, such as most paints, clothing, and flowers, is due to pigmentary color. This type of color does not change significantly with viewing angle, though it may change significantly if a different light source is used. The object can be crushed to a powder, but the powder will still have the same color. This is because the color is a property of the material of which the object is made, not the way the object is constructed.

Alternatively, the intensity and spectral distribution of the reflected light may be due to electromagnetic phenomena such as scattering, diffraction, and thin film interference. This type of color is called *structural color*, since the nature of the reflected light is caused by the structure of the object rather than the properties of the material comprising it. This

type of color can have interesting properties: the color is often very intense and highly saturated, and the color often changes with viewing angle. This second property is known as iridescence. Another remarkable feature of structural color is that the color can be changed or even eliminated by immersing the object in a liquid with an appropriate index of refraction.

A familiar example of structural color is a soap bubble. The liquid itself is often colorless. However, the bubble exhibits a rainbow-like iridescent phenomenon. This effect can be explained by thin-film interference. The bubble material does not necessarily contain a dye or pigment that selectively absorbs light; rather, it is the structure itself that causes the iridescence. If the bubble is popped, the color will disappear.

### 1.2.2 Structural Color in Butterflies

Many species of butterfly display vibrant iridescent coloration that is widely believed to be caused by structural color. This research focuses on several species that possess unique coloration. The goal here is not to create an accurate computational model for any particular species. Rather, it is to create a generic model that exhibits many of the observed characteristics, and then vary the parameters of the model to determine the effect of changes to various structural features. Data in the literature is used as a basis for the computational models. The FDTD method is used to calculated the spectral characteristics of the reflected light, and colorimetry is then used to determine the observed color.

The first butterflies considered are various species from the genus *Morpho*. These butterflies are common in South America. The male butterflies are brightly colored on the dorsal side (top) and brown on the ventral side (bottom), as shown in Figure 1.4. The insect shown is a *Morpho menelaus*. To demonstrate the dramatic change in color that can occur when the wing is immersed in a liquid with a different index of refraction, the wing was immersed in acetone (index of refraction $n = 1.36$). As shown in Figure 1.4(c), the color changed to a yellowish-green. It immediately returned to blue when the acetone evaporated.

To show some of the variety in the *Morpho* genus, the *M. menelaus* and two other

(a)



(b)

(c)

Figure 1.4: Photograph of a male *Morpho menelaus* butterfly. (a) Dorsal side. (b) Ventral side. (c) Dorsal side, immersed in acetone.

species are shown in Figure 1.5. As compared to the *M. menelaus*, the *M. rhetenor* has an intense blue color that could be described as "metallic" in appearance. In contrast, the *M. didius* has a less intense color. The color could be described as "milky" in appearance.

Two other species of butterfly are considered in this work. The *Troides magellanus*, which is native to the Philippines, is remarkable due to the interplay of structural and pigmentary color. The *Ancyluris meliboeus*, which is native to Peru, is interesting because it is the ventral, rather than the dorsal, side of the wings that display iridescence. Only certain regions of the wing are iridescent, and only these regions will be considered. These species will be discussed in more detail in Chapter 7.

The wings of the butterflies are covered with a large number of small scales that are easily visible using a low-power microscope. For example, a magnified image of the *M. rhetenor* is shown in Figure 1.6(a). It is actually the scales that produce the color, and the study of structural color of butterflies is the study of the butterfly scales. The scales are covered with a series of quasi-periodic ridges that are less that 1 $\mu$m apart. Each ridge is a tree-like structure with 4-12 branches on both sides, as shown in the electron microscope image in Figure 1.6(b) [22, Figure 12]. The structure is made of chitin with an approximate complex index of refraction $\tilde{n} = 1.56 - j0.06$ [23]. From an analysis standpoint, the ridge will be considered the "unit cell".

### 1.2.3 Overview of Previous Research

Scientific interest in structural color of insects has persisted for well over a century. A. A. Michelson, in 1911, studied certain iridescent butterflies and proposed that the colors are metallic in nature [24]. In the literature, this theory is called "selective reflection." Michelson believed that the metallic appearance of the insects is no coincidence — the physical mechanism at work is the same as for thin metallic films.

A competing theory, advocated by Mallock [25] and Lord Rayleigh [26], proposed that the colors are caused by interference effects; that is, the colors are structural. Lord Rayleigh pointed out that the observed colors change hue when the insects are immersed in liquids with different indices of refraction, which strongly implies that the colors are due to some

(a)

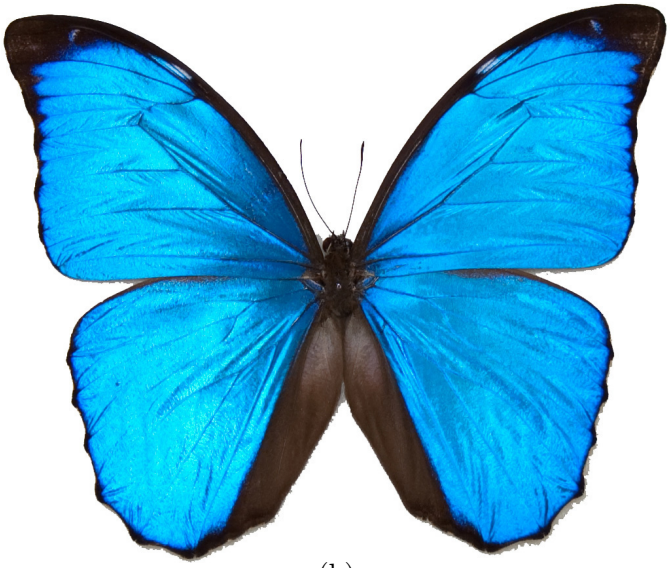

(b)

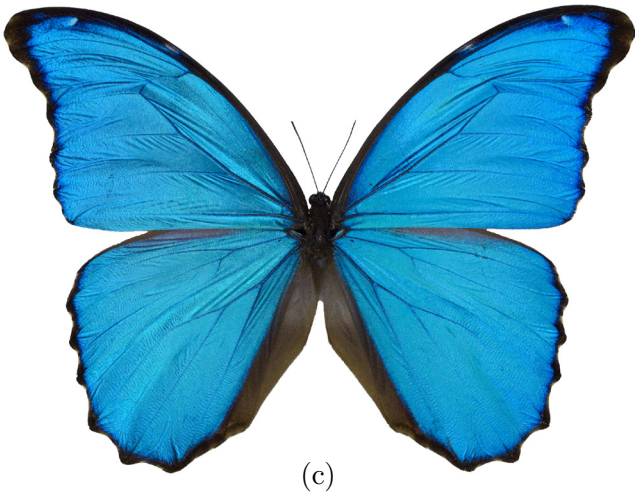

(c)

Figure 1.5: Photographs of male *Morpho* butterflies. (a) *M. rhetenor*. (b) *M. menelaus*. (c) *M. didius*.

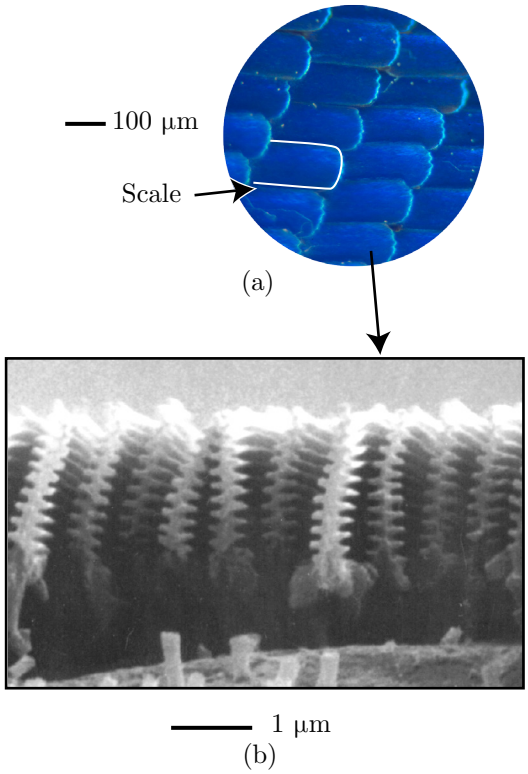


Figure 1.6: Photograph of a male *Morpho rhetenor* butterfly. (a) Detail of wing showing scales as viewed under an optical microscope. (b) Cross section of scale showing individual ridges as viewed using a scanning electron microscope. SEM image courtesy S. Kinoshita [22, Figure 12].

from of optical interference.

Mason in 1926 and 1927 concluded, through optical microscope studies, that the color of certain butterflies, including the *Morpho*, is structural in origin [27–29]. He presented guidelines for determining whether a given color is structural or pigmentary, and presented a model for the scale of the *Morpho* that included a series of ridges made up of thin films.

Much more detailed descriptions of the scales became available once the electron microscope was used [30]. Since structural effects necessarily are caused by interference on scales that are close to the wavelength of the scattered light, it is not possible to directly see the details of the structure using only an optical microscope. The images from the electron microscope studies confirmed that Mason and the other advocates of structural color were on the right track.

Ghiradella has done extensive work examining the structure of the butterfly scales [31–35]. Her research has focused not only on the structures themselves, but also on the biological process involved in creating them and the purpose served by such intense coloration. She proposed the concept of a "generic scale" that is then specialized by the different species to produce different colors. Her research, among others, has been used to develop a classification scheme for butterflies based on the structural characteristics [36].

A great many optical measurements have been made of the reflection characteristics of the butterfly wings. For example, Pillai measured the spectral reflectance of a *Morpho* (he did not identify the species) butterfly using a Wright spectrophotometer [37]. However, as has been discussed previously, it is the scales themselves that are colored. Vukusic et al. were the first to measure the reflection and transmission characteristics of an individual scale [23]. They compared their measured results to the theoretical reflection from a stack of infinitely wide, thin films.

The first published study that considered the finite width of the tree structure was reported by Gralak et al. [38]. They used lamellar grating theory to model a tree structure made up of a stack of layers with a finite width.

A problem with modeling the structure as a periodic array is that one would expect to only see reflected light over a very narrow range, since the array factor would focus the

reflected light. This is not consistent with observations. Kinoshita et al. proposed that random vertical positioning of the individual ridges eliminates the coherent interference between ridges, so that the reflected light is due only to a single ridge [39]. We study this hypothesis is Chapter 7 and develop a technique to use the periodic FDTD method to study models of the butterfly scales.

The application of the FDTD method to the study of structural color has been recently reported by Plattner [40]. His model was a simplified two-dimensional structure with a finite number of periods. Banerjee et al. also used a modified FDTD method to study two-dimensional models of *Morpho* butterflies [41]. However, these previous studies employed restrictions, such as only modeling a two-dimensional structure, that are not employed in this research.

### *1.3 Outline and Contributions of Research*

This thesis presents a new method for incorporating periodic boundary conditions into the FDTD method, and then applies that method to the study of structural color in butterflies. Since the two subjects are self-contained, the FDTD portion is presented first. In Chapter 2, the details of the FDTD method are given. An aim of this research was to use the most recent refinements to the method in application to structural color. The convolutional PML is used for grid termination for non-periodic surfaces, and the "nearly perfect" plane-wave injector is used as an excitation.

In Chapter 3, the two-dimensional version of the new technique for incorporating PBCs into the FDTD method is presented. The chapter begins by reviewing periodic structures and the unique electromagnetic properties associated with them. The new algorithm is then presented in detail. This algorithm is an improvement over previous approaches because it is simple to implement and works for all angles in the range $0 \leq \phi_i < 90^\circ$. Various implementation issues and optimizations are discussed. Finally, an example is shown that demonstrates excellent agreement with an independent frequency-domain technique for periodic structures.

The two-dimensional version of the algorithm can be used for three-dimensional geometries, but the incident wave vector must be in a cardinal plane. To remove this limitation, a more elaborate algorithm for three-dimensional, doubly-periodic problems is presented in Chapter 4. This algorithm loses some of the simplicity of the 2D algorithm, and also exhibits certain additional limitations not present in the 2D case. These issues are discussed in detail. The chapter closes with a series of canonical problems that demonstrate the accuracy of the 3D algorithm.

In Chapter 5, a near-to-far-field transformation for a perfect periodic structure is developed. First, the transformation for the far-zone scattered field from finite objects is discussed and validated for cylindrical scatterers. Next, a method for computing the far-zone scattered field for a periodic array of scatterers illuminated by a finite-width plane-wave source is presented. It is validated by comparing the calculated results for a periodic structure to a large finite array.

In Chapter 6, the topic of colorimetry is introduced. This chapter addresses the issue of human color vision in regards to structural color of butterflies. A method for converting the electromagnetic quantities calculated by the FDTD method to observed colors is given. Finally, the presentation of color data on a chromaticity diagram is explained.

In Chapter 7, a computational model for a generic butterfly ridge structure is presented. The structure is quasi-periodic; a method for modeling such a structure using the periodic FDTD method is presented. Three types of butterflies are analyzed: *Morpho* (various species), *Troides magellanus*, and *Ancyluris meliboeus*. Several of the features of the scales are varied and the changes in color that result are discussed. The goal was not to create exact computational models; rather, it was to study the effect of varying the geometrical parameters on a generic scale. This analysis is the most detailed analysis performed to date of these butterflies. Concluding remarks and suggestions for future research are given in Chapter 8.

This thesis also contains two appendices on a different topic: transverse electromagnetic (TEM) horn antennas. This work was conducted early in the author's graduate career and was considered as a possible thesis topic. This antenna is made up of two triangular

metal plates. In Appendix A, the characteristic impedance, $Z_c$, of the TEM horn antenna is discussed. It is shown that some of the available analytical solutions in the literature are incorrect. A numerical calculation is used to identify the correct analytical solution. The accuracy of a common approximation, the "microstrip approximation", is also addressed. A parametric study of the performance of this antenna is then performed for the common choice of $Z_c = 100\,\Omega$. In Appendix B, a complete derivation of the characteristic impedance of the TEM horn is given. This derivation is based on conformal mapping. The bow-tie antenna is a special case of the TEM horn; the solution is shown to simplify to the solution of the bow-tie antenna for that special case.

# CHAPTER II

# FINITE-DIFFERENCE TIME-DOMAIN METHOD

In this chapter, the finite-difference time-domain (FDTD) algorithm is presented. The method is a direct numerical implementation of Maxwell's equations. The basic algorithm is derived first. The dispersive characteristics of the FDTD method are discussed and an exact dispersion relation is shown. This relation is used for the implementation of a plane wave source. Finally, the convolutional perfectly matched layer (CPML) boundary condition, which is a recent method of terminating the grid for an open region scattering problem, is discussed. This chapter serves as a overview, and the reader is referred to texts such as [17] for more detail.

## *2.1 Derivation of the Basic Method*

The finite-difference time-domain (FDTD) method is a technique for directly solving Maxwell's equations in the time domain. In differential form, Maxwell's equations are:

$$\nabla \times \vec{\mathcal{H}}(\vec{r};t) - \frac{\partial \vec{\mathcal{D}}(\vec{r};t)}{\partial t} = \vec{\mathcal{J}}(\vec{r};t) \qquad \text{Ampère-Maxwell law} \qquad (2.1)$$

$$\nabla \times \vec{\mathcal{E}}(\vec{r};t) + \frac{\partial \vec{\mathcal{B}}(\vec{r};t)}{\partial t} = 0 \qquad \text{Faraday's law} \qquad (2.2)$$

$$\nabla \cdot \vec{\mathcal{D}}(\vec{r};t) = \rho(\vec{r};t) \qquad \text{Gauss' electric law} \qquad (2.3)$$

$$\nabla \cdot \vec{\mathcal{B}}(\vec{r};t) = 0 \qquad \text{Gauss' magnetic law} \qquad (2.4)$$

The quantities that we use in this thesis are summarized in Table 2.1.

In simple media, $\vec{\mathcal{D}}$ and $\vec{\mathcal{H}}$ are related to $\vec{\mathcal{E}}$ and $\vec{\mathcal{B}}$ through constitutive relationships:

$$\vec{\mathcal{D}} = \epsilon \vec{\mathcal{E}} \qquad (2.5)$$

$$\vec{\mathcal{H}} = \frac{1}{\mu}\vec{\mathcal{B}}. \qquad (2.6)$$

If we consider only the $z$ component of (2.1), use the constitutive relationships, and assume

Table 2.1: Electromagnetic Quantities

| Symbol | Definition | Unit |
|---|---|---|
| $\vec{\mathcal{E}}$ | Electric field strength | V/m |
| $\vec{\mathcal{B}}$ | Magnetic field strength | T |
| $\vec{\mathcal{D}}$ | Electric excitation | $C/m^2$ |
| $\vec{\mathcal{H}}$ | Magnetic excitation | A/m |
| $\vec{\mathcal{J}}$ | Volume density of current | $A/m^2$ |
| $\rho$ | Volume density of charge | $C/m^3$ |
| $\epsilon$ | Permittivity | F/m |
| $\epsilon_o$ | Permittivity of free space $(8.8541\ldots \times 10^{-12})$ | F/m |
| $\mu$ | Permeability | H/m |
| $\mu_o$ | Permeability of free space $(4\pi \times 10^{-7})$ | H/m |
| $c$ | Speed of light in free space (299,792,458) | m/s |
| $\vec{k}$ | Wave vector | $m^{-1}$ |
| $\omega$ | Angular frequency | $s^{-1}$ |
| $f$ | Frequency | Hz |
| $\lambda$ | Wavelength | m |

Based on [1, Table 1.2]

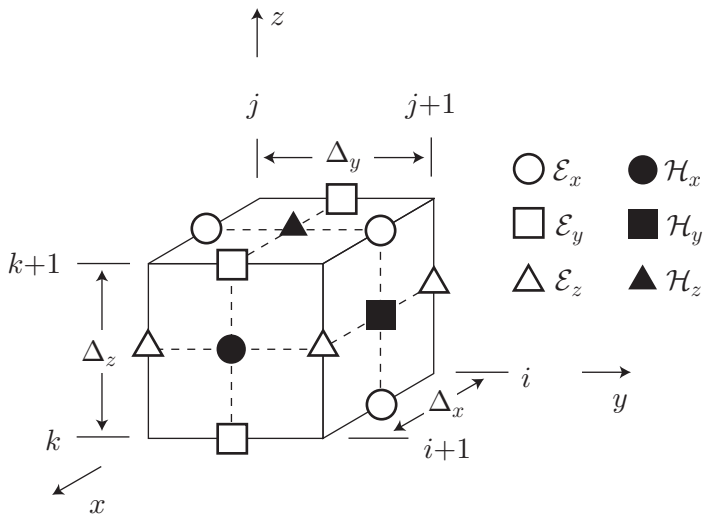


Figure 2.1: Three-dimensional FDTD cell showing the locations of the field components.

a source-free region so that $\vec{\mathcal{J}} = 0$, we have

$$\epsilon \frac{\partial \mathcal{E}_z}{\partial t} = \frac{\partial \mathcal{H}_y}{\partial x} - \frac{\partial \mathcal{H}_x}{\partial y}. \tag{2.7}$$

If the derivatives are replaced by central differences centered at $(\vec{r}_{\rm o}; t_{\rm o})$, we have

$$\begin{aligned} &\epsilon(\vec{r}_{\rm o}) \frac{\mathcal{E}_z\big(\vec{r}_{\rm o}; t_{\rm o} + \frac{\Delta_t}{2}\big) - \mathcal{E}_z\big(\vec{r}_{\rm o}; t_{\rm o} - \frac{\Delta_t}{2}\big)}{\Delta_t} \\ &= \frac{\mathcal{H}_y\big(\vec{r}_{\rm o} + \frac{\Delta_x}{2}\hat{x}; t_{\rm o}\big) - \mathcal{H}_y\big(\vec{r}_{\rm o} - \frac{\Delta_x}{2}\hat{x}; t_{\rm o}\big)}{\Delta_x} - \frac{\mathcal{H}_x\big(\vec{r}_{\rm o} + \frac{\Delta_y}{2}\hat{y}; t_{\rm o}\big) - \mathcal{H}_x\big(\vec{r}_{\rm o} - \frac{\Delta_y}{2}\hat{y}; t_{\rm o}\big)}{\Delta_y}. \end{aligned} \tag{2.8}$$

Examining this equation, we see that the field components are offset in both space and time. The arrangement in space is shown in Figure 2.1. The components are indexed by $(i, j, k)$ in space, and by $n$ in time. We will use the common notation for compactly denoting a field component, e.g.

$$\mathcal{E}_z\big|^n_{i,j,k+1/2} = \mathcal{E}_z\big[i\Delta_x\hat{x} + j\Delta_y\hat{y} + (k + 1/2)\Delta_z\hat{z}; n\Delta_t\big]. \tag{2.9}$$

Next, we rearrange terms to isolate $\mathcal{E}_z\big(\vec{r}_{\rm o}; t_{\rm o} + \frac{\Delta_t}{2}\big)$ on the left side. We use the compact notation, and set $\vec{r}_{\rm o} = i\Delta_x\hat{x} + j\Delta_y\hat{y} + (k + 1/2)\Delta_z\hat{z}$ and $t_{\rm o} = (n + 1/2)\Delta_t$:

$$\begin{aligned} \mathcal{E}_z\big|^{n+1}_{i,j,k+1/2} = \mathcal{E}_z\big|^n_{i,j,k+1/2} &\\ + \frac{\Delta_t}{\epsilon\big|_{i,j,k+1/2}\Delta_x}\Big[\mathcal{H}_y\big|^{n+1/2}_{i+1/2,j,k+1/2} - \mathcal{H}_y\big|^{n+1/2}_{i-1/2,j,k+1/2}\Big] &\\ - \frac{\Delta_t}{\epsilon\big|_{i,j,k+1/2}\Delta_y}\Big[\mathcal{H}_x\big|^{n+1/2}_{i,j+1/2,k+1/2} - \mathcal{H}_x\big|^{n+1/2}_{i,j-1/2,k+1/2}\Big]. & \end{aligned} \tag{2.10}$$

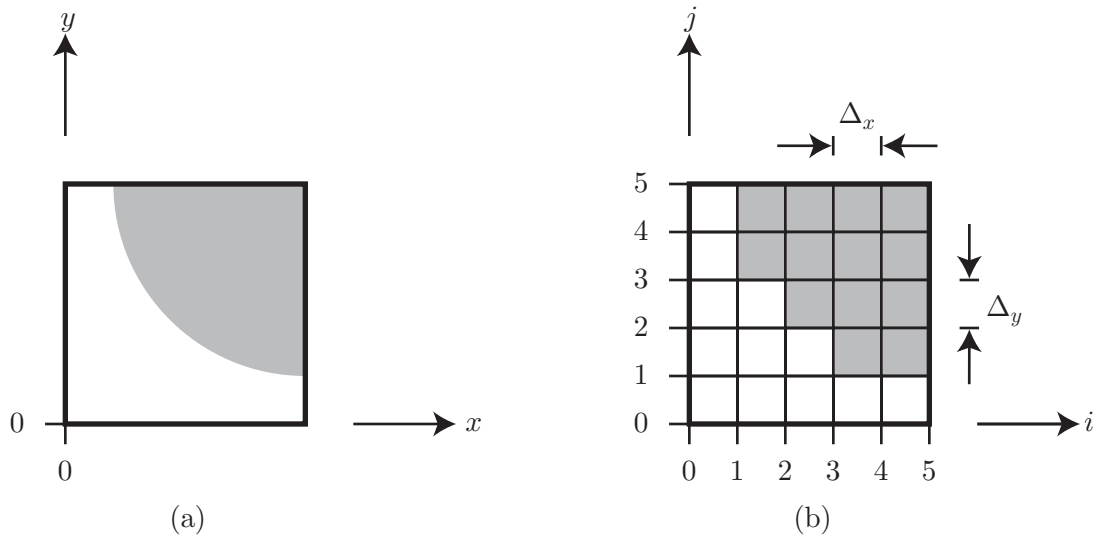


Figure 2.2: Illustration of the discretization process. On the left is a cylindrical dielectric wedge. On the right is a staircased approximation to the object suitable for modeling using the FDTD method.

Notice that (2.10) is an update equation that relates a future value of $\mathcal{E}_z$ to past values of $\mathcal{E}_z$, $\mathcal{H}_x$, and $\mathcal{H}_y$. As written, the update has two multiplies and four add/subtracts. If the field components are scaled by the cell length, for example, $\mathcal{E}_z^\Delta = \Delta_z \mathcal{E}_z$, fewer operations are required, and the update equation becomes

$$\begin{aligned}\mathcal{E}_z^\Delta\big|_{i,j,k+1/2}^{n+1} &= \mathcal{E}_z^\Delta\big|_{i,j,k+1/2}^{n} \\ &\quad + \frac{\Delta_t \Delta_z}{\epsilon|_{i,j,k+1/2}\Delta_x\Delta_y}\Big[\mathcal{H}_y^\Delta\big|_{i+1/2,j,k+1/2}^{n+1/2} - \mathcal{H}_y^\Delta\big|_{i-1/2,j,k+1/2}^{n+1/2} \\ &\quad\quad - \mathcal{H}_x^\Delta\big|_{i,j+1/2,k+1/2}^{n+1/2} + \mathcal{H}_x^\Delta\big|_{i,j-1/2,k+1/2}^{n+1/2}\Big].\end{aligned} \tag{2.11}$$

This is the basic form that will be used in this thesis. Similar equations can be derived for the remaining field components.

Modeling a structure using the FDTD method involves approximating the structure using material blocks. The process is illustrated in Figure 2.2. The original structure is "staircased" as closely as possible using cubes, and the material properties are then constant across each cube.

To ensure stability, the time step $\Delta_t$ must be sufficiently small. A necessary and sufficient

condition for stability is [3]

$$\Delta_t < \frac{1}{c\sqrt{\left(\frac{1}{\Delta_x}\right)^2 + \left(\frac{1}{\Delta_y}\right)^2 + \left(\frac{1}{\Delta_z}\right)^2}}. \tag{2.12}$$

For accuracy, the space steps must be electrically small. A commonly used rule of thumb is

$$\Delta_{x,y,z} < \frac{\lambda}{20}, \tag{2.13}$$

in which $\lambda$ is the minimum wavelength of interest. Since the cells are electrically small, the staircased approximation is usually very good.

## *2.2 Order of Accuracy*

The FDTD method is a second-order accurate numerical technique. This statement means that the error introduced by numerical approximations is reduced by a factor of $r^2$ when the cell size is decreased by a factor of $r$. This follows directly from the finite difference approximation. We start with the Taylor series for $f(x + \Delta_x/2)$ and $f(x - \Delta_x/2)$:

$$f(x + \Delta_x/2) = f(x) + \frac{\Delta_x}{2} f'(x) + \frac{\Delta_x^2}{8} f''(x) + \frac{\Delta_x^3}{48} f^{(3)}(x_f) \tag{2.14}$$

$$f(x - \Delta_x/2) = f(x) - \frac{\Delta_x}{2} f'(x) + \frac{\Delta_x^2}{8} f''(x) - \frac{\Delta_x^3}{48} f^{(3)}(x_b), \tag{2.15}$$

in which $x \leq x_f \leq x + \Delta_x/2$ and $x - \Delta_x/2 \leq x_b \leq x$ [42]. We next subtract (2.15) from (2.14) and solve for $f'(x)$:

$$\begin{aligned} f'(x) &= \frac{f(x + \Delta_x/2) - f(x - \Delta_x/2)}{\Delta_x} - \frac{\Delta_x^2}{48}\left[f^{(3)}(x_f) + f^{(3)}(x_b)\right] \\ &= \frac{f(x + \Delta_x/2) - f(x - \Delta_x/2)}{\Delta_x} + \mathcal{O}(\Delta_x^2). \end{aligned} \tag{2.16}$$

The remainder term $\mathcal{O}(\Delta_x^2)$ is second order with respect to the step size.

## *2.3 Dispersion*

In free space, the wave number $k$ is defined as

$$\frac{\omega}{c} = k. \tag{2.17}$$

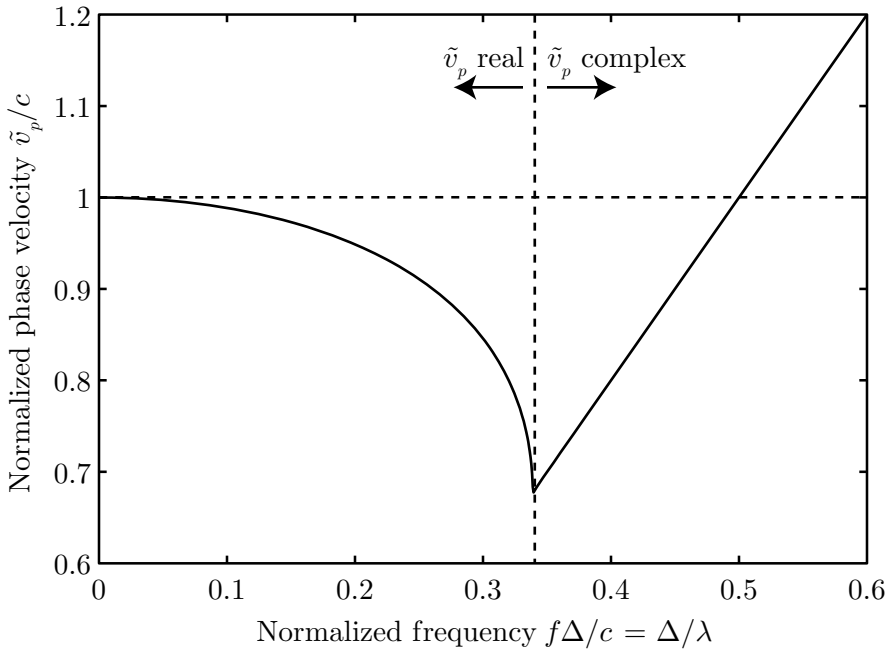


Figure 2.3: Normalized numerical phase velocity versus normalized frequency. For this plot, the FDTD cells are cubes with side length $\Delta$, the time step is $\Delta_t = 0.99\Delta/(c\sqrt{3})$, and $\hat{k} = \hat{x}$. The horizontal dashed line is the free space phase velocity, $v_p = c$. The vertical dashed line marks the transition from real to complex $\tilde{v}_p$.

For a plane wave propagating in an arbitrary direction $\hat{k}$, the vector wave number is $\vec{k} = k\hat{k}$. In this case, the dispersion relation can be written as

$$\frac{\omega^2}{c^2} = \vec{k} \cdot \vec{k}. \tag{2.18}$$

The phase velocity, $v_p = \omega/k$, is equal to the speed of light $c$.

In the FDTD grid, the dispersion relation is more complex. If we first define a numerical wave number $\tilde{k}$, numerical wave vector $\vec{K}$, and numerical angular frequency $\Omega$,

$$\vec{K} = \sum_{i=x,y,z} \frac{2}{\Delta_i} \sin\left(\frac{\tilde{k}\hat{k} \cdot \hat{\imath}\Delta_i}{2}\right)\hat{\imath} \tag{2.19}$$

$$\Omega = \frac{2}{\Delta_t} \sin\left(\frac{\omega\Delta_t}{2}\right), \tag{2.20}$$

the numerical dispersion relation can be written in a concise form [16, 43]:

$$\frac{\Omega^2}{c^2} = \vec{K} \cdot \vec{K}. \tag{2.21}$$

This equation can be solved for the numerical wavenumber $\tilde{k}$ using Newton's method. The numerical phase velocity is then $\tilde{v}_p = \omega/\text{real}(\tilde{k})$. A plot of the numerical phase velocity

versus frequency is shown in Figure 2.3. Note that $\vec{K} \rightarrow \vec{k}$ and $\Omega \rightarrow \omega$ in the limit for small cell sizes.

There are several interesting observations that can be made about this plot. First, the numerical phase velocity is frequency-dependent. The numerical phase velocity is close to $c$ when the cell size is small compared to the wavelength. As the frequency increases, the numerical phase velocity decreases. This implies that low-frequency waves will travel faster than high-frequency waves in the grid. As the frequency continues to increase, a critical point is reached. Past this point, the numerical phase velocity increases, and the numerical wavenumber is complex. In this region, plane waves decay as they travel across the grid. If the cell size is greater than $\lambda/2$, the phase velocity is greater than the speed of light. This observation will become relevant in the implementation of periodic boundary conditions.

## *2.4 Plane-Wave Injector*

Some of the earliest applications of the FDTD method were scattering problems. Taflove and Brodwin used the method to solve for the scattering from dielectric cylinders in 1975 [3]. They used a "soft" line source which launched a plane wave in both directions, and thus was not a true plane-wave injector. The total-field/scattered-field interface approach was first suggested by Merewether et al. in 1980 using equivalent currents on a closed Huygens' surface [13]. Mur suggested direct modification of the update equations on the interface by adding or subtracting the incident field, as appropriate [5]. This is the approach we use in this thesis.

Referring to Figure 2.4, we can see that there are three types of fields: incident field $\vec{\mathcal{E}}_i$, scattered field $\vec{\mathcal{E}}_s$, and total field $\vec{\mathcal{E}}_t$. The FDTD grid has been divided into a total field region and a scattered field region. For the labeled total field $\mathcal{E}_{t,z}^{\Delta}$, the update equation

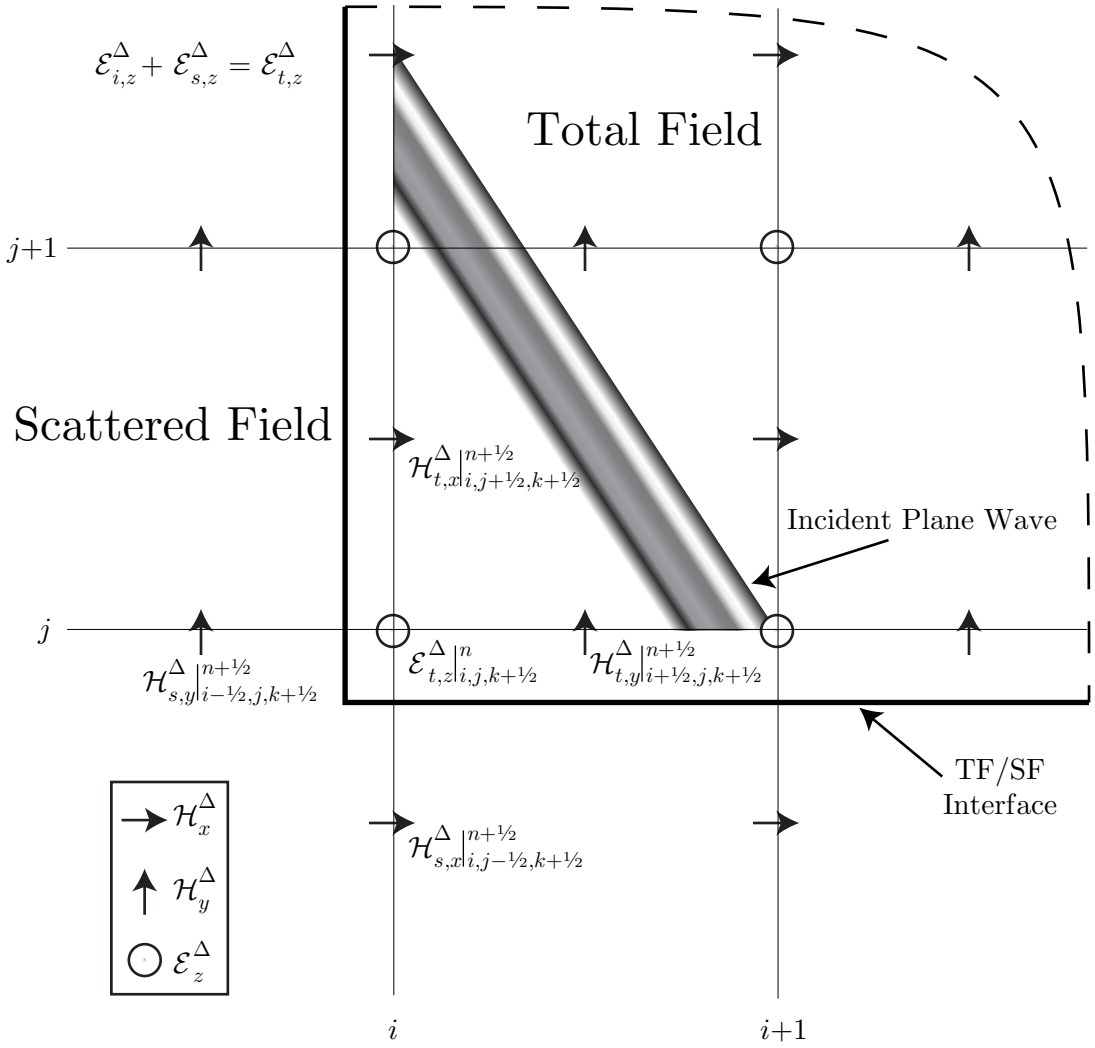


Figure 2.4: Schematic showing the division of the FDTD grid into the total field and scattered field regions.

(using scaled field values, and assuming that the entire region is free space) is:

$$\begin{aligned}
\mathcal{E}^{\Delta}_{t,z}\big|^{n+1}_{i,j,k+1/2} &= \mathcal{E}^{\Delta}_{t,z}\big|^{n}_{i,j,k+1/2} \\
&\quad + \frac{\Delta_t \Delta_z}{\epsilon_{\mathrm{o}} \Delta_x \Delta_y}\Big[\mathcal{H}^{\Delta}_{t,y}\big|^{n+1/2}_{i+1/2,j,k+1/2} - \mathcal{H}^{\Delta}_{t,y}\big|^{n+1/2}_{i-1/2,j,k+1/2} \\
&\qquad\qquad - \mathcal{H}^{\Delta}_{t,x}\big|^{n+1/2}_{i,j+1/2,k+1/2} + \mathcal{H}^{\Delta}_{t,x}\big|^{n+1/2}_{i,j-1/2,k+1/2}\Big] \\
&= \mathcal{E}^{\Delta}_{t,z}\big|^{n}_{i,j,k+1/2} \\
&\quad + \frac{\Delta_t \Delta_z}{\epsilon_{\mathrm{o}} \Delta_x \Delta_y}\Big[\mathcal{H}^{\Delta}_{t,y}\big|^{n+1/2}_{i+1/2,j,k+1/2} - \mathcal{H}^{\Delta}_{s,y}\big|^{n+1/2}_{i-1/2,j,k+1/2} \\
&\qquad\qquad - \mathcal{H}^{\Delta}_{t,x}\big|^{n+1/2}_{i,j+1/2,k+1/2} + \mathcal{H}^{\Delta}_{s,x}\big|^{n+1/2}_{i,j-1/2,k+1/2}\Big] \\
&\quad \left\{ + \frac{\Delta_t \Delta_z}{\epsilon_{\mathrm{o}} \Delta_x \Delta_y}\Big[\mathcal{H}^{\Delta}_{i,x}\big|^{n+1/2}_{i,j-1/2,k+1/2} - \mathcal{H}^{\Delta}_{i,y}\big|^{n+1/2}_{i-1/2,j,k+1/2}\Big] \right\}.
\end{aligned} \tag{2.22}$$

In the final equation, the update equation has been written in terms of available field quantities plus the correction for the incident field (in braces). Similar equations can be found for the remaining field components.

Mur's original suggestion was to use the analytical expression for the incident field in (2.22). The problem with this approach is that it completely ignores numerical dispersion. The incident field is assumed to travel across the total field region at the speed of light. However, as previously shown, the phase velocity in the FDTD grid is less than $c$, and therefore the cancelation will be imperfect.

There have been several proposals to more accurately calculate the incident field. One approach is to calculate the incident field using an auxiliary one-dimensional simulation [17]. Such an approach works perfectly for grid-aligned propagation. Through interpolation, it can be extended to non grid-aligned propagation, but the calculation will be less accurate.

A more general solution is to use the numerical dispersion relation given in (2.21) in the calculation of the incident field. For our purposes, the incident field in the time domain is

$$\vec{\mathcal{E}}_i(\vec{r};t) = \hat{e}\,\mathcal{G}(t - \hat{k}_i \cdot \vec{r}/c), \tag{2.23}$$

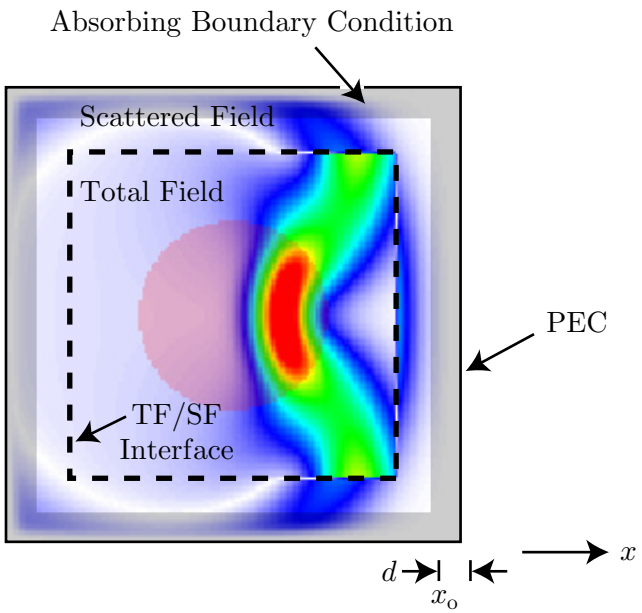


Figure 2.5: Structure of an FDTD grid with a plane wave injector and an absorbing boundary condition (CPML).

in which $\mathcal{G}$ is arbitrary scalar function. In the frequency domain, the incident field is

$$\vec{E}_i(\vec{r};\omega) = \hat{e}\, G(\omega) e^{-j\tilde{k}\hat{k}_i\cdot\vec{r}}. \tag{2.24}$$

$G(\omega)$ is the Fourier transform of $\mathcal{G}(t)$, and the numerical wavenumber $\tilde{k}$ has been substituted for the free space wavenumber $k$. An inverse Fourier transform can then be used to calculate the incident field in the time domain:

$$\vec{\mathcal{E}}_i(\vec{r};t) = \hat{e}\, \mathcal{F}^{-1}\left[G(\omega) e^{-j\tilde{k}\hat{k}_i\cdot\vec{r}}\right]. \tag{2.25}$$

In practice, the scalar function $G(\omega)$ is known in advance. Therefore, it is possible to accurately compute the incident field in the grid without performing an auxiliary FDTD simulation.

When the incident field is calculated in this way, the injector leakage is approximately 90 dB below the waveform peak. This level is sufficiently small that the injector leakage is not a limiting factor in the accuracy of the FDTD simulation.

## *2.5 Convolutional Perfectly Matched Layer*

For an open region problem, such as a scattering or antenna problem, it is necessary to terminate the FDTD grid using some form of absorbing boundary condition. In this work,

the convolutional perfectly matched layer (CPML) is used, which is an artificial lossy material that is impedance matched to free space [12]. As shown in Figure 2.5, the PML is implemented in the scattered field region. Inside the CPML, the spatial coordinates are "stretched":

$$\tilde{x} = \int_{x_o}^{x} s_x(x')dx'. \tag{2.26}$$

The stretching term $s_x$ uses the complex frequency shifted form:

$$s_x(x) = \kappa_x(x) + \frac{\sigma(x)}{a_x(x) + j\omega\epsilon_o}. \tag{2.27}$$

A wave incident on the CPML passes into the material without reflection. It is then attenuated inside the CPML, reflects off the outer PEC boundary, and then is attenuated more on the return trip. The portion of the wave that is not absorbed is reflected back into the simulation space. The ratio of the reflected to incident wave is the reflection coefficient $R$. For maximum accuracy, $R$ should be as small as possible.

The PML parameters $a_x$, $\kappa_x$, and $\sigma_x$ are graded as a function of depth $x - x_o$ into the PML. In this work, polynomial grading is used. If the thickness of the PML is $d$, the grading is

$$a_x(x) = a_{x,\max}\left(\frac{d - x + x_o}{d}\right)^m \tag{2.28}$$

$$\kappa_x(x) = 1 + (\kappa_{x,\max} - 1)\left(\frac{x - x_o}{d}\right)^m \tag{2.29}$$

$$\sigma_x(x) = \sigma_{x,\max}\left(\frac{x - x_o}{d}\right)^m. \tag{2.30}$$

The theoretical reflection coefficient $R_{\text{theory}}$ for a normally incident plane wave, assuming $\kappa_x = 1$ and $a_x = 0$, is

$$R_{\text{theory}} = e^{-2\eta_o\sigma_{x,\max}d/(m+1)}. \tag{2.31}$$

For a given value of the reflection coefficient, the maximum value of $\sigma_x$ can be found:

$$\sigma_{x,\max} = -\frac{(m+1)\ln(R_{\text{theory}})}{2\eta_o d}. \tag{2.32}$$

The actual reflection coefficient $R_{\text{num}}$ for the CPML as implemented in the FDTD method is shown in Figure 2.6. This value was calculated by launching a normally incident

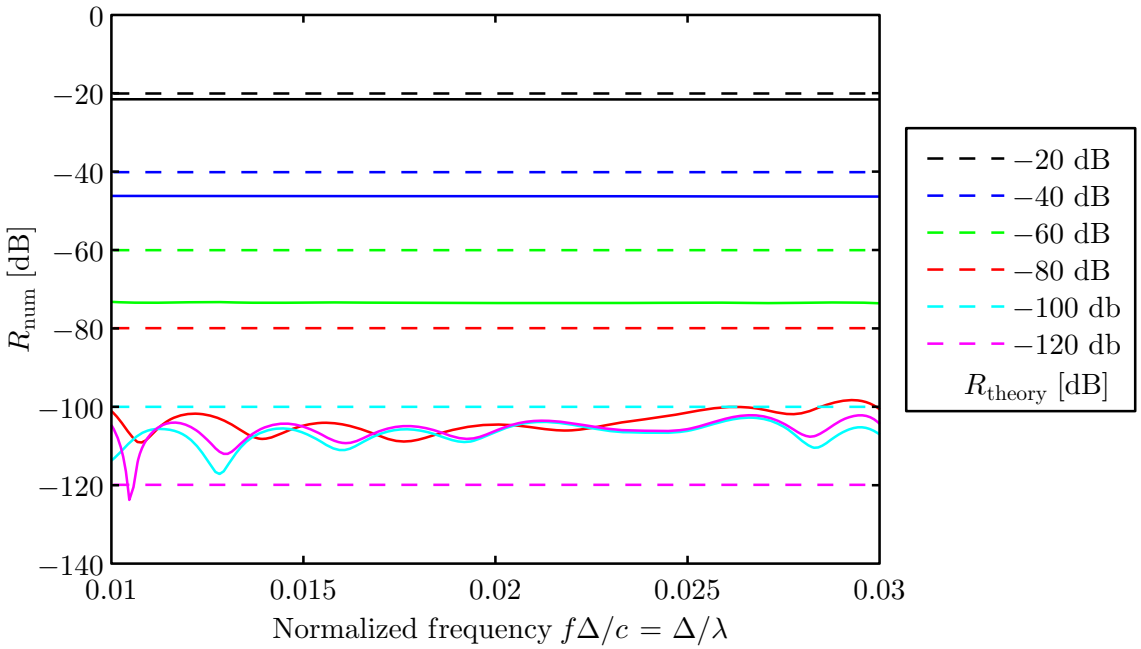


Figure 2.6: Numerical performance of the CPML for a normally incident plane wave. Each curve is for a different value of $R_{\text{theory}}$. In all cases, $a_x = 0$, $\kappa_x = 1$, $m = 3.5$, and $d = 10\Delta_x$.

plane wave towards the CPML and measuring the magnitude of the field in the scattered field region. For each value of $R_{\text{theory}}$, the corresponding value of $\sigma_{x,\max}$ is found using (2.32). The CPML actually performs better than the theory suggests, which is surprising but has been noted before in the literature [44]. Past a certain point, increasing $R_{\text{theory}}$ does not result in a corresponding increase in $R_{\text{num}}$. This behavior is examined more closely in Figure 2.7. In this plot, we examine how $R_{\text{num}}$ changes as a function of $R_{\text{theory}}$ for different thicknesses. It is clear that the maximum performance of the CPML increases as the thickness increases. For $d = 10\Delta_x$, the performance appears to peak for $R_{\text{theory}} \approx -100\,\text{dB}$. This is the value used in this thesis.

An advantage of the CPML versus other implementations is that the performance is improved for evanescent waves and waves that are obliquely incident on the PML [45]. In addition, since the CPML is implemented as a set of current sources in the FDTD update equations, it is easy to model structures in which a material penetrates the CPML. This is useful, for example, in the modeling of a infinitely thick substrate (a half space).

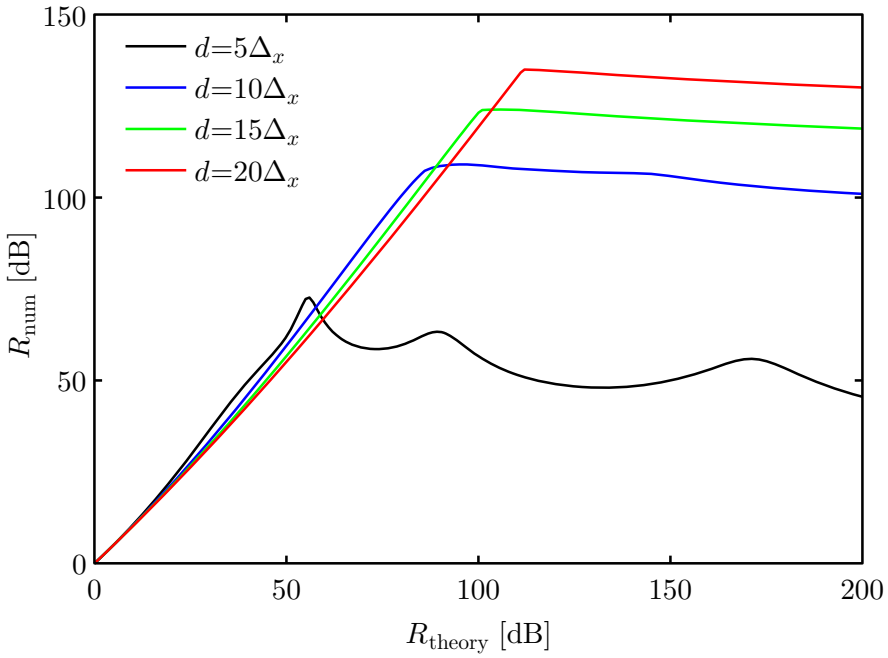


Figure 2.7: Numerical performance of the CPML for a normally incident plane wave. Each curve is for a different thickness of the PML $d$. In all cases, $a_x = 0$, $\kappa_x = 1$, $m = 3.5$.

## *2.6 Implementation of FDTD on a Parallel Distributed Memory Computer Cluster*

The FDTD method requires substantial computational resources. In order to be able to perform simulations of electrically large structures, the software developed as part of this research was implemented on a parallel, distributed memory computer cluster (a Beowulf cluster). The parallel scheme is shown in Figure 2.8. The grid at the top is distributed onto two computers, known as nodes. All of cells with $i \leq i_o$ are computed on node 1, and all of the cells with $i \geq i_o$ are computed on node 2. At the end of each time step, the tangential magnetic field components at $i = i_o \pm 1/2$ are copied to the other node. In this way, it is possible to model a significantly larger problem than would be possible on a single computer. A typical workstation PC has $2 - 4$ CPU cores and $2 - 4$ GB of memory. In contrast, the cluster in the Electromagnetics Laboratory, shown in Figure 2.9, consists of approximately 100 interconnected computers with approximately 64 GB of total memory. This cluster is actually rather small compared to many clusters in the world.

The division method outlined above is not the most computationally efficient, since the

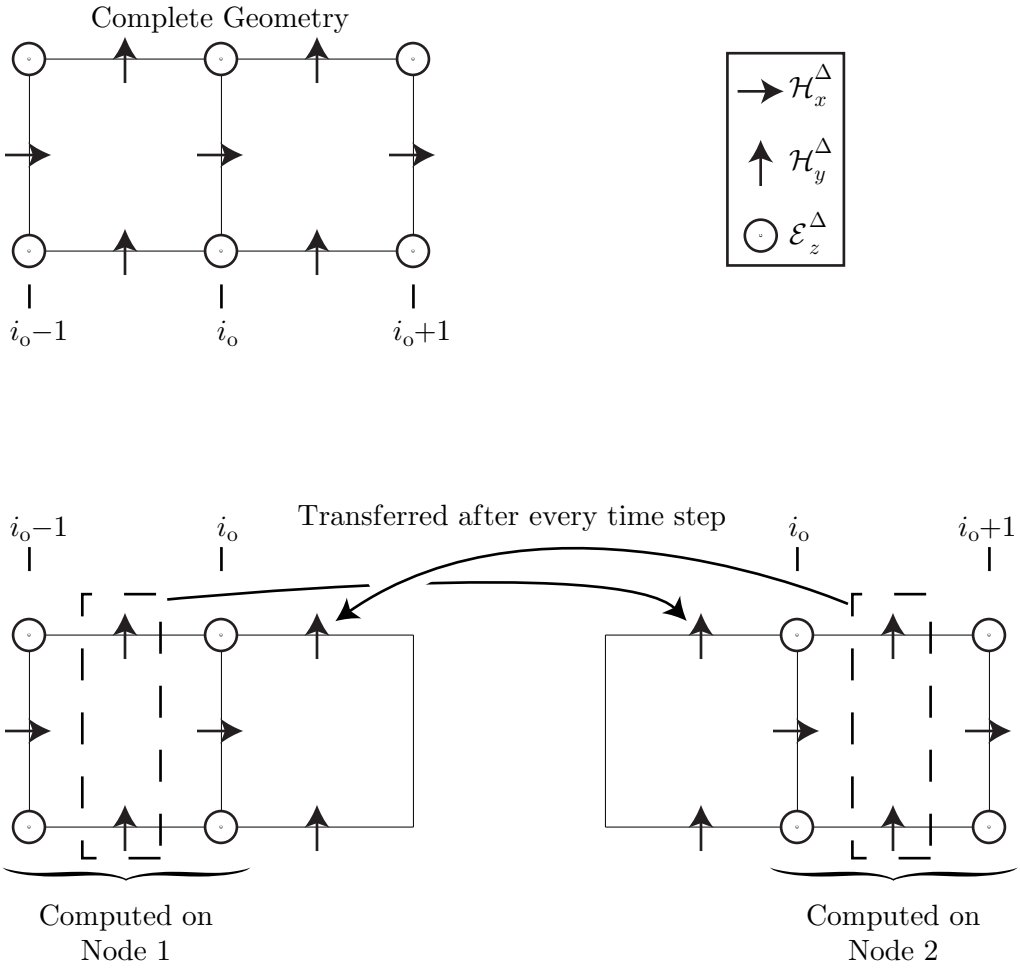


Figure 2.8: Schematic showing the division of the FDTD grid across two computer nodes.

Figure 2.9: Photograph of a portion of the computer cluster in the Georgia Tech Electromagnetics Laboratory.

components at $i = i_o$ are computed on both nodes. An alternative method involves sending the tangential electric field components in one direction and the magnetic field components in the other. However, the method outlined here ends up being easier to program, and for a large problem, the additional overhead is negligible.

## *2.7 Summary*

In this chapter, we have reviewed some of the more important aspects of the FDTD method. Numerous other aspects, including material modeling and near-to-far-field transforms, have not been discussed. The near-to-far-field transform will be discussed in Chapter 5. The other material is not unique to this thesis and is documented elsewhere [17].

# CHAPTER III

# PERIODIC BOUNDARY CONDITIONS IN FDTD THE TWO-DIMENSIONAL CASE

In this chapter, a new method for incorporating periodic boundary conditions into the FDTD method is presented. We start by reviewing the theory of periodic structures. We then explain why periodic boundary conditions are difficult to implement in the time domain, and present the new method. Some strategies to improve the efficiency are shown, and finally the method is demonstrated by comparing the results to those from other computational techniques for periodic structures. Portions of this work were previously published in [46].

## *3.1 Periodic Boundary Conditions in the Time Domain*

In the following discussion, we assume a two-dimensional structure, such as the one shown in Figure 3.1, that is finite in the $x$ direction, periodic in the $y$ direction with period $y_p$, and invariant in the $z$ direction. This structure is an array, and the volume $0 < y < y_p$ is the "unit cell" of the array. The excitation is any incident field that satisfies

$$\vec{\mathcal{E}}_i(\vec{r} + ny_p\hat{y}; t) = \vec{\mathcal{E}}_i(\vec{r}; t - n\tau_{dy}), \quad n = \text{integer}, \tag{3.1}$$

in which $\tau_{dy}$ is a time delay. Only cases for which $\tau_{dy} < y_p/c$ are considered in this work.

An interesting excitation that satisfies this form is a uniform plane wave,

$$\vec{\mathcal{E}}_i(\vec{r}; t) = \hat{e}\,\mathcal{G}(t - \hat{k}_i \cdot \vec{r}/c), \tag{3.2}$$

in which $\mathcal{G}$ is an arbitrary scalar waveform. In this case, we have

$$\vec{\mathcal{E}}_i(\vec{r} + ny_p\hat{y}; t) = \hat{e}\,\mathcal{G}\big[t - (\hat{k}_i \cdot \vec{r})/c - (\hat{k}_i \cdot \hat{y})ny_p/c\big] \tag{3.3}$$

$$\vec{\mathcal{E}}_i(\vec{r}; t - n\tau_{dy}) = \hat{e}\,\mathcal{G}\big[t - (\hat{k}_i \cdot \vec{r})/c - n\tau_{dy}\big]. \tag{3.4}$$

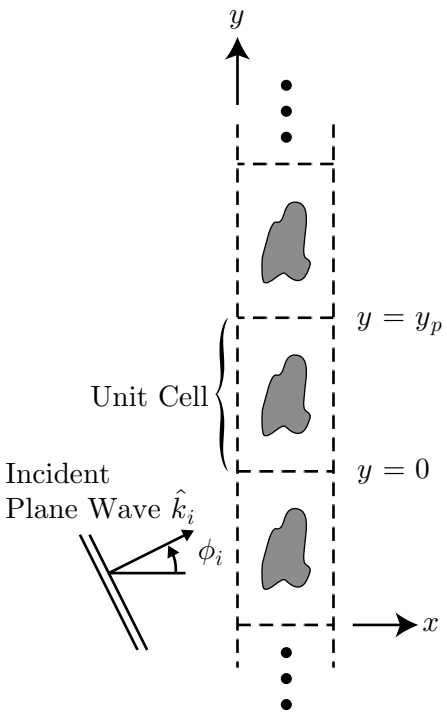


Figure 3.1: Schematic drawing for the two-dimensional infinite array. The period for the array is $y_p$.

Therefore, the uniform plane wave satisfies (3.1) with

$$\tau_{dy} = \frac{(\hat{k}_i \cdot \hat{y}) y_p}{c}. \tag{3.5}$$

Since the structure and the excitation are periodic, the electromagnetic field $\vec{\mathcal{F}}$ is the same in every unit cell of the array except for the time shift. Therefore, (3.1) applies to the scattered field (and, by extension, to the total field):

$$\vec{\mathcal{F}}(\vec{r} + n y_p \hat{y}; t) = \vec{\mathcal{F}}(\vec{r}; t - n\tau_{dy}), \quad n = \text{integer}, \tag{3.6}$$

At first inspection, this equation seems to be a useable boundary condition. However, for a marching-in-time procedure, such as the FDTD method, it can present a problem, because it requires time-advanced values of the field that have not yet been computed.

The difficulty can be explained using Figure 3.2. The time delay $\tau_{dy}$ has been converted into a discrete delay $N_{dy}$, according to

$$N_{dy} = \frac{\tau_{dy}}{\Delta_t}. \tag{3.7}$$

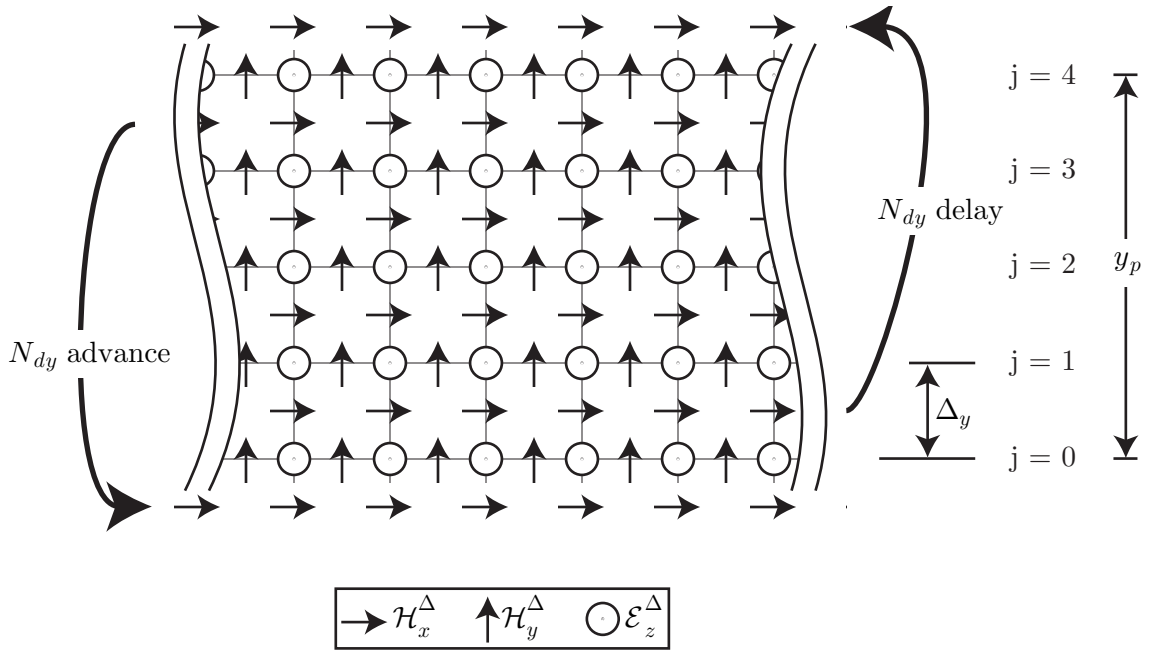


Figure 3.2: Two-dimensional FDTD grid showing how periodic boundary conditions can be used to terminate the grid. The top and bottom boundaries are periodic. The left and right boundaries are terminated with an absorbing boundary condition.

The example has four rows of FDTD cells along the $y$ direction; the $x$ direction is terminated with an absorbing boundary condition, though this detail is not shown. The grid is periodic with a period $y_p = 4\Delta_y$. We wish to update every field component in the range $0 \leq j \leq 4$. Therefore, the magnetic field components just past the edge of the grid at $j = -1/2$ and $j = 4 1/2$ are needed. These components can be related to components inside the grid using the periodic shift conditions:

$$\mathcal{H}_x^\Delta\big|_{i,4\,1/2}^{n+1/2} = \mathcal{H}_x^\Delta\big|_{i,1/2}^{n+1/2-N_{dy}} \tag{3.8}$$

$$\mathcal{H}_x^\Delta\big|_{i,-1/2}^{n+1/2} = \mathcal{H}_x^\Delta\big|_{i,3\,1/2}^{n+1/2+N_{dy}}. \tag{3.9}$$

The first condition presents no difficulty; these required values are in the past and are therefore available. The second condition, however, is more troublesome. Since the required values occur in the future, they are not available. Note that the boundary condition has been expressed in terms of the tangential magnetic field; it could just as easily be expressed in terms of the tangential electric field, but the algorithm is somewhat easier to implement using the tangential magnetic field.

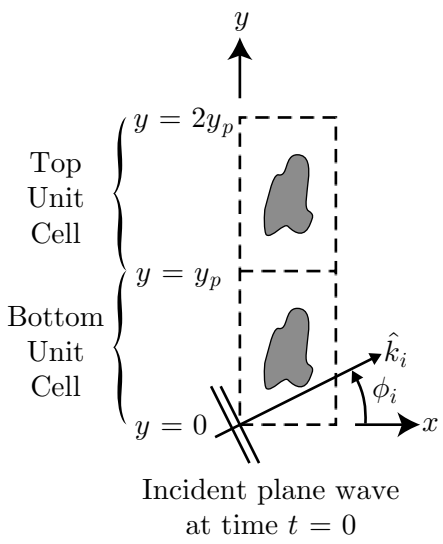


Figure 3.3: Structure formed from two adjacent unit cells of the array. The incident wave first encounters the structure at $x = 0, y = 0$ when $t = 0$.

### *3.2 Development of the Algorithm*

In this section, a simple graphical description of the algorithm is presented. Consider the geometry shown in Figure 3.3. It consists of two adjacent unit cells of the array; they will be referred to as the top unit cell and the bottom unit cell. The excitation is an incident, uniform plane wave propagating in the direction $\hat{k}_i$ that is a pulse of finite duration in time. The electromagnetic field in the structure is initially zero, and the incident wave first encounters the structure at time $t = 0$ ($x = 0, y = 0$, at the lower left-hand corner in Figure 3.3). At this time a truncation error is caused by the lack of information on the boundary at $y = 0$ (it is an error in the sense that the field is not the correct one for the infinite structure).

The key observation is that this error travels at the speed of light $c$, so it takes the time

$$\tau_{ey} = y_p/c \tag{3.10}$$

to traverse the bottom unit cell and reach the boundary at $y = y_p$. On the other hand, the incident wave takes the time

$$\tau_{dy} = (\hat{k}_i \cdot \hat{y})y_p/c \tag{3.11}$$

to traverse the bottom unit cell and reach the boundary. Thus, for $\phi_i < 90°$, we have

$\tau_{dy} < \tau_{ey}$; that is, the incident plane wave reaches the boundary before the error. This means that there will be an interval in time $\tau_{dy} < t < \tau_{ey}$ during which "good" data is added to the top unit cell; that is, values of the field will be determined in the unit cell that are not corrupted by the truncation error. Now we must construct a repetitive procedure in which this observation is repeatedly used to obtain the uncorrupted electromagnetic field throughout a unit cell of the *infinite array* for the entire time of observation.

The repetitive procedure will be explained using the illustration in Figure 3.4. This will be done for the first two cycles of the procedure; the top row in Figure 3.4 is for the first cycle, and the middle row is for the second cycle. A portion of the third cycle is shown in the bottom row. In each row, we show the evolution of the field with time within the same pair of adjacent unit cells shown in Figure 3.3.

Initially, at time $t = 0$, the field is zero everywhere in both unit cells (diagram on the left in the top row). The field on the upper boundary of the top unit cell ($y = 2y_p$) is always a time-delayed copy of the field on the boundary between the two unit cells ($y = y_p$). The field at the lower boundary ($y = 0$) is left alone; recall this is the source of the error. Now as time advances (going from left to right in the top row), the error from the lower boundary moves upward through the bottom unit cell. The region in which there is an error is patterned in the figure. As expected, the excitation moves upward faster than the error. At time $t = \tau_{ey}$ (diagram on the right in the top row), the error has just reached the upper boundary of the bottom unit cell ($y = y_p$). Hence, at this time the field everywhere in the top unit cell is still correct. Notice that this cycle of the procedure (cycle 1) obtains the correct field in a unit cell of the *infinite array* from the time $t' = t - \tau_{dy} = 0$ when the excitation first enters the lower left-hand corner of the unit cell to the time $t' = \tau_{ey} - \tau_{dy}$.

Now we can use the field in the top unit cell at the times $t = \tau_{ey} - \tau_{dy}$ and $t = \tau_{ey}$ (unit cells in the middle and right in the top row) to construct the correct field in both the top and bottom unit cells at the time $t = \tau_{ey} - \tau_{dy}$. This field is shown in the diagram on the left in the middle row. It is obtained by copying the field from the top unit cell at time $t = \tau_{ey}$ (marked B) into the bottom unit cell and the field from the top unit cell at the earlier time $t = \tau_{ey} - \tau_{dy}$ (marked A) into the top unit cell.

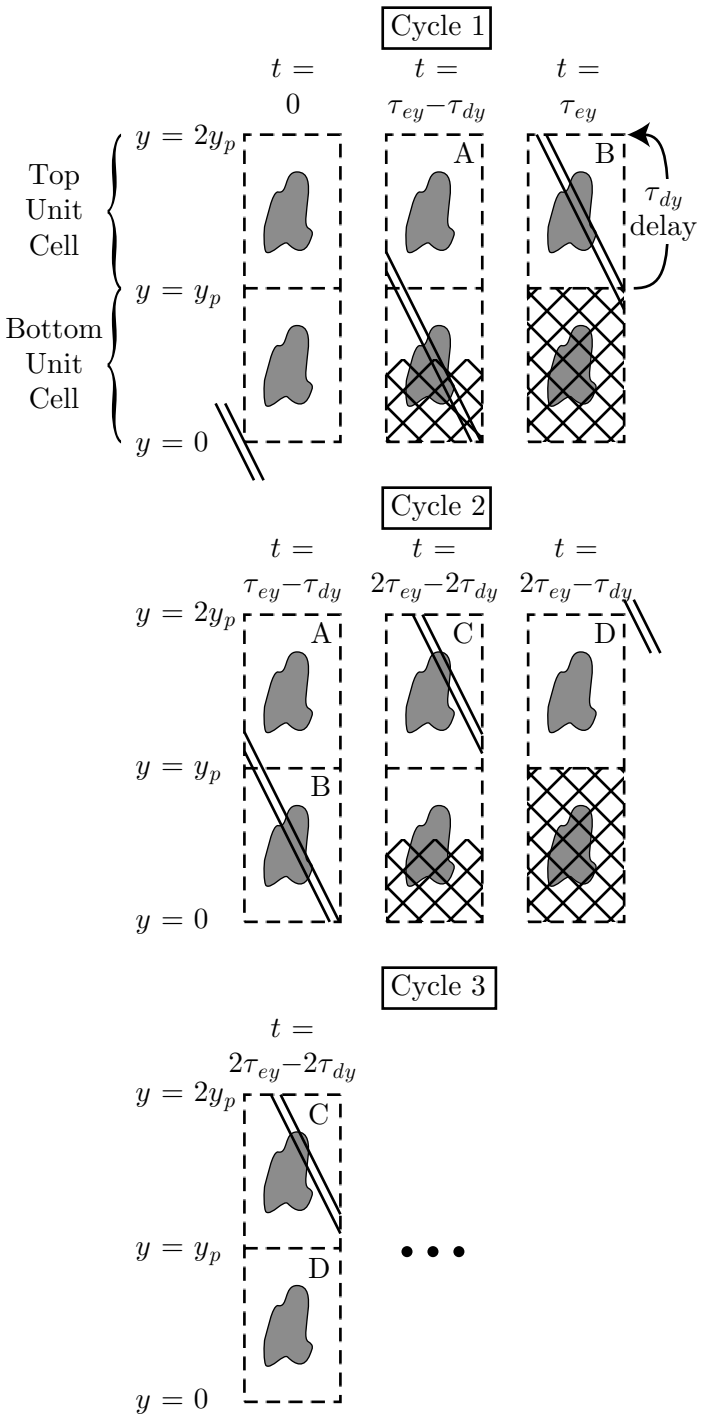


Figure 3.4: Illustration showing the development of the algorithm. The error and the excitation both start at $y = 0$ when $t = 0$. The error (patterned region) travels upwards reaching the boundary between the two unit cells at time $\tau_{ey}$, while the incident wave reaches the boundary at the earlier time $\tau_{dy} < \tau_{ey}$. The left diagram in the middle row is obtained by combining the middle and right diagrams from the top row, marked A and B. The diagram in the bottom row is obtained by combining the middle and right diagrams from the middle row, marked C and D.

The next cycle of the procedure (cycle 2) obtains the correct field in a unit cell of the *infinite array* over the time interval $\tau_{ey} - \tau_{dy} \leq t' \leq 2(\tau_{ey} - \tau_{dy})$. At the completion of cycle 2 (at time $t = 2\tau_{ey} - \tau_{dy}$), the field in the top unit cell at time $t = 2\tau_{ey} - 2\tau_{dy}$ (marked C in the middle diagram of the middle row) and time $t = 2\tau_{ey} - \tau_{dy}$ (marked D in the right diagram of the middle row) are combined to obtain the correct field in both unit cells at time $t = 2\tau_{ey} - 2\tau_{dy}$ (diagram in the bottom row). It then follows that we can obtain the field in the unit cell of the *infinite array* for any time interval $0 \leq t' \leq t'_{\text{fin}}$ by performing the above operations $n$ times, such that $n(\tau_{ey} - \tau_{dy}) > t'_{\text{fin}}$. An obvious penalty of the procedure is seen by substituting the relationships for $\tau_{ey}$ and $\tau_{dy}$ into the last expression:

$$n > \left(\frac{1}{1 - \sin\phi_i}\right)\left(\frac{ct'_{\text{fin}}}{y_p}\right). \tag{3.12}$$

As the angle $\phi_i$ approaches 90°, the number of times the operations must be repeated can become very large. This is because each cycle lasts for the period $\tau_{ey}$ but produces new information only for the period $\tau_{ey} - \tau_{dy}$.

A cost of the algorithm can be defined based on these observations. The algorithm is cheapest for normal incidence, $\phi_i = 0°$. For simulations with an incident plane wave in the direction $\phi_i$, the cost $M$ can be defined as

$$M = \frac{\text{runtime}, \phi_i}{\text{runtime}, \phi_i = 0°}. \tag{3.13}$$

This cost is plotted in Figure 3.5. As shown, the cost of the algorithm goes to infinity as the incident plane wave approaches grazing incidence.

## *3.3 Implementation of the Algorithm in the FDTD Method*

In this section, the algorithm just described is implemented in the FDTD method for a two-dimensional, transverse electric (TE) problem. In this case, only three field components are required: $\mathcal{E}_z^{\Delta}$, $\mathcal{H}_x^{\Delta}$, and $\mathcal{H}_y^{\Delta}$. The emphasis is on saving run time and storage space, so the implementation is a bit more involved than the simple outline presented in Figure 3.4. The implementation presented here is different from the one originally proposed in [46]. In the original algorithm, the boundary conditions were implemented using the tangential

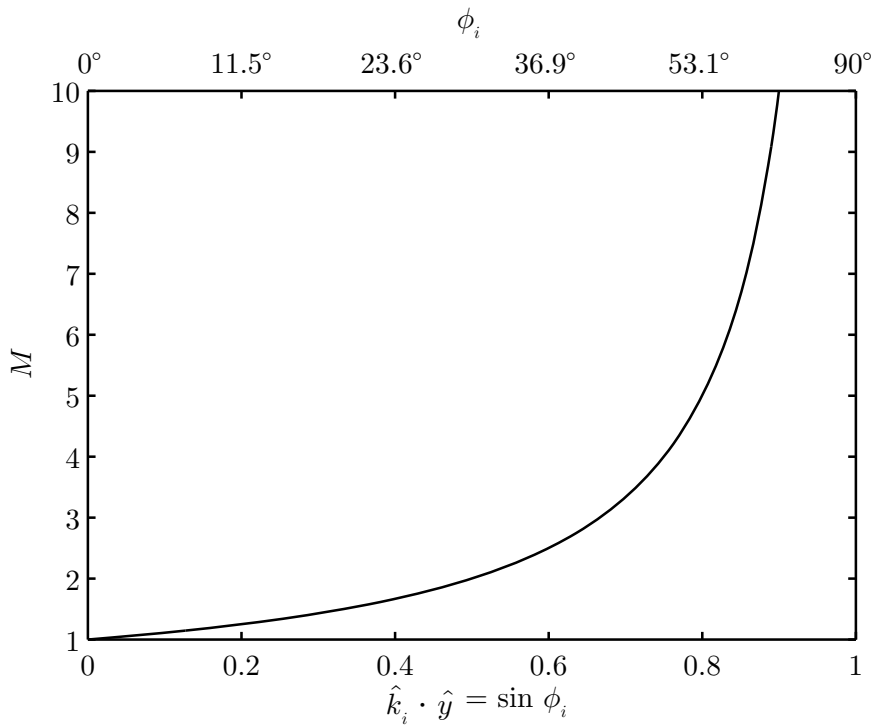


Figure 3.5: Graph showing the relative computational cost of the algorithm as a function of direction of the incident plane wave. The $y$ component of the incident wave vector is shown on the lower horizontal axis, and the corresponding angle $\phi_i$ is shown on the top vertical axis.

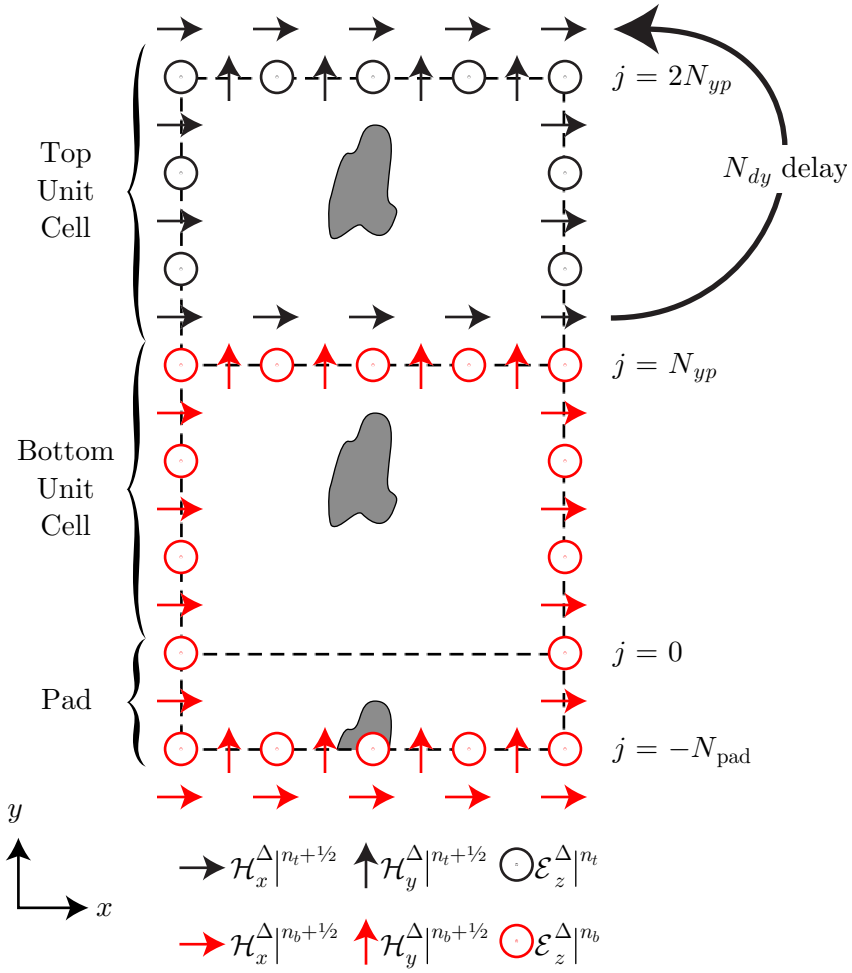


Figure 3.6: Illustration of the FDTD grid. The total grid is partitioned into two regions: The field components with black symbols are at time index $n = n_t$, and the field components with red symbols are at time index $n = n_b$.

electric field. Here we use the tangential magnetic field, which is simpler to implement and is consistent with the approach used for parallelizing the code for a Beowulf cluster.

The spatial step in the direction of periodicity, $\Delta_y$, is chosen so that $y_p = N_{yp}\Delta_y$. The time step, $\Delta_t$, is chosen so that $\Delta_t = \tau_{dy}/N_{dy}$, in which $N_{dy}$ is the smallest possible integer that still results in a stable time step. In addition, $N_{ey}$ is specified as $N_{ey} = \text{floor}(\tau_{ey}/\Delta_t)$, in which floor() is a function that returns the largest integer less than or equal to the argument. It is required that $N_{dy} < N_{ey}$; this condition is more restrictive than $\tau_{dy} < \tau_{ey}$, but it is still possible for $\tau_{dy}$ to be as close to $\tau_{ey}$ as desired by choosing a smaller time step $\Delta_t$.

A simplified FDTD grid is shown in Figure 3.6 in which the electromagnetic field components are only shown on the boundaries. The sides of the grid at $x_{\min}$ and $x_{\max}$ are terminated with a PML, but this is not shown. A pad that is a fraction of a unit cell ($N_{\text{pad}}$ FDTD cells in length) is added to the bottom of the grid; this is necessary for accuracy as will be discussed later. In Figure 3.6, the FDTD grid is partitioned into two regions with different time indices. The upper region, which is the top unit cell, includes all of the field components with black symbols and is at time index $n = n_t$. The lower region, which is the bottom unit cell plus the pad, includes all of the field components with red symbols and is at time index $n = n_b$. In addition, values of the tangential component of the magnetic field, $\mathcal{H}_x^{\Delta}$, at the boundary between the regions at $j = N_{yp} + 1/2$ are saved for the time indices $n_t + 1/2 - N_{dy}, \ldots, n_t - 1/2, n_t + 1/2$ in a buffer.

At the start of a simulation, the field is set to zero throughout the grid, the time indices are set to $n_t = N_{dy}$ and $n_b = 0$, and the buffer is filled with zeros. Referring to Figure 3.6, all of the red electric field components are at time step $n_b$ and the red magnetic field components are at time step $n_b + 1/2$. The black electric field components are at time step $n_t = n_b + N_{dy}$ and the black magnetic field components are at time $n_t + 1/2$. First, the red electric field components (those in the lower region) are updated in the usual way. Next, the red magnetic field components are updated in the usual way. The magnetic field components at $j = N_{yp} + 1/2$ are updated using data in the buffer. This is possible because the upper region is at a later time than the lower region, and thus, the buffer is filled with future field values. At the end of each loop, only $n_b$ is incremented. This procedure, which is considered stage 1, is repeated until $n_t = n_b$. Note that this procedure does not modify the data in the buffer.

Once the two time indices, $n_t$ and $n_b$, are equal, the algorithm enters stage 2. During this stage, the entire grid is updated. The electric and magnetic field updates are performed in the usual way. At the end of the magnetic field update, the earliest value is the buffer is discarded and the $\mathcal{H}_x^{\Delta}$ components at $j = N_{dy} + 1/2$ are stored. The oldest remaining values in the buffer are then used to update the magnetic field components at $j = 2N_{yp} + 1/2$. At the end of each loop, both $n_t$ and $n_b$ are incremented. This procedure is repeated until

$n_t = n_b = N_{ey}$.

At the beginning of the $n_t = n_b = N_{ey}$ loop, the data from the upper region is copied over the data in the lower region, as shown in Figure 3.7. Since the lower region is larger than the upper region, the copy also includes $N_{\text{pad}}$ rows from the top of the lower region. This operation means that the upper region is still at $n_t = N_{ey}$, but the lower region is now at $n_b = N_{ey} - N_{dy}$. The algorithm continues in stage 1 until $n_t = n_b$ once again, at which point it switches back to stage 2. The next shift occurs after $N_{ey}$ time steps. The algorithm continues in this way, periodically switching between stage 1 and stage 2, until $n_t$ reaches the desired stopping value.

As for the extra FDTD cells on the bottom of the grid, they are necessary for accuracy. In an FDTD grid, spatially undersampled waves can propagate faster than the speed of light, but with exponential attenuation [14]. This was shown in the last chapter in Figure 2.3 for $\Delta/\lambda > 0.5$. Since $N_{ey}$ was specified assuming $\tau_{ey} = y_p/c$, this type of error could enter the upper region if it originated at $j = 0$. Moving the bottom boundary down a few FDTD cells prevents this error from entering the upper region. In our experience, 10 to 20 extra FDTD cells has been sufficient.

In Figure 3.8, snapshots from FDTD simulation using the above techniques are shown. The simulation is for a plane wave propagating through free space. In the first snapshot, labeled (a), the incident field is about to enter the bottom cell. There is no need to update the top cell during this time since we are in stage 1. The simulation continues until the incident field is about to enter the top cell, as shown in (b), at which point both cells are updated (that is, the algorithm enters stage 2). As the simulation continues, the truncation error from the lower boundary travels upward. In snapshot (c), the truncation error is about to enter the top cell. At this point, the top cell is copied over the bottom, and the result is shown in (d). The algorithm then continues in stage 1, with only the bottom cell being updated. At the time step shown in (e), the lower cell and upper cell are at the same time, $n_t = n_b = N_{ey}$. At this point, the algorithm continues with both cells being updated (stage 2) until the truncation error is about to once again enter the top cell, which is shown in (f). This algorithm proceeds in this fashion, periodically switching between stage 1 and

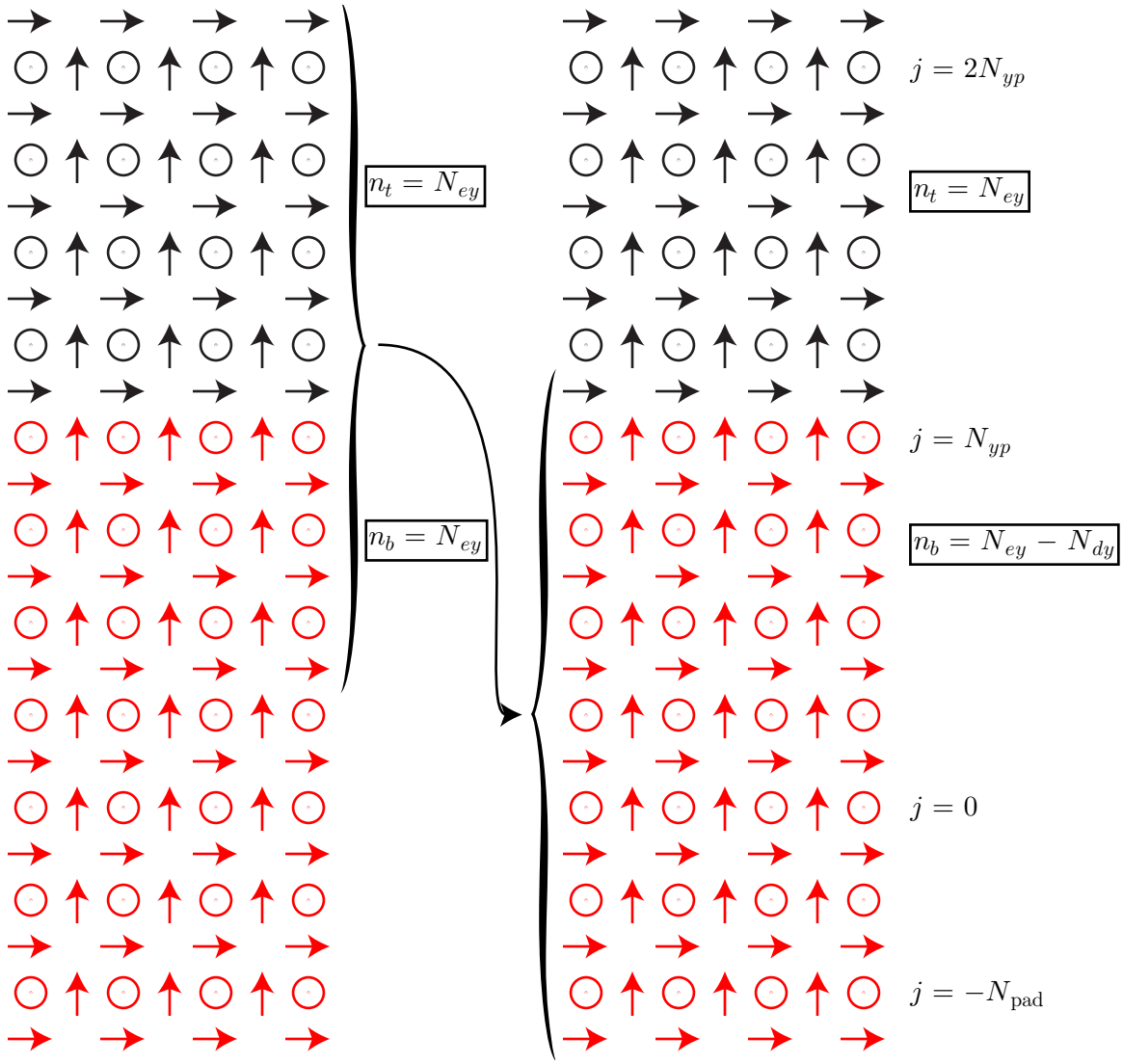


Figure 3.7: At time index $n_t = n_b = N_{ey}$, a copy procedure is used to prevent the error from entering the upper region. This procedure involves copying the indicated components from the upper region to the lower region. This procedure also resets the time index for the lower region so that $n_b \rightarrow n_b - N_{dy}$.

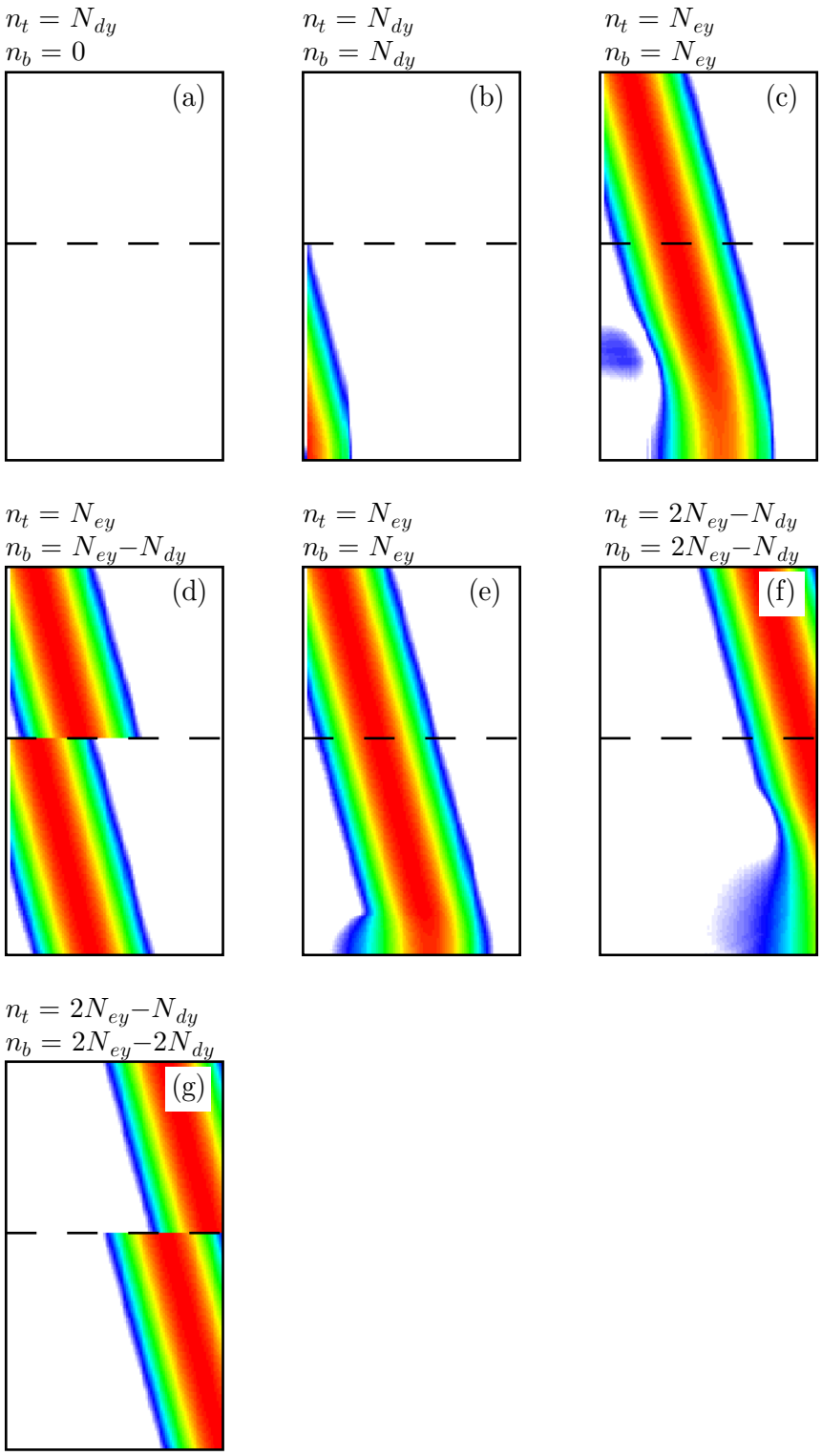


Figure 3.8: Snapshots of an FDTD simulation for a plane wave propagating in free space using periodic boundary conditions. The dashed line marks the boundary between the upper and lower regions.

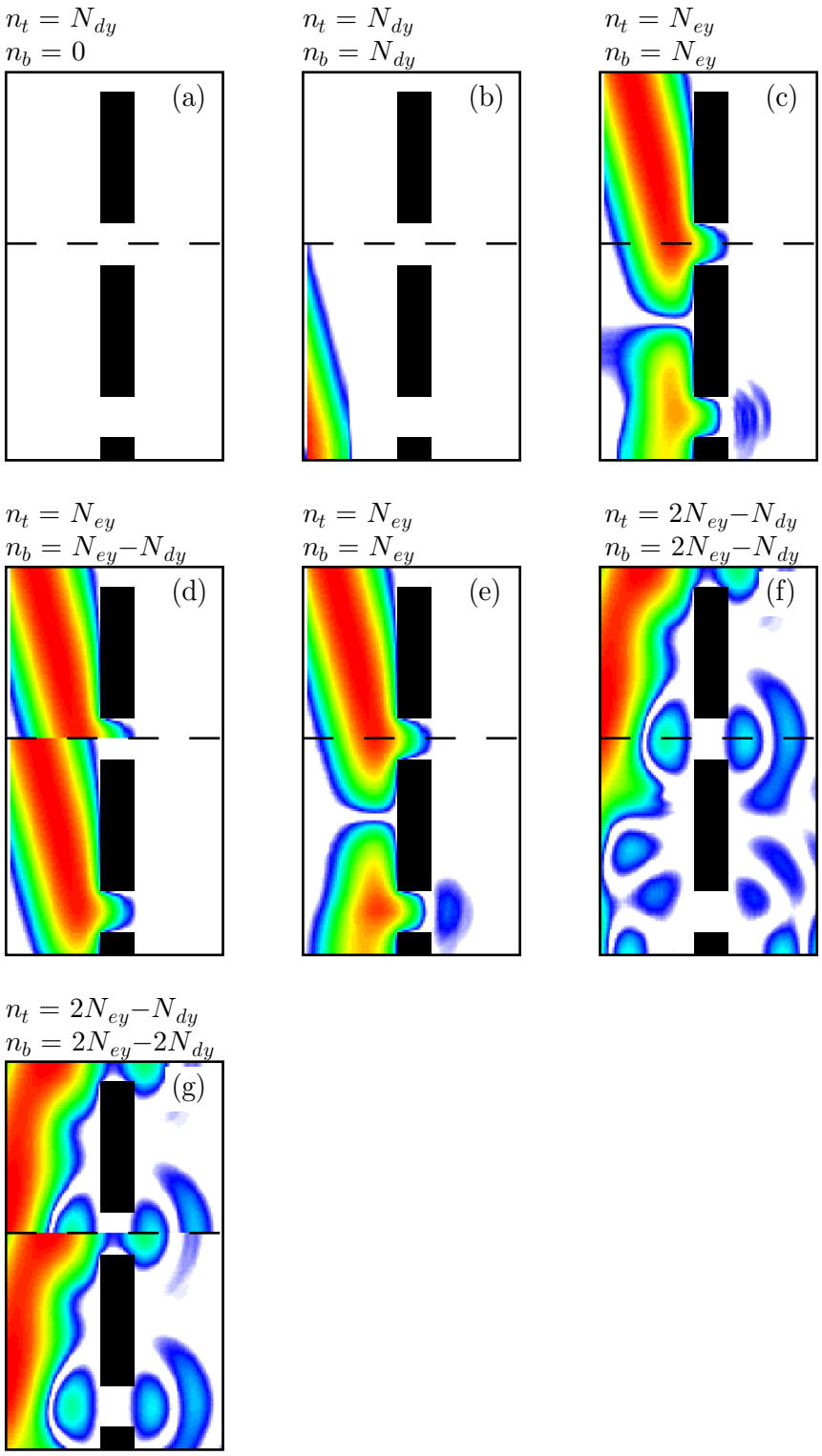


Figure 3.9: Snapshots of an FDTD simulation of the scattering of a plane wave by an array of PEC bricks using periodic boundary conditions. The dashed line marks the boundary between the upper and lower regions.

stage 2, until the fields in the top cell have decayed to a negligible level.

In Figure 3.9, snapshots from another FDTD simulation are shown. In this figure, the scatterer is a PEC brick, but the period and direction of the incident wave are unchanged from the case discussed earlier. This set of snapshots shows how the algorithm behaves when a scatterer is present.

A key observation is that the error from the bottom boundary is never allowed to enter the upper region, so the upper region is always correct. Any calculation, such as a near-field to far-field transform, can be performed as usual on the upper region only; however, the calculations should only be performed on time steps when the upper region is being updated (i.e., only when $n_t = n_b$). The upper region is the desired solution; the lower region is ignored in any additional processing.

## *3.4 Demonstration*

To demonstrate the accuracy of the technique, the transmission through an array (diffraction grating) of infinitely-long, rectangular conducting bars of conductivity $\sigma$ is analyzed. The incident plane wave is linearly polarized with the electric field in the $\hat{z}$ direction (TE case). The various geometrical parameters for the array are shown in Figure 3.10. For this study, $w/g = 1$, $w/d = 4$, and $1/\sigma d = 63\,\Omega$. This structure is identical to the structure discussed by Maloney and Kesler in [18]. Since the structure is periodic, the far-zone (radiated) field can be written as a finite sum of uniform plane waves. The electric field for the plane wave of diffraction order $m$ is given by [18]

$$\vec{E}_m^{sr}(\omega) = \frac{1}{y_p} \int_0^{y_p} \vec{E}(\omega, y) \exp[j(2\pi m y/y_p + k_o y \sin\phi_i)] dy, \tag{3.14}$$

in which $k_o = \omega/c$, and the Roman font indicate a frequency domain quantities. This equation is discretized and applied to a transform surface ($x =$ constant) to the right of the array in Figure 3.10.

For validation, the results from the FDTD simulations are compared with results from an accurate frequency-domain, mode-matching technique [47]. First, to demonstrate that the proposed technique is accurate over a wide range of angles of incidence, five different simulations were performed in which $\phi_i$ varied from 15° to 75°. The transmission coefficient

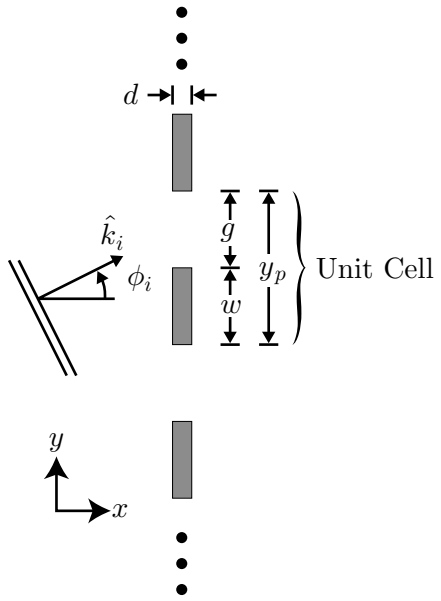


Figure 3.10: Array of infinitely-long, rectangular bars (diffraction grating). The parameters used in the demonstration are $w/g = 1$, $w/d = 4$, and $1/\sigma d = 63\,\Omega$.

of the array for the $m = 0$ order is shown in Figure 3.11 as a function of the normalized frequency, $y_p/\lambda$. There is excellent agreement between the results from the two techniques.

To demonstrate that the technique is capable of modeling the entire spectrum of diffracted waves, and not just the fundamental order ($m = 0$), a simulation was performed for the angle of incidence of $\phi_i = 60°$. Over the frequency range examined, the $m = -4$ to $m = 0$ orders can propagate. Figure 3.12 shows the transmission coefficients for these five orders as a function of the normalized frequency. Again, there is excellent agreement between the results from the two techniques.

## *3.5 Summary*

In this chapter, a straightforward, conceptually simple technique for incorporating periodic boundary conditions into the FDTD method has been presented and verified. The proposed method is simple to implement and valid over a wide range of angles of incidence. Furthermore, the method introduces no new complications to the FDTD method, since the two unit cells used in the procedure can contain any structures that could be placed in a traditional FDTD grid. In the next chapter, this method will be generalized to three-dimensional geometries.

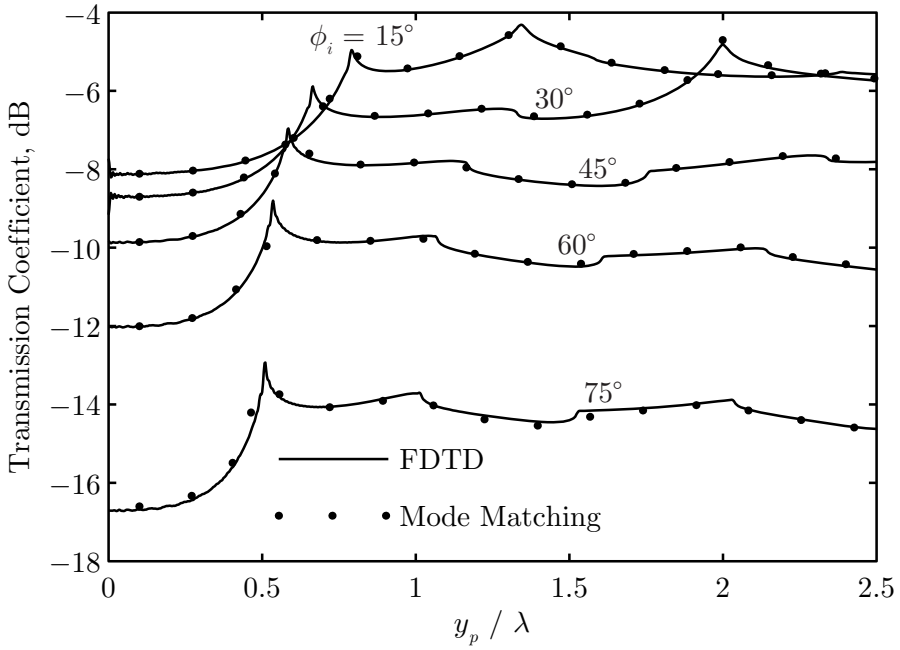


Figure 3.11: Transmission coefficient for the fundamental order ($m = 0$) for several angles of incidence. The results from the FDTD method (solid lines) are compared to the results from a mode-matching technique (dots) [47].

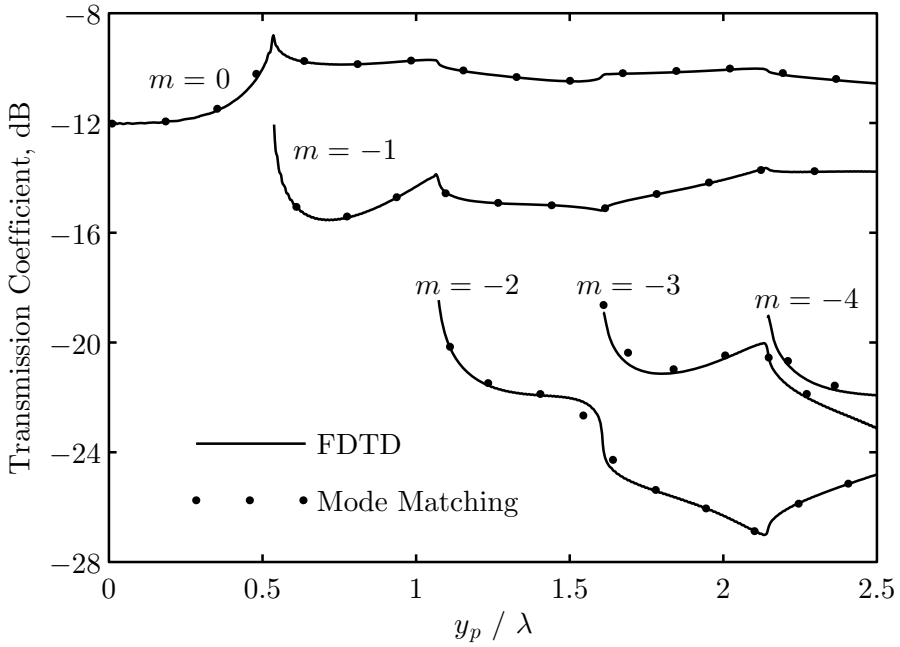


Figure 3.12: Transmission coefficients for the first five orders ($m = -4, -3, -2, -1, 0$) when the angle of incidence is $\varphi_i = 60°$. The results from the FDTD method (solid lines) are compared to the results from a mode-matching technique (dots) [47].

# CHAPTER IV

# PERIODIC BOUNDARY CONDITIONS IN FDTD THE THREE-DIMENSIONAL CASE

In this chapter, the new method for incorporating periodic boundary conditions into the FDTD method that was presented in the last chapter is generalized to three-dimensional (3D), doubly-periodic geometries. The computational burden and range of validity of the proposed method is studied. Two examples problems are used to demonstrate the accuracy of the method. Portions of this work were previously published in [48].

## *4.1 Motivation*

Many periodic structures, such as a planar antenna array or a three-dimensional diffraction grating, are periodic in two directions. As in the previous chapter, we wish to analyze a single cell of the infinite structure using periodic boundary conditions. In the following discussion, we assume a 3D structure, such as the one shown in Figure 4.1, that is finite in the $x$ direction, periodic in the $y$ direction with period $y_p$, and periodic in the $z$ direction with period $z_p$. The volume ($-\infty < x < \infty, 0 \le y \le y_p$, $0 \le z \le z_p$) is the "unit cell" of the array. The excitation is any incident field that satisfies

$$\vec{\mathcal{E}}_i(\vec{r} + n_y y_p \hat{y} + n_z z_p \hat{z}; t) = \vec{\mathcal{E}}_i(\vec{r}; t - n_y \tau_{dy} - n_z \tau_{dz}), \quad n_y, n_z = \text{integer}, \tag{4.1}$$

in which $\tau_{dy}$ and $\tau_{dz}$ are time delays. A uniform plane wave,

$$\vec{\mathcal{E}}_i(\vec{r}; t) = \hat{e}\, \mathcal{G}(t - \hat{k}_i \cdot \vec{r}/c), \tag{4.2}$$

in which $\mathcal{G}$ is an arbitrary scalar waveform, satisfies this form. In this case, we have

$$\vec{\mathcal{E}}_i(\vec{r} + n_y y_p \hat{y} + n_z z_p \hat{z}; t) = \hat{e}\, \mathcal{G}\big[t - (\hat{k}_i \cdot \vec{r})/c - (\hat{k}_i \cdot \hat{y}) n_y y_p/c - (\hat{k}_i \cdot \hat{z}) n_z z_p/c\big] \tag{4.3}$$

$$\vec{\mathcal{E}}_i(\vec{r}; t - n_y \tau_{dy} - n_z \tau_{dz}) = \hat{e}\, \mathcal{G}\big[t - (\hat{k}_i \cdot \vec{r})/c - n_y \tau_{dy} - n_z \tau_{dz}\big]. \tag{4.4}$$

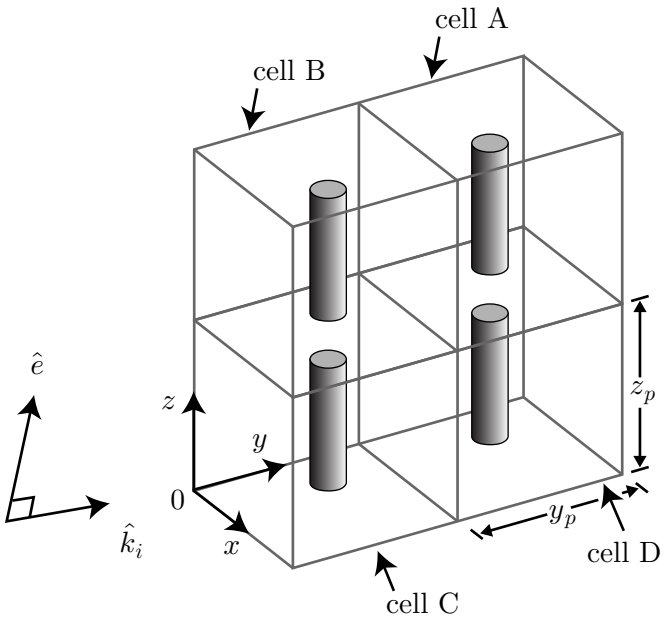


Figure 4.1: Schematic drawing for a generic periodic structure.

Therefore, the uniform plane wave satisfies (4.1) with

$$\tau_{dy} = \frac{(\hat{k}_i \cdot \hat{y}) y_p}{c} \tag{4.5}$$

$$\tau_{dz} = \frac{(\hat{k}_i \cdot \hat{z}) z_p}{c}. \tag{4.6}$$

These time delays are a generalization of the delays given in the previous chapter. As for the two-dimensional algorithm, the time shift condition applies to the total electromagnetic field:

$$\vec{\mathcal{F}}(\vec{r} + n_y y_p \hat{y} + n_z z_p \hat{z}; t) = \vec{\mathcal{F}}(\vec{r}; t - n_y \tau_{dy} - n_z \tau_{dz}), \quad n_y, n_z = \text{integer}. \tag{4.7}$$

However, since time-advanced values of the field are required, this condition cannot be directly implemented. In this chapter, the two-dimensional algorithm is extended to the more general case in Figure 4.1. The adaptation of the approach to 3D, doubly-periodic problems requires additional steps and imposes new limitations not present for the simpler 2D, singly-periodic problems. We will only consider scattering problems, but the approach will work just as well for antenna problems.

## 4.2 Development of the Algorithm

Consider the geometry in Figure 4.1, which is a generic three-dimensional periodic structure. We assume that the structure is finite in the $x$ direction and only free space exists for $x < 0$. Four unit cells of the structure are shown. The goal is for the cell labeled A, which is the volume $-\infty < x < \infty, y_p < y < 2y_p, z_p < z < 2z_p$, to contain the correct electromagnetic field for the infinite periodic structure; the remaining three cells (B, C, and D) are necessary for the implementation of the algorithm, but the field in these cells is not considered part of the solution. The excitation is an incident, uniform plane wave propagating in the direction $\hat{k}_i$ that is a pulse of finite duration in time. Without loss of generality, the direction $\hat{k}_i$ will be assumed to be positive in the $x$, $y$, and $z$ directions, i.e., $\hat{k}_i \cdot x > 0$, $\hat{k}_i \cdot y > 0$, and $\hat{k}_i \cdot z > 0$. The electromagnetic field in the structure is initially zero, and the incident wave first encounters the four cells at $x = 0, y = 0, z = 0$ at time $t = 0$.

Since the field at the boundaries at $y = 2y_p$ and $z = 2z_p$ can be specified using previous values of the field at $y = y_p$ and $z = z_p$, according to (4.7), we assume that these surfaces do not present a problem. On the other hand, the boundaries at $y = 0$ and $z = 0$ require knowledge of future values of the field at $y = y_p$ and $z = z_p$. Since these future values are not available, a truncation error is caused by the lack of data for these boundaries. This error travels at the speed of light $c$, so it takes at least the time $\tau_e = \min(y_p/c, z_p/c)$ for the error to first enter cell A. On the other hand, the incident wave takes the time

$$\tau_d = \tau_{dy} + \tau_{dz} = \frac{1}{c}\hat{k}_i \cdot (y_p\hat{y} + z_p\hat{z}) \tag{4.8}$$

to traverse cell C and reach cell A. As long as $\tau_d < \tau_e$, there will be an interval in time $\tau_d < t < \tau_e$ during which the excitation has entered cell A but the truncation error has not. During this interval, the field in cell A is identical to the field in an element of an infinite periodic structure.

To demonstrate how this observation can be used to obtain the correct electromagnetic field for a unit cell of a periodic structure (cell in Figure 4.1), we extend the argument presented in Chapter 3 to this three-dimensional case. For ease of illustration, we will

assume that the incident field is a delta-function in time,

$$\vec{\mathcal{E}}_i(\vec{r},t) = \delta(t - \hat{k}_i \cdot \vec{r}/c)\hat{e}, \tag{4.9}$$

and that the direction of the electric field, $\hat{e}$, is arbitrary except for the requirement that $\hat{k}_i \cdot \hat{e} = 0$. The geometry on the plane $x = 0$ in Figure 4.1 is shown in Figure 4.2. The incident field is represented by a solid line; this is the intersection of a plane of constant amplitude for the field ($t - \hat{k}_i \cdot \vec{r}/c = 0$) with the plane $x = 0$. Six snapshots in time on this plane are shown in Figure 4.2. Note that each snapshot contains the same structure, but that the labels for the cells have been omitted in every snapshot except the first.

Initially, at time $t = 0$ (top left in Figure 4.2), the field is zero everywhere in all four cells. The excitation is just entering the group of four cells at $x = 0, y = 0, z = 0$. As time advances, the field on the boundaries at $y = 0$ and $z = 0$ cannot be set correctly; this is the source of the truncation error. These errors, which are represented by the patterned area in Figure 4.2, travel away from the boundaries at the speed of light. The field on the boundaries at $y = 2y_p$ and $z = 2z_p$ can be set correctly, so these boundaries do not have truncation errors. As is clear from the snapshot in the top right in Figure 4.2 for time $t = \tau_e - \tau_{dy} - \tau_{dz}$, the excitation is approaching cell A faster than the truncation error.

At time $t = \tau_e$, the error has just reached the boundary of cell A, as shown in the snapshot in the bottom left of Figure 4.2. Since the error has not yet corrupted the field in cell A, the field in this cell still satisfies (4.7) for the infinite periodic structure. We can use the field in cell A at the times $t = \tau_e$ (bottom left in Figure 4.2), $t = \tau_e - \tau_{dz}$ (middle right), $t = \tau_e - \tau_{dy}$ (middle left), and $t = \tau_e - \tau_{dy} - \tau_{dz}$ (top right) to construct the correct field in all four cells at time $t = \tau_e - \tau_{dy} - \tau_{dz}$ (bottom right). Specifically, the field in cell A at time $t = \tau_e$, marked **4**, must be copied to cell C. The field in cell A at time $t = \tau_e - \tau_{dz}$, marked **3**, must be copied to cell B. The field in cell A at time $t = \tau_e - \tau_{dy}$, marked **2**, must be copied to the cell D. And finally, the field in cell $A$ at $t = \tau_e - \tau_{dy} - \tau_{dz}$, marked **1**, must be copied to cell A. At the completion of these steps, called the "combining procedure", the four cells contain the correct field for the infinite structure at time $t = \tau_e - \tau_{dy} - \tau_{dz}$, which is shown in the bottom right of Figure 4.2. The copy procedures have completely removed

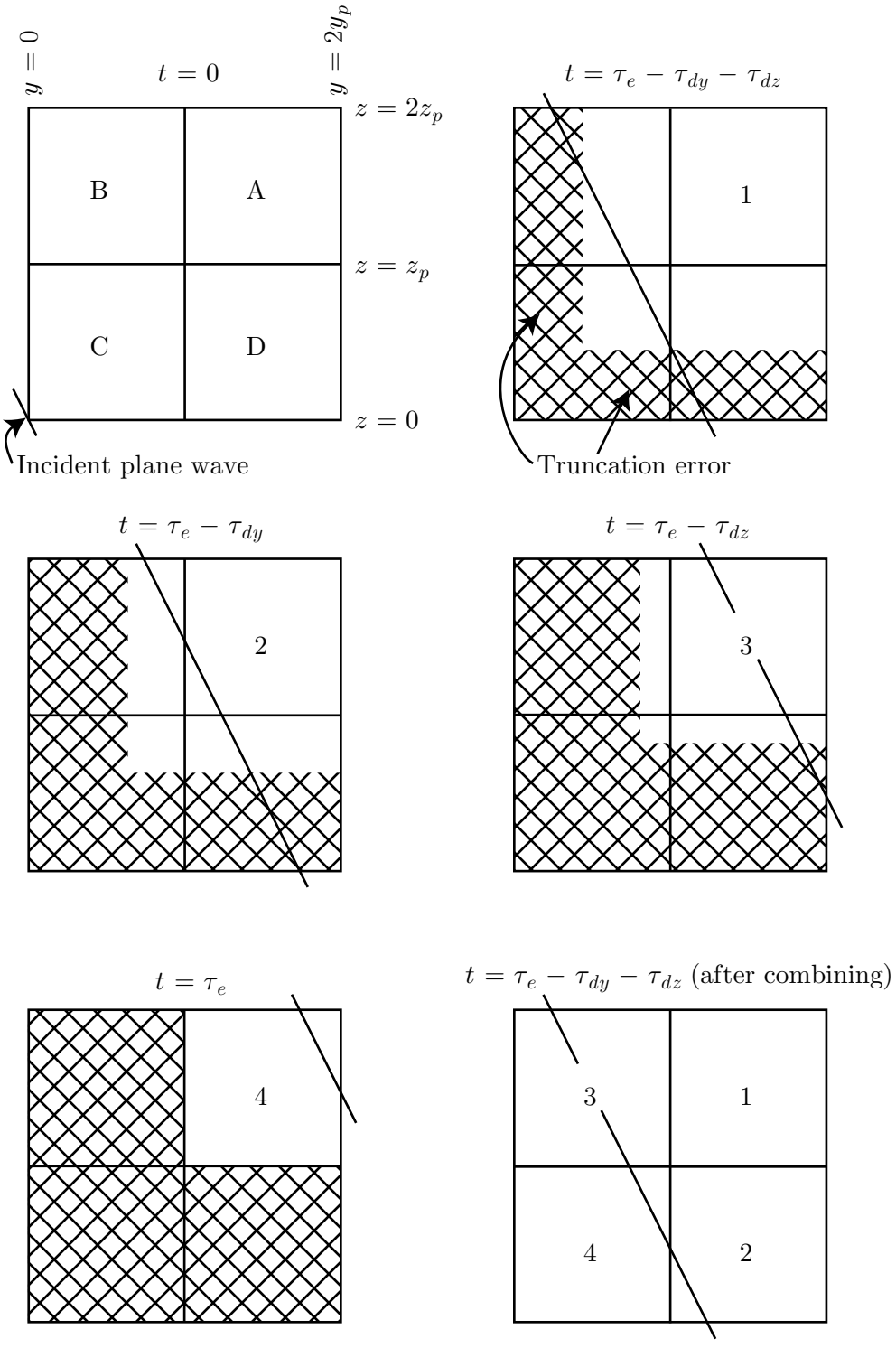


Figure 4.2: Illustration showing the development of the algorithm.

the truncation errors from the four cells. The above procedure represents one cycle of the algorithm. This procedure is repeated as many times as necessary to obtain the field in a unit cell of an infinite periodic structure at any future time.

Before presenting the details for the implementation of this algorithm in the FDTD method, two inherent limitations of the approach will be described: a restriction on the direction of propagation for the incident plane wave, and the increase in the time for computation. The discussion for both will make use of Figure 4.3.

As shown above, the algorithm works provided the times $\tau_d$ and $\tau_e$ satisfy the inequality $\tau_d < \tau_e$, which when expressed in terms of the direction of the incident wave and the periodicities for the structure becomes

$$y_p \left( \hat{k}_i \cdot \hat{y} \right) + z_p \left( \hat{k}_i \cdot \hat{z} \right) < \min(y_p, z_p). \tag{4.10}$$

For periodic structures with a square lattice, this reduces to

$$\hat{k}_i \cdot (\hat{y} + \hat{z}) < 1. \tag{4.11}$$

In Figure 4.3, the $\hat{y}$ and $\hat{z}$ components of the direction of propagation $\hat{k}_i$ are shown. For a square lattice, the region within which the algorithm works is white in the figure, and the region within which the algorithm does not work is shaded gray. The black region is not relevant; the incident waves within this region are evanescent. Notice that the algorithm works for all directions of incidence when the direction of propagation, $\hat{k}_i$, lies in one of the principal planes: $\hat{k}_i \cdot \hat{y} = 0$ or $\hat{k}_i \cdot \hat{z} = 0$ (the $xz$ and $xy$ planes in Figure 4.1).

There is a penalty paid in time when using the algorithm, because a cycle of the algorithm takes the period $\tau_e$ to complete, but it only generates useful data over the period

$$\tau_e - \tau_d = \frac{1}{c} \left[ \min(y_p, z_p) - y_p \left( \hat{k}_i \cdot \hat{y} \right) - z_p \left( \hat{k}_i \cdot \hat{z} \right) \right]. \tag{4.12}$$

Now we can define a relative cost for the use of the algorithm:

$$M = \frac{\tau_e}{\tau_e - \tau_d}. \tag{4.13}$$

Notice that this is just the ratio of the time interval obtained from running the algorithm for one cycle for normal incidence, $\hat{k}_i = \hat{x}$, to the time interval obtained from running the

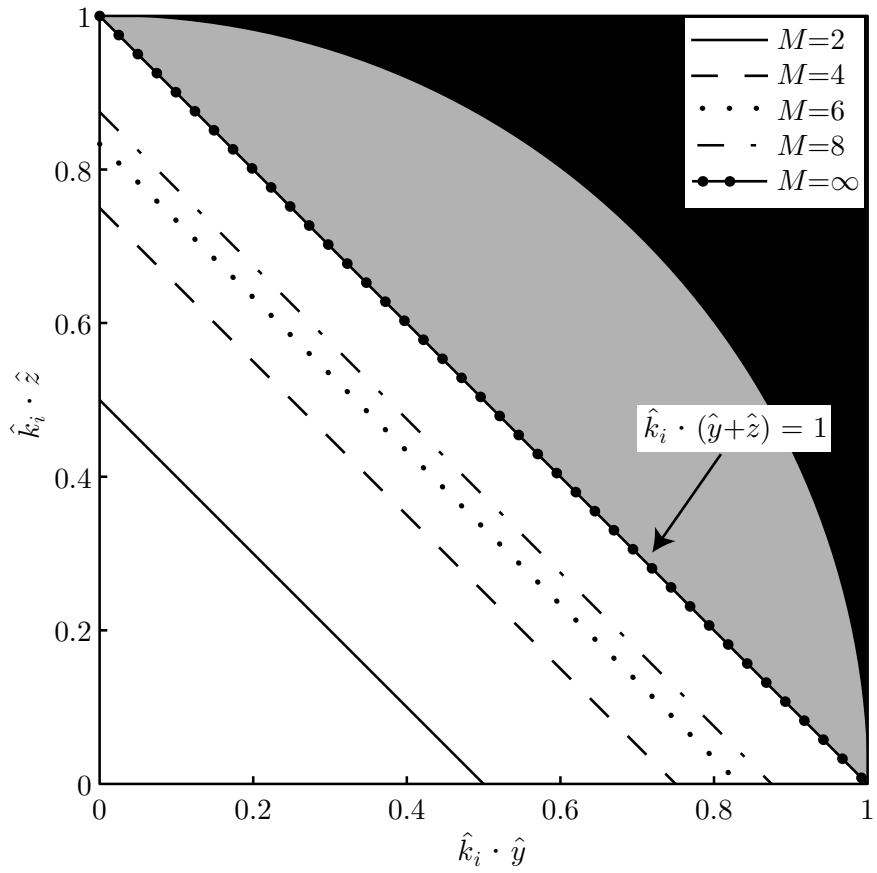


Figure 4.3: Graph showing the directions of propagation for which the method works (white area) and the relative cost, $M$, of the algorithm as a function of this direction. The black area is not relevant, because it represents evanescent waves. The gray area represents directions of propagation that are not possible with the proposed algorithm. The results are for a square lattice.

algorithm for one cycle for the direction of incidence $\hat{k}_i$. For example, if $\tau_d = \tau_e/2$, then $M = 2$. In this case, a calculation using the periodic FDTD method will require at least twice the number of operations as for the equivalent finite model. For a square lattice, the cost is simply

$$M = \frac{1}{1 - \hat{k}_i \cdot (\hat{y} + \hat{z})}. \tag{4.14}$$

Contours of constant $M$ for a square lattice are drawn in Figure 4.3. The increase in cost for the algorithm is seen to be small for directions near normal incidence and to grow as one approaches the line $\hat{k}_i \cdot (\hat{y} + \hat{z}) = 1$, with the cost becoming infinite when this line is reached.

## *4.3 Implementation in the FDTD Method*

The algorithm as previously discussed can be implemented in the FDTD method in a straightforward way. The spatial steps in the directions of periodicity are chosen so that $y_p = N_{yp}\Delta_y$ and $z_p = N_{zp}\Delta_z$, in which $N_{dy}$ and $N_{dz}$ are integers. The discrete delay periods are given by $N_{dy} = \text{round}(\tau_{dy}/\Delta_t)$ and $N_{dz} = \text{round}(\tau_{dz}/\Delta_t)$. The time step, $\Delta_t$, must be chosen to satisfy the usual Courant stability criterion [17]. Due to the discretization, and depending on the values of $\tau_{dy}$, $\tau_{dz}$, and $\Delta_t$, the plane wave direction may be slightly different from the one desired; instead, the direction is

$$\hat{k}_i \cdot \hat{y} = \frac{N_{dy} c \Delta_t}{y_p} \tag{4.15}$$

$$\hat{k}_i \cdot \hat{z} = \frac{N_{dz} c \Delta_t}{z_p} \tag{4.16}$$

$$\hat{k}_i \cdot \hat{x} = \sqrt{1 - \left(\hat{k}_i \cdot \hat{y}\right)^2 - \left(\hat{k}_i \cdot \hat{z}\right)^2} \ . \tag{4.17}$$

By choosing the time step $\Delta_t$ to be smaller than necessary for stability, the numerical plane wave direction can be made as close to the desired direction as necessary. The discrete error period, $N_e$, is found as $N_e = \text{floor}(\tau_e/\Delta_t)$, in which floor() is a function that returns the largest integer less than or equal to the argument. The algorithm works for $N_{dy} + N_{dz} < N_e$. As for the 2D algorithm, this requirement is more restrictive than $\tau_{dy} + \tau_{dz} < \tau_e$.

A slice of the FDTD grid (plane $x$ = constant) is shown in Figure 4.4. The labels, A — D, correspond to the notation in Figure 4.1. The surfaces to the front and back of this plane ($x_{\max}$ and $x_{\min}$) are terminated with perfectly matched layers (PMLs). A pad of FDTD cells has been added to the left ($y_{\min}$) and bottom ($z_{\min}$) sides of the grid, the purpose of which will be discussed later. The $j = N_{yp} + 1/2$ and $j = 2N_{yp} + 1/2$ surfaces, indicated by the red dashed lines, form a master/slave pair, since the tangential magnetic field components on these surfaces are related by

$$\mathcal{H}_x^{\Delta}\big|_{i,2N_{yp}+1/2,k+1/2}^{n+1/2} = \mathcal{H}_x^{\Delta}\big|_{i,N_{yp}+1/2,k+1/2}^{n+1/2-N_{dy}} \tag{4.18}$$

$$\mathcal{H}_z^{\Delta}\big|_{i+1/2,2N_{yp}+1/2,k}^{n+1/2} = \mathcal{H}_z^{\Delta}\big|_{i+1/2,N_{yp}+1/2,k}^{n+1/2-N_{dy}}. \tag{4.19}$$

The tangential magnetic field components on the master surface ($j = N_{yp} + 1/2$) are stored in buffers for the time indices $n - N_{dy} + 1/2, \ldots, n + 1/2$. These buffers can be implemented as queues, so that new data from the master surface are inserted at one end of the queue, and delayed data from the other end are used to specify the field on the slave surface. A similar arrangement is used for the other pair of master/slave surfaces, $k = N_{zp} + 1/2$ and $k = 2N_{zp} + 1/2$, which are shown as blue dashed line in Figure 4.4:

$$\mathcal{H}_x^{\Delta}\big|_{i,j+1/2,2N_{zp}+1/2}^{n+1/2} = \mathcal{H}_x^{\Delta}\big|_{i,j+1/2,N_{zp}+1/2}^{n+1/2-N_{dz}} \tag{4.20}$$

$$\mathcal{H}_y^{\Delta}\big|_{i+1/2,j,2N_{zp}+1/2}^{n+1/2} = \mathcal{H}_y^{\Delta}\big|_{i+1/2,j,N_{zp}+1/2}^{n+1/2-N_{dz}}. \tag{4.21}$$

At the start of the simulation, the buffers are filled with zeros. The FDTD algorithm continues in a normal leapfrog fashion, with the electric field update followed by the magnetic field update. After the magnetic field update, the buffers are rotated, so that the oldest value in the buffer is dropped and every other value is shifted one time step. Next, the tangential magnetic field components on the $j = N_{yp} + 1/2$ and $k = N_{zp} + 1/2$ surfaces are inserted into the buffers. Finally, the tangential magnetic field components on the $j = 2N_{yp} + 1/2$ and $k = 2N_{zp} + 1/2$ surfaces are set based on the oldest values in each buffer. The simulation continues in this fashion for $n = 0$ to $n = N_e$.

Snapshots of the field in the "good" cell (cell A) must be saved at intermediate time steps. They will be used at the end of the $n = N_e$ time step to construct the correct field

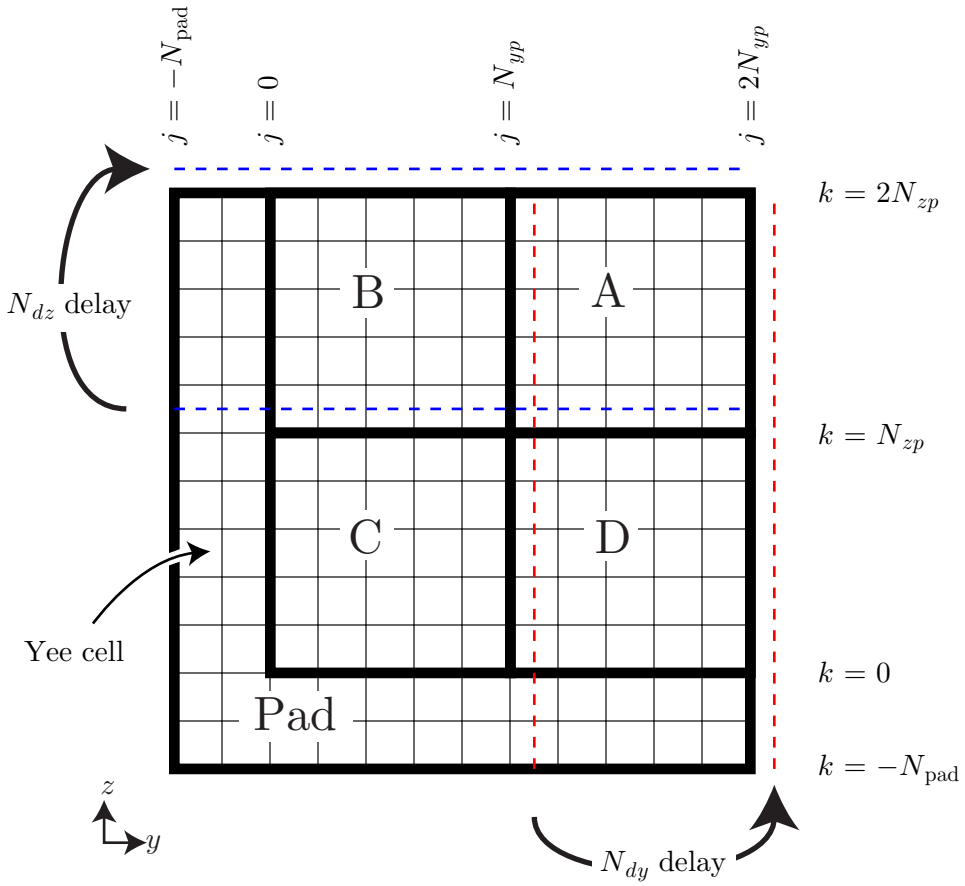


Figure 4.4: Illustration of the FDTD grid. The labels for the cells correspond to those in Figure 4.1.

at time step $n = N_e - N_{dy} - N_{dz}$. To accommodate the pad of extra cells, some of these intermediate snapshots must be enlarged. In the following discussion, the copies include everything that is within the given range, including auxiliary fields in the PML and fields in the time-delay buffers.

At the end of the $n = N_e - N_{dy} - N_{dz}$ time step, cell A, as shown in Figure 4.4, should be stored. All field components in the range $(i = 0 \ldots N_x, j = N_{yp} \ldots 2N_{yp}, k = N_{zp} \ldots 2N_{zp})$ should be saved. Note that this region includes portions of both the right buffers (which are for data going from $j = N_{yp}$ to $j = 2N_{yp}$) and the top buffers (which are for data going from $k = N_{zp}$ to $k = 2N_{zp}$).

At the end of the $n = N_e - N_{dy}$ time step, the stored region must be enlarged to accommodate the pad. All field components in the range $(i = 0 \ldots N_x, j = N_{yp} \ldots 2N_{yp}, k = N_{zp} - N_{\text{pad}} \ldots 2N_{zp})$ should be saved. Note that this region includes portions of the right buffers, but does not include any portion of the top buffers.

At the end of the $n = N_e - N_{dz}$ time step, the stored region must also be enlarged to accommodate the pad. All field components in the range $(i = 0 \ldots N_x, j = N_{yp} - N_{\text{pad}} \ldots 2N_{yp}, k = N_{zp} \ldots 2N_{zp})$ should be saved. Note that this region includes portions of the top buffers, but does not include any portion of the right buffers.

Finally, at the end of the $n = N_e$ time step, the combining procedure is applied. All field components in the range $(i = 0 \ldots N_x, j = N_{yp} - N_{\text{pad}} \ldots 2N_{yp}, k = N_{zp} - N_{\text{pad}} \ldots 2N_{zp})$ are copied over the field components in the range $(i = 0 \ldots N_x, j = -N_{\text{pad}} \ldots N_{yp}, k = -N_{\text{pad}} \ldots N_{zp})$. This step is illustrated in Figure 4.5. There is no need to save this data, since the copy can be done immediately. However, the order that the components are copied must be programmed carefully, since the source and destination regions partially overlap. This step does not involve any of the buffers.

The three saved regions are copied to the destinations indicated in Figure 4.2 (bottom right). For example, the region from time step $n = N_e - N_{dy}$ is copied over the region $(i = 0 \ldots N_x, j = N_{yp} \ldots 2N_{yp}, k = -N_{\text{pad}} \ldots N_{zp})$. When all of the field shifts are completed, the new effective time step is $n = N_e - N_{dy} - N_{dz}$. The FDTD algorithm then continues normally, and another combining procedure is required after $N_e$ time steps have elapsed.

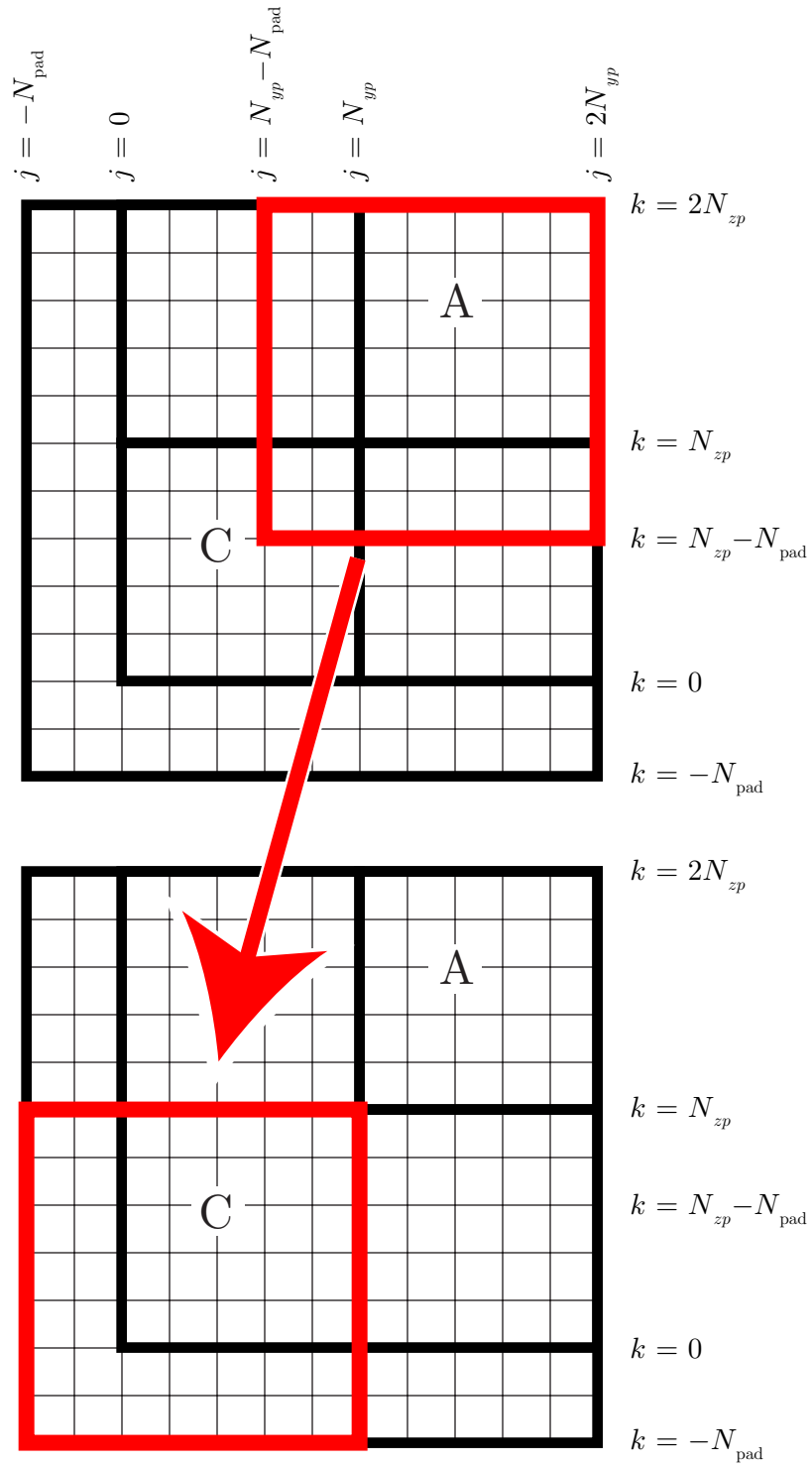


Figure 4.5: Illustration of one of the field shifts for the combining procedure. The source and destination regions must be enlarged to accommodate the extra cells of padding.

The intermediate saves occur relative to the time step of the next combining procedure. Since the second copy occurs at $n = 2N_e - N_{dy} - N_{dz}$, intermediate values are required at $n = 2N_e - 2N_{dy} - 2N_{dz}$, $n = 2N_e - 2N_{dy} - N_{dz}$, and $n = 2N_e - N_{dy} - 2N_{dz}$.

The extra FDTD cells for padding, which were introduced earlier, are required for accuracy. In an FDTD grid, spatially undersampled waves can propagate faster than the speed of light, but with exponential attenuation [14]. Since $N_{ey}$ and $N_{ez}$ were specified assuming $\tau_{ey} = y_p/c$ and $\tau_{ez} = z_p/c$, this type of error can enter cell $A$ if it originated at $j = 0$ and $k = 0$. Moving the boundaries out a few FDTD cells prevents this error from corrupting the result. In our experience, 10 to 20 extra FDTD cells on each side are sufficient.

Another interesting observation is that good performance of the PML on the surfaces $x_{\min}$ and $x_{\max}$ is critical for obtaining accurate results. For periodic structures that are electrically large, higher order modes (higher diffraction orders for a grating) are present in the scattered field. The direction of propagation for these modes is frequency dependent, and for frequencies close to the turn-on frequency of a mode, the direction of propagation can be nearly parallel to the surface of the PML (grazing incidence). It is well known that the performance of the standard PML can be poor in this situation [49]. To partially alleviate this problem, we have used the convolutional implementation of the complex frequency shifted PML (CPML) [12]. This PML has been shown to have a more favorable performance for obliquely incident waves than the uniaxial PML [44].

## *4.4 Demonstration*

To demonstrate the accuracy of the technique, we will first consider the power reflection coefficient for a plane wave obliquely incident on a dielectric slab of thickness $d$ lying in the $yz$ plane. The dielectric slab is useful as a verification case because it can be considered a doubly periodic problem with an arbitrary period, and the exact solution is readily available [50]. Also, the result only depends on the angle $\psi$ between the direction of propagation, $\hat{k}_i$, and the normal to the slab, $\hat{n} = -\hat{x}$. For the example, the electrical parameters for the dielectric slab are $\epsilon = 4\epsilon_o$ and $\mu = \mu_o$. The incident plane wave is linearly polarized,

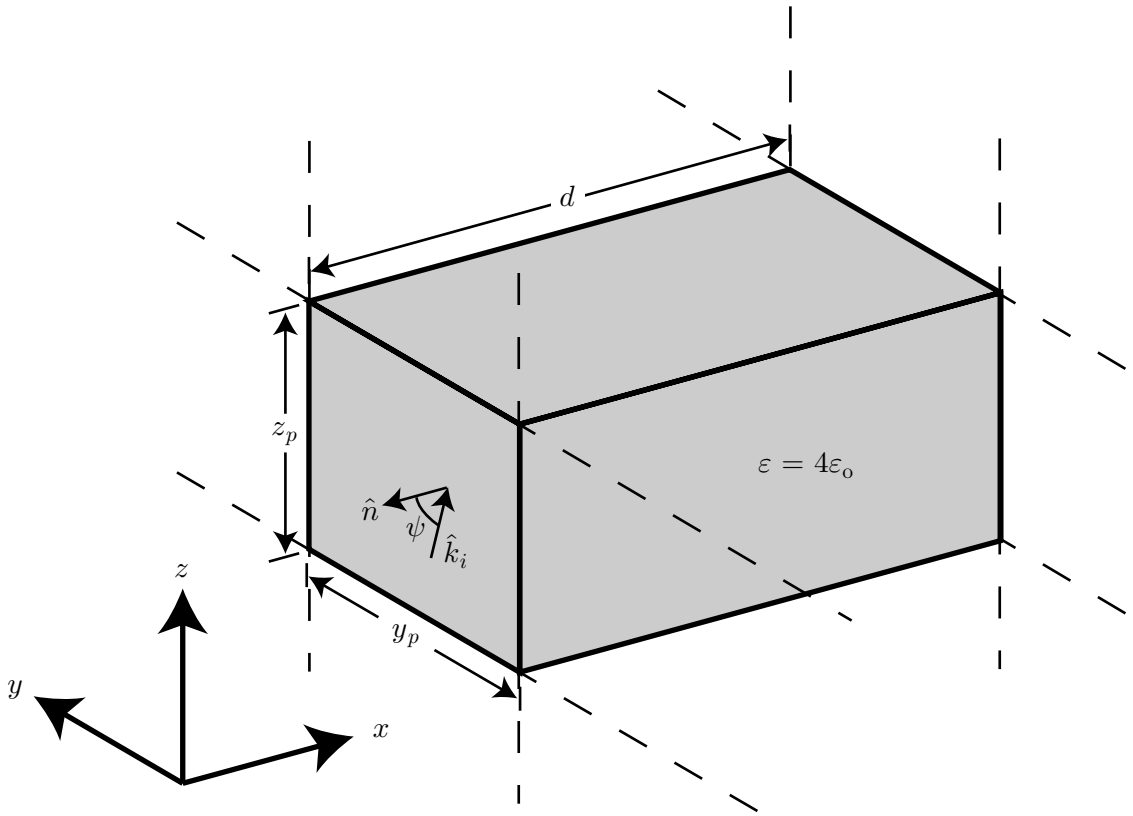


Figure 4.6: Geometry for a unit cell from a dielectric slab of thickness $d$. The periods $y_p$ and $z_p$ are arbitrary.

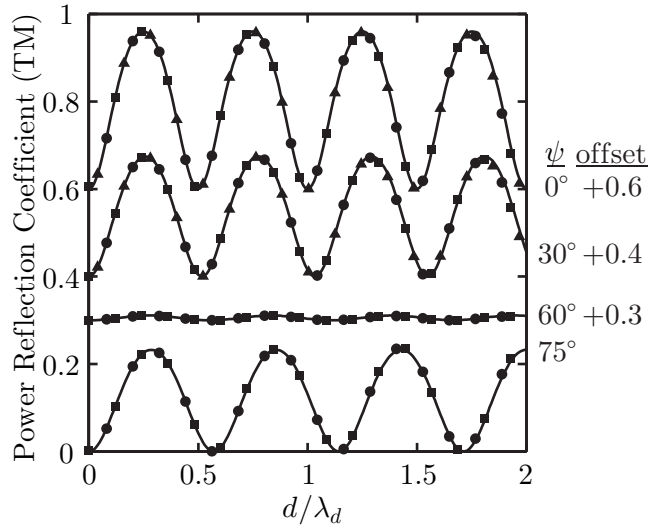


(a) TM polarization

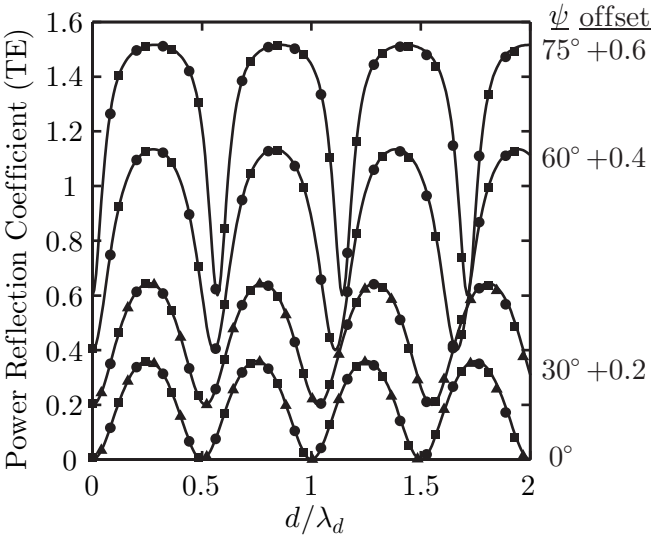


(b) TE polarization

Figure 4.7: Power reflection coefficient for a linearly polarized plane wave incident on a dielectric slab with $\epsilon = 4\epsilon_o$, $\mu = \mu_o$ and thickness $d$. The exact solution is the solid line. The square symbols are for a periodic FDTD simulation with $\hat{k}_i \cdot \hat{z} = 0$, the circles are for a periodic FDTD simulation with $\hat{k}_i \cdot \hat{y} = 0$, and the triangles are for a periodic FDTD simulation with $\hat{k}_i \cdot \hat{y} = \hat{k}_i \cdot \hat{z}$. The angle of incidence $\psi$ is given to the right of each curve. Some of the curves are offset for legibility, and the offset is noted.

and two polarizations are considered: the case in which the electric field is in the plane of incidence (TM), and the case in which the electric field is normal to the plane of incidence (TE). A unit cell from this slab is shown in Figure 4.6. The spatial periods for the unit cell are $y_p$ and $z_p$. For the numerical example, $y_p = z_p = d/2$ and the discretization was $\Delta_x = \Delta_y = \Delta_z = d/40$.

The power reflection coefficient calculated with the periodic FDTD method is compared to the exact analytical result in Figure 4.7. The angle $\psi$ is noted to the right of each curve. A constant offset has been added to separate some of the curves on the plot; these offsets are noted to the right of the legend for a curve. The reflection coefficient is plotted versus $d/\lambda_d$, with $\lambda_d$ being the wavelength in the slab. The direction of propagation is constrained to be in the $xy$ plane (marked as squares in the figure), the $xz$ plane (marked as circles), or along the diagonal in which case $\hat{k}_i \cdot \hat{y} = \hat{k}_i \cdot \hat{z}$ (marked as triangles). For the TM polarization, shown in Figure 4.7a, the Brewster angle is $\approx 63^\circ$, which explains the small reflection coefficient for the $\psi = 60^\circ$ case. Since $\mu = \mu_o$, there is no Brewster angle for the TE polarization, shown in Figure 4.7b. Note that the $\psi = 60^\circ$ and $\psi = 75^\circ$ cases are not shown for the direction of propagation along the diagonal; these cases would lie in the forbidden (gray) region of Figure 4.3. There is excellent agreement between the numerical and exact results for all of the orientations for the incident plane wave.

To demonstrate that the proposed method is also capable of accurately modeling periodic structures that are large enough to excite higher-order waves, we consider Babinet's principle for a pair of complementary planar structures [1]. The two structures are shown in Figure 4.8. The first structure, denoted *APS*, is a periodic array of square apertures of side length $s$ in a perfectly conducting, infinitesimally thin screen. The complementary structure, denoted *OBS*, is a periodic array of perfectly conducting, infinitesimally thin, square obstacles of the same shape as the apertures. Both structures are located in the $x = 0$ plane.

In the frequency domain, the far-zone scattered field for these problems can be written as a finite sum of uniform plane waves. Assuming that the incident wave has a positive component in the $x$ direction ($\hat{k}_i \cdot \hat{x} > 0$), the vector wave number of the transmitted

scattered wave of order $(m, n)$ is

$$k_{y,mn} = k_{\mathrm{o}}(\hat{k}_i \cdot \hat{y}) + \frac{2\pi m}{y_p} \tag{4.22}$$

$$k_{z,mn} = k_{\mathrm{o}}(\hat{k}_i \cdot \hat{z}) + \frac{2\pi n}{z_p} \tag{4.23}$$

$$k_{x,mn} = \sqrt{k_{\mathrm{o}}^2 - k_{y,mn}^2 - k_{z,mn}^2}\ , \tag{4.24}$$

in which $m$ and $n$ are integers, $k_{\mathrm{o}} = \omega/c$, and the wave propagates only if $k_{x,mn}$ is real. The electric field that propagates away from the structure is given by [1]

$$E_{y,mn} = \frac{1}{y_p z_p} \int_{z_p}^{2z_p} \int_{y_p}^{2y_p} \hat{y} \cdot \vec{E}(x = x_o, y, z) e^{j(k_{y,mn} y + k_{z,mn} z)} dy dz \tag{4.25}$$

$$E_{z,mn} = \frac{1}{y_p z_p} \int_{z_p}^{2z_p} \int_{y_p}^{2y_p} \hat{z} \cdot \vec{E}(x = x_o, y, z) e^{j(k_{y,mn} y + k_{z,mn} z)} dy dz \tag{4.26}$$

$$E_{x,mn} = -\left( \frac{k_{y,mn}}{k_{x,mn}} E_{y,mn} + \frac{k_{z,mn}}{k_{x,mn}} E_{z,mn} \right). \tag{4.27}$$

The use of Roman font indicates that these variables are frequency domain quantities. These equations are discretized and applied to a transform surface ($x = x_o$) either in front of or behind the structure, depending on whether reflected or transmitted field quantities are desired. The limits of integration are chosen to include only the field of cell A, as shown in Figure 4.1. An efficient time-domain method for computing these integrals is in [18].

For problem *APS*, the incident electric field is oriented in the $\hat{\theta}$ direction, and for problem *OBS*, the incident electric field is oriented in the $-\hat{\phi}$ direction. Because the incident electric fields are related by

$$\vec{E}^i_{APS} = \hat{k}_i \times \vec{E}^i_{OBS}, \tag{4.28}$$

according to Babinet's principle, the electric fields on the transmission side ($x > 0$) are related by [1]

$$\vec{E}_{APS} = -\hat{k}_{mn} \times \vec{E}^s_{OBS}. \tag{4.29}$$

Note that (4.29) relates the total field for problem *APS* to the scattered field for problem *OBS*; this distinction is only significant for the fundamental order, $m = n = 0$.

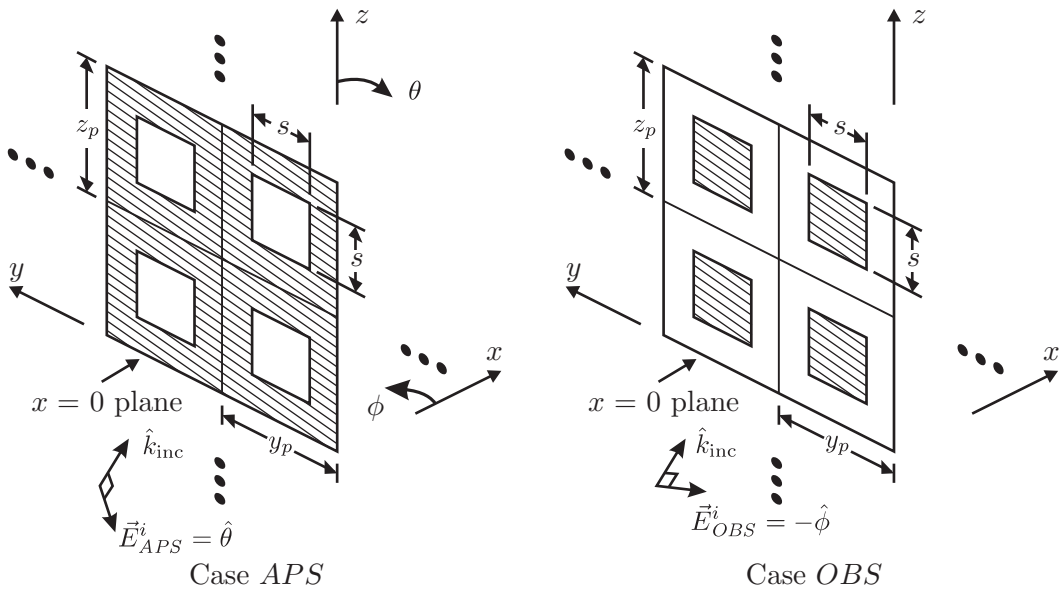


Figure 4.8: Pair of infinitesimally thin, perfectly conducting complementary structures. The structure on the left (case $APS$) is an array of square apertures in a screen, while the structure on the right (case $OBS$) is an array of square obstacles. For both cases, $y_p = z_p = 2s$.

For the numerical examples, we will take the periods to be $y_p = z_p = 2s$. The first example is for an incident wave with direction $\hat{k}_i = 0.99\hat{x} + 0.099\hat{y} + 0.099\hat{z}$ ($\theta = 84.32°, \phi = 45°$). In this case, $(\tau_e - \tau_d)/\tau_e \approx 0.8$, which means that about 80% of each cycle of the algorithm generates "good" data. In Figure 4.9, the total electric field for the aperture problem, $\vec{E}_{APS}$, is compared to the scattered electric field for the obstacle problem, $-\hat{k}_{mn} \times \vec{E}^s_{OBS}$. Only the $\hat{\theta}$ component is shown. The agreement is seen to be good for the fundamental order as well as for all of the propagating higher orders. A constant offset has been added to each of the higher orders to separate the curves on the plot. These offsets are noted on the right-hand side of the legend for each curve.

The second example is for an incident wave with direction $\hat{k}_i = 0.81\hat{x} + 0.57\hat{y} + 0.16\hat{z}$ ($\theta = 80.82°, \phi = 74.32°$). In this case, $(\tau_e - \tau_d)/\tau_e \approx 0.27$, which means that only about 27% of each cycle of the algorithm generates "good" data. As seen in Figure 4.10, the agreement is once again good for the fundamental order as well as all of the propagating higher orders.

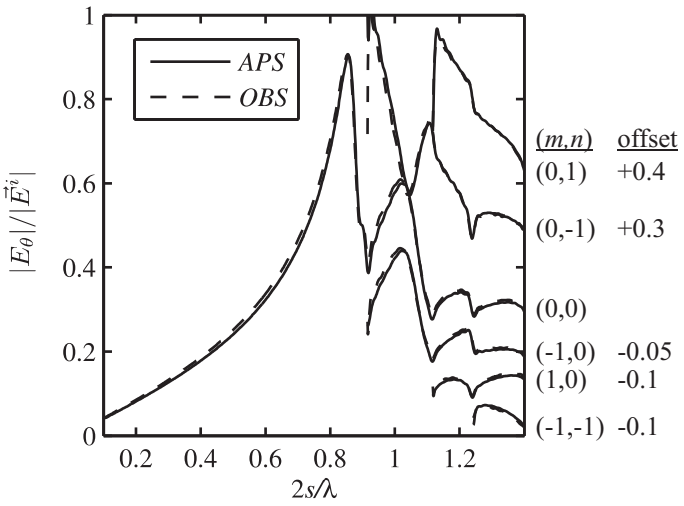


Figure 4.9: Electric field on the transmission side ($x > 0$) of the complementary structures for $\hat{k}_i = 0.99\hat{x} + 0.099\hat{y} + 0.099\hat{z}$ ($\theta = 84.32°, \phi = 45°$). For case $APS$, the total field, $\vec{E}_{APS}$, is shown. For case $OBS$, the scattered field is shown, and the field is transformed in accordance with Babinet's principle, so $-\hat{k}_{mn} \times \vec{E}^s_{OBS}$ is shown. The diffraction order is noted to the right of each curve. The curves are offset for legibility, and the offsets are noted.

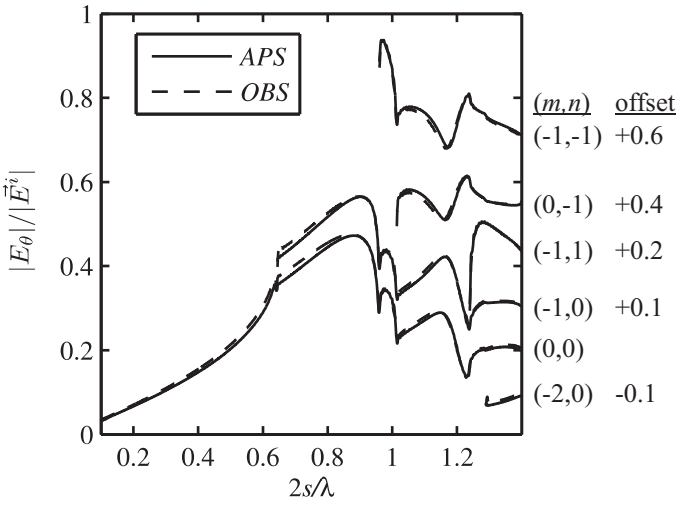


Figure 4.10: Electric field on the transmission side ($x > 0$) of the complementary structures for $\hat{k}_i = 0.81\hat{x} + 0.57\hat{y} + 0.16\hat{z}$ ($\theta = 80.82°, \phi = 74.32°$).

## *4.5 Summary*

In this chapter, the new algorithm for incorporating periodic boundary conditions into the FDTD method has been extended to the general case of oblique incidence and to structures that are periodic in two dimensions. Unlike the algorithm in Chapter 3, the incident plane wave is not restricted to the $xy$ or $xz$ plane. The algorithm cost has been shown to depend on the direction of propagation for the incident plane wave (equivalently, the cost depends of the time delays $\tau_{dy}$ and $\tau_{dz}$). The new method has been demonstrated by modeling a dielectric slab and comparing the result to the exact solution, and by modeling a pair of complementary planar structures and showing that the results are consistent with Babinet's principle.

# CHAPTER V

# NEAR-TO-FAR-FIELD TRANSFORMATION

In this chapter, the computation of the far-zone scattered field using the FDTD method is discussed. Only the frequency-domain near-to-far-field transformation is presented. For periodic problems, a method for computing the far-zone field for an array illuminated by a finite-width plane wave is discussed.

## *5.1 Scattering from Finite Objects*

In this section, the calculation of the far-zone scattered field from a finite object in free space is explained. The calculation can be performed either in the time domain or the frequency domain. The time-domain approach is more efficient when broadband results are needed for only a few directions in space, while the frequency-domain approach is more efficient when complete patterns are needed for only a few frequencies. For structural color problems, complete patterns are needed for many frequencies, so neither method is better. The frequency-domain approach is used because it offers more flexibility in post-processing.

The theory is developed and validated for a two-dimensional scatterer. The three-dimensional case is similar, but will not be discussed in detail.

### 5.1.1 Theory

Consider an isolated arbitrary structure in free space, as shown in Figure 5.1. The excitation is a plane wave launched by a total-field/scattered-field interface [16]. For simplicity, a two-dimensional structure ($z$-invariant) will be examined.

In the FDTD method, time-domain field quantities at offset positions in the Yee cell are available. The tangential field quantities on the surface $\mathcal{S}$ are calculated using linear interpolation. The frequency-domain quantities are calculated using an "on-the-fly" discrete

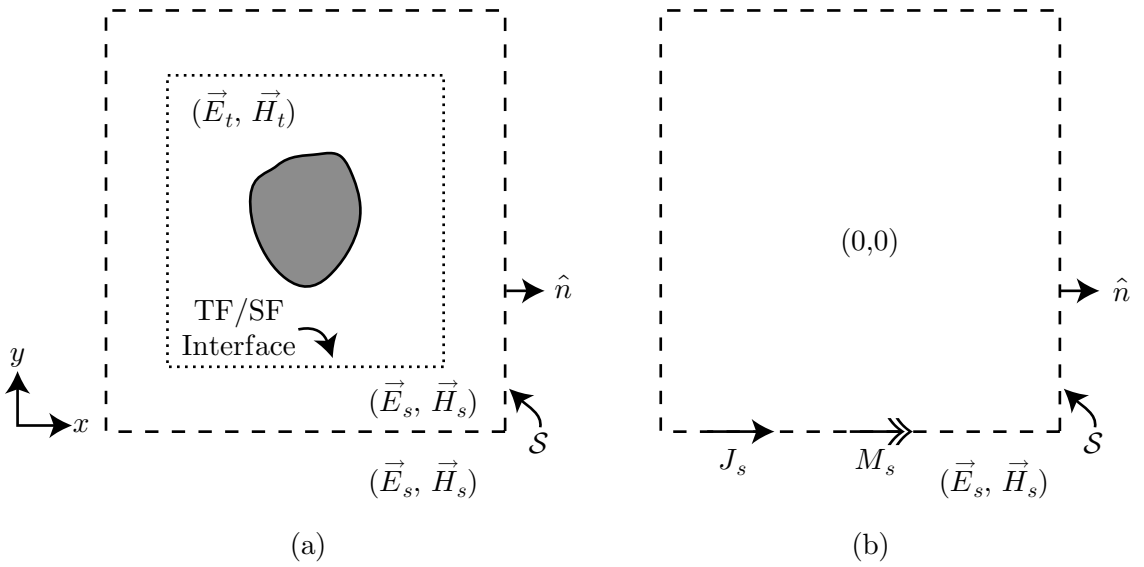


Figure 5.1: (a) Arbitrary scatterer inside of a plane-wave injector. (b) Equivalent problem using the surface equivalence principle. The field inside $\mathcal{S}$ is zero for the equivalent problem, and the fields outside $\mathcal{S}$ are identical in the two problems.

Fourier transform (DFT):

$$\vec{E}(\omega) = \sum_{n=0}^{\infty} \vec{\mathcal{E}}(n\Delta_t) e^{-j\omega n \Delta_t} \tag{5.1}$$

$$\vec{H}(\omega) = \sum_{n=0}^{\infty} \vec{\mathcal{H}}[(n + 1/2)\Delta_t] e^{-j\omega(n+1/2)\Delta_t}. \tag{5.2}$$

The surface equivalence principle is used to define equivalent electric and magnetic currents on the closed surface $\mathcal{S}$, such that the field due to these currents is identically zero inside $\mathcal{S}$ and unchanged outside $\mathcal{S}$, as shown in Figure 5.1 [51]. The equivalent currents are

$$\vec{J}_s = \hat{n} \times \vec{H} \tag{5.3}$$

$$\vec{M}_s = -\hat{n} \times \vec{E}, \tag{5.4}$$

and they are considered as sources, with the far-zone field calculated by a source-field relationship.

Referring to Figure 5.2, the goal is to calculate the field at an arbitrary position $\vec{\rho}$ due to the equivalent currents on $\mathcal{S}$. The field will be expressed in terms of the magnetic vector potential $\vec{A}$ and the electric vector potential $\vec{F}$. The potentials are obtaining by convolving

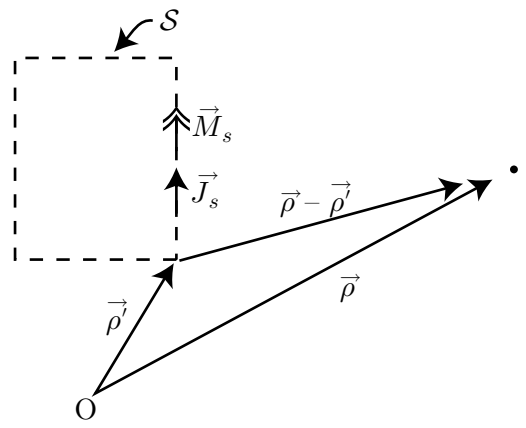


Figure 5.2: Coordinates for the evaluation of the near-to-far-field transformation.

the currents with a Green function[1]:

$$\vec{A}(\vec{\rho}) = \mu_o \oint_S \vec{J}_s(\vec{\rho'}) G(\vec{\rho}, \vec{\rho'}) dS' \tag{5.5}$$

$$\vec{F}(\vec{\rho}) = \epsilon_o \oint_S \vec{M}_s(\vec{\rho'}) G(\vec{\rho}, \vec{\rho'}) dS'. \tag{5.6}$$

For the two-dimensional geometry in question, the Green function is

$$G(\vec{\rho}, \vec{\rho'}) = \frac{1}{4j} H_0^{(2)}(k|\vec{\rho} - \vec{\rho'}|), \tag{5.7}$$

in which $H_0^{(2)}$ is the Hankel function of second kind and order 0. In the far-field, the Hankel function is replaced by the large-argument asymptotic form; $|\vec{\rho} - \vec{\rho'}|$ is replaced by $\rho$ for amplitude variations; and $|\vec{\rho} - \vec{\rho'}|$ is replaced by $\rho - \hat{\rho} \cdot \vec{\rho'}$ for phase variations. The far-field version of the Green function is

$$G^r(\vec{\rho}, \vec{\rho'}) = \left( \frac{e^{-jk\rho}}{\sqrt{\rho}} \right) \sqrt{\frac{1}{8j\pi k}} e^{jk\hat{\rho} \cdot \vec{\rho'}}. \tag{5.8}$$

The factor in parentheses accounts for cylindrical spreading. The far-field potentials are then

$$\sqrt{\rho} e^{jk\rho} \vec{A}^r(\vec{\rho}) = \frac{\mu_o}{\sqrt{8j\pi k}} \oint_{\mathcal{S}} \vec{J}_s(\vec{\rho'}) e^{jk\hat{\rho} \cdot \vec{\rho'}} ds' \tag{5.9}$$

$$\sqrt{\rho} e^{jk\rho} \vec{F}^r(\vec{\rho}) = \frac{\epsilon_o}{\sqrt{8j\pi k}} \oint_{\mathcal{S}} \vec{M}_s(\vec{\rho'}) e^{jk\hat{\rho} \cdot \vec{\rho'}} ds'. \tag{5.10}$$

[1]Harrington [51] uses the convention $\vec{H} = \nabla \times \vec{A}$, but the more common $\vec{B} = \nabla \times \vec{A}$ is used here.

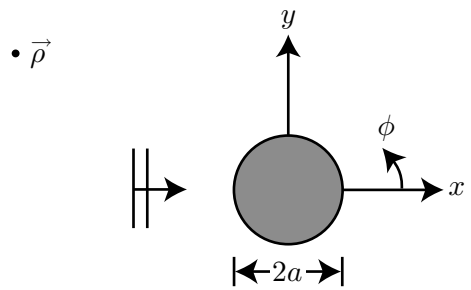


Figure 5.3: Geometry for calculating the scattering from an infinite cylinder.

These integrals are performed numerically using the equivalent currents on $\mathcal{S}$. In terms of the vector potentials, the far-zone electric field is then

$$\sqrt{\rho}e^{jk\rho}\vec{E}^r(\vec{\rho}) = j\omega\left[\hat{\rho}\times\hat{\rho}\times\sqrt{\rho}e^{jk\rho}\vec{A}^r(\vec{\rho}) + \eta_o\vec{\rho}\times\sqrt{\rho}e^{jk\rho}\vec{F}^r(\vec{\rho})\right]. \tag{5.11}$$

### 5.1.2 Validation of FDTD Implementation: Scattering from a Dielectric Cylinder

As a validation, the scattering from an infinite right circular dielectric cylinder of radius $a$ was calculated. The geometry is shown in Figure 5.3. The cylinder is centered at the origin and the scattered field is evaluated at the position $\vec{\rho} = \rho(\hat{x}\cos\phi + \hat{y}\sin\phi)$.

The incident electric field is $\vec{E}^i = \hat{y}E^i_y + \hat{z}E^i_z$, and the exact scattered field in cylindrical coordinates is obtained by a series expansion [52, replacing $e^{-i\omega t}$ with $e^{j\omega t}$ and $H^{(1)}$ with $H^{(2)}$]. The relationship between the incident and scattered field is

$$\begin{pmatrix} E^s_z \\ E^s_\phi \end{pmatrix} = \frac{e^{-jk\rho}}{\rho}e^{-j3\pi/4}\sqrt{\frac{2}{\pi k}}\begin{pmatrix} T_1 & 0 \\ 0 & T_2 \end{pmatrix}\begin{pmatrix} E^i_z \\ E^i_y \end{pmatrix}, \tag{5.12}$$

$$T_1 = b_0 + 2\sum_{n=1}^{\infty} b_n\cos n\phi, \tag{5.13}$$

$$T_2 = a_0 + 2\sum_{n=1}^{\infty} a_n\cos n\phi. \tag{5.14}$$

In terms of the logarithmic derivative

$$D_n(\alpha) = \frac{J'_n(\alpha)}{J_n(\alpha)} \tag{5.15}$$

and the normalized radius $x = k_o a$, the scattering series coefficients $a_n$ and $b_n$ are

$$a_n = \frac{[D_n(mx)/m + n/x]J_n(x) - J_{n-1}(x)}{[D_n(mx)/m + n/x]H_n^{(2)}(x) - H_{n-1}^{(2)}(x)} \tag{5.16}$$

$$b_n = \frac{[mD_n(mx) + n/x]J_n(x) - J_{n-1}(x)}{[mD_n(mx) + n/x]H_n^{(2)}(x) - H_{n-1}^{(2)}(x)}. \tag{5.17}$$

The scattering from a representative cylinder has been calculated for three wavelengths and is shown in Figure 5.4. The parameters for the cylinder are $a = 200\,\text{nm}$, $\epsilon_r = 2.56$, and $\sigma = 6398\,\text{S/m}$. The cell size was $\Delta_x = \Delta_y = 10\,\text{nm}$. These parameters are similar to the ones used for the structural color simulations in the later chapters. In the figure, the real and imaginary parts of the scattering functions are plotted. While plotting magnitude and phase may be more customary, plotting in this way demonstrates that the transform works correctly while avoiding complex issues of phase unwrapping. The agreement between the FDTD solution and the exact series solution is extremely good for all frequencies considered.

## *5.2 Scattering from Arrays*

### 5.2.1 Theory

The technique presented above for equivalent currents on a closed surface can be adapted for equivalent currents that are defined on a plane. In this case, it is possible to find the field in a half-space, as shown in Figure 5.5. The original problem, shown in Figure 5.5(a), can be converted into two possible equivalent problems, one involving the surface $\mathcal{S}_1$ and the other involving the surface $\mathcal{S}_2$. In the first, shown in Figure 5.5(b), equivalent currents are defined on the surface $\mathcal{S}_1$, defined as the plane $x = x_s$, such that the field to the left of $\mathcal{S}_1$ is unchanged and the field to the right of $\mathcal{S}_1$ is zero. The far-field magnetic vector potential for $\mathcal{S}_1$ is

$$\begin{aligned}\sqrt{\rho}e^{jk\rho}\vec{A}^r(\vec{\rho}) &= \frac{\mu_o}{\sqrt{8j\pi k}}\int_{\mathcal{S}_1}\vec{J}_s(\vec{\rho'})e^{jk\hat{\rho}\cdot\vec{\rho'}}ds' \\ &= \frac{\mu_o}{\sqrt{8j\pi k}}e^{jk\hat{\rho}\cdot\hat{x}x_s}\int_{-\infty}^{\infty}\vec{J}_s(y')e^{jk\hat{\rho}\cdot\hat{y}y'}dy'.\end{aligned} \tag{5.18}$$

The far-field electric vector potential for $\mathcal{S}_1$ follows by duality. Similar relations can be used to define potentials for $\mathcal{S}_2$.

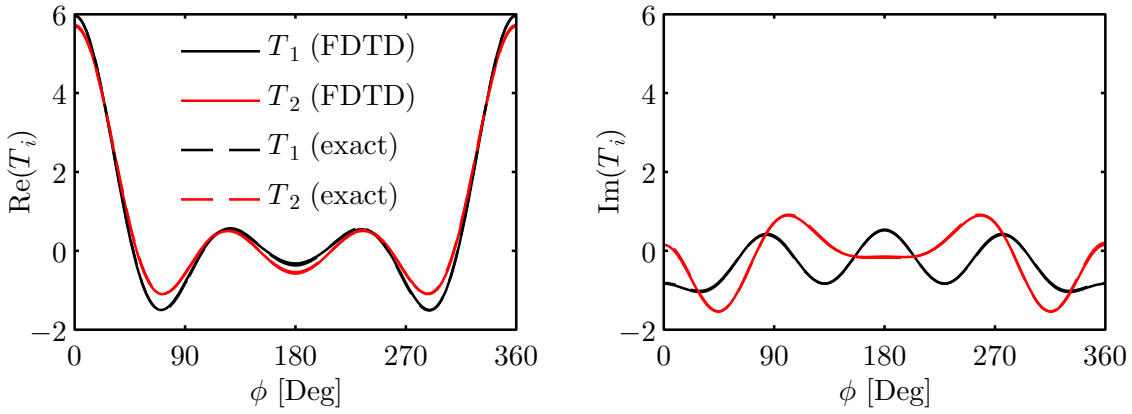


(a) $\lambda = 380$ nm

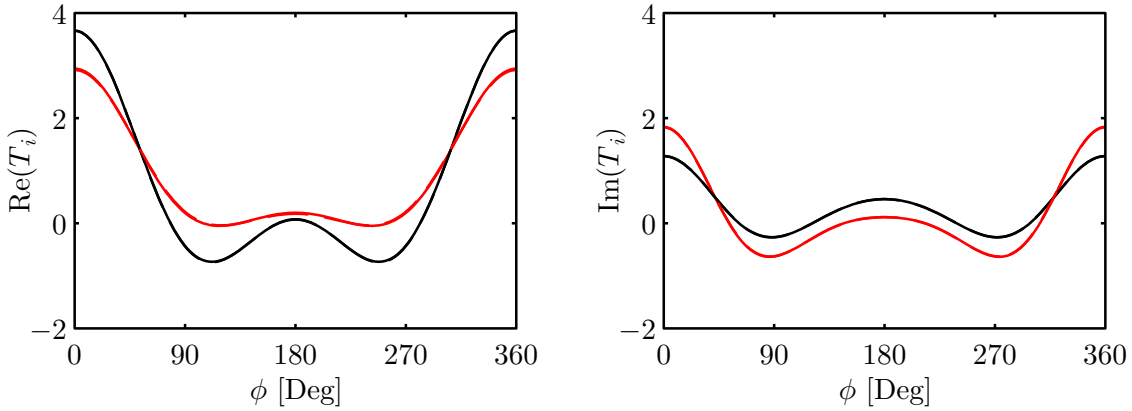


(b) $\lambda = 580$ nm

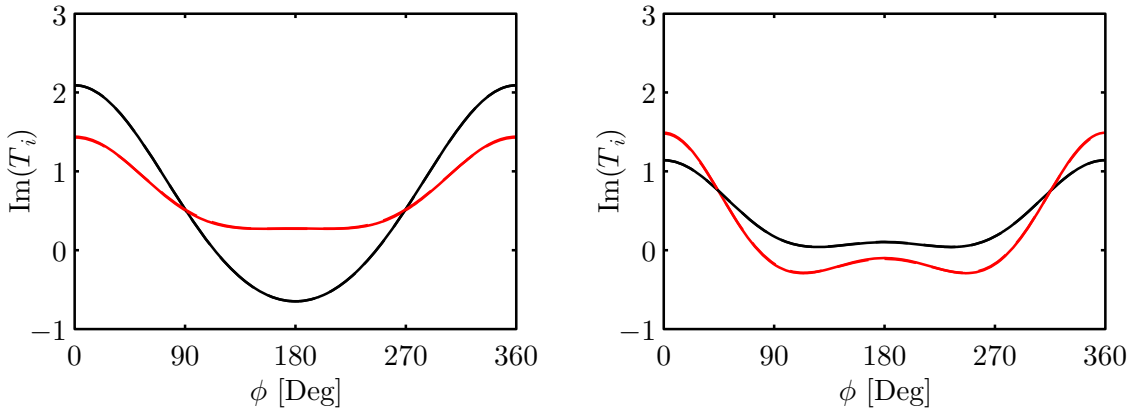


(c) $\lambda = 780$ nm

Figure 5.4: Scattering matrix elements for lossy dielectric cylinder with $a = 200\,\text{nm}$, $\epsilon_r = 2.56$ and $\sigma = 6398\,\text{S/m}$. The solid lines are computed with the FDTD method and the dashed lines are based on the series solution.

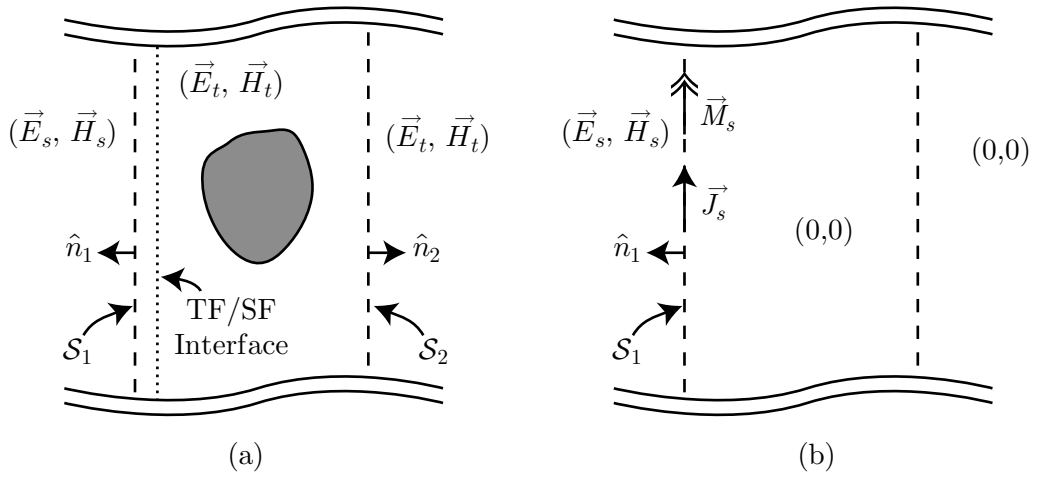


Figure 5.5: Surface equivalence principle for a half-space.

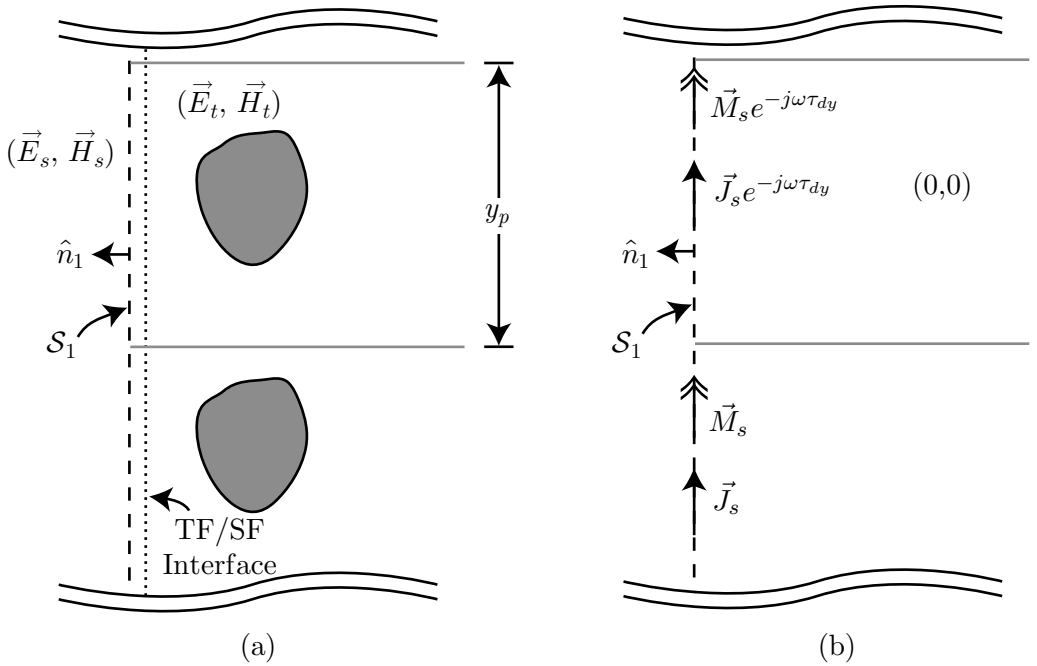


Figure 5.6: Surface equivalence principle for a half-space in a periodic problem.

For a periodic structure with a periodic excitation, it is possible to define the surface currents on $\mathcal{S}_1$ in a convenient way. Referring to the geometry in Figure 5.6, the problem is set up using a TF/SF interface (a plane-wave source) as an excitation. As previously discussed, this means that there is a constant time delay between adjacent periodic cells. This time delay,

$$\vec{\mathcal{E}}(\vec{\rho} + \hat{y}y_p; t) = \vec{\mathcal{E}}(\vec{\rho}; t - \tau_{dy}), \tag{5.19}$$

can also be expressed as a phase shift:

$$\vec{E}(\vec{\rho} + \hat{y}y_p; \omega) = \vec{E}(\vec{\rho}; \omega)e^{-j\omega\tau_{dy}}. \tag{5.20}$$

Since the equivalent currents are defined in terms of the field, this property also holds for the equivalent currents, as shown in Figure 5.6(b). The equivalent currents can be written as the spatial convolution of the currents on a single periodic cell, $\vec{J}_s^p$, with a replication term $R$. Two forms of the replication term will be useful: $R_{\text{odd}}$, will be centered at the origin; and $R_{\text{even}}$, which will be shifted by $y_p/2$:

$$\begin{aligned} R_{\text{odd}}(y) &= \sum_{\mu=-\infty}^{\infty} \delta(y - \mu y_p)e^{-j\omega\mu\tau_{dy}} \\ &= e^{-j\omega\tau_{dy}y/y_p} \sum_{\mu=-\infty}^{\infty} \delta(y - \mu y_p) \end{aligned} \tag{5.21}$$

$$\begin{aligned} R_{\text{even}}(y) &= \sum_{\mu=-\infty}^{\infty} \delta\left(y - \mu y_p - \frac{y_p}{2}\right) e^{-j\omega\mu\tau_{dy}} e^{-j\omega\tau_{dy}/2} \\ &= e^{-j\omega\tau_{dy}y/y_p} \sum_{\mu=-\infty}^{\infty} \delta\left(y - \mu y_p - \frac{y_p}{2}\right). \end{aligned} \tag{5.22}$$

If the excitation is of finite width in space, as shown in Figure 5.7, then an approximate solution is to assume a periodic structure and multiply by the profile of the excitation, $W(y)$. In this case, the approximate equivalent currents are

$$\vec{J}_s(y) = \left[\vec{J}_s^p(y) * R(y)\right] W(y). \tag{5.23}$$

If we define wavenumbers $k_x = k\hat{\rho} \cdot \hat{x}$ and $k_y = k\hat{\rho} \cdot \hat{y}$, the potential function $\vec{A}^r$ can be

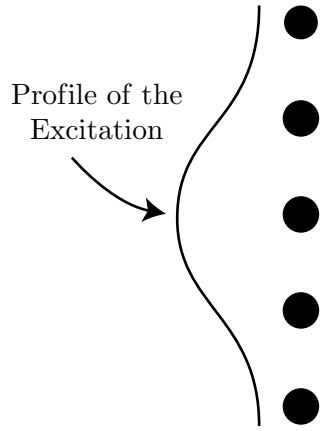


Figure 5.7: Illustration of an incident wave with a finite width.

expressed as

$$\begin{aligned}\sqrt{\rho}e^{jk\rho}\vec{A}^r(k_x,k_y) &= \frac{\mu_o}{\sqrt{8j\pi k}}e^{jk_x x_s}\int_{-\infty}^{\infty}\vec{J}_s(y')e^{jk_y y'}dy' \\ &= \frac{2\pi\mu_o}{\sqrt{8j\pi k}}e^{jk_x x_s}\left\{\frac{1}{2\pi}\int_{-\infty}^{\infty}\vec{J}_s(y')e^{jk_y y'}dy'\right\}.\end{aligned} \tag{5.24}$$

The expression has been rearranged so that the term in braces is an inverse Fourier transform. If we use the notation

$$f(k_y) = \frac{1}{2\pi}\int_{-\infty}^{\infty}F(y)e^{jk_y y}dy, \tag{5.25}$$

the entire expression can be simplified to

$$\begin{aligned}\sqrt{\rho}e^{jk\rho}\vec{A}^r(k_x,k_y) &= \frac{2\pi\mu_0}{\sqrt{8j\pi k}}e^{jk_x x_s}\vec{j}_s(k_y) \\ &= \frac{2\pi\mu_0}{\sqrt{8j\pi k}}e^{jk_x x_s}\left\{2\pi\left[\vec{j}_s^{\,p}(k_y)r(k_y)\right] * w(k_y)\right\}.\end{aligned} \tag{5.26}$$

This expression leaves three terms to be determined: $\vec{j}_s^{\,p}$, $r$, and $w$. These terms will be considered one at a time, and then they will be used to calculate $\vec{j}_s$.

#### *5.2.1.1 $r(k_y)$, the inverse transform of $R(y)$*

The replication term, $R$, is an infinite series of delta-functions. If we start with the transform pair

$$\frac{1}{y_p}\sum_{m=-\infty}^{\infty}\delta\left(k_y - \frac{2\pi m}{y_p}\right) \leftrightarrow \sum_{\mu=-\infty}^{\infty}\delta(y-\mu y_p), \tag{5.27}$$

it follows that the two choices for $r$ are

$$r_{\text{odd}}(k_y) = \frac{1}{y_p} \sum_{m=-\infty}^{\infty} \delta\left(k_y - \frac{2\pi m}{y_p} - \frac{\omega\tau_{dy}}{y_p}\right) \tag{5.28}$$

$$r_{\text{even}}(k_y) = \frac{1}{y_p} \sum_{m=-\infty}^{\infty} \delta\left(k_y - \frac{2\pi m}{y_p} - \frac{\omega\tau_{dy}}{y_p}\right) e^{j\pi m}. \tag{5.29}$$

#### 5.2.1.2 $\vec{j}_s^p(k_y)$, the inverse transform of $\vec{J}_s^p(y)$

The equivalent current $\vec{J}_s^p(y)$ is not known in advance and the transform must be computed numerically. However, since only $\vec{j}_s^p(k_y)r(k_y)$ is needed, the numerical inverse transform is only performed for the values of $k_y$ for which the argument of $r(k_y)$ is nonzero; that is, only for

$$k_y = \frac{2\pi m + \omega\tau_{dy}}{y_p}. \tag{5.30}$$

#### 5.2.1.3 $w(k_y)$, the inverse transform of $W(y)$

There are a few obvious choices for the window term. For a hard edged window, a "pulse" function can be used:

$$p_a(u) = \begin{cases} 1, & |u| < a \\ 0, & |u| > a \end{cases}. \tag{5.31}$$

This choice of window yields the transform

$$\frac{\sin(ax)}{\pi x} = \frac{a}{\pi}\text{sinc}\left(\frac{ax}{\pi}\right) \leftrightarrow p_a(u). \tag{5.32}$$

The sinc() function is the normalized version as defined by MATLAB. For a smoother transition, a gaussian window can be used:

$$\frac{a}{2\sqrt{\pi}} e^{-(ax)^2/4} \leftrightarrow e^{-(u/a)^2}. \tag{5.33}$$

#### 5.2.1.4 Evaluation of $\vec{j}_s(k_y)$

The function $\vec{j}_s(k_y)$, which is the inverse transform of the equivalent current for the truncated periodic structure, depends on the choice of $R(y)$. For $R_{\text{odd}}$, the result is

$$\vec{j}_{s,\text{odd}}(k_y) = \frac{2\pi}{y_p} \sum_{m=-\infty}^{\infty} \vec{j}_s^p\left(\frac{2\pi m}{y_p} + \frac{\omega\tau_{dy}}{y_p}\right) w\left(k_y - \frac{2\pi m}{y_p} - \frac{\omega\tau_{dy}}{y_p}\right), \tag{5.34}$$

and for $R_{\text{even}}$, the result is

$$\vec{j}_{s,\text{even}}(k_y) = \frac{2\pi}{y_p} \sum_{m=-\infty}^{\infty} \vec{j}_s^{\,p} \left( \frac{2\pi m}{y_p} + \frac{\omega \tau_{dy}}{y_p} \right) w \left( k_y - \frac{2\pi m}{y_p} - \frac{\omega \tau_{dy}}{y_p} \right) e^{j\pi m}. \tag{5.35}$$

### 5.2.2 Validation of FDTD Implementation: Scattering from an Array of Dielectric Cylinders

As a validation, the scattering from an array of 21 identical cylinders was calculated. The cylinders are identical to the one from the previous section and are spaced 1000 nm apart. The excitation is a normally incident plane wave. This corresponds to the hard edged window above. The calculation was performed using the FDTD method for a 21 cylinder finite array using the transform for finite objects, and for a single cylinder using periodic boundary conditions and the transform for periodic objects. The comparison of the scattered electric field for two polarizations of the incident field is shown in Figure 5.8. There is very good agreement for all frequencies examined for most directions. However, the scattered electric field near the plane of the array ($\phi = 90^\circ, 270^\circ$) does not agree. In these directions, the truncation effects on the edge of the finite array are most significant, but these effects are not included in the periodic model.

The simulation demonstrates an important feature of arrays. For even relatively small arrays, the coherent interference between elements causes the scattered field to be focused in only a few directions. These directions are determined by the spacing of the array. This focusing will be of interest in the study of structural color in the later chapters.

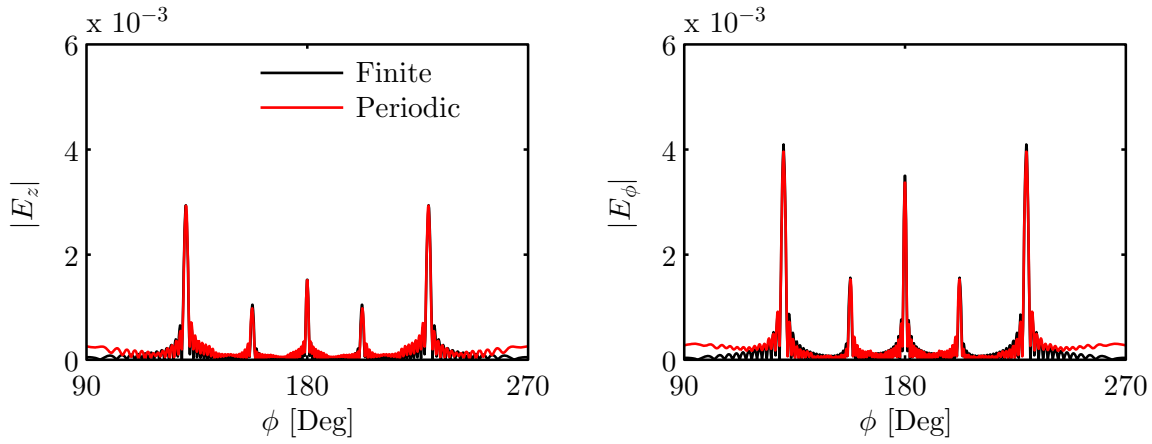


(a) $\lambda = 380$ nm

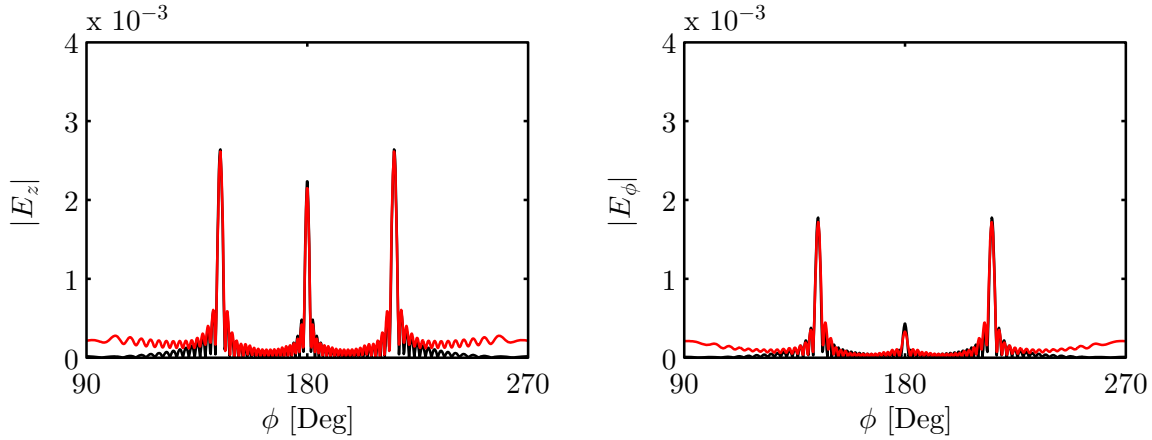


(b) $\lambda = 580$ nm

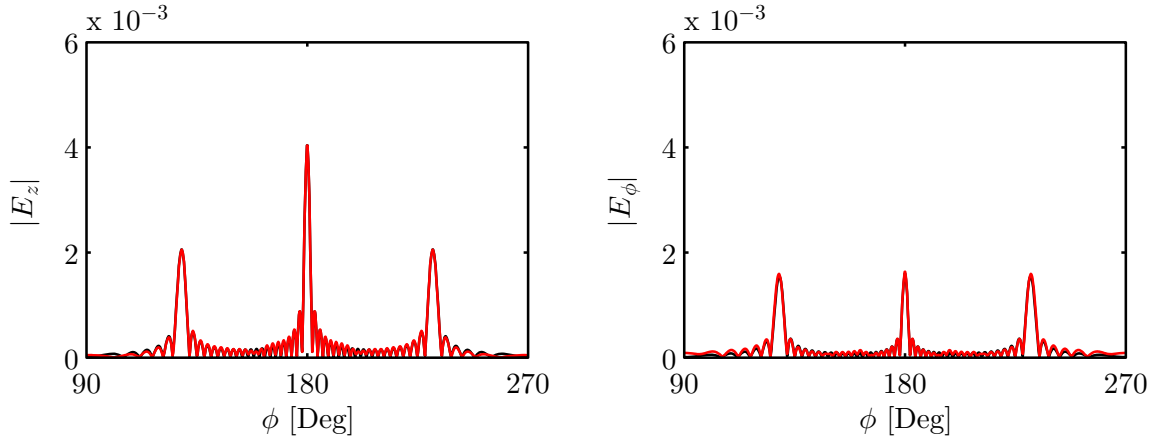


(c) $\lambda = 780$ nm

Figure 5.8: Scattered electric field for an array of 21 lossy dielectric cylinders with $a = 200\,\text{nm}$, $\epsilon_r = 2.56$, and $\sigma = 6398\,\text{S/m}$. The spacing between the cylinders is 1000 nm.

# CHAPTER VI

# COLORIMETRY

In this chapter, the problem of converting from computed electromagnetic data to observed color is addressed. First, the electromagnetic quantities available from the FDTD method are expressed in terms of radiometric quantities. These radiometric quantities are then converted into tristimulus values using color matching functions. Finally, the tristimulus values are converted into RGB values that can be displayed or printed.

## *6.1 Calculating Radiometric Quantities with FDTD*

It is convenient to use standard radiometric quantities as defined by [53] in colorimetry calculations. The quantities can be easily calculated from electromagnetic field values from an FDTD simulation. The excitation is a linearly polarized plane wave that is a pulse in time,

$$\vec{\mathcal{E}}_i(\vec{r};t) = \hat{e}\,\mathcal{G}(t - \hat{k}_i \cdot \vec{r}/c). \tag{6.1}$$

In the frequency domain, the incident field is

$$\vec{E}_i(\vec{r};\omega) = \hat{e}\,G(\omega)e^{-j\vec{k}_i\cdot\vec{r}}. \tag{6.2}$$

In the following calculations, it is assumed that the spectrum of the incident field, $G(\omega)$, is divided out so that the effective incident field is

$$\vec{E}_i(\vec{r};\omega) = \hat{e}\,e^{-j\vec{k}_i\cdot\vec{r}}. \tag{6.3}$$

This wave is incident on a periodic structure made up of $n_y$ by $n_z$ periods, each of size $y_p$ by $z_p$. Therefore, the area of the object is

$$A = n_y n_z y_p z_p. \tag{6.4}$$

A certain amount of power, called *radiant flux* and denoted by $\Phi_e$, is incident on the object. The total radiant flux is the projection of the time-average Poynting vector of the incident

field onto the unit normal $\hat{n}$ multiplied by the area,

$$\Phi_e = \mathrm{Re}(-\hat{n} \cdot \vec{S}_c)A = \frac{1}{2\eta_o}|\vec{E}_i|^2|\hat{k}_i \cdot \hat{n}|A. \tag{6.5}$$

Radiant flux has units of watts ($W$). A related quantity is the power incident on the structure per unit area. This quantity is called the *irradiance* and is denoted by $E_e$,

$$E_e = \frac{d\Phi_e}{dA} = \mathrm{Re}(-\hat{n} \cdot \vec{S}_c) = \frac{1}{2\eta_\mathrm{o}}|\vec{E}_i|^2|\hat{k}_i \cdot \hat{n}|. \tag{6.6}$$

Irradiance has units of watts per square meter ($W \cdot \mathrm{m}^{-2}$).

In the far-zone, the scattered electric field has a $1/r$ dependence. The frequency-domain near-to-far-field transform from the previous chapter is used to calculate $|rE_\theta|$ and $|rE_\phi|$, which are the far-zone electric fields without the $1/r$ dependance. To calculate the *radiant intensity*, which is the reflected radiant flux per unit solid angle and denoted by $I_e$, the time-average Poynting vector without the $1/r^2$ power dependence is needed. This quantity is measured in watts per steradian ($W \cdot \mathrm{sr}^{-1}$) and is given by

$$I_e = \frac{1}{2\eta_\mathrm{o}}\left(|rE_\theta|^2 + |rE_\phi|^2\right). \tag{6.7}$$

The final quantity is the *radiance*, which is the radiant intensity per unit of projected area. Radiance is denoted by $L_e$ and is measured in watts per steradian per square meter ($W \cdot \mathrm{sr}^{-1} \cdot \mathrm{m}^{-2}$):

$$L_e = \frac{dI_e}{dA(\hat{r} \cdot \hat{n})} = \frac{1}{2\eta_\mathrm{o}A(\hat{r} \cdot \hat{n})}(|rE_\theta|^2 + |rE_\phi|^2). \tag{6.8}$$

These quantities are generally considered *spectral* quantities. This means that the functions are per unit wavelength. For example, assuming that wavelengths are measured in nanometers, spectral irradiance has units of watts per square meter per nanometer ($W \cdot \mathrm{m}^{-2} \cdot \mathrm{nm}^{-1}$).

## *6.2 Brightness Calibration*

To determine the brightness of a object, a reference is needed for comparison. Typically, a perfect reflecting diffuser (also known as a Lambertian surface) is used as a standard. This artificial structure has a radiant intensity that is a function of the observation direction,

$$I_e^n(\hat{r}) = I_e^n(\hat{n})\hat{r} \cdot \hat{n}. \tag{6.9}$$

Here the superscript $n$ indicates that this is the quantity we will use for normalization. The above equation is a vectorial expression of Lambert's cosine law. Since the surface reflects all light incident on it, the integral of the radiant intensity over a half-space must equal the incident radiant flux. For the specific case of $\hat{n} = \hat{z}$, this implies

$$\begin{aligned}\Phi_e &= \int_0^{2\pi}\int_0^{\pi/2} I_e^n(\theta,\phi)\cos\theta\sin\theta d\theta d\phi \\ &= 2\pi I_e^n(\theta=0)\left(\frac{1}{2}\sin^2\theta\Big|_0^{\pi/2}\right) \\ &= \pi I_e^n(0).\end{aligned} \tag{6.10}$$

Therefore, the radiant intensity of a Lambertian surface is

$$I_e^n(\hat{r}) = \frac{\Phi_e}{\pi}\hat{r}\cdot\hat{n}. \tag{6.11}$$

The radiant intensity of a Lambertian surface depends on the viewing direction. However, the radiance is constant for all directions:

$$L_e^n = \frac{\Phi_e}{\pi A}. \tag{6.12}$$

Implicit in the idea of radiance is the understanding that the object is large enough for it to look larger than a point source. If the object is too small, then the perceived area, $A\hat{r}\cdot\hat{n}$ from the above expressions, is the same in all directions. In that case, the radiant intensity is just

$$I_e^n = \frac{\Phi_e}{2\pi}. \tag{6.13}$$

Because the butterfly scales are so small, we will use this definition for the color calculations reported in the next chapter.

To characterize a material, the usual metric is the reflectance factor, $R_\lambda$. This is defined as the "ratio of the flux reflected from the specimen to the flux reflected from the perfect reflecting diffuser under the same geometric and spectral conditions of measurements" [53]. In terms of the radiometric quantities defined above, we have

$$R_\lambda(\hat{r}) = \frac{I_e(\hat{r})}{I_e^n}. \tag{6.14}$$


Figure 6.1: Color as a function of wavelength in the visible spectrum

## *6.3 Conversion of Spectral Data to Color*

The conceptual setup for calculating the color of a material is as shown in Figure 1.3. The reflected light is viewed by the observer and interpreted as color. For a monochromatic light, the human eye sees the light as a pure spectral color (that is, a color from the rainbow), as shown in Figure 6.1. In this figure, the spectrum is very dark at the minimum and maximum wavelengths; the human eye is not very sensitive to light at these wavelengths. For a general light, the color is a weighted mix of the spectral colors.

The light source is arbitrary. It can be, for example, an incandescent light or daylight. Any source can be used in which the power emitted as a function of wavelength is known. For color calculations, only the relative power is required, and the *relative spectral power distribution* $S_\lambda$ is defined as [54]:

$$S_\lambda = \frac{\Phi_e(\lambda)}{\Phi_e(560\,\mathrm{nm})}. \tag{6.15}$$

A light defined by a spectral power distribution is known as an *illuminant*, and several standard illuminants have been defined by the International Commission on Illumination (CIE). For modeling natural daylight, the series of $D$ illuminants are recommended. In this thesis, $D_{65}$ is used. This illuminant has a correlated color temperature of 6504 K [55], and the spectral power distribution is shown in Figure 6.2.

The human eye contains three types of color-sensitive cones [54]. Each type is sensitive to light in a range of wavelengths. Rather than directly using the cone sensitivity data (cone fundamentals), the standard method is to use a set of three color-matching functions $\bar{x}_\lambda$, $\bar{y}_\lambda$, and $\bar{z}_\lambda$. These functions were derived based on color-matching experiments with small group of individuals, and have been standardized by the CIE and ASTM. There are several choices for color-matching functions; in this thesis, the 1931, 2° observer functions,

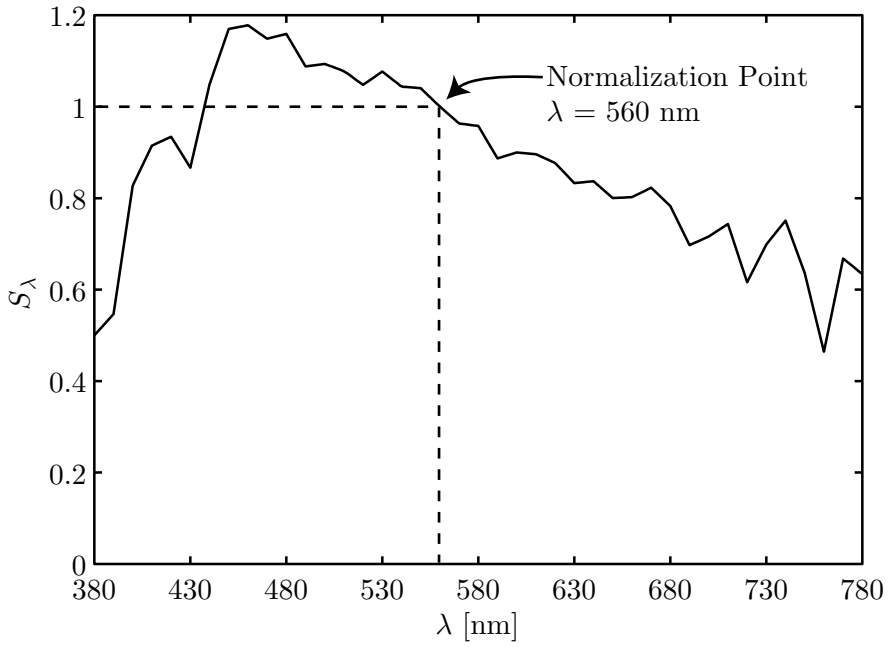


Figure 6.2: Spectral power distribution for CIE standard illuminant $D_{65}$ [56].

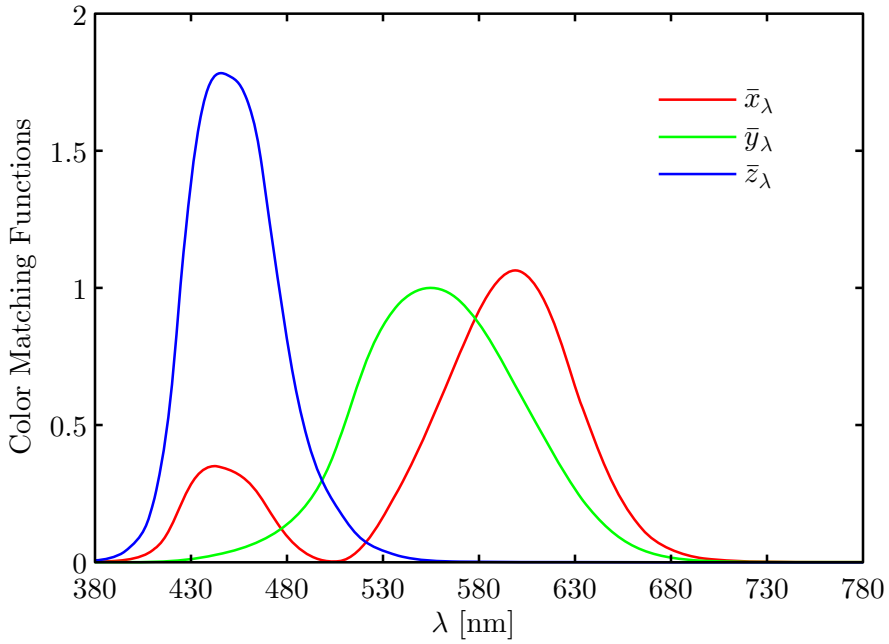


Figure 6.3: Color matching functions for the CIE 1931 2° standard observer [56].

shown in Figure 6.3, are used, but other choices are available.

For any particular object with a reflectance factor given by $R_\lambda$, the illuminant and color-matching functions are used to define the tristimulus values $(X, Y, Z)$ of the reflected light. These quantities are given by summing the product of the illumination, $S_\lambda$; the reflectance factor, $R_\lambda$; and one of the three CIE standard color matching functions, $\bar{x}_\lambda$, $\bar{y}_\lambda$, or $\bar{z}_\lambda$, as follows:

$$X = k \sum_\lambda S_\lambda R_\lambda \bar{x}_\lambda \Delta_\lambda \tag{6.16}$$

$$Y = k \sum_\lambda S_\lambda R_\lambda \bar{y}_\lambda \Delta_\lambda \tag{6.17}$$

$$Z = k \sum_\lambda S_\lambda R_\lambda \bar{z}_\lambda \Delta_\lambda. \tag{6.18}$$

In this thesis, $\Delta_\lambda = 5\,\text{nm}$, and the constant $k$ is set so that a perfect diffuser ($R^n_\lambda = 1$) has the value $Y_n = 100$:

$$k = \frac{100}{\sum_\lambda S_\lambda \bar{y}_\lambda \Delta\lambda}. \tag{6.19}$$

With this definition, the tristimulus value for the perfect diffuser, $(X_n, Y_n, Z_n)$, is known as the "white point."

This choice of color-matching functions has a unique feature. The human eye is not equally sensitive to all wavelengths. For example, two lights with equal radiance but different wavelengths will not be perceived as equally bright. The sensitivity versus wavelength is known as the luminous efficiency function. The function $\bar{y}_\lambda$ is equal to this function. Therefore, the value $Y$ is the luminance of the light.

A related quantity is the chromaticity coordinate. This is defined by normalizing the tristimulus values.

$$x = \frac{X}{X + Y + Z} \tag{6.20}$$

$$y = \frac{Y}{X + Y + Z} \tag{6.21}$$

$$z = \frac{Z}{X + Y + Z}. \tag{6.22}$$

Since $x+y+z=1$, only two of these values, typically $x$ and $y$, are required. Defined in this way, the chromaticity coordinates specify the color and purity of the light, and the value $Y$ specifies the luminance.

Using the above method gives a color in the CIEXYZ device-independent color space. To convert to an $RGB$ value (a device-dependent color space) that can be displayed on a computer monitor or printed, a transform matrix is required. Although a matrix to go from $XYZ$ to $RGB$ is desired, it is easier to derive an $RGB$ to $XYZ$ matrix, then invert it. Specifically, a matrix $[M]$ is required that satisfies

$$\begin{bmatrix} R \\ G \\ B \end{bmatrix} = [M] \begin{bmatrix} X \\ Y \\ Z \end{bmatrix}. \tag{6.23}$$

The inverse matrix can then be specified as

$$\begin{bmatrix} X \\ Y \\ Z \end{bmatrix} = \underbrace{\begin{bmatrix} X_{r,max} & X_{g,max} & X_{b,max} \\ Y_{r,max} & Y_{g,max} & Y_{b,max} \\ Z_{r,max} & Z_{g,max} & Z_{b,max} \end{bmatrix}}_{[M]^{-1}} \begin{bmatrix} R \\ G \\ B \end{bmatrix}. \tag{6.24}$$

Each of the matrix entries is a tristimulus value when the corresponding channel is set to maximum and the others are turned off, e.g., $X_{r,max}$ is the value of $X$ that corresponds to $RGB = [1,0,0]$. A computer monitor can be calibrated so that the chromaticity of the phosphors are adjusted to known values. Specifically, they are adjusted to the sRGB standard [57]. It is convenient to express each of the elements of the matrix $[M]^{-1}$ in terms of chromaticity coordinates and luminances.

$$[M]^{-1} = \begin{bmatrix} x_r/y_r & x_g/y_g & x_b/y_b \\ 1 & 1 & 1 \\ z_r/y_r & z_g/y_g & z_b/y_b \end{bmatrix} \begin{bmatrix} Y_{r,max} & 0 & 0 \\ 0 & Y_{g,max} & 0 \\ 0 & 0 & Y_{b,max} \end{bmatrix}. \tag{6.25}$$

The chromaticity matrix is known and the luminance matrix must be determined.

To determine the luminance matrix, the assumption is that $RGB = [1,1,1]$ maps to

white, $XYZ = [X_n, Y_n, Z_n]$. Expressing things once again in terms of chromaticity coordinates and luminances, we get

$$\begin{bmatrix} \frac{x_n}{y_n}Y_n \\ Y_n \\ \frac{z_n}{y_n}Y_n \end{bmatrix} = \begin{bmatrix} x_r/y_r & x_g/y_g & x_b/y_b \\ 1 & 1 & 1 \\ z_r/y_r & z_g/y_g & z_b/y_b \end{bmatrix} \begin{bmatrix} Y_{r,max} & 0 & 0 \\ 0 & Y_{g,max} & 0 \\ 0 & 0 & Y_{b,max} \end{bmatrix} \begin{bmatrix} 1 \\ 1 \\ 1 \end{bmatrix}. \tag{6.26}$$

Assuming $Y_n = 100$ (the convention in the sRGB standard is that luminances range from 0 to 100), everything but the phosphor luminances is known. These are then determined by

$$\begin{bmatrix} Y_{r,max} \\ Y_{g,max} \\ Y_{b,max} \end{bmatrix} = \begin{bmatrix} x_r/y_r & x_g/y_g & x_b/y_b \\ 1 & 1 & 1 \\ z_r/y_r & z_g/y_g & z_b/y_b \end{bmatrix}^{-1} \begin{bmatrix} \frac{x_n}{y_n}Y_n \\ Y_n \\ \frac{z_n}{y_n}Y_n \end{bmatrix}. \tag{6.27}$$

The chromaticity coordinates for the phosphors and the white point are (from the sRGB standard)

$$x_r = 0.64 \qquad x_g = 0.3 \qquad x_b = 0.15 \qquad x_n = 0.3127 \tag{6.28}$$

$$y_r = 0.33 \qquad y_g = 0.6 \qquad y_b = 0.06 \qquad y_n = 0.3290 \tag{6.29}$$

$$z_r = 0.03 \qquad z_g = 0.1 \qquad z_b = 0.79 \qquad z_n = 0.3583 \tag{6.30}$$

In reality, this does not give the luminances for the monitor. Rather, the ratio $Y_{r,max} : Y_{g,max} : Y_{b,max} = 21.2639 : 71.5169 : 7.2192$ is now known. The necessary transform matrix $[M]$ is, therefore,

$$[M] = \begin{bmatrix} 3.2410 \times 10^{-2} & -1.5374 \times 10^{-2} & -4.9861 \times 10^{-3} \\ -9.6924 \times 10^{-3} & 1.8760 \times 10^{-2} & 4.1555 \times 10^{-4} \\ 5.5630 \times 10^{-4} & -2.0398 \times 10^{-3} & 1.0570 \times 10^{-2} \end{bmatrix}. \tag{6.31}$$

Now the matrix $[M]$ is known, and the desired $RGB$ values are

$$\begin{bmatrix} R \\ G \\ B \end{bmatrix} = [M] \begin{bmatrix} X \\ Y \\ Z \end{bmatrix}. \tag{6.32}$$

These $RGB$ values are linear $RGB$ values; that is, the luminance of $[1, 1, 1]$ is twice the luminance of $[0.5, 0.5, 0.5]$. However, computer monitors are gamma-corrected. This means that the displayed value (the percent of the maximum for each channel) is nonlinearly related to the input value. For each channel, to get the required value $C'$, in which $C$ represents $R$, $G$, or $B$, we use

$$C' = C^{1/\gamma}. \tag{6.33}$$

For monitors calibrated to the sRGB standard, $\gamma \approx 2.2$.

In summary, the tristimulus values $XYZ$ are calculated first. These are transformed to $RGB$ using the linear transformation. The monitor gamma is then backed out to get $R'G'B'$. The corrected values $R'G'B'$ are the values that can be directly displayed on the monitor.

## *6.4 The Chromaticity Diagram*

Color is a three-dimensional quantity that can be expressed in a number of equivalent ways. As shown above, the chromaticity coordinates $x$ and $y$ together express the dominant wavelength and purity of a color. The chromaticity coordinates of pure monochromatic light is just the value of the color matching function at the wavelength of the light. If these coordinates are plotted with wavelength as a parameter, the plot is a horseshoe shape, as shown in Figure 6.4. The boundary of this plot is the spectral locus, with represents pure spectral colors. The purity of a color is indicated by the distance from the spectral locus. The "white point", $(x_n = 0.3127, y_n = 0.3290)$, is the shown as grey near the center of the area enclosed by the spectral locus. Chromaticity coordinates outside the spectral locus do not represent physically realizable colors.

If we wish to produce a colored chromaticity diagram, then the coordinates $x$, $y$, and $Y$ are required. At first glance, it seems that a constant $Y$ value should be used for the entire plot. Unfortunately, this is not practical. Since the luminous efficiency function is largest near the green part of the spectrum, it is difficult to plot a green color and, for example, a blue color that are perceived as equally bright. The entire graph would have to be very dark to achieve a constant luminance. Instead, the luminance is assigned as $Y = y$,

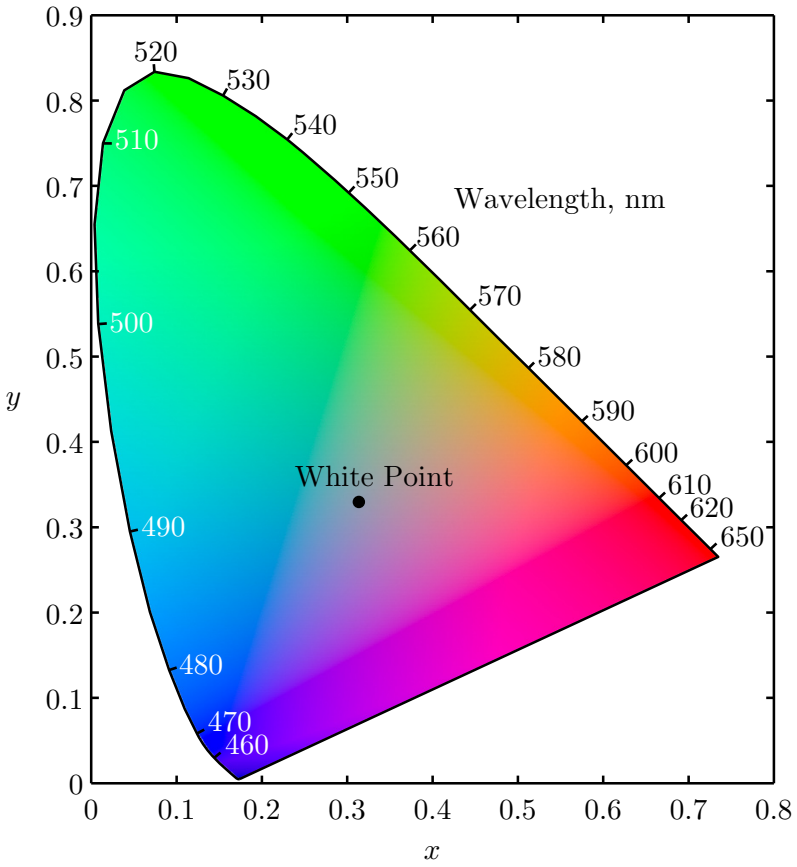


Figure 6.4: Chromaticity diagram using the 1931, 2° color matching functions. The wavelengths of the pure spectral colors are labeled on the spectral locus.

and the remaining tristimulus values are $X = x$ and $Z = 1 - x - y$. These values of $X$, $Y$, and $Z$ are converted to $RGB$ values as explained above. In this way, an approximate color can be specified at each chromaticity coordinate. Note that one must be very careful in assigning too much weight to this color; the gamut of possible colors producible on a computer monitor or a printable on a page is limited. Therefore, the color on the diagram should only be used as an guide.

The principle use of the chromaticity diagram is as tool for plotting changes in color. This approach will be taken in the following chapter.

# CHAPTER VII

# ANALYSIS OF BUTTERFLIES

In this chapter, the results of numerically modeling several butterflies exhibiting structural color are presented. The computational model is presented first. A technique for calculating the scattered field from an imperfect periodic structure is then developed. Finally, results are presented for computational models similar to various species from the *Morpho* genus, as well as the *Troides magellanus* and *Ancyluris meliboeus* butterflies.

## *7.1 Overview of Structure for a Scale*

The male *Morpho rhetenor*, shown in Figure 7.1, is a typical butterfly that exhibits structural color. This species is a very intense blue that fades to a deep violet when viewed near grazing. The wings are covered with a large number of small scales that are easily visible using a low-power optical microscope. The scales, in turn, are covered with a series of quasi-periodic ridges that are less than $1\,\mu$m apart, which are shown in Figure 7.1(c). Each ridge is a tree-like structure with 4–12 branches on both sides. The structure is made of cuticle with an approximate complex index of refraction $\tilde{n} = 1.56 - j0.06$ [23].

In some species of butterfly, there are two types of scales. The first type, known as a ground scale, is similar to the scales on the *M. rhetenor*. In addition, a second type of scale, known as a cover scale, is layered over the ground scales. These scales are semi-transparent and serve to diffuse the scattering from the ground scales [32]. The research reported in this thesis is primarily concentrated on ground scales, though some simplified cover scales are considered.

Several of the features of the scale were varied and the resulting changes in color were observed. These changes are plotted in several ways in the following sections. The goal was not to create an exact computational model for the *M. rhetenor* or any other butterfly; rather, it was to study the effect of varying geometrical parameters on a generic scale.

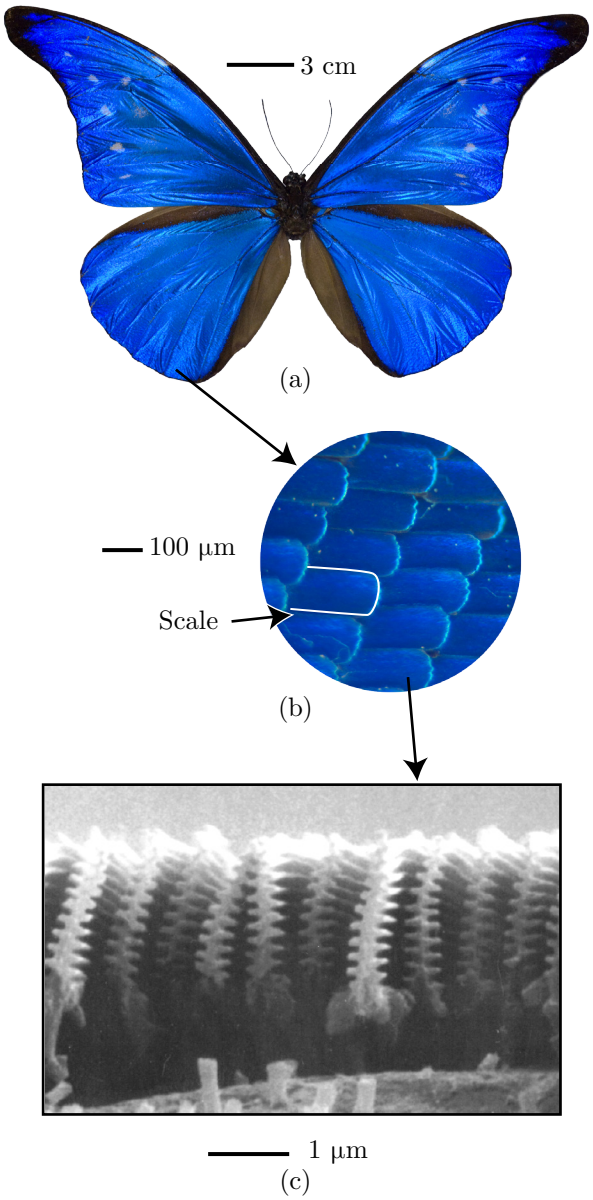


Figure 7.1: Images of a male *Morpho rhetenor* butterfly. (a) Dorsal side (top) of full size insect. (b) Detail of wing showing scales as viewed under an optical microscope. (c) Cross section of scale showing individual ridges as viewed using a scanning electron microscope. SEM image courtesy S. Kinoshita [22, pg. 13, Figure 12].

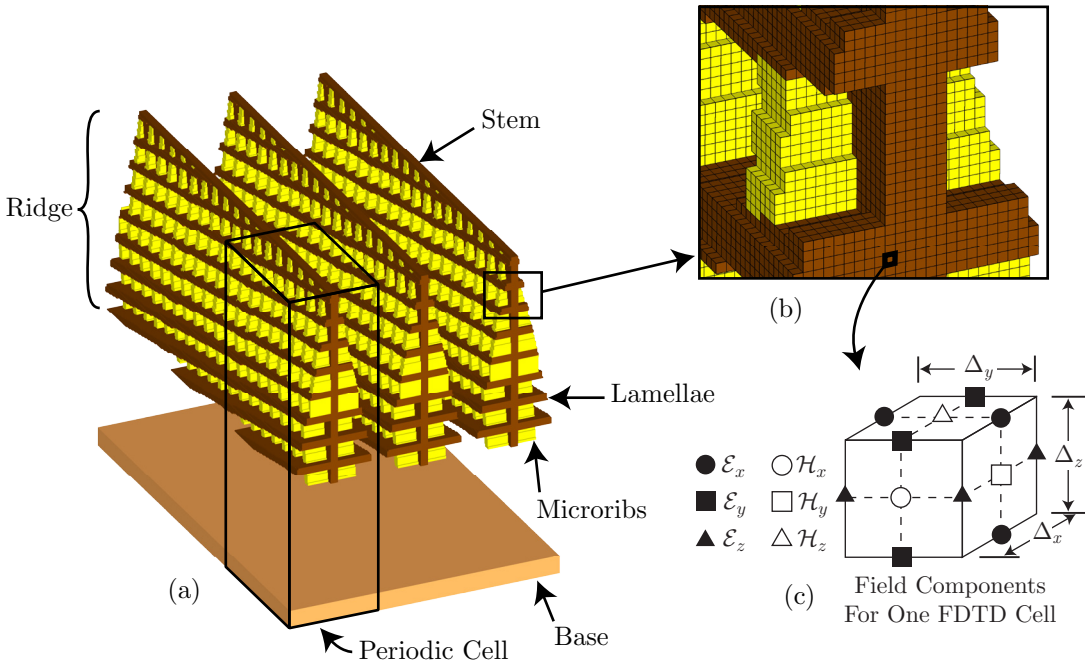


Figure 7.2: The computational model. (a) Portion of a scale showing three ridges. The volume within the black frame is the volume used for the periodic FDTD calculations. (b) Detail of a single ridge showing the individual FDTD cells. (c) Arrangement of the electromagnetic field components within a single FDTD cell.

## *7.2 Computational Model*

### 7.2.1 Discretized Geometry

By examining electron micrographs such as Figure 7.1(c), a computational model for a generic butterfly scale can be developed. An example of such a model is shown in Figure 7.2(a). In this model, the base, which is the relatively featureless cuticle sheet at the bottom of Figure 7.1(c), is modeled as a dielectric slab. The upper structure, known as a ridge, is a set of dielectric slabs with different dimensions and orientations. First, there is a central stem that supports the structure. On either side of this stem are branch-like arms called lamellae. The lamellae are often tapered, with those closest to the base being the widest. Usually, the lamellae are slightly tilted in the longitudinal direction ($y$) with respect to the base; however, some species have a very high tilt, as will be discussed below. In addition to the lamellae, there is sometimes a second set of layers nearly orthogonal to the first. These layers are smaller than the main layers and are called microribs. In Figure 7.2, the components of the ridge are drawn in different colors for ease of identification. In the model,

they all have the same electrical properties: electrical permittivity $\epsilon = 2.43\epsilon_o$, magnetic permeability $\mu = \mu_o$, and electrical conductivity $\sigma = 6.4 \times 10^3\,\mathrm{S/m}$. The permittivity and conductivity were obtained from the aforementioned complex index of refraction, $\tilde{n}$, at the wavelength $\lambda = 488\,\mathrm{nm}$.

The structure in Figure 7.2(a) is periodic along both the $x$ and $y$ axes. The periodic cell, indicated by the black frame, is repeated three times in each lateral direction ($x$ and $y$) in this figure. The periodic cell is examined in more detail in Figure 7.3. In this figure, the width of the periodic cell, $x_p$, is the period of the ridges, and the length, $y_p$, is determined by the spacing between the lamellae, $g$, the thickness of the lamellae, $h$, and the tilt angle of the lamellae with respect to the base, $\alpha$, according to

$$y_p = (g + h)/\sin\alpha. \tag{7.1}$$

If present, the width and spacing of the microribs, $f$ and $e$, respectively, are constrained so that an integer number of microribs lie within a single periodic cell.

Figure 7.3(a)–(c) show three variations on the generic model. The number of lamellae in all cases is $N$. In (a) the lamellae are all of the same width, $a$, and those on the left and right sides of the stem are aligned. In (b) some of the lamellae are tapered, so the maximum width is $a$ and the minimum width is $d$. Finally, in (c) the lamellae on the left and right sides of the stem are offset instead of aligned, and two additional features that are modeled as dielectric layers are added: the base layer below the ridge and the diffusing layer above the ridge, which is a highly simplified model for the effect of a cover scale.

In the actual scales, there is also structure between the ridges and the base that supports the ridges. Calculations, not presented here, show that this structure has little effect on the color of the scattered light, so it is omitted in this model.

### 7.2.2 Modeling of Natural Light

We will consider butterfly scales exposed to natural light (daylight). Natural light is incoherent light that is unpolarized. Here it is modeled by making two separate calculations (1

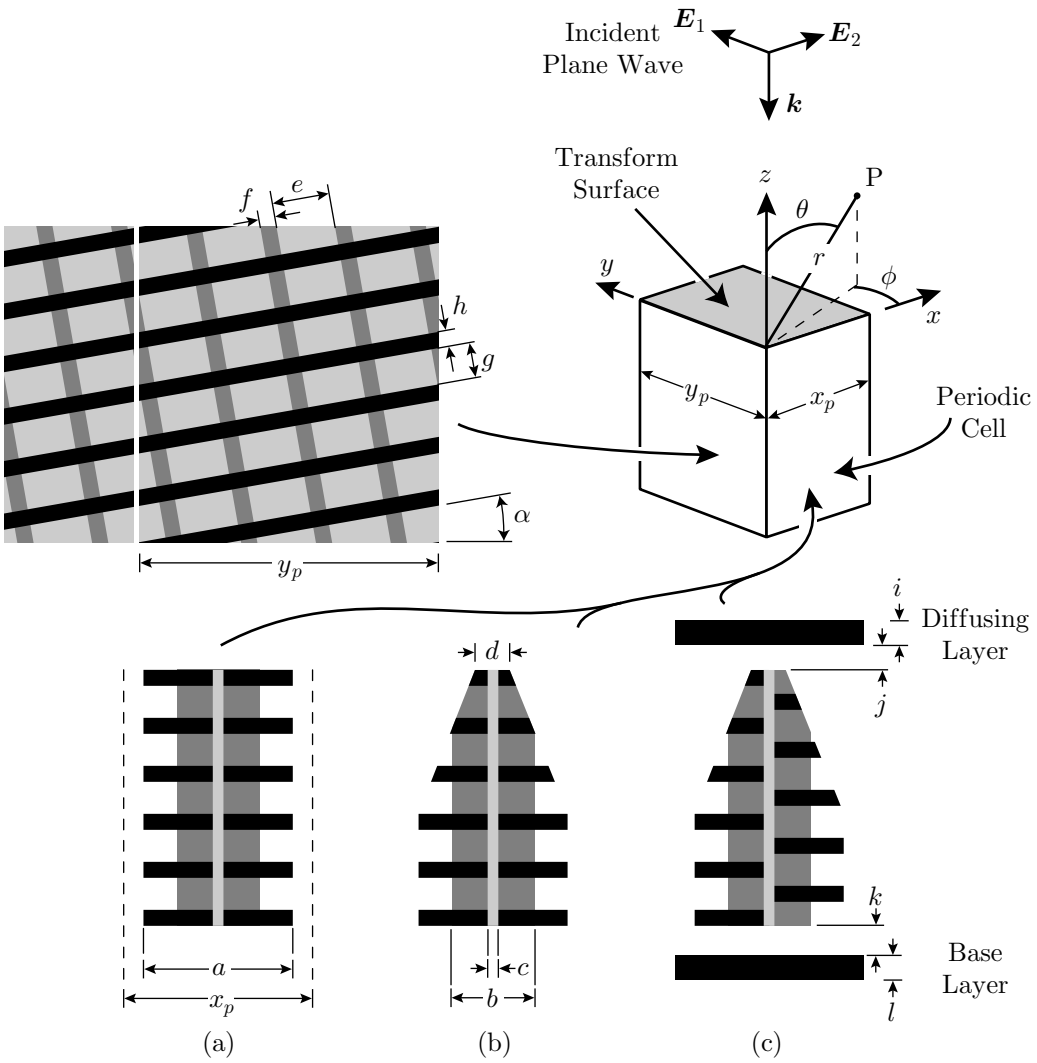


Figure 7.3: Parameters used to describe the geometry of a periodic cell and the coordinates for a point P in space.

and 2) in which the states of linear polarization of the incident plane waves are orthogonal:

$$\vec{\mathcal{E}}_1^i(\vec{r};t) = \hat{e}_1\,\mathcal{G}(t - \hat{k}_i \cdot \vec{r}/c) \tag{7.2}$$

$$\vec{\mathcal{E}}_2^i(\vec{r};t) = \hat{e}_2\,\mathcal{G}(t - \hat{k}_i \cdot \vec{r}/c), \tag{7.3}$$

with

$$\hat{e}_1 \cdot \hat{e}_2 = 0. \tag{7.4}$$

All subsequent calculations based on these fields, such as reflection and transmission coefficients, involve the *power*, and they are obtained by averaging the appropriate powers for the two states.

## *7.3 The Effect of Randomness on the Geometry*

The scales on a butterfly wing are covered with a series of quasi-periodic ridges that are less than $1\,\mu$m apart. The scales are approximately $100\,\mu$m wide, which corresponds to about 100 ridges for a typical scale. In light of the results for scattering from periodic structures presented in Chapter 5, such a large array should demonstrate highly directional scattering. These insects, however, possess colors that are visible over a fairly wide range of angles even though the structures are periodic. There are several possible reasons for this difference.

An incident plane wave is not a complete model for the illumination. This type of wave has an infinite transverse coherence length, $l_c$. Such a source does not exist in the real world. An obvious illumination source is light from the sun. If the sun is assumed to be a circular distribution of incoherent point sources, then the transverse coherence length $l_c$ is [58]

$$l_c = \frac{1.22\bar{\lambda}_o}{\theta}, \tag{7.5}$$

in which $\bar{\lambda}_o$ is the average wavelength of the light, and $\theta$ is the angular width of the sun at the observation point. On earth, the angular width of the sun is approximately $0.5^\circ$ [59], which means that the coherence length is in the range $50\,\mu$m to $100\,\mu$m for $\lambda_o$ within the visible spectrum. This length includes almost an entire scale ($50 - 100$ ridges in a typical case); therefore, the finite transverse coherence length does not explain the broad scattering.

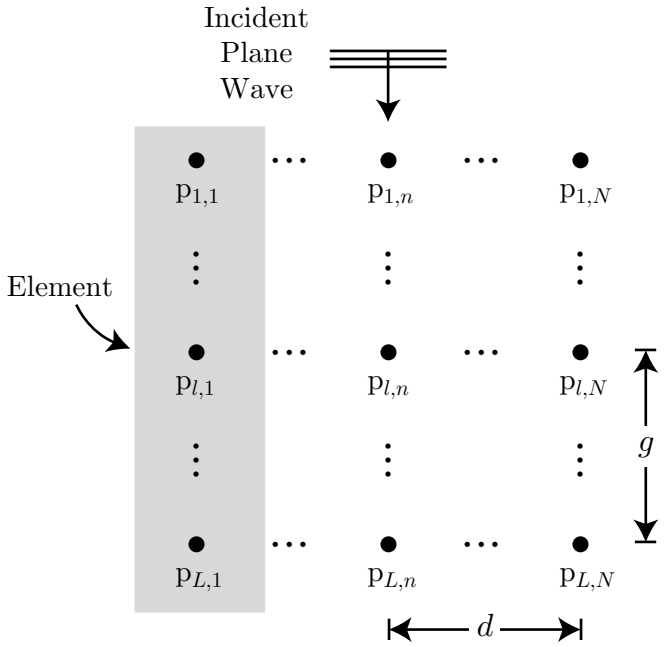


Figure 7.4: Geometry for an array of point scatterers.

While incoherence clearly limits the distance over which the scattering from the ridge adds coherently, it is not sufficient to explain the broad scattering from the butterfly scale. Another possible explanation is that the structures are not perfectly periodic. Rather, there is a certain amount of irregularity in the positioning of the ridges on the scale. This irregularity was discussed by Kinoshita and Yoshioka [60]. In that work, they showed that random positioning of the ridges could eliminate the coherent addition of the scattering from the individual ridges. This observation implies that the scattering pattern is due to a single ridge only, not due to the pattern of the ridge and an array factor. We will adopt this assumption in the following analysis.

### 7.3.1 Numerical Experiment - Point Scatterers

To better understand this assumption and how it is to be implemented in the FDTD method, a number of simple numerical experiments were performed. First, the behavior of an array of point scatterers was modeled analytically. The geometry is shown in Figure 7.4. In this setup, the $L$ points in each column will be called an "element". The element can be thought of as representing the stack of lamellae in a ridge. There are then $N$ elements in the complete array and $LN$ total points. Each point scatters the incident field as a spherical

wave centered at its location; secondary scattering is not considered. The scattering pattern for this array is then

$$F(\hat{r}) = \Big| \sum_{n=1}^{N} \sum_{l=1}^{L} e^{jk\hat{r}\cdot\vec{\mathrm{p}}_{l,n}} e^{-jk\hat{k}\cdot\vec{\mathrm{p}}_{l,n}} \Big|^2. \tag{7.6}$$

We will only consider the pattern in the plane of the array.

In Figure 7.5(a), the pattern is calculated using (7.6) with the values $L = 2$, $N = 10$, $g = 200\,\mathrm{nm}$, $d = 600\,\mathrm{nm}$, and $\lambda_1 = 380\,\mathrm{nm}$. These dimensions are comparable to the typical dimensions for the butterflies we considered. As expected, the pattern has very distinct grating lobes due to coherent scattering. Now, consider the case in which each element (entire column) is randomly shifted by a maximum of $\lambda_1/2$ along the $y$ direction, that is,

$$\vec{\mathrm{p}}_{0,j} \rightarrow \vec{\mathrm{p}}_{0,j} + \mathrm{rand}()\lambda_1\hat{y}, \tag{7.7}$$

in which rand() generates random numbers uniformly distributed between $-0.5$ and 0.5. This case is shown in Figure 7.5(b). The pattern is still focused in certain directions. If we now take an ensemble average of many arrays, in which the elements in each one are independently randomly distributed,

$$< F(\hat{r}) >= \frac{1}{M} \sum_{m=1}^{M} F_m(\hat{r}), \tag{7.8}$$

we get the pattern of a large group of irregularly arrays in which the scattering from the arrays add incoherently. The ensemble average can be thought of as representing the scattering from many scales on a small section of a wing. Result, for $M = 1000$, are shown in Figure 7.5(c). For comparison, the pattern for a single element (red curve) is also shown. Notice that the pattern for the ensemble average is similar to the pattern for the single element.

The choice of distribution for the random number generator is very important for studying irregular arrays over a wide bandwidth. To illustrate this point, we consider the previous example when the wavelength of the excitation is changed from $\lambda_1 = 380\,\mathrm{nm}$ to $\lambda_2 = 480\,\mathrm{nm}$. No other changes are made; all spacings remain the same. In this case, the grating lobes reappear, as shown in Figure 7.5(d). The reason for this is that the random positioning causes a uniform distribution in phase over $0 - 2\pi$ for $\lambda_1$, but only a uniform distribution in phase over $0 - 4\pi/3$ for $\lambda_2$.

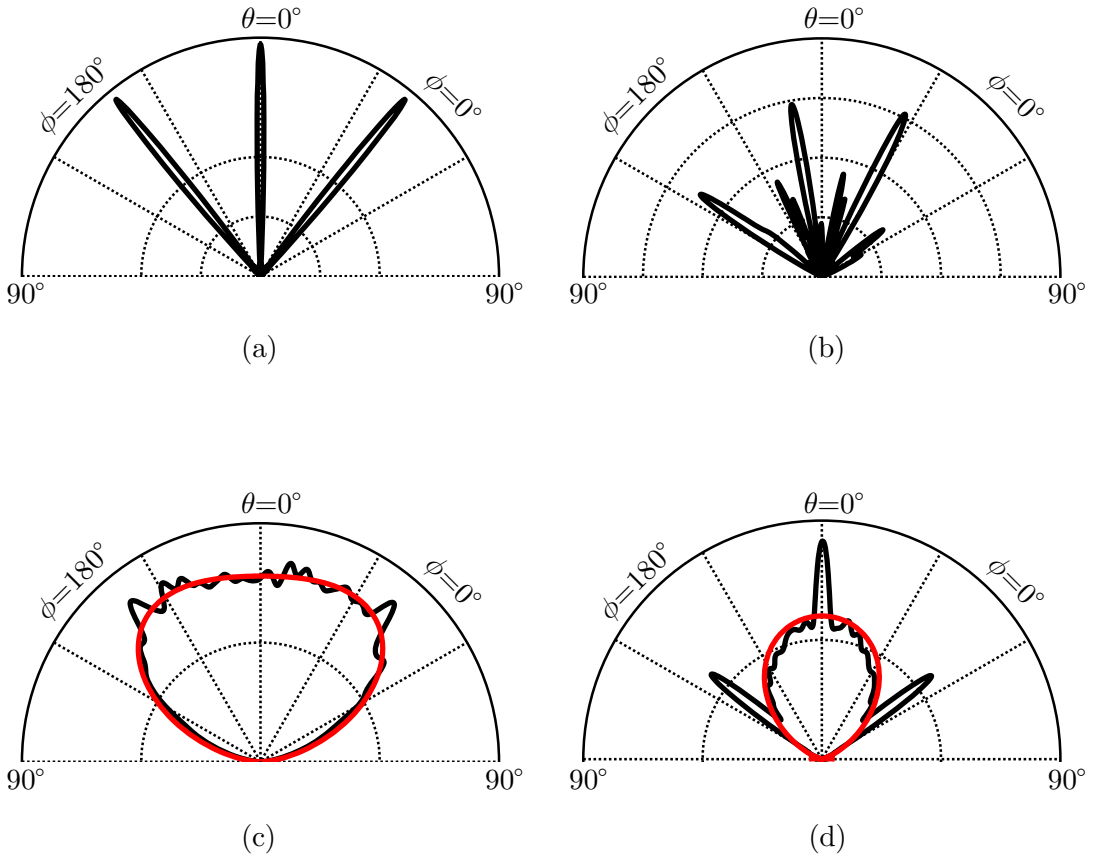


Figure 7.5: Scattering pattern for an array of point scatterers. For all cases, $L = 2$ and $N = 10$. (a) Pattern of a single array, $\lambda_1 = 380\,\text{nm}$. (b) Pattern of a single array with random positioning using a random number generator with a uniform distribution. (c) Pattern for an ensemble average (black curve) of 1000 arrays of 10 elements each with random positioning, $\lambda_1 = 380\,\text{nm}$. The pattern for a single element is also shown (red curve). (d) Same as (c), but for $\lambda_2 = 480\,\text{nm}$.

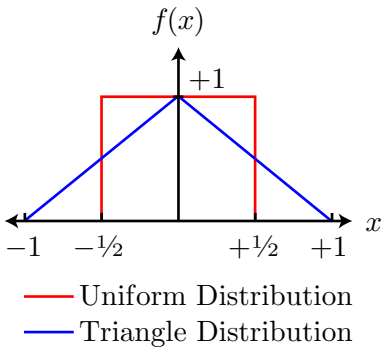


Figure 7.6: Probability density functions for uniform and triangular distributions for the random number generator.

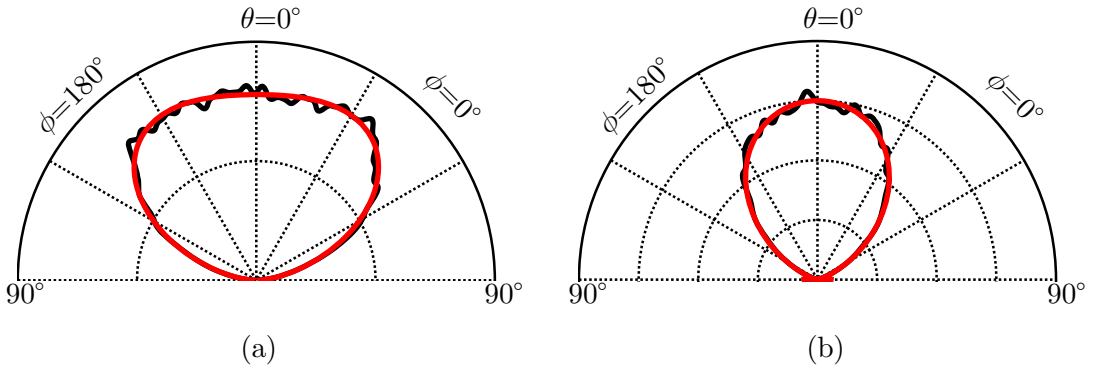


Figure 7.7: (a) Pattern for an ensemble average (black curve) of 1000 arrays of 10 elements each with random positioning using a random number generator with a triangle distribution, $\lambda_1 = 380\,\text{nm}$. The pattern for a single element is also shown (red curve). (b) Same as (a), but for $\lambda_2 = 480\,\text{nm}$.

This problem can be alleviated by using a different distribution for the random number generator. For example, a random number generator with a triangle probability density function, as shown in Figure 7.6, can be used. The previous calculations were repeated with a maximum random shift of 550 nm and a triangular distribution for the random numbers. The results are shown in Figure 7.7. In this case, the pattern for the ensemble average and the pattern for the single element are similar for both $\lambda_1$ and $\lambda_2$. These results suggest that it is possible for the scattering from the array with imperfections to be similar to the scattering from a single element of the array over a bandwidth.

### 7.3.2 Numerical Experiment - Simple Models in FDTD

The previous example was based on ideal point scatterers. To better understand this behavior and how it is to be implemented in the FDTD method, a numerical experiment was performed on the simplified, two-dimensional version of the butterfly-ridge structure shown in Figure 7.8. The dimensions are $N = 8$, $c = 60\,\text{nm}$, $a = 620\,\text{nm}$, $d = 140\,\text{nm}$, $h = 60\,\text{nm}$, $g = 140\,\text{nm}$, and $x_p = 750\,\text{nm}$.

A random array was simulated using 50 ridges. The heights of the ridges, $\Delta h$, were varied randomly with a triangular probability density. The range for the displacements was $-275\,\text{nm} \leq \Delta h \leq 275\,\text{nm}$. This process was repeated 100 times using a different set of random heights for each simulation. The ensemble average of the 100 simulations was then

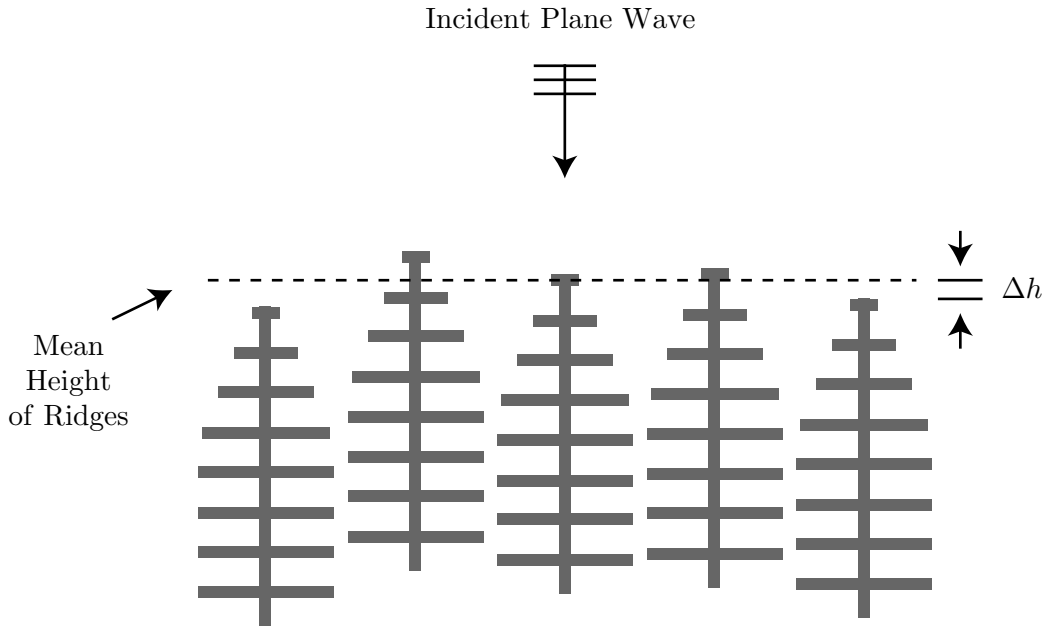


Figure 7.8: Two-dimensional geometry used for the numerical experiment in FDTD.

computed. To be more specific, the time-average scattered powers per unit area in each direction $\theta$ were averaged to obtain the far-field scattering pattern in the $xy$ plane. The results from these calculations are shown for four different wavelengths in Figure 7.9(a). Notice the small "noise-like" variations along each curve, which are due to the random aspect of the calculation.

The periodic FDTD can be used to produce results similar to those presented above. First, the periodic FDTD method is applied to the unit cell containing a single ridge shown in Figure 7.10. Note, because of the periodic boundary conditions in this calculation, the field within the unit cell includes the influence of all of the other ridges in the array. Next, the scattered electromagnetic field on the transform surface is used to calculate the far-field scattering pattern in the $xz$ plane by the method described in Section 5.1. Only a single surface (the top surface in Figure 7.10) is used. The results from this calculation are shown in Figure 7.9(b), and they are to be compared to those for the random array in Figure 7.9(a). The scattering patterns for the two methods are very similar.

The power reflection coefficient is a measure of the total power scattered per ridge of the scale. It is obtained by integrating the normal component of the Poynting vector over the

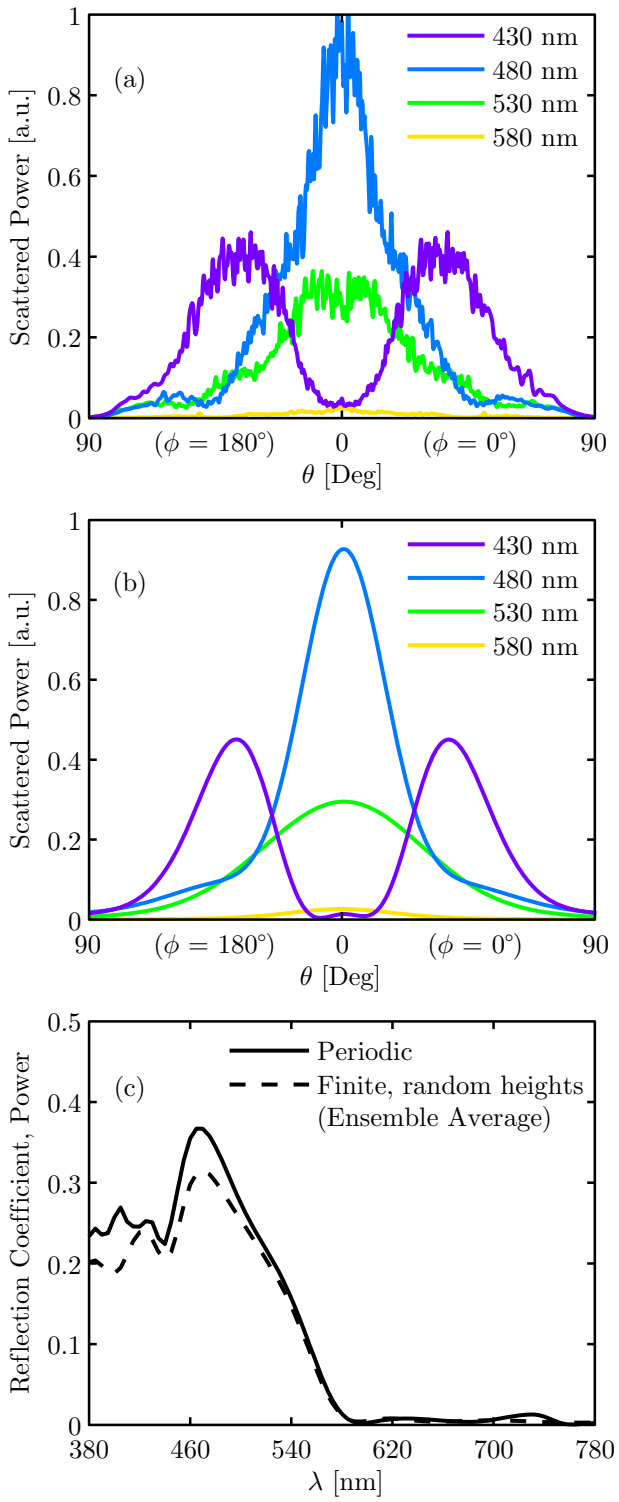


Figure 7.9: Comparison of results from an ensemble average of randomized finite models and a periodic model. (a) Far-field scattering pattern for the ensemble average of 100 simulations with 50 randomly spaced ridges per simulation. (b) Far-field scattering pattern for the periodic model. (c) Comparison of the reflection coefficients for the ensemble average and the periodic model.

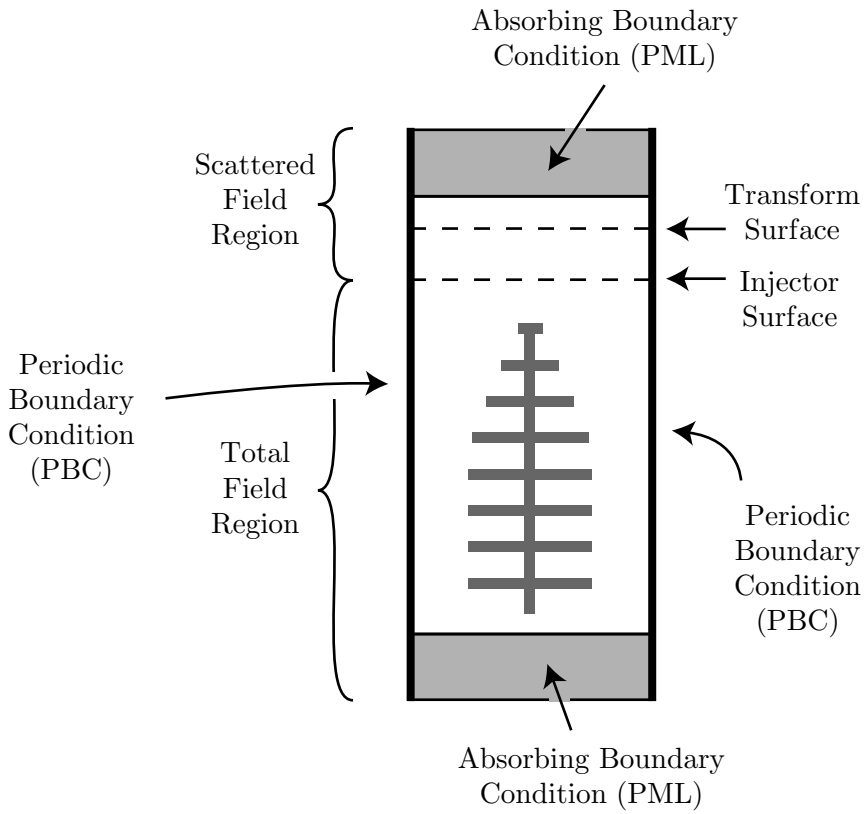


Figure 7.10: Schematic drawing showing elements within an FDTD periodic cell.

transform surface then dividing by the total power incident on this surface. Note, for the periodic calculation, the transform surface is the area above the ridge (unit cell), whereas for the random calculation, it is the area above the 50 ridges that make up one element in the ensemble. The power reflection coefficients for the two methods are compared in Figure 7.9(c). As for the scattering patterns, we see that the results using a single element in the periodic structure and an ensemble average for the random array are very similar.

Thee results presented above show that the FDTD calculation based on the single periodic cell can be used to estimate the scattering, in an average sense, from a scale containing a large number of irregularly spaced ridges. For the actual insects, the observer always sees many scales at once, each of which is covered with hundreds to thousands of ridges. Therefore, the ensemble average is a reasonable model for the observation of butterfly wing.

## *7.4 Interpretation of Scattering as Observed Color*

In the previous section, we described the use of the 3D, periodic FDTD method to calculate the scattered field from a scale with irregularly positioned ridges. In this section, we will explain the procedure used to obtain the observed color of a butterfly model from the results of the FDTD simulations. The goal is to calculate the observed color as a function of observer location when the structure is illuminated by an unpolarized light source located infinitely far away.

Referring to the flowchart in Figure 7.11, the first step is to specify the incident field. Two simulations are performed using plane-wave excitations with orthogonal states of polarization. The scattered field is recorded on the transform surface above the structure. Although the computational method is a time-domain method, frequency-domain quantities are desired. Therefore, the scattered field is converted to the frequency-domain using an on-the-fly discrete Fourier transform (DFT) [17]. The frequencies used correspond to 81 wavelengths spaced in 5 nm increments between $\lambda = 380\,\text{nm}$ and $\lambda = 780\,\text{nm}$. This set of wavelengths covers the visible spectrum.

After the simulations are completed, the far-zone scattered field is calculated using the previously described frequency-domain, near-to-far-field transform. From the far-zone field,

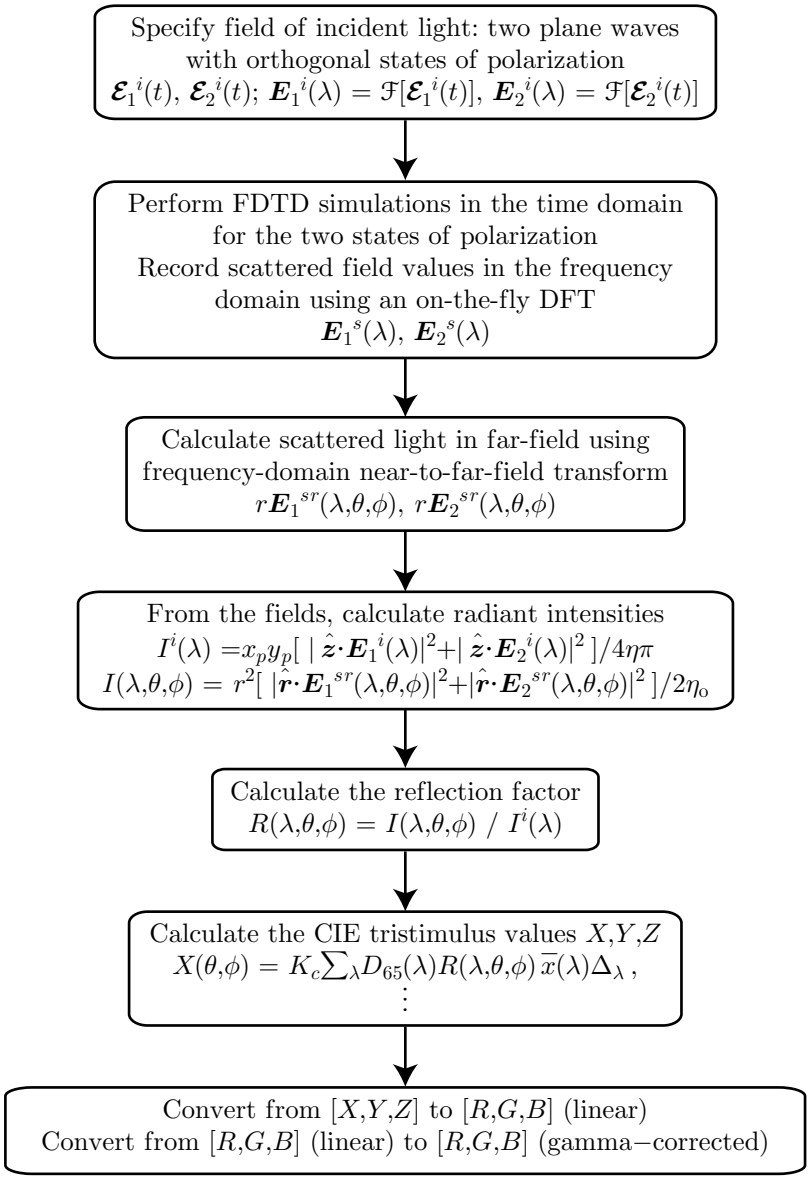


Figure 7.11: Flowchart illustrating the steps used to calculate the observed color using the periodic FDTD method. $\mathcal{F}$ indicates the Fourier transform, and $\eta$ is the intrinsic impedance of free space.

the radiant intensity, $I$, of the scattered light is found. In addition, the radiant flux of the incident light, $I^i$, is calculated. Note that both quantities are functions of wavelength, but the scattered radiant intensity is also a function of direction. The reflection factor, $R(\lambda, \theta, \phi)$, is calculated as the ratio of the scattered radiant intensity to the incident radiant flux [53].

At each observation direction, the reflection factor is converted into tristimulus values $(X, Y, Z)$; for example,

$$X(\theta, \phi) = K_c \sum_{\lambda} D_{65}(\lambda) R(\lambda, \theta, \phi) \bar{x}(\lambda) \Delta_\lambda, \tag{7.9}$$

in which $D_{65}$ is the spectrum of a standard reference white light source with an approximate color temperature of $6500\,K$, and $\bar{x}$ is a color matching function. For this work, the 1931 CIE 2° standard observer color matching functions are used [54]. By using these functions, the tristimulus value $Y$ corresponds to the luminance factor. The constant $K_c$ is set so that a perfect diffuser, that is, $R(\lambda, \theta, \phi) =$ constant, is white. Although the $(X, Y, Z)$ values uniquely specify a color, it is more convenient to convert to sRGB values that can be displayed on a standard computer monitor [53, 55].

The observed color is plotted as a 3D pattern; the procedure is shown schematically in Figure 7.12. The radial vector from the origin O is proportional to the luminance factor $Y$. The small patch of surface (angular size $\Delta\theta, \Delta\phi$) at the end of this vector is the color that would be seen by an observer viewing the structure from that direction $(\theta, \phi)$. By examining such patterns, one can see how the luminance and color of the scattered light changes with the direction of observation.

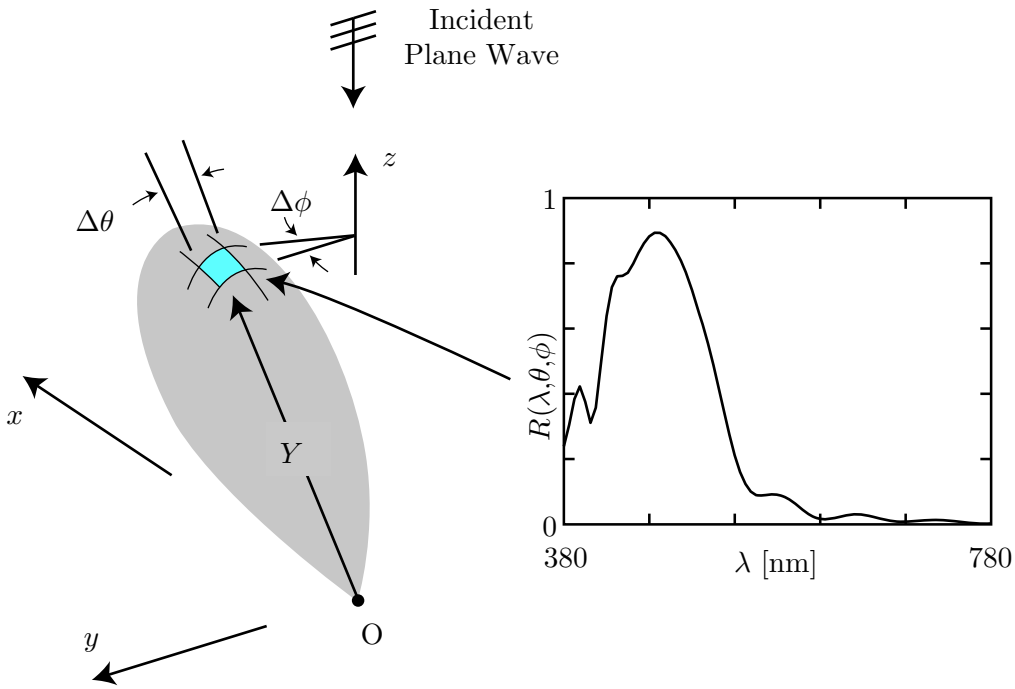


Figure 7.12: Illustration for the 3D representation of the observed color as a function of the direction of observation.

## *7.5 Results*

### 7.5.1 Models for *Morpho* Butterflies

In this section, we examine the scattering from structures that are similar to a *Morpho rhetenor* scale (once again, the computational model is inspired by the specific insect, but it is not meant to be an exact model). The dimensions of the structure are based on the observations described in [61] and are summarized in the first column of Table 7.1.

Figure 7.13 shows the observed color for normally incident light ($\theta^i = 0°$) as a function of the location of the observer $(\theta, \phi)$. Each subplot corresponds to a change in the structure. Notice the small inset in Figure 7.13(a); it is a simplified model that shows the orientation of the ridge. In this figure, and in all similar figures that follow, logarithmic scaling is used; that is, the length of the radial vector is proportional to $\log_{10}(Y/Y_{\max})$, and the range displayed is two decades. Here, $Y_{\max}$ is the maximum value for a subplot, and it is given for each subplot in the caption of the figure. Using these values, we can compare the relative luminance values for the subplots. The dashed lines drawn on the figures are sample paths that are used for plotting on chromaticity diagrams.

Figure 7.13(a) is for the simplest model; it is the one in Figure 7.3(a) with a base and without microribs. The eight lamellae on the left and right sides of the stem are aligned, and all have the same width. Notice that the color is a highly saturated blue and is concentrated in a small angular sector — a beam. The beam is narrowest in the direction of the ridge. This behavior is consistent with observations for actual butterflies [23, 62]. In addition, the main beam is tilted at approximately the angle $\theta = 2\alpha = 20°$. That is, the tilt of the lamellae with respect to the plane of the wing (base) causes a rotation in the beam that is approximately twice the tilt angle. This rotation is the same as one would expect for specular reflection from a tilted dielectric slab. The power reflection coefficient versus wavelength for this case is shown in Figure 7.14(a). There is a definite peak at approximately $\lambda \approx 470\,\text{nm}$, which is in the blue range of the visible spectrum. The reflection coefficient is similar to the measurement of Berthier [63, Figure 8.20].

For Figure 7.13(b), the structure is identical to that for Figure 7.13(a), except the top four lamellae are tapered in width, as in Figure 7.3(b). The pattern of the scattered light is

Table 7.1: Dimensions for Butterfly Models

| Parameter | *Morpho* | *T. magellanus* | *A. meliboeus* |
|---|---|---|---|
| **Ridge** | | | |
| spacing, $x_p$ | 750 nm | 1200 nm | 700 nm |
| **Lamellae** | | | |
| number, $N$ | 8 | 6 | 6 |
| width (max), $a$ | 620 nm | 400 nm | 400 nm |
| width (min), $d$ | 60 nm | 60 nm | 400 nm |
| thickness, $h$ | 60 nm | 60 nm | 40 nm |
| tilt angle, $\alpha$ | 10° | 54° | 30° |
| air gap, $g$ | 140 nm | 150 nm | 260 nm |
| **Stem** | | | |
| width, $c$ | 60 nm | 60 nm | 60 nm |
| **Microribs** | | | |
| thickness, $f$ | 60 nm | | 40 nm |
| air gap, $e$ | 130 nm | | 130 nm |
| width, $b$ | 400 nm | | 200 nm |
| **Base layer** | | | |
| thickness, $l$ | 150 nm | | 150 nm |
| air gap, $k$ | 1 $\mu$m | | 1 $\mu$m |
| **Diffusing layer** | | | |
| thickness, $i$ | 20 nm | | |
| air gap, $j$ | 100 nm | | |

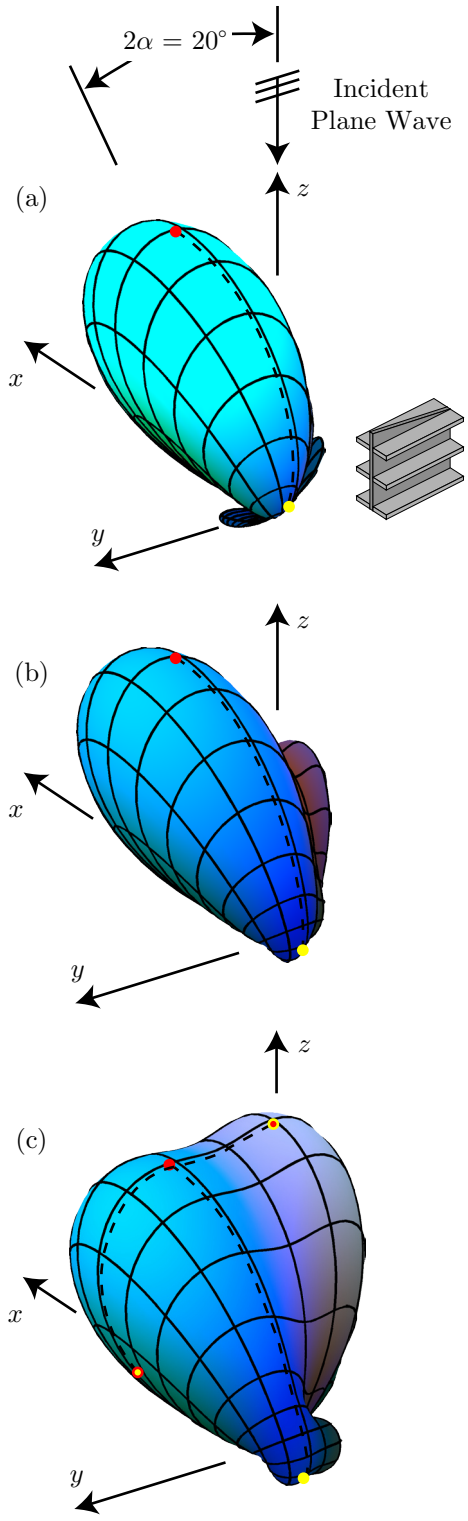


Figure 7.13: Observed color as a function of direction for *Morpho*-like models with aligned lamellae and a base. (a) Eight lamellae without taper. $Y_{max} = 1.0$. (b) Eight lamellae with the top four lamellae tapered. $Y_{max} = 0.30$. (c) Eight tapered lamellae plus a diffusing layer above the structure. $Y_{\max} = 0.28$.

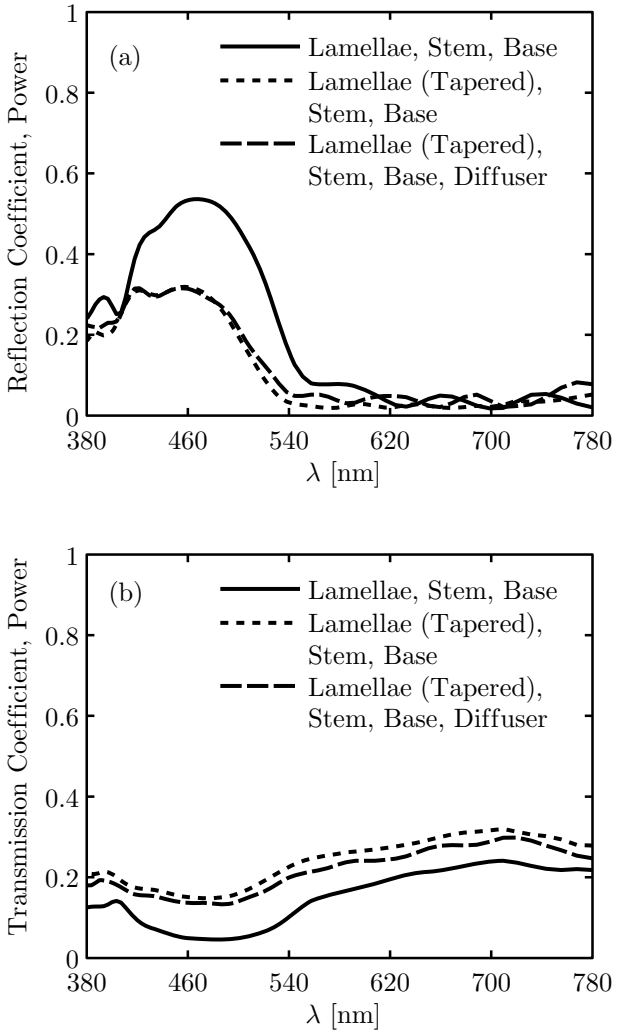


Figure 7.14: Power reflection coefficients (a) and transmission coefficients (b) for *Morpho*-like models with aligned lamellae.

similar for both cases. However, as the power reflection coefficient in Figure 7.14(a) shows, the intensity of the light is lower with the taper. This is also evident from the luminance scale factors for Figs. 7.13(a) and 7.13(b): $Y_{\max} = 1.0$ versus $Y_{\max} = 0.30$.

For Figure 7.13(c), the model is changed once again by adding a diffusing layer above the ridge. Recall that this layer is to represent a cover scale, which is prevalent in *Morpho*-type butterflies but not the *M. rhetenor* [23]. Two beams can now be identified in the pattern: a beam due to specular reflection from the ridge ($\theta = 2\alpha = 20°$), which is similar in shape and hue to the one in Figure 7.13(b), and a beam due to specular reflection from the diffusing layer ($\theta = 0°$), which is of different hue and less saturated. The combination produces a pattern that is broader than in Figure 7.13(b), which is consistent with the concept of a diffusing layer. Referring now to Figure 7.14(a), the reflection coefficient is seen to be essentially unaltered by the addition of the diffusing layer. The decrease in saturation with the addition of the diffusing layer is consistent with observations of the *M. didius*, for which the wings are less glossy than the *M. rhetenor*, and the observed color is whitish-blue [64].

In Figure 7.14(b), the power transmission coefficients versus wavelength for the three cases are shown. In contrast to the reflection coefficients, the transmission coefficients are relatively independent of the wavelength and generally small due to significant absorption. The tapering of the lamellae results in an increase in the transmission through the structure, and the addition of the diffusing layer causes very little change.

The observed color can also be plotted on a chromaticity diagram, which describes color only; luminance is not shown. The chromaticity coordinates calculated along the dashed lines in Figure 7.13 are plotted in Figure 7.15. The colored dots indicate the orientation of the paths. In a plane orthogonal to the ridge, at $\theta = 70°$, the observed colors are highly saturated, since the curves are close to the spectral locus. There is, however, only limited iridescence in this plane. Samples are also plotted in the plane parallel to the ridges for the case with the diffusing layer (c). In this plane, the color shifted from blue-green to blue, and then becomes less saturated for observation near $\theta = 0°$.

In Figures 7.16 and 7.17, the previous study is repeated, but the lamellae on the left and right sides of the stem are offset from each other as is the case for some *Morpho* butterflies.

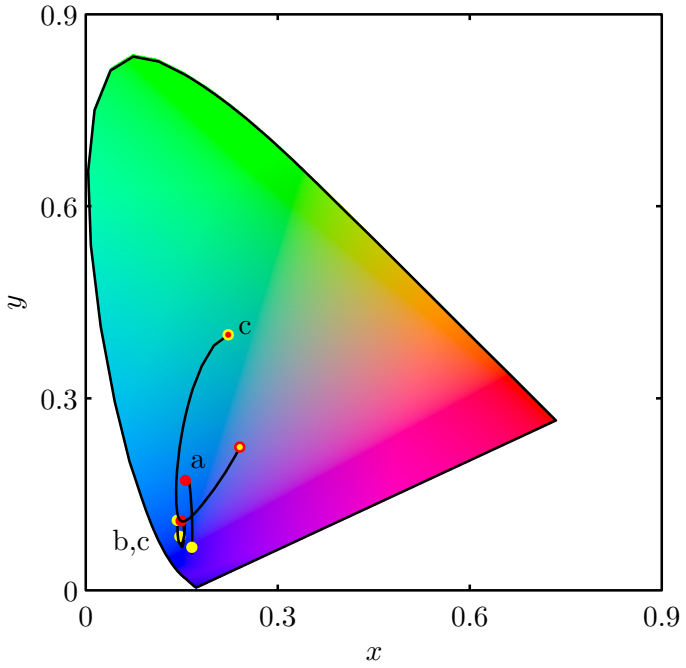


Figure 7.15: Chromaticity coordinates of observed color for the *Morpho*-like models with aligned lamellae as calculated along the dashed lines in Figure 7.13. The orientation of the lines is indicated by the colors of the endpoints.

As seen in Figure 7.16(a), the main beam due to specular reflection is now split into two, with a relative null in between, and it is less intense than for the case with aligned lamellae. A small beam in the backscatter direction ($\theta = 0°$) is also present. This split in the beam is consistent with the observations of Vukusic et al. [23] and Berthier et al. [62] and the calculations of Plattner [40]. In addition, the hue of the light is more violet, which suggests a shift to shorter wavelengths. This observation is confirmed by comparing the power reflection coefficients in Figs. 7.14(a) and 7.17(a). The reflection and transmission coefficients computed using this method are similar to results of Gralak et al. computed using lamellar grating theory [38].

For Figure 7.16(b), the top four lamellae are tapered in width. The taper is seen to shift the hue slightly towards violet. The effect of the taper on the intensity is more dramatic, a significant decrease as can be seen in the power reflection coefficient in Figure 7.17(a) and in the scale factors for the luminance: $Y_{\max} = 0.96$ versus $Y_{\max} = 0.23$.

Finally, the effect of a diffusing layer (cover scale) is shown in Figure 7.16(c). The addition of the diffusing layer causes a significant change in the pattern; it is now a beam

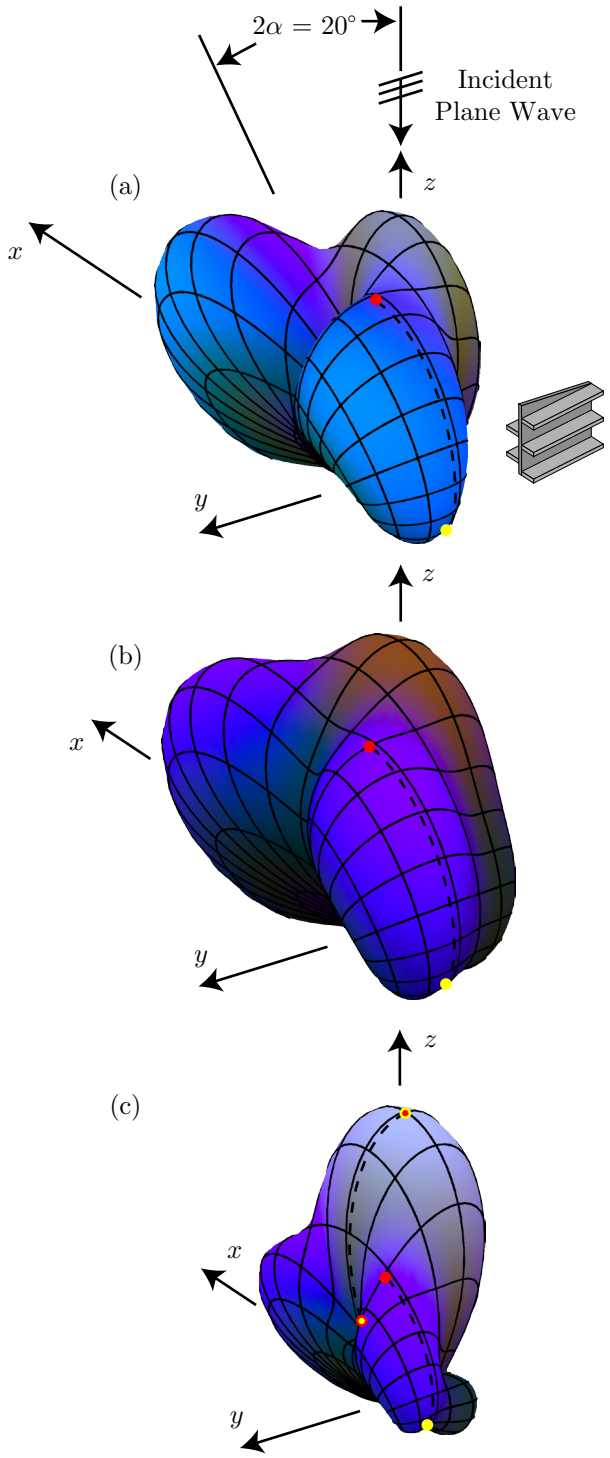


Figure 7.16: Observed color as a function of direction for *Morpho*-like models with offset lamellae and a base. (a) Eight lamellae without taper. $Y_{\max} = 0.96$. (b) Eight lamellae with the top four lamellae tapered. $Y_{\max} = 0.23$. (c) Eight lamellae, tapered, plus a diffusing layer above the ridge. $Y_{\max} = 1.0$.

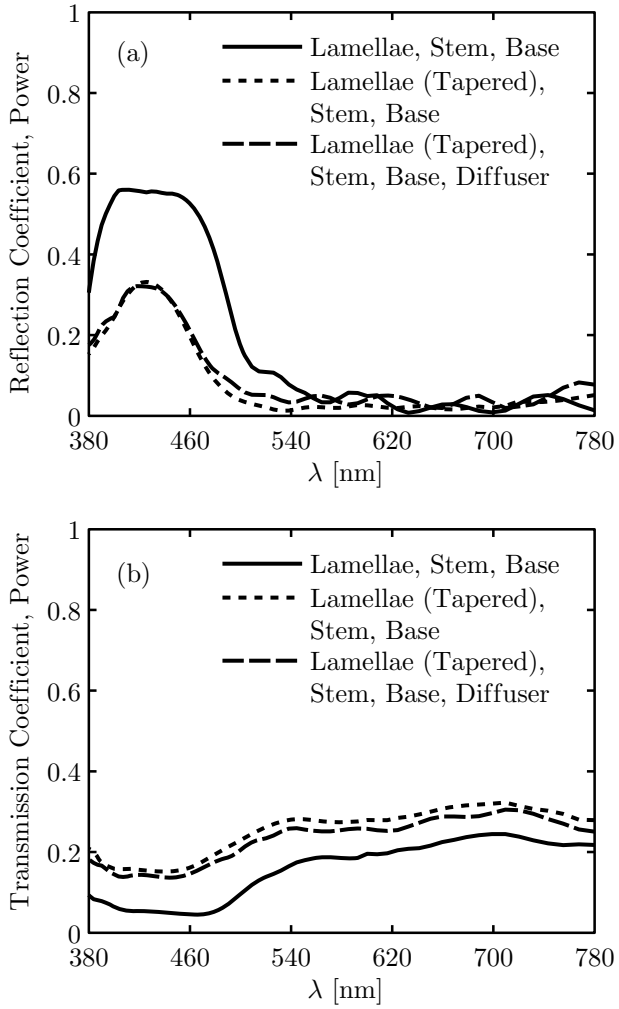


Figure 7.17: Power reflection coefficients (a) and transmission coefficients (b) for *Morpho*-like models with offset lamellae.

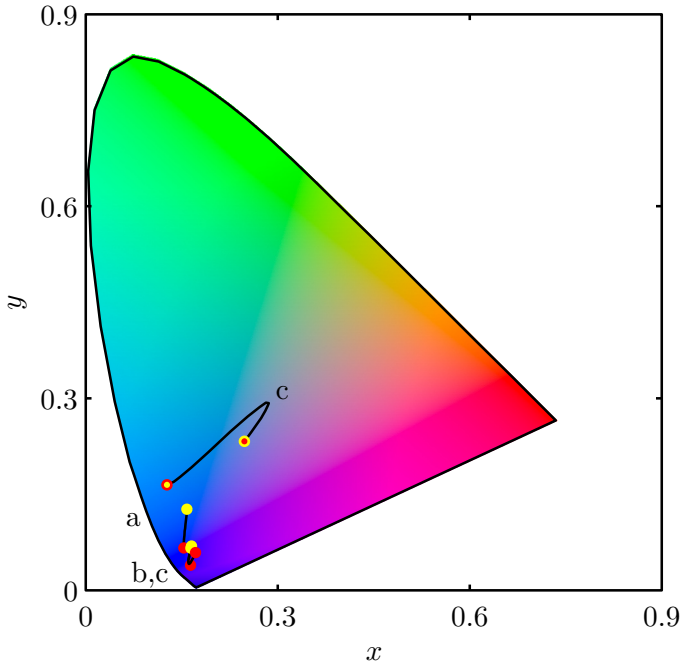


Figure 7.18: Chromaticity coordinates of observed color for the *Morpho*-like models with aligned lamellae as calculated along the dashed lines in Figure 7.16.

caused mainly by a specular reflection from the layer. The specular reflection from the diffusing layer is similar for the models used in Figs. 7.13(c) and 7.16(c). However, the reflection from the ridge is weaker for the offset lamellae as mentioned above; thus, the reflection from the diffusing layer becomes the dominant feature.

The chromaticity coordinates calculated along the dashed lines in Figure 7.16 are plotted in Figure 7.18. In the plane orthogonal to the ridges, the color shifts towards shorter wavelengths as the structure is tapered, but there is little iridescence. The coordinates for the *Morpho*-like models with offset lamellae are closer to the spectral locus than for the cases with aligned lamellae, which indicates that the colors are more saturated. The addition of the diffusing layer causes the observed color to be less saturated (more white) near normal; this is indicated by the change in the chromaticity coordinates in the plane parallel to the ridges.

Now the effect of adding microribs to the *Morpho*-like models will be examined. Recall, the microribs are the small layers that are perpendicular to the lamellae, as shown in Figs. 7.2 and 7.3. The microribs will be added to the models with aligned and offset lamellae

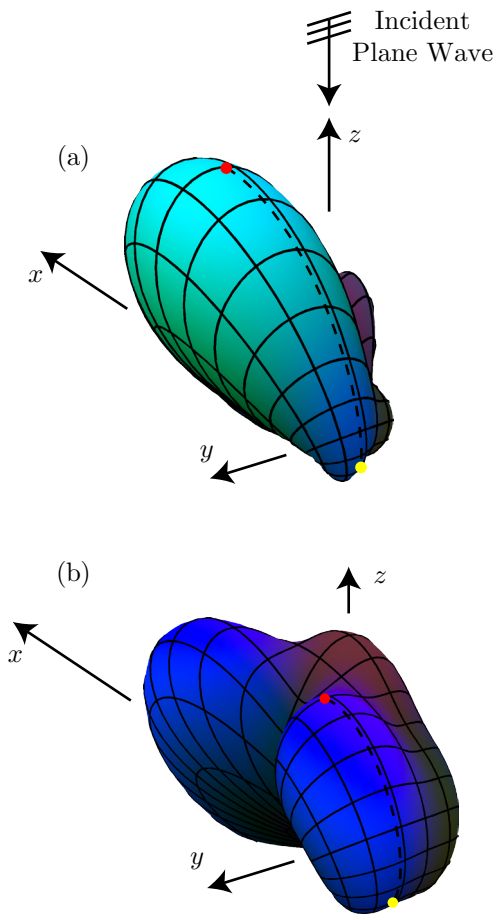


Figure 7.19: Observed color as a function of direction for *Morpho*-like models that include microribs. (a) Eight aligned, tapered lamellae. $Y_{\max} = 1.0$. (b) Eight offset, tapered lamellae. $Y_{\max} = 0.19$.

with taper. Results for these cases were presented earlier in Figs. 7.13(b) and 7.16(b). The results in Figure 7.19 show that the addition of the microribs causes very little change in the shape of the patterns and only a small change in the hue for the *Morpho*-like models. The reason is straightforward: The lamellae are tilted at a slight angle (10°) relative to the base; thus, the microribs are nearly perpendicular to the base. Therefore, specular scattering from the microribs is mainly reflected into the adjacent structure rather than back at the observer.

The chromaticity coordinates, shown in Figure 7.20, are very similar for the case with offset lamellae and microribs. However, the case with aligned lamellae and microribs exhibits more iridescence, which is indicated by the shifted in the chromaticity coordinates with

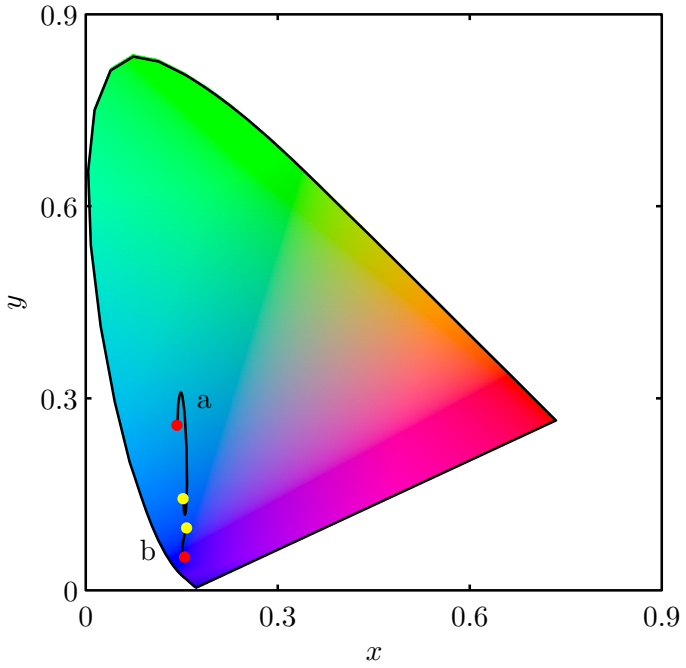


Figure 7.20: Chromaticity coordinates of observed color for the *Morpho*-like models with microribs as calculated along the dashed lines in Figure 7.19.

viewing direction.

Finally, the effect of immersing the *Morpho*-like model in acetone is studied. The model with aligned lamellae and a base, which is shown in Figure 7.13(a), was immersed in acetone by filling the open spaces with a material with an index of refraction of $n = 1.36$. As shown in Figure 7.21, the observed color changes to a bright green with immersed in acetone. The observed color for these two cases can also be plotted on a chromaticity diagram, shown in Figure 7.22. There is a clear shift from the blue region to the green region of the diagram. This behavior is similar to the behavior shown in the photographs of the *M. menelaus* in Figure 1.4.

In summary, the calculations for *Morpho*-like scales have demonstrated several interesting characteristics of the structural color for these butterflies, some of which are present in the measurements of previous investigators. The calculations have shown that:

- The basic structure, which consists of a stack of lamellae with the appropriate dimensions, produces the blue color for the scattered light with some iridescence. The intensity of the scattered blue light can be high, with the power reflection coefficient

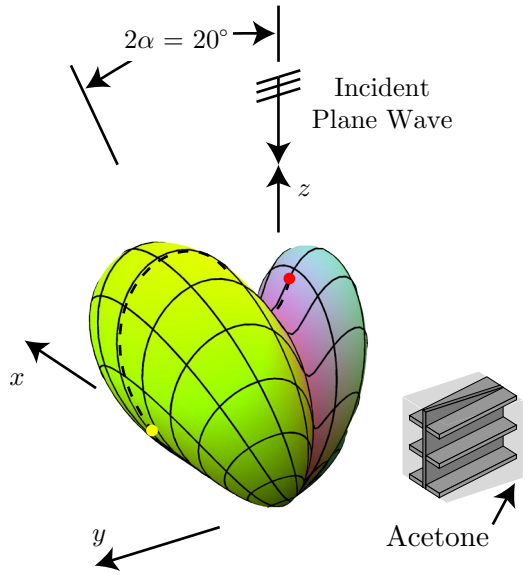


Figure 7.21: Observed color as a function of direction for *Morpho*-like model with aligned lamellae, base, and immersed in acetone ($n = 1.36$). $Y_{\max} = 0.83$.

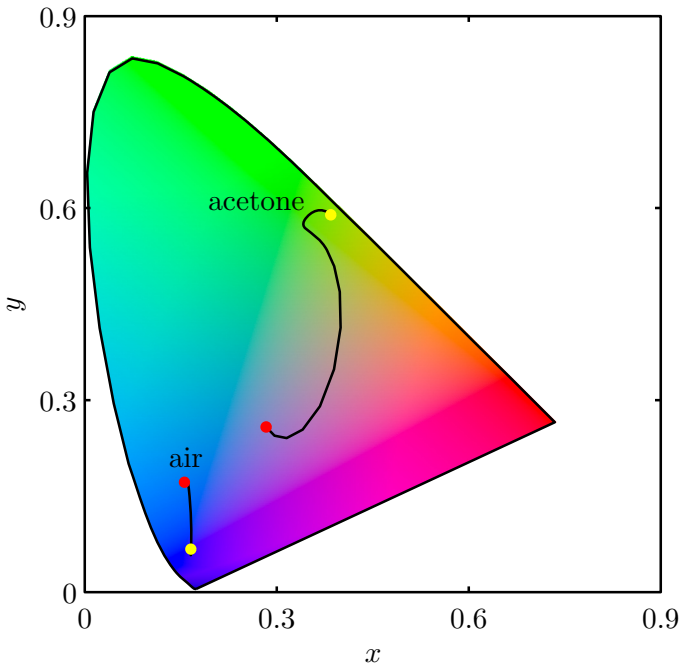


Figure 7.22: Chromaticity coordinates of observed color for the *Morpho*-like model with aligned lamellae and base, as shown in Figure 7.13(a), and immersed in acetone, as shown in Figure 7.21. The chromaticity coordinates are calculated along the dashed lines on the 3D patterns.

being greater that 50%.

- The beam of light scattered from the lamellae is mainly in the specular direction, which is rotated from the direction of incident light when the lamellae are tilted. When the lamellae on the two sides of the stem are offset this beam is bifurcated.

- Offsetting the lamellae produces a definite shift in hue and iridescence, with the color moving from blue towards violet. Tapering the width of the lamellae and the addition of microribs to the structure cause smaller shifts in hue and iridescence.

- Addition of a cover scale oriented parallel to the base (modeled as a dielectric layer) produces a second beam of scattered light. The combination of the scattering from the lamellae and the cover scale can produce more diffuse scattering with a blue color that is less saturated.

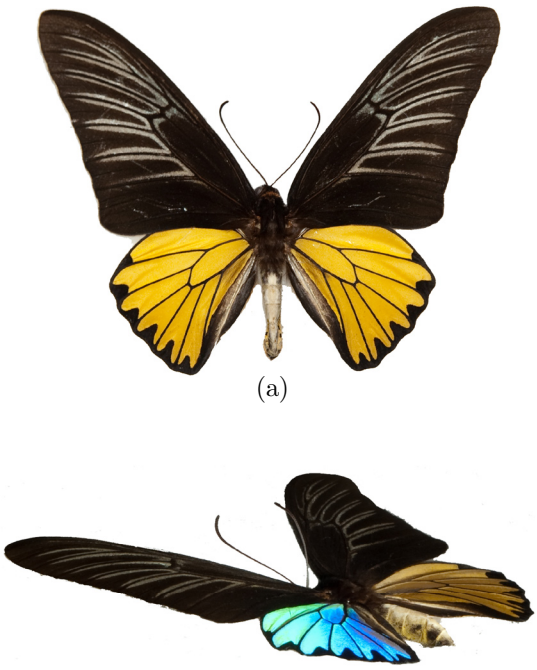

(a)

(b)

Figure 7.23: Photographs of the dorsal side of a male *Troides magellanus* butterfly. In both views, the light source is located near the observation point. (a) From most observation directions, the observed color of the lower wings is yellow. (b) When viewed near grazing, the color of the lower wings changes abruptly with a change in angle to blue.

### 7.5.2 *Troides magellanus* Butterfly

Next, the scattering from a structure similar to the male *Troides magellanus* butterfly scale is studied. This insect, shown in Figure 7.23(a), is remarkable due to the interplay of structural and pigmentary color [65]. When viewed at any angle other than near grazing, the lower wings of the butterfly are yellow. However, when the observer and the light source are co-located in a direction near grazing, the observed color changes with angle to blue, as shown in Figure 7.23(b).

The parameters used in the model for this butterfly are given in the second column of Table 7.1; they are based on values given in [65]. The key feature is that the tilt angle of the lamellae is large, $\alpha \approx 54°$. Recall that the tilt angle was only 10° for the *Morpho*-like structures. The other parameters for the lamellae are similar to those for the *Morpho*-like models; therefore, it is expected that the observed color will be similar under certain conditions. Specifically, when the direction of the incident light is near normal to the

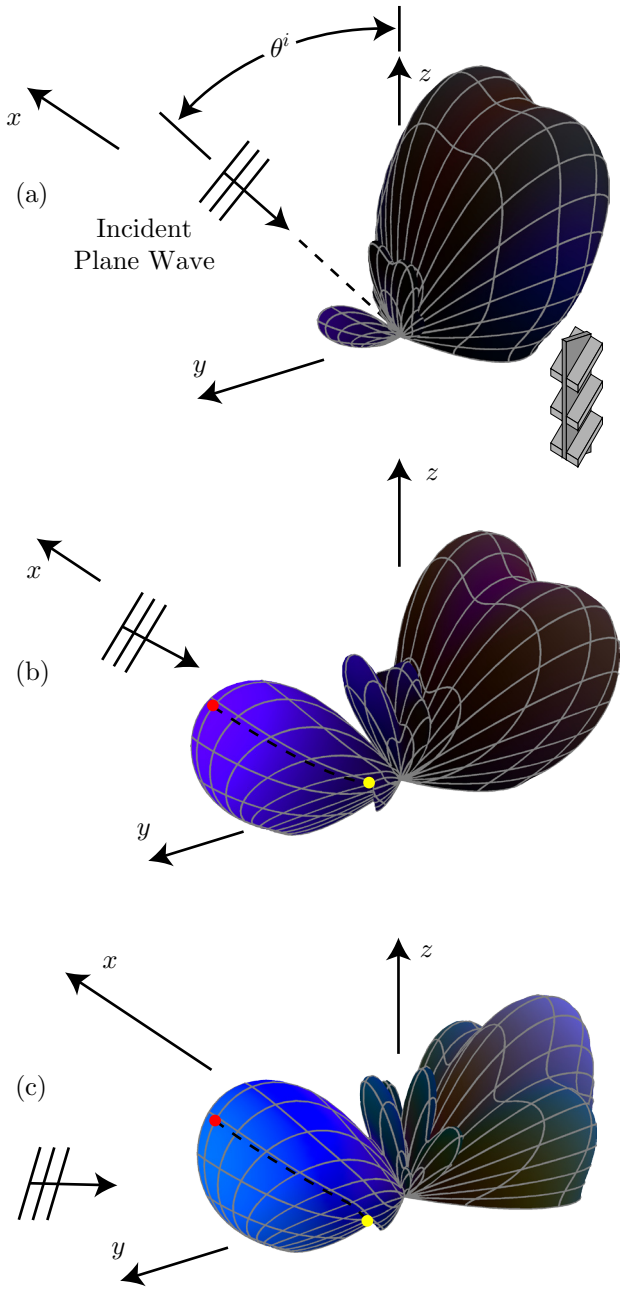


Figure 7.24: Observed color as a function of direction for *Troides magellanus* model. The details for the model are the same for all cases and only the direction of the incident light is changed. (a) $\theta^i = 40°$. $Y_{\max} = 0.08$. (b) $\theta^i = 50°$. $Y_{\max} = 0.15$ (c) $\theta_i = 70°$. $Y_{\max} = 1.0$.

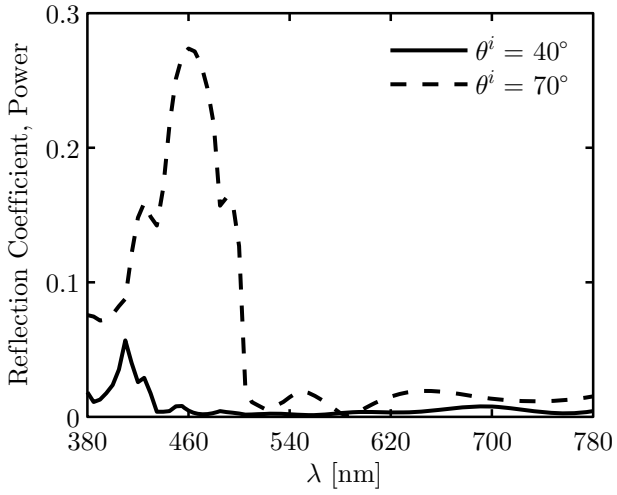


Figure 7.25: Power reflection coefficient for *Troides magellanus* model. The rapid increase in the intensity of the iridescent color is shown by comparing the reflection coefficient for $\theta^i = 40°$ and $\theta^i = 70°$.

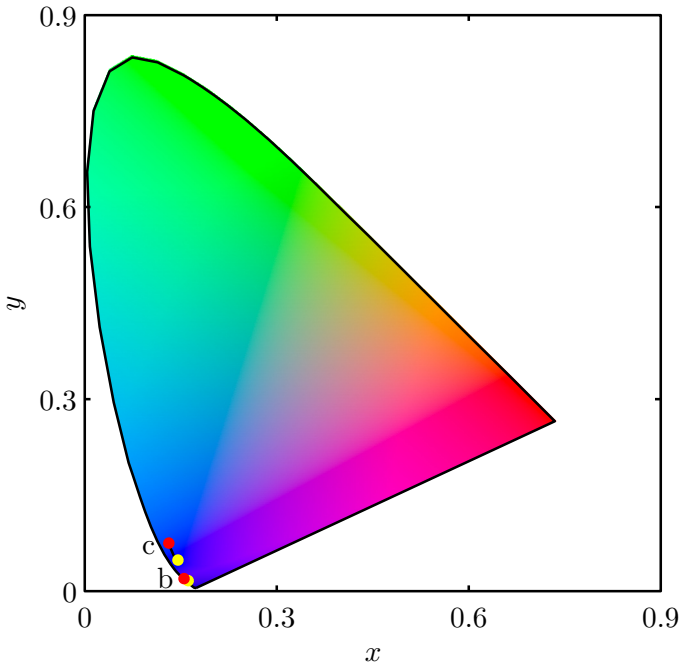


Figure 7.26: Chromaticity coordinates of observed color for the *Troides magellanus* model as calculated along the dashed lines in Figure 7.24.

lamellae (nearly grazing to the wing), then the observed color should be blue.

This hypothesis is confirmed by examining the plots in Figs. 7.24 and 7.25. When the angle of incidence is well away from grazing, the scattering from the structure is very weak. This is the case in Figure 7.24(a), which is for $\theta^i = 40°$. Notice that the scale factor for the luminance is $Y_{\max} = 0.08$. The color is brown, not yellow as for the actual butterfly, because the yellow color is due pigmentation, which is not included in the model. As the angle of incidence is increased slightly towards grazing, a lobe that is distinctly blue in color appears, as in Figure 7.24(b), which is for $\theta^i = 50°$. This blue lobe is even more pronounced when $\theta^i = 70°$, as in Figure 7.24(c). Notice that the scale factor for the luminance is now $Y_{\max} = 1.0$. As for the *Morpho*, an intense blue appears when the light is nearly normally incident on the lamellae.

The power reflection coefficient is plotted versus wavelength for two angles of incidence, $\theta^i = 40°$ and $\theta^i = 70°$, in Figure 7.25. These results clearly show the increase in scattering that occurs as the angle of incidence approaches grazing. They also clearly indicate the blue color for the structural scattering. By examining the chromaticity diagrams for these cases, shown in Figure 7.26, it is clear that the color is highly saturated, because the chromaticity coordinates are very close to the spectral locus.

### 7.5.3 *Ancyluris meliboeus* Butterfly

The final model examined is for the *Ancyluris meliboeus* butterfly. In contrast to the previous butterflies, it is the ventral side (bottom) of the wing that displays iridescence. Only small regions on this side are iridescent, and we will restrict our discussion to these regions. This butterfly has been studied by Vukusic et al. [66], and the dimensions in column three of Table 7.1 are based on their estimates for the dimensions of the ventral scales. We were unable to obtain an *A. meliboeus* specimen, but several photographs of a similar species, the *A. eudaemon*, are shown in Figure 7.27. In all cases, the light source, which was the flash on the camera, is located near the observation point. The dorsal side, which is not iridescent, is shown in Figure 7.27(a), and the ventral side is shown in (b)-(e). Figure 7.27(a) and (b) are for normal incidence. When the ventral side of the wing is tilted so that the antennae are away from the observer, the wing remains dark, as shown in (c). When tilted the other way, so that the antenna are closer to the observer, certain areas on the wing turn a bright yellow or blue, as shown in (d). This color is only observed over a limited range of angles. In (e), the insect has been rotated and much of the color on one wing has disappeared. Our analysis will focus on the iridescent yellow scales near the center of the wings.

The computational model is similar to the *Morpho*-like model with aligned lamellae discussed above. The most significant changes are that the lamellae are tilted by 30° relative to the plane of the wing, and the spacing between the lamellae is increased to 260 nm. The increased spacing between the lamellae causes the scattered light to shift towards longer wavelengths. As a result, the observed color, shown by the color pattern in Figure 7.28(a), is yellow instead of blue.

The presence of microribs has a more significant effect on the observed color for this model than for the *Morpho*-like models. The observed color for the model with microribs added is shown in Figure 7.28(b). The shape of the beam, which is largest near the specular direction ($\theta = 60°$), is not significantly changed, but the color is shifted towards longer wavelengths. In addition, a second lobe appears. This lobe is believed to be caused by the scattering from the microribs acting as a second set of lamellae. The shift in color with the

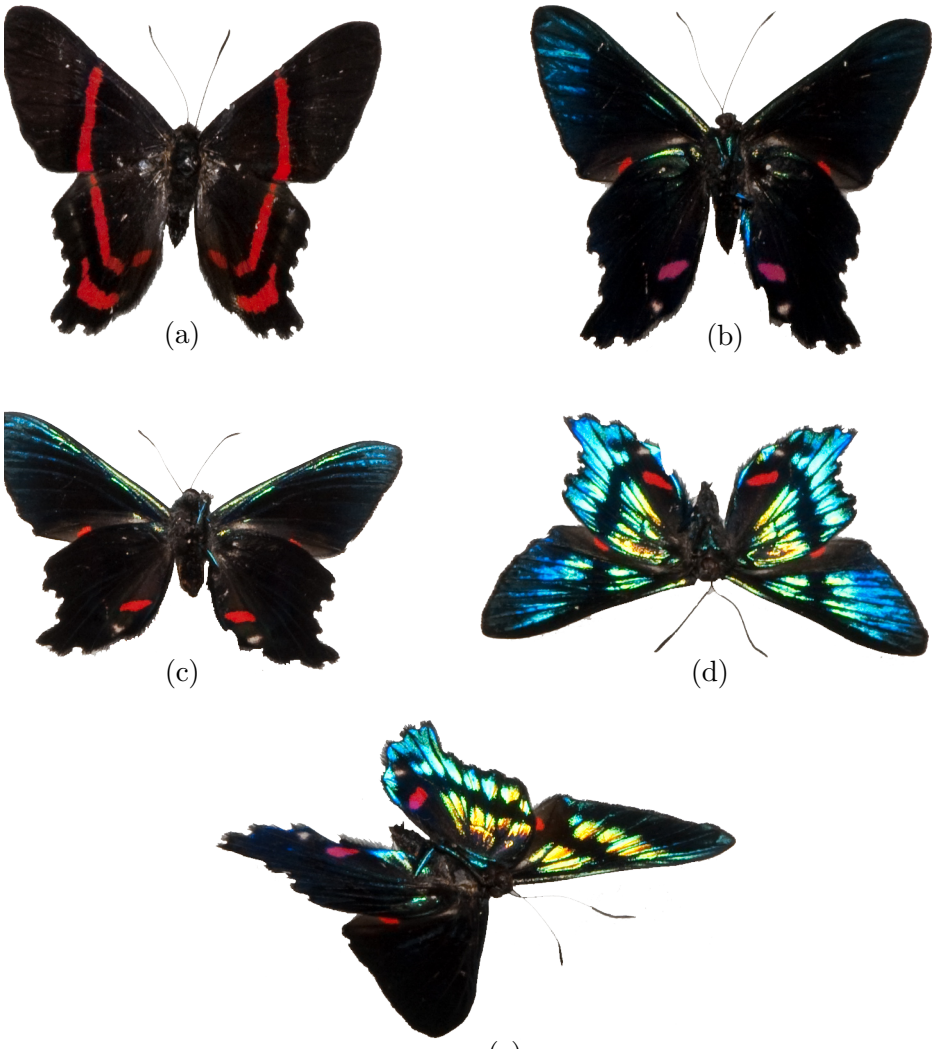


Figure 7.27: Photographs of a male *Ancyluris eudaemon* butterfly. In all views, the light source is located near the observation point. (a) Dorsal side. (b-e) Ventral side. (a) and (b) are for normal incidence. When the insect is viewed so that the antenna are away from the observer, as in (c), the color remains dark. When viewed so that the antenna are closer to the observer, as in (d), intense regions of yellow and blue appear on some of the scales. As the insect is rotated, as in (e), the color begins to disappear.

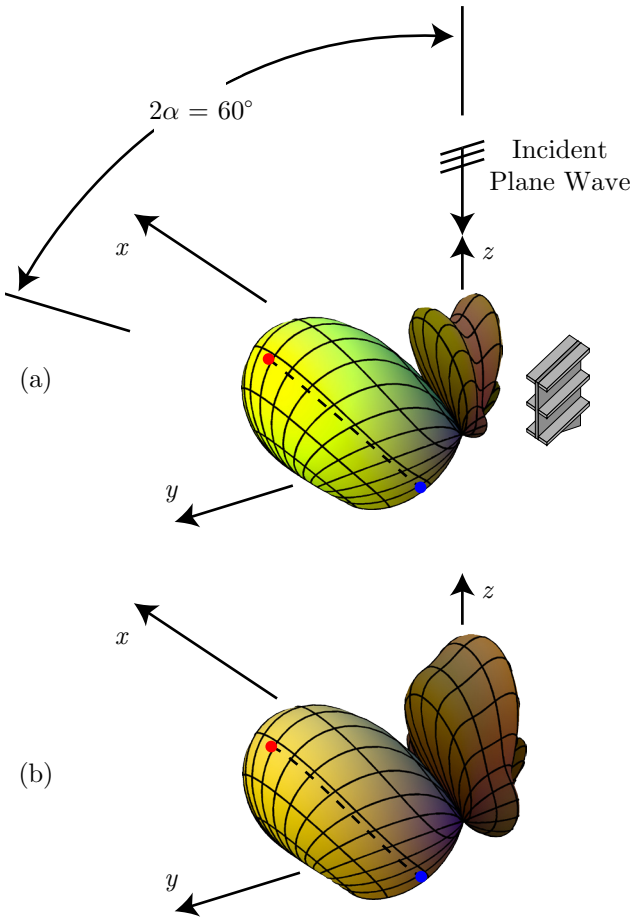


Figure 7.28: Observed color as a function of direction for *Ancyluris meliboeus* model with aligned lamellae and a base. (a) Six lamellae. $Y_{\max} = 1.0$. (b) Six lamellae with microribs. $Y_{\max} = 0.48$.

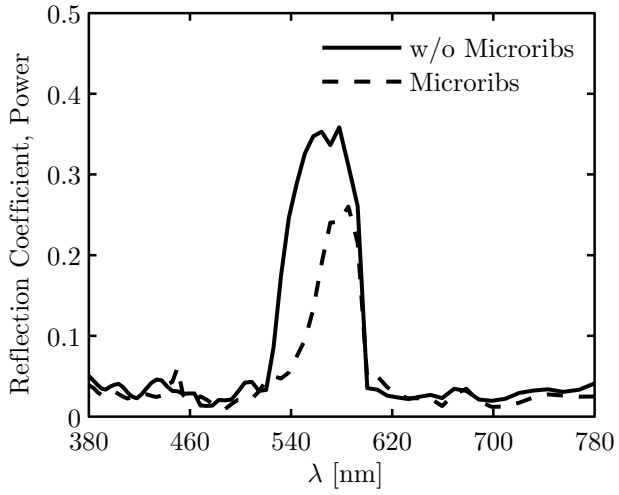


Figure 7.29: Power reflection coefficient for *Ancyluris meliboeus* model. The addition of the microribs causes the peak in the reflection coefficient to shift to longer wavelengths.

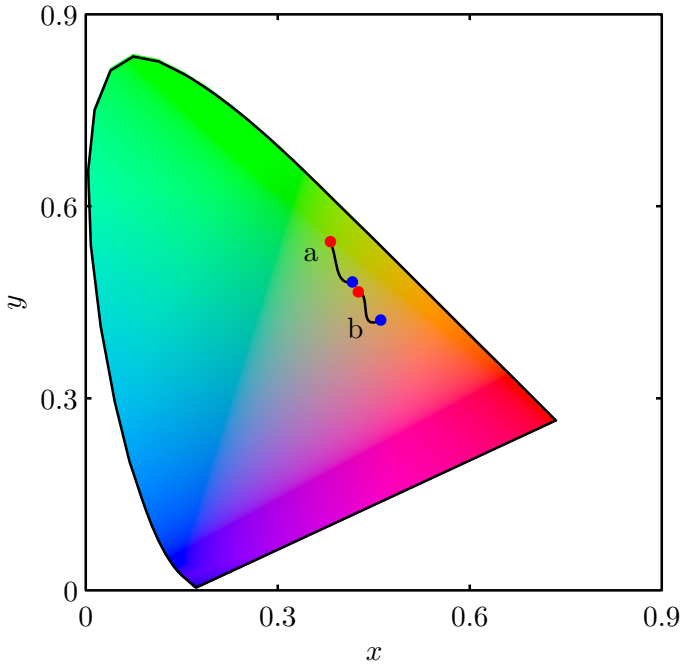


Figure 7.30: Chromaticity coordinates of observed color for the *Ancyluris meliboeus* model as calculated along the dashed lines in Figure 7.28.

addition of the microribs is also indicated by the power reflection coefficients in Figure 7.29. The observed color is similar to the photographs of a specimen taken by Vukusic et al. [66].

The change in color can also be observed on a chromaticity diagram, as shown in Figure 7.30. Both the original model and the model with microribs exhibit iridescence, which is indicated by the change in chromaticity coordinates with observer location. The shift towards longer wavelengths with the addition of the microribs observed in Figure 7.28 is also confirmed by the shift in chromaticity coordinates.

# CHAPTER VIII

# CONCLUSIONS

This thesis has consisted of two conceptual parts: the development of a new technique for modeling periodic structures in the finite-difference time-domain (FDTD) method, and the application of this technique to the study of structural color in insects.

## *8.1 Periodic Boundary Conditions*

The FDTD method for finite structures was presented first. Various important features of the method, such as the dispersion relationship, were discussed. State of the art techniques, such as a nearly-perfect plane-wave injector and a convolutional perfectly-matched layer absorbing boundary condition, were used. The software developed in this work was implemented on a parallel, distributed-memory computer cluster.

The analysis of periodic structures in the time domain was then presented. The goal was to develop a method to model a periodic structure by considering only a single periodic unit cell bounded by periodic boundary conditions (PBCs). A new technique for incorporating PBCs into the FDTD method was presented. The technique is conceptually simple and straightforward to implement. Accuracy was demonstrated by comparing simulation results to the results from an independent frequency-domain technique.

The initial version of the new technique for PBCs has a limitation on the direction of the incident plane wave: The wave vector must lie in a principle plane (e.g., the $xy$ plane). For many problems, the limitation is too restrictive; therefore, a modification to allow for excitations in which the wave vector is not in a principle plane was developed. This modification introduced several additional complications to the implementation. Also, it was not possible to use a completely arbitrary direction; the limitations and cost of the implementation were analyzed. Finally, the accuracy was demonstrated by modeling two canonical problems. First, the scattering from a dielectric slab was modeled, which can be considered as a periodic structure with an arbitrary period. Next, a pair of complementary structures

were modeled, and the results were shown to be consistent with Babinet's principle.

Techniques like the FDTD method only model a finite region. Often, the field far outside this region is desired. In this case, a near-to-far-field transform is used. A technique for using the periodic FDTD method to calculate the scattered field from an array illuminated by a plane wave of finite width was developed. Although this technique was not used for the structural color research, it should be useful for other problems.

## *8.2 Structural Color*

The periodic FDTD method was then applied to the study of structural color in insects. First, an overview of color theory was presented. A technique for using the results from a periodic FDTD calculation to determine observed color was developed.

Next, a computational model for a generic butterfly ridge structure was developed. This model was based on measurements presented in the literature. It was general enough that butterflies that differ greatly in appearance can be considered by changing the geometrical parameters. Although the model was periodic, a technique was developed for calculating the scattered field from a quasi-periodic structure such as a butterfly wing. This technique was based on the observations of Kinoshita and Yoshioka for the coherence of the scattering from the ridges.

A series of experiments were performed to study the underlying assumptions of the quasi-periodic modeling technique. Calculations were performed using analytical expressions for simple point scatterers, which established that certain types of random positioning can cause the scattered field from a large number of quasi-periodic structures to be similar to the scattered field from a single element of a periodic structure. A numerical experiment in the FDTD method was then performed using a simplified, two-dimensional butterfly ridge structure. This model was simple enough that it was possible to perform a large number of simulations of large finite structures with random positions. The ensemble average for the scattered field of these simulations was compared to the scattered field calculated using the periodic FDTD method. Based on this experiment, it was concluded that the scattered field from a single ridge was sufficient to predict the scattering, in an average sense, from a

large number of irregularly spaced ridges.

Butterflies exhibiting structural color were studied, but the goal was not to create an exact model for any particular insect. Rather, it was to study the effect of structural changes on the observed color. The models were, however, similar to specific insects. First, several models were studied similar to *Morpho* butterflies. It was found that the dimensions of the lamellae within the ridge is the dominant factor in determining the color for these insects. The tilt of the lamellae determined the direction of maximum luminance. The lamellae are arranged on either side of a central stem. When the two sides are aligned, the observed color is blue with limited iridescence. When the two sides are offset, the observed color shifts from blue towards violet. The effect of other structural changes, such as tapering the lamellae, adding microribs, and adding a simple cover scale, were also studied for the *Morpho* butterfly.

The *Troides magellanus* butterfly exhibits both structural and pigmentary color. Only the structural color was studied. Since the lamellae are highly tilted with respect to the base, the iridescence is only seen near grazing. In addition, the structural color is highly saturated, which was indicated by the location of the observed color on the chromaticity diagram.

The final butterfly examined was the *Ancyluris meliboeus*. This butterfly is interesting since the iridescence occurs on the ventral rather than the dorsal side. In addition, only certain regions of the wings are covered with iridescent scales, and the analysis was restricted to those regions. The lamellae are more widely spaced than for the other models, and this increased spacing causes a shift to longer wavelengths in the observed color. The presence of microribs in this model had a larger effect than for the other models.

## *8.3 Suggestions for Future Work*

There are several potential improvements that could be made to the periodic FDTD method. First, the boundary condition was developed based on the assumption that time delays in periodic structures in FDTD were the same as time delays in the physical model. As we saw from the dispersion discussion, the speed of light in FDTD is a frequency dependent

quantity, and this dependence should be considered. For example, the time delay could be

$$\tau_{dy} = \frac{(\hat{k}_i \cdot \hat{y}) y_p}{\tilde{v}_p}, \tag{8.1}$$

in which $\tilde{v}_p$ is the numerical phase velocity. A method for directly doing this in the time domain has not yet been found.

Another potential improvement is related to the limitation on the direction of the incident plane wave for the doubly-periodic method. This limitation is caused by the fact that the excitation has to travel farther than the truncation error in this case. Therefore, the excitation will not always enter the good cell before the truncation error, which limits the range of validity. If, instead, the unit cell is defined differently, this limitation could be removed. For example, consider the unit cells in Figure 8.1. In (a), the original method does not work, since the truncation error will enter the "good" cell before the excitation. In (b), the unit cell has been redefined, and the excitation will enter the good cell before the truncation error. This redefined cell has the potential to greatly expand the range of the doubly-periodic technique.

The available future work in structural color is vast. A pigment model could be added to the FDTD code to allow for a more detailed study of insects such as the *Troides magellanus* butterfly. Models for other animals exhibiting structural color, such as the peacock, could be developed and studied. It is hoped that this thesis will prove useful to researchers in both computational electromagnetics and structural color.

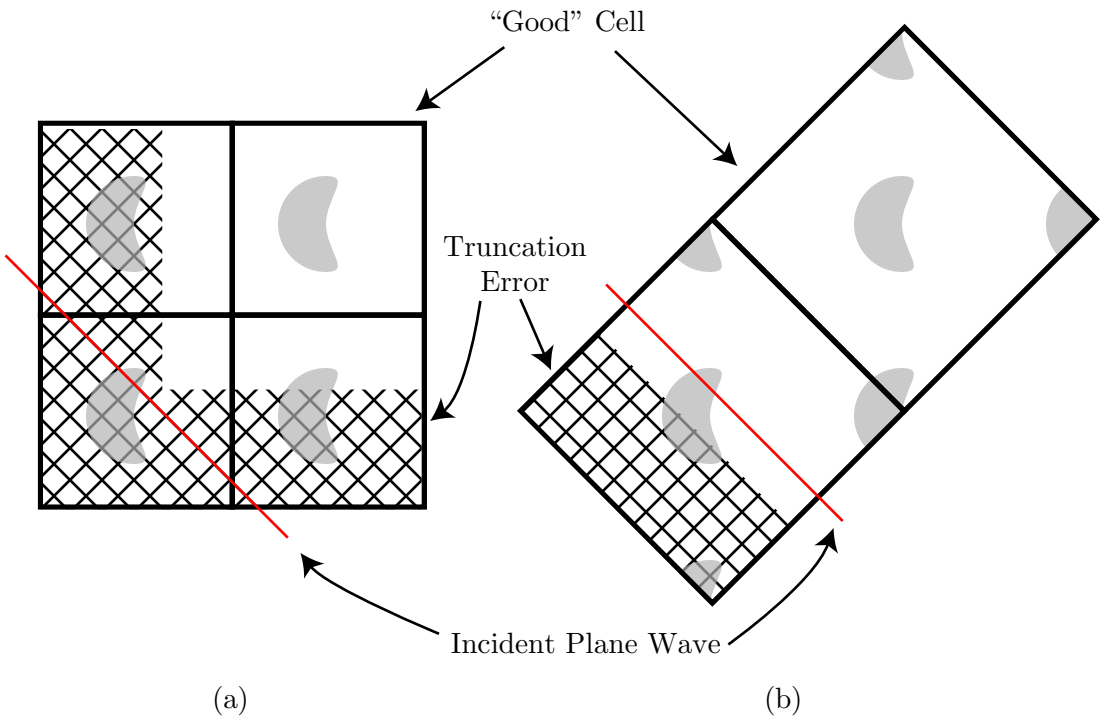


Figure 8.1: Proposed new periodic unit cell for doubly-periodic problems. This cell should allow angles of incidence greater than 45° when the incident plane is obliquely incident.

# APPENDIX A

# DESIGN STUDY FOR TEM HORN ANTENNAS

In this appendix, some earlier work on transverse electromagnetic (TEM) horn antennas is presented. First, the calculation of the characteristic impedance of the infinite antenna is discussed. A numerical technique is then used to perform a design study for the TEM horn antenna with a characteristic impedance of $100\,\Omega$. Portions of this research were previously published in [67] and [68].

## *A.1 Introduction*

The TEM horn is a popular broadband antenna. As shown in Figure A.1, it consists of two perfectly conducting triangular plates. The angle of each plate at the drive point of the horn is $\alpha$ ($0 < \alpha < 180°$), and the angular separation between the plates is $\beta$ ($0 < \beta \leq 180°$). For the special case $\beta = 180°$, the plates are coplanar, and the geometry becomes that of the bow-tie antenna. A key parameter for the design of the horn is the characteristic impedance $Z_c$ for the TEM spherical wave ($E_r = H_r = 0$) on the infinitely long antenna ($s \to \infty$).

Over the years, researchers have proposed analytical solutions for the characteristic impedance. In 1958, Carrel used a conformal mapping approach to solve for the characteristic impedance of the TEM horn [69]. In 1976, independently of Carrel, Yang and Lee solved for the characteristic impedance in a technical report [70]. As it was not widely published, this solution escaped notice for many years. In the mid 1990s, two groups of investigators pointed out that there were significant differences between Carrel's results for the characteristic impedance and measurements. Maloney and Smith showed that Carrel's results for the characteristic impedance did not agree with results obtained by numerically solving Laplace's equation except in the special case of the bow-tie antenna [71], while Lambert et al. identified the error in Carrel's original formulation and offered a new formula, again based on conformal mapping [72].

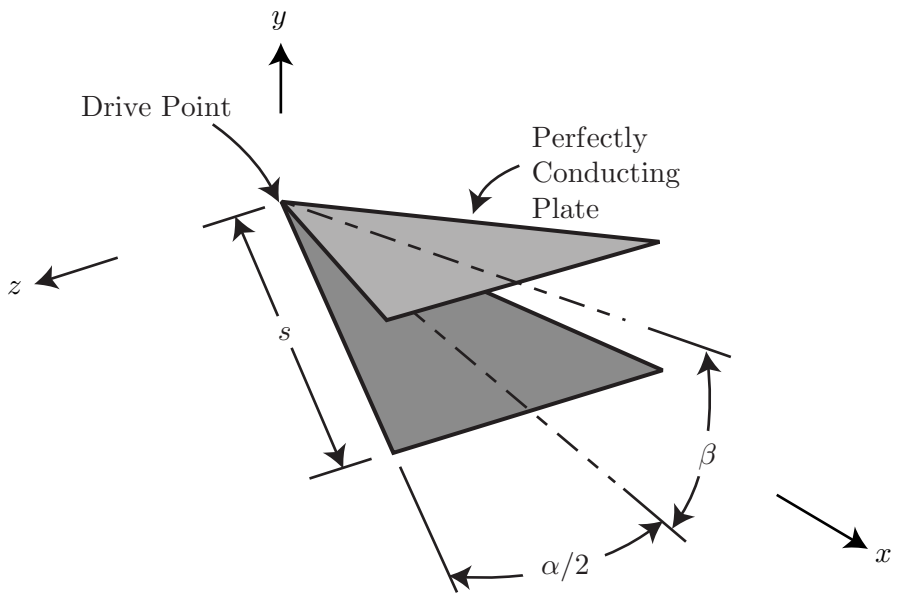


Figure A.1: Geometry for the TEM horn antenna.

In this appendix, the various analytical solutions that have been offered are compared to a numerical solution. As expected, Carrel's solution is found to agree only for the bow-tie configuration. The solution of Lambert et al. agrees well for low elevation angles, $\beta$, and the Yang and Lee solution agrees for all angles. After correcting for a branch cut error, the solution of Lambert et al. also agrees with the numerical solution. In Appendix B, a complete derivation of the characteristic impedance is presented. The formulation is equivalent to the other analytical solutions, but is somewhat simpler due to various mathematical substitutions.

Next, we turn our attention to optimization of the antenna. Much of the previous research has focused on modifying the antenna's structure to improve the performance. These modifications include resistive loading along the plates [73, 74] and shaping of the plates [75]. What is interesting is that there is very little design information available for the basic TEM horn, as compared to what is available for other horns, such as sectoral and pyramidal horns [76]. This design information is presented in this appendix.

## *A.2 Characteristic Impedance*

### A.2.1 Formulation of the Problem

The characteristic impedance for the TEM-mode in the horn can be treated as a problem in electrostatics. To show this, assume that there is a TEM spherical wave in the horn:

$$\vec{E} = \vec{e}_t(\theta,\phi)\frac{e^{-jk_o r}}{r} \tag{A.1}$$

$$\vec{H} = \vec{h}_t(\theta,\phi)\frac{e^{-jk_o r}}{r} \tag{A.2}$$

where the subscript $t$ means that there are only transverse components ($\hat{\theta}$, $\hat{\phi}$) to the vectors.

From Faraday's law, $\nabla \times \vec{E} = -j\omega\mu_o\vec{H}$, we obtain

$$\hat{r} \cdot [\nabla \times \vec{e}_t(\theta,\phi)] = 0, \tag{A.3}$$

Now we let

$$\vec{e}_t = -r\nabla\Phi(\theta,\phi), \tag{A.4}$$

in which $\Phi$ is a scalar potential function. This form for $\vec{e}_t$ satisfies (A.3).

Next, we substitute (A.1) and (A.4) into Gauss' electric law, $\nabla \cdot \vec{E} = 0$, to obtain

$$\begin{aligned} \nabla \cdot (-e^{-jk_o r}\nabla\Phi) = -e^{-jk_o r}(-jk_o\hat{r} \cdot \nabla\Phi + \nabla^2\Phi) = 0 \\ -e^{-jk_o r}\nabla^2\Phi = 0, \end{aligned} \tag{A.5}$$

which implies that the potential, $\Phi$, satisfies Laplace's equation:

$$\nabla^2\Phi = 0. \tag{A.6}$$

Therefore, the question of finding the field distribution for the TEM-mode reduces to one of solving Laplace's equation on a sphere, with the boundary conditions that one plate is held at $\Phi = +V$ and the other is held at $\Phi = -V$.

The characteristic impedance is computed from the potential. First, we determine the total charge per unit length on one of the plates, with the factor $e^{-jk_o r}$ suppressed, from the integral

$$Q = -\epsilon_o \oint_C (\hat{n} \cdot \nabla\Phi)dl, \tag{A.7}$$

where $C$ is a contour that encircles only one of the plates and $\hat{n}$ is an outward pointing unit vector normal to $C$. From the charge per unit length, the characteristic impedance is given by [77]:

$$Z_c = \frac{2V}{cQ}. \tag{A.8}$$

### A.2.2 Numerical Solution

The characteristic impedance is calculated numerically using the technique proposed in [71]. To reduce the problem space, the $xz$ plane is made a perfect electric conductor (PEC image plane), and the $xy$ plane is made a perfect magnetic conductor (PMC image plane). The antenna becomes a half-plate defined by

$$\phi = \beta/2 \tag{A.9}$$

$$90^\circ - \frac{\alpha}{2} \leq \theta \leq 90^\circ. \tag{A.10}$$

On the unit sphere ($r = 1$), shown in Figure A.2, Laplace's equation for the potential function $\Phi(\theta, \phi)$, i.e.,

$$\frac{\partial^2 \Phi}{\partial \theta^2} + \cot\theta \frac{\partial \Phi}{\partial \theta} + \frac{1}{\sin^2\theta} \frac{\partial^2 \Phi}{\partial \phi^2} = 0, \tag{A.11}$$

must be solved subject to the boundary conditions $\Phi = V$ on the half-plate and $\Phi = 0$ on the $xz$ plane.

Once the scalar potential is known, the charge per unit length on the half-plate is determined from (A.7) (note that the charge computed in this way is one-half the total charge). The contour $C$ is shown as a dotted line in Figure A.2. Finally, the characteristic impedance of the full (two-plate) TEM horn antenna is obtained from the charge per unit length (A.8).

The procedure described above was implemented by solving Laplace's equation (A.11) for the potential $\Phi$ using finite differences on the spherical grid shown in Figure A.2. The contour $C$ in (A.7) was placed between grid points, and the gradient operation approximated by central differences. The integration in (A.7) was approximated using the trapezoidal rule. The angles $\alpha$ and $\beta$ were varied in $2^\circ$ steps over the ranges $2^\circ \leq \alpha \leq 178^\circ$ and $2^\circ \leq \beta \leq 180^\circ$, resulting in a total of 8010 impedance calculations.

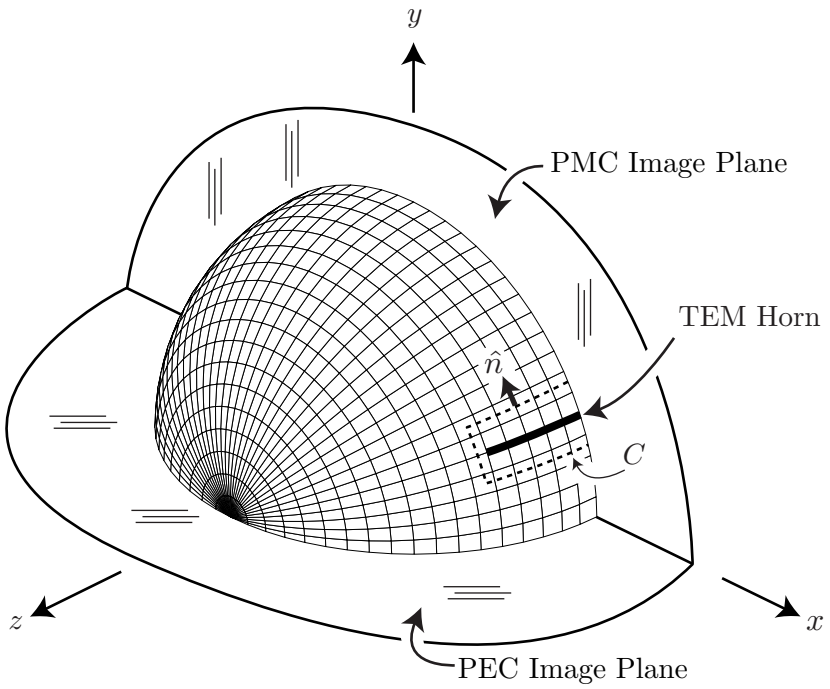


Figure A.2: Geometry used for the numerical solution of Laplace's equation on the unit sphere. The cross section of the horn and the contour $C$ for computing the charge per unit length are marked.

### A.2.3 Analytical Solutions

Carrel's solution for the characteristic impedance is given in [69], but, as already mentioned, it is in error. As such, it will not be repeated here. However, as shown in [71], Carrel's solution is correct for the bow-tie configuration.

The solution offered by Lambert et al. is readily available in [72] and will not be repeated here. It should be noted that a branch cut error was made in their analysis [78]. To correct this, the minus sign on the right-hand sides of [72, (16) and (18)] should be changed to plus signs. This error makes little difference for small plate separation angles ($\beta \lesssim 60°$), but becomes significant as the plate separation increases.

In Figure A.3, we compare the results for a TEM horn antenna with $Z_c = \eta_o/2$ calculated using the numerical solution, Carrel's formula, and Lambert et al.'s uncorrected formula. Each line represents the combinations of the angles $\alpha, \beta$ that produce a horn with this characteristic impedance. This value of the characteristic impedance was chosen because it is the impedance of a planar self-complimentary antenna. For the bow-tie antenna, this

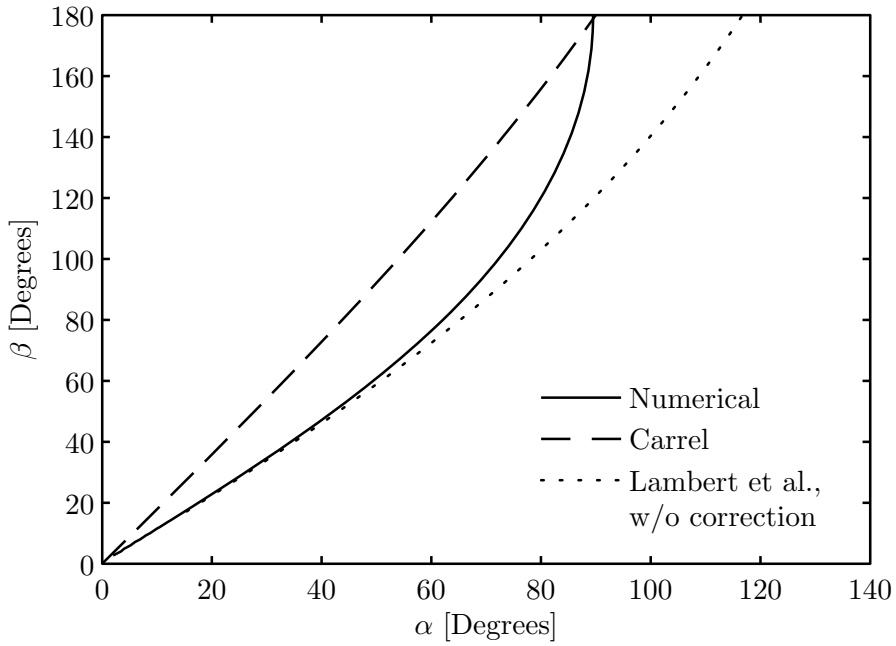


Figure A.3: Results for a TEM horn antenna with characteristic impedance $Z_c = \eta_o/2$.

corresponds to $\alpha = 90°$ and $\beta = 180°$. As expected, Carrel's result, shown as a dashed line, only applies for the bow-tie configuration. The original solution of Lambert et al. shown as a dotted line, agrees with the numerical results for small values of $\alpha, \beta$; however, it differs significantly once $\beta \gtrsim 60°$.

The correct analytical solution can be written in a number of equivalent ways. These solutions are implicit; i.e., given a desired characteristic impedance $Z_c$, the angles $\alpha, \beta$ that produce this impedance are obtained. Here we use the solution derived in Appendix B. An equivalent solution was derived by Yang and Lee [67, 70]. The special functions used are defined in Appendix B. The value of $\alpha$ can be determined as a function of $Z_c$ and $\beta$ as follows:

$$Z_c = \eta_o \frac{K(k')}{K(k)} \tag{A.12}$$

$$n = k^2 \operatorname{sn}^2 \left[ \frac{\beta}{2\pi} K(k), k \right] \tag{A.13}$$

$$\phi = \sin^{-1} \sqrt{\frac{1}{n} \left[ 1 - \frac{K(k)}{\Pi(n,k)} \right]} \tag{A.14}$$

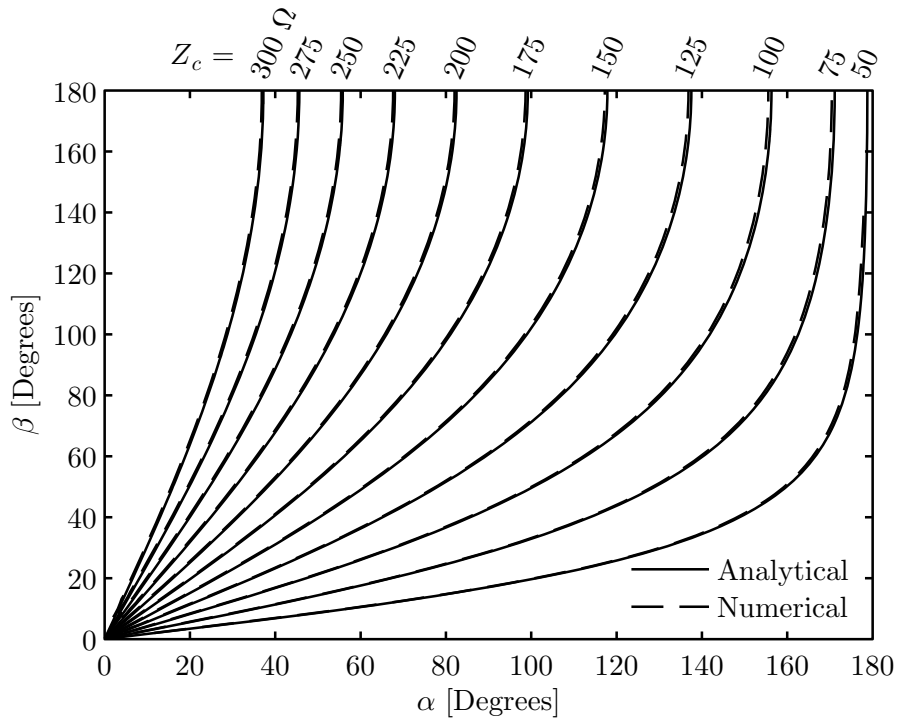


Figure A.4: The characteristic impedance $Z_c$ of the TEM horn antenna as a function of the angles $\alpha$ and $\beta$.

$$R = \exp\left\{2\sqrt{\frac{(1-n)(k^2-n)}{n}}\left[\Pi(n,k)\frac{F(\phi,k)}{K(k)} - \Pi(\phi,n,k)\right]\right\} \tag{A.15}$$

$$\alpha = 2\sin^{-1}\left(\frac{R^2-1}{R^2+1}\right) \tag{A.16}$$

### A.2.4 Impedance Curves

By fixing $Z_c$ and varying $\beta$ ($0 < \beta \leq 180°$), a set of impedance curves can be obtained. Each curve represents the possible combinations of angles to achieve a given characteristic impedance. The curves in Figure A.4 were generated using the analytical solution (solid line) and the numerical solution (dashed line). Notice that the two are in excellent agreement for all angles. These curves should be useful in the design of TEM horn antennas.

### A.2.5 Microstrip Approximation

For small values of $\alpha$ and $\beta$, a commonly used approximation is to assume that the characteristic impedance of the TEM horn is the same as twice that of a comparable microstrip transmission line filled with free space [74]. If an infinite PEC image plane is placed on

the $xz$ plane in Figure A.1, then any transverse cross section ($x$ = constant) of the horn is similar to that of a microstrip transmission line. The characteristic impedance of the microstrip is determined by the ratio of the width of the strip $w$ to the height of the strip above the image plane $h$. For the TEM horn, $w/h$ is related to the angles $\alpha$, $\beta$ by

$$\alpha = 2 \arctan \left[ \frac{w \sin(\beta/2)}{2h} \right]. \tag{A.17}$$

Any one of a number of published formulas can be used for the characteristic impedance of the microstrip transmission line. Here we use the approximate formula given in [79]:

$$A = \frac{\pi Z_c}{\eta_o} \tag{A.18}$$

$$\frac{w}{h} = \begin{cases} 8/(e^A - 2e^{-A}) & , w/h < 2 \\ 2[\pi^2/A - 1 - \ln(2\pi^2/A - 1)]/\pi & , w/h > 2 \end{cases} \tag{A.19}$$

For a vacuum-filled microstrip, a much more complicated exact formula for the characteristic impedance is also available [80]. However, for the range of angles where the microstrip approximation applies, the difference between the approximate formula and the exact formula is negligible.

In Figure A.5, the results from the analytical formula are shown as solid lines and those from the microstrip approximation, (A.17) – (A.19), are shown as dashed lines. As expected, the agreement is good for small values of $\alpha$ and $\beta$. Notice that the approximate formula, (A.17) – (A.19), is explicit and involves no special functions. Therefore, it is much easier to use than the exact formula, (A.12) – (A.16).

## *A.3 Design Study*

### A.3.1 Characteristic Impedance

As discussed above, the characteristic impedance of the TEM horn antenna is a function of only the angles $\alpha$ and $\beta$. In this study, antennas with the commonly used value $Z_c = 100\,\Omega$ are examined. For an antenna of finite length that is reasonably long, the characteristic impedance is a good approximation to the input impedance of the antenna. As an example, the calculated input impedance $Z_{\text{ant}}$ of an antenna with $\alpha = 47.30°$ and $\beta = 20°$, for which $Z_c = 100\,\Omega$, is shown as a function of the electrical length $s/\lambda$ in Figure A.6. The

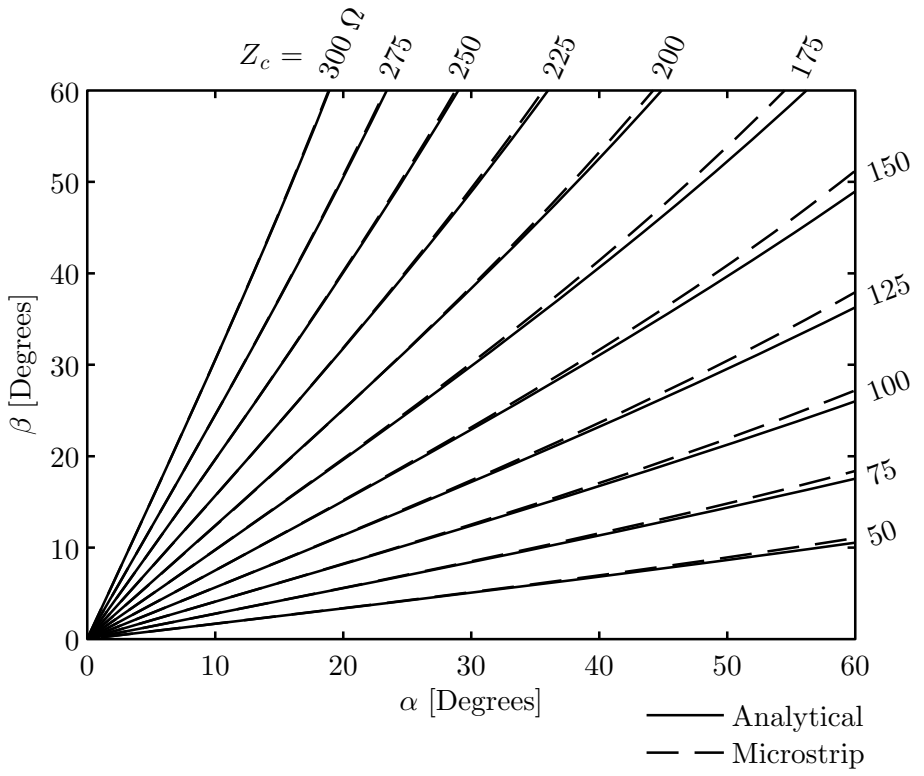


Figure A.5: Comparison of the analytical result with the microstrip approximation for the characteristic impedance $Z_c$ of the TEM horn antenna.

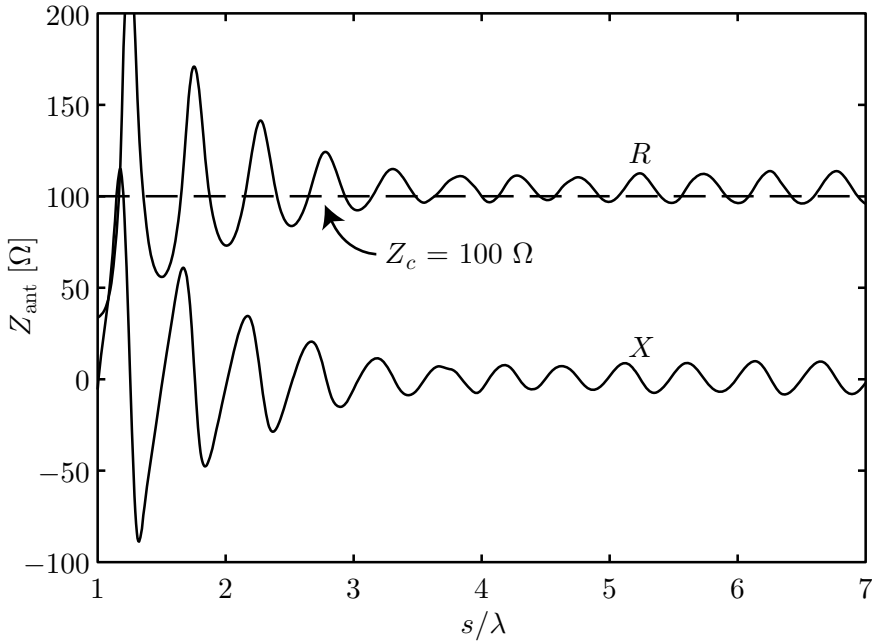


Figure A.6: Input impedance, $Z_{\text{ant}} = R + jX$, versus electrical length of the horn antenna. For this antenna, $\alpha = 47.30°$, $\beta = 20°$, and $Z_c = 100\,\Omega$.

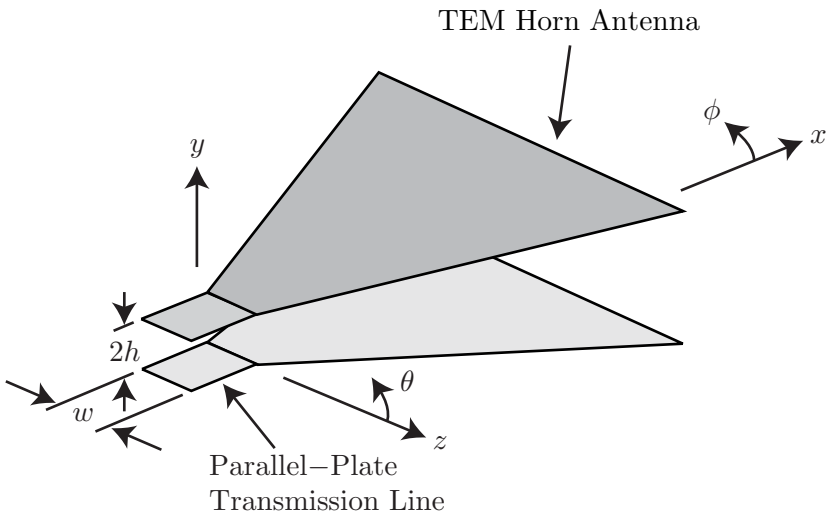


Figure A.7: A TEM horn antenna fed by a parallel-plate transmission line.

input resistance $R$ oscillates around $100\,\Omega$, and the reactance $X$ oscillates around $0\,\Omega$. For antennas with $s/\lambda > 3$, the amplitude of the oscillations is fairly small, $\approx \pm 10\,\Omega$. To minimize the reflection at the transmission-line/antenna junction, the characteristic impedances of the feeding transmission line and the antenna are generally chosen to be the same value. With $Z_c$ specified, one of the angles for the horn can be treated as a free variable and the other determined using Figure A.4. For this study, the angle $\beta$ is treated as the free variable, and $\alpha$ is the dependent variable.

### A.3.2 Model for the Antenna

As mentioned in the introduction, the geometry of the basic TEM horn antenna does not require a particular choice of feeding method. One possibility is to use a parallel-plate transmission line, and then flare the plates outward to form the antenna. This geometry is shown in Figure A.7. In the illustration, the relative size of the transmission line is exaggerated for clarity.

In this study, the antenna is modeled using FEKO, a commercial, method-of-moments software package [81]. Since this study involves the realized gain of the antenna, an accurate calculation of the input impedance is required. While standard delta-gap models are available for directly calculating the input impedance, these models suffer from the difficulty that the input susceptance depends on the level of the discretization. To avoid this

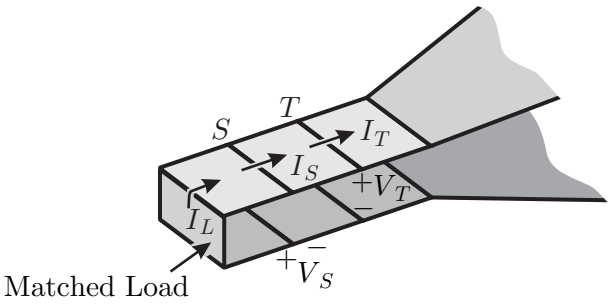


Figure A.8: The detail of the model used for feeding the TEM horn antenna in the numerical simulations.

problem, a different feeding scheme is used.

When a two-conductor line is operating below cutoff for all non-TEM modes, the only wave that will propagate down the line is the TEM mode. This means that, regardless of the feed employed, the propagating wave will quickly become a TEM wave. As shown in Figure A.8, delta-gap voltage sources, $V_S$, are applied at the location marked $S$ on both plates of the transmission line. These sources launch waves in both directions along the transmission line. Away from the sources, the propagating wave is essentially TEM. At the terminals of the antenna, the voltage $V_T$ between the plates is computed by integrating the electric field between the plates at the location marked $T$. Since the method of moments program solves for the surface current, the current $I_T$ is also available at this location. The input impedance of the antenna, as determined at location $T$, is then given by

$$Z_{\text{ant}} = \frac{V_T}{I_T}. \tag{A.20}$$

While a delta-gap source is used in this scheme, this source is used only to inject power into the system; the actual voltage and current are determined away from the source. Therefore, the typical difficulties associated with using delta-gap sources are avoided.

The physical size of the feed and the frequency, $f$, (wavelength $\lambda$) remain constant throughout all of the simulations. The actual length of the antenna is changed to vary quantities such as $s/\lambda$. Keeping the physical size of the feed constant insures that any parasitic effects near the feed remain the same for all antennas. Along the transmission line segment, the width of the plates, $w$, is $\lambda/10$ and the height, $h$, is $w/4.912$, which sets the characteristic impedance of the parallel-plate transmission line to $100\,\Omega$ [80]. The spacing

between the source location and the measurement location is twice the width of the plates. To minimize the unwanted radiation from the section of transmission line, the back end of the line (away from the antenna) is terminated with a matched load: a resistor equal to $Z_c$.

From the calculated surface current, the radiated electric field, $r\vec{E}$, on axis is found. To convert this field into the gain or realized gain, the total power radiated is required. Ignoring any radiation from the transmission line, this is equal to the power accepted by the antenna at its terminals[1]:

$$P_{\text{rad}} = \frac{1}{2}\text{Re}(V_T I_T^*). \tag{A.21}$$

The gain on axis is then given by

$$G = \frac{2\pi|r\vec{E}|^2}{\eta_{\text{o}} P_{\text{rad}}}, \tag{A.22}$$

where $\eta_{\text{o}}$ is the wave impedance of free space. Note that the gain, $G$, is the same as the directivity, $D$, for the lossless antennas considered here. The realized gain (gain including mismatch) is given by

$$G_r = (1 - |\Gamma|^2)G, \tag{A.23}$$

in which $\Gamma$ is the voltage reflection coefficient in the transmission line.

### A.3.3 Design Graphs

In this section, the results of a parametric study are presented. The gain and related quantities are determined for different electrical lengths of the antenna, $s/\lambda$. The angle $\beta$ is treated as a parameter over the range $10° \leq \beta \leq 35°$, and the angle $\alpha$ is determined using the results in Figure A.4 so that $Z_c = 100\,\Omega$.

Figure A.9 shows the gain on axis ($\theta = 90°$, $\phi = 0°$) versus the electrical length of the antenna, $s/\lambda$, for six different values of the separation angle, $\beta$. When the small ripples on the curves are ignored, the gain increases with increasing electrical length for any fixed separation angle. For short antennas, $s/\lambda \leq 2$, the gain also increases as the separation angle increases; however, for longer antennas the gain first increases then decreases with increasing

[1] Another procedure for calculating the radiated power is to subtract the power dissipated in the termination ($P_{\text{diss}} = \frac{1}{2}|I_L|^2 Z_c$) from the power of the gap sources ($P_{\text{in}} = \text{Re}(V_S I_S^*)$). This method was also tried and gave essentially the same results.

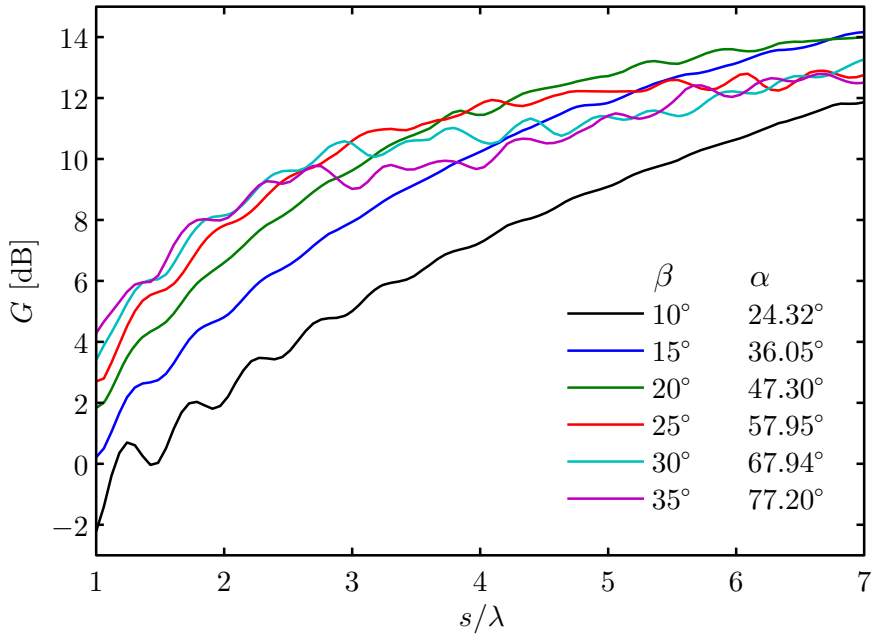


Figure A.9: Gain on axis ($\theta = 90°$, $\phi = 0°$) for TEM horn antennas versus electrical length. For all antennas $Z_c = 100\,\Omega$.

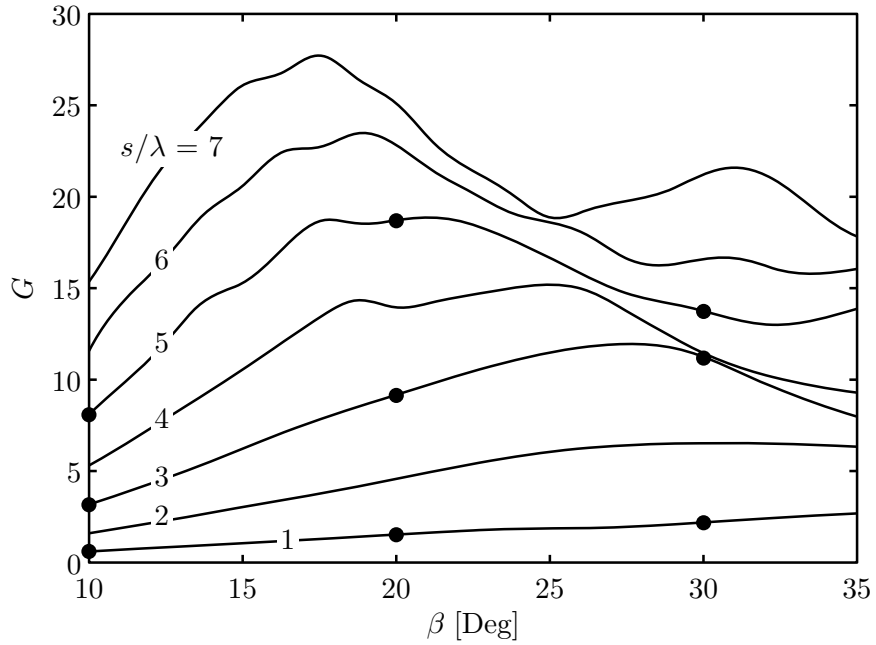


Figure A.10: Gain on axis ($\theta = 90°$, $\phi = 0°$) for TEM horn antennas versus the separation angle for the plates. For all antennas $Z_c = 100\,\Omega$. Note, in this graph, a linear scale is used for the gain.

separation angle. To examine this point further, the gain is graphed in Figure A.10 as a function of the separation angle with the electrical length of the antenna as a parameter. For the longer antennas, $s/\lambda \geq 3$, there is a clear peak in the gain, and the peaks occur at progressively smaller separation angles as the electrical length is increased. The causes for this behavior in the gain can be understood by examining radiation patterns for the antenna.

Figure A.11 presents an array of three-dimensional gain patterns for the antenna. Each row in Figure A.11 shows the gain of an antenna of a particular length ($s/\lambda = 1, 3, 5$) for three different separation angles ($\beta = 10°, 20°, 30°$). The antennas for which patterns are given are indicated by the solid dots in Figure A.10.

For the shortest antennas ($s/\lambda = 1$) considered, shown in the bottom row of Figure A.11, the radiation pattern is maximum in a direction ($\theta = 90°$, $\phi = 90°$) broadside to the axis of the antenna. Hence, the gain on axis is fairly low for all of the separation angles considered (bottom curve in Figure A.10). For the longer antennas ($s/\lambda = 5$), shown in the top row of Figure A.11, the radiation pattern is a split beam in the vertical plane at low separation angle ($\beta = 10°$), a directive beam along the axis of the antenna at moderate separation angle ($\beta = 20°$), and finally a split beam in the horizontal plane at high separation angle ($\beta = 30°$). Hence, the gain on axis, Figure A.10, exhibits a definite peak when $\beta \approx 20°$. The behavior of the radiation pattern described above is easily explained in terms of traditional antenna analysis.

For determining the pattern in the vertical plane ($xy$ plane), the horn can be likened to a traveling-wave Vee antenna. In the vertical plane, each arm of the Vee produces a pattern with a symmetric pair of lobes, as shown in Figure A.12(a) [1]. Notice that the direction of radiated electric field for each lobe is indicated on the figure. When the separation angle is small, e.g. $\beta = 10°$, the lobes $A$ and $A'$ partially overlap and their fields subtract, as do the fields for lobes $B$ and $B'$. This produces a pattern in the vertical plane that is a split beam with a null on axis, as shown in Figure A.12(b) for the $\beta = 10°$ case. For larger separation angles, lobes $B$ and $A'$ overlap and their fields add. This produces a pattern in the vertical plane that is a beam with its maximum on axis, as shown in Figure A.12(b) for the $\beta = 20°$

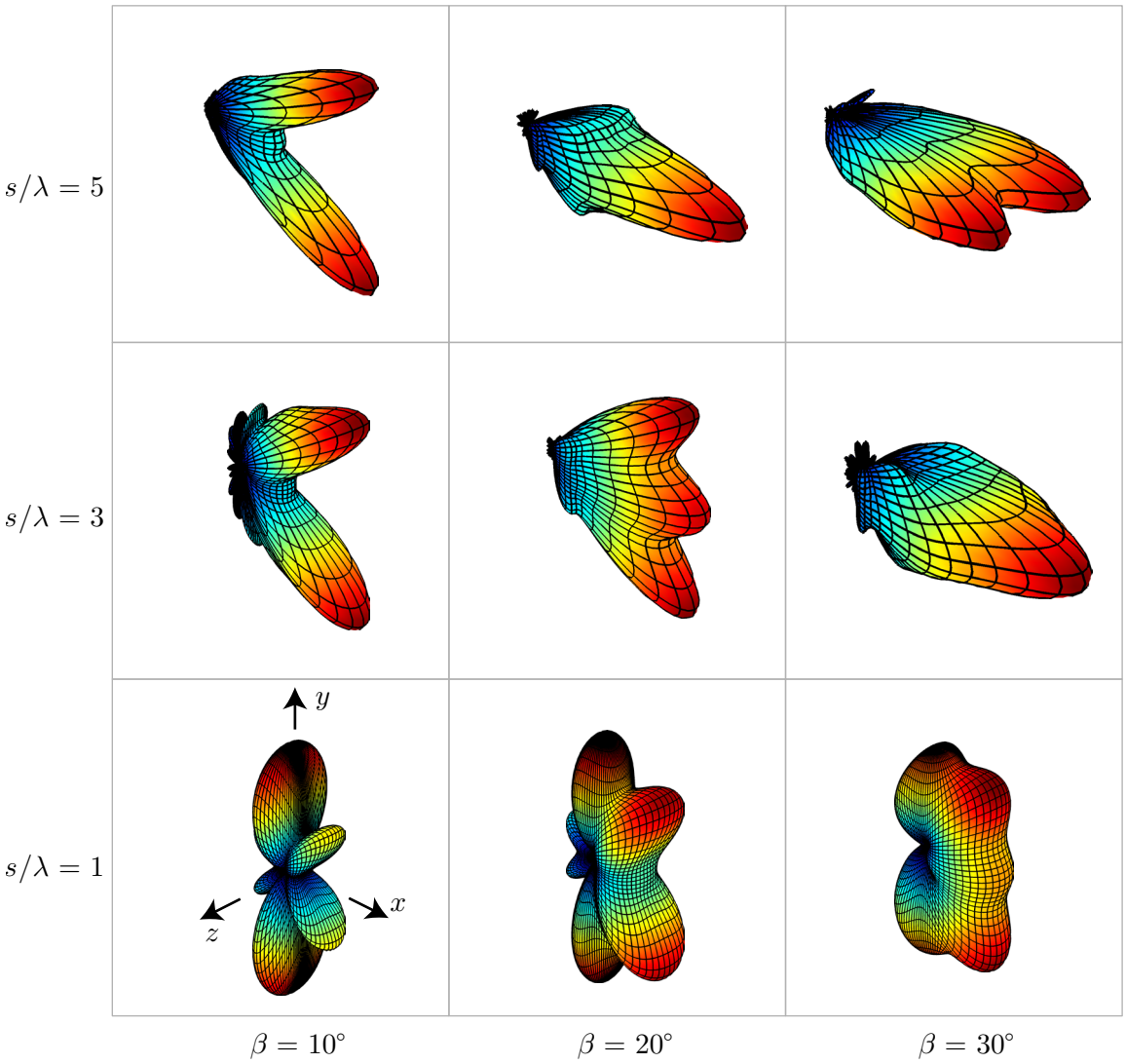


Figure A.11: Representative gain patterns for TEM horn antennas. The antenna length increases from $s/\lambda = 1$ to $s/\lambda = 5$ moving from bottom to top, and the separation angle of the plates increases from $\beta = 10°$ to $\beta = 30°$ moving from left to right. For all antennas $Z_c = 100\,\Omega$.

and 30° cases.

For determining the pattern in the horizontal plane ($xz$ plane), the horn can be likened to a uniformly illuminated, rectangular aperture with a quadratic phase variation across its width ($z$ direction). This phase variation is due to the spherical wave in the horn intersecting the aperture plane. As the separation angle increases, the width of the plates also increases, hence the phase variation across the aperture increases. Figure A.12(c) shows patterns in the horizontal plane of a uniform aperture with the same phase variation as the horn. As the separation angle increases from $\beta = 10°$ to $\beta = 30°$, the pattern goes from one with a single lobe to one with a split lobe in the horizontal plane.

Figure A.13 shows the fraction of the incident power lost due to mismatch, $1 - |\Gamma|^2$, for these antennas. Notice that the mismatch loss is generally greater the smaller the separation angle. This causes the realized gain (A.23) to be significantly lower than the gain (A.22) for the shorter antennas, $s/\lambda \lesssim 2$, with $\beta \lesssim 20°$. However, once $s/\lambda \gtrsim 3$, all of the antennas are fairly well matched to the transmission line ($|\Gamma| < 0.3, 1 - |\Gamma|^2 < 0.5\,\mathrm{dB}$), so the realized gain (A.23) and the gain (A.22) are essentially the same.

### A.3.4 Comparison with Measurement

Model antennas were constructed, and measurements made on these antennas were used to check the accuracy of the numerical calculations. An image-equivalent was used for the measurements in which one-half of the antenna was mounted over a large aluminum image plane ($6\,\mathrm{m} \times 6\,\mathrm{m}$) and fed through the image plane by a coaxial line with the characteristic impedance $Z_c = 50\,\Omega$. The geometry is shown in Figure A.14.

The gain of the antenna was determined using the two-antenna method with the drive points of the two identical antennas separated by the distance $r = 96.1\,\mathrm{cm}$ [82]. The scattering parameters ($S_{11}, S_{21}$) for the two-port network formed by the antennas were measured using a vector network analyzer (Agilent 8720D) over the frequency range $50\,\mathrm{MHz} - 16.05\,\mathrm{GHz}$, and the reflections from the edges of the image plane were removed by windowing in the time domain. The gain of the antenna (excluding mismatch) was then determined

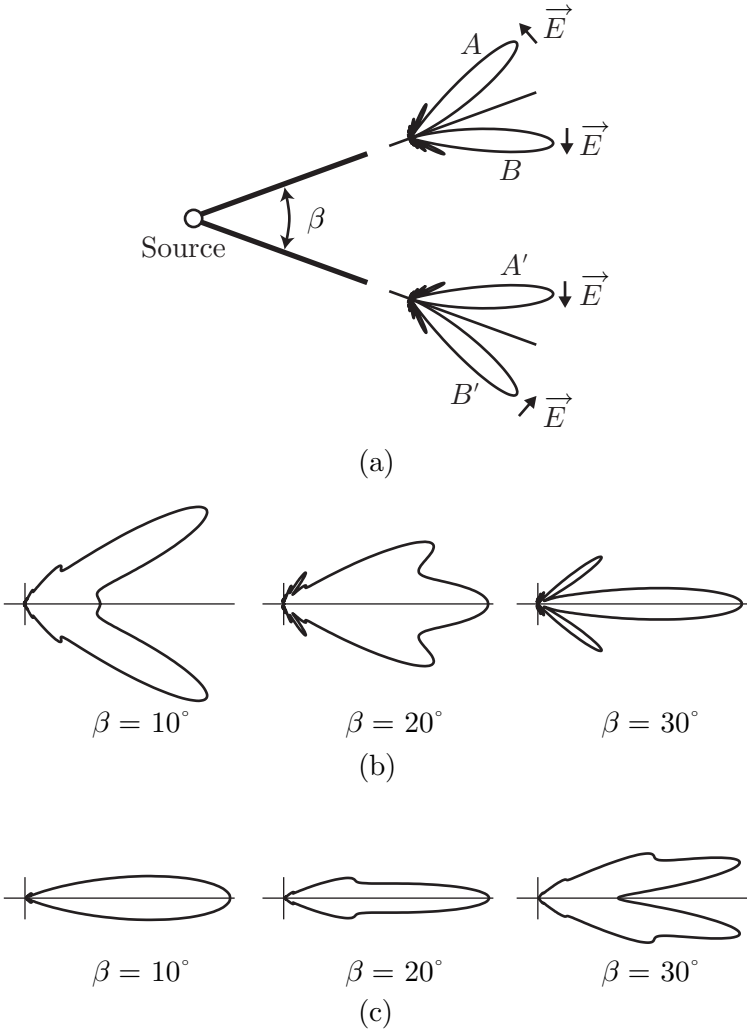


Figure A.12: Explanations for the variation in the gain patterns of the TEM horn antennas with $s/\lambda = 5$. (a) Patterns in the vertical plane ($xy$ plane) for the two traveling-wave elements that make up a Vee dipole antenna, and (b) their superposition for various separation angles. (c) Patterns in the horizontal plane ($xz$ plane) for a uniformly illuminated aperture with a quadratic phase variation across its width that is equal to the phase variation for the TEM horn.

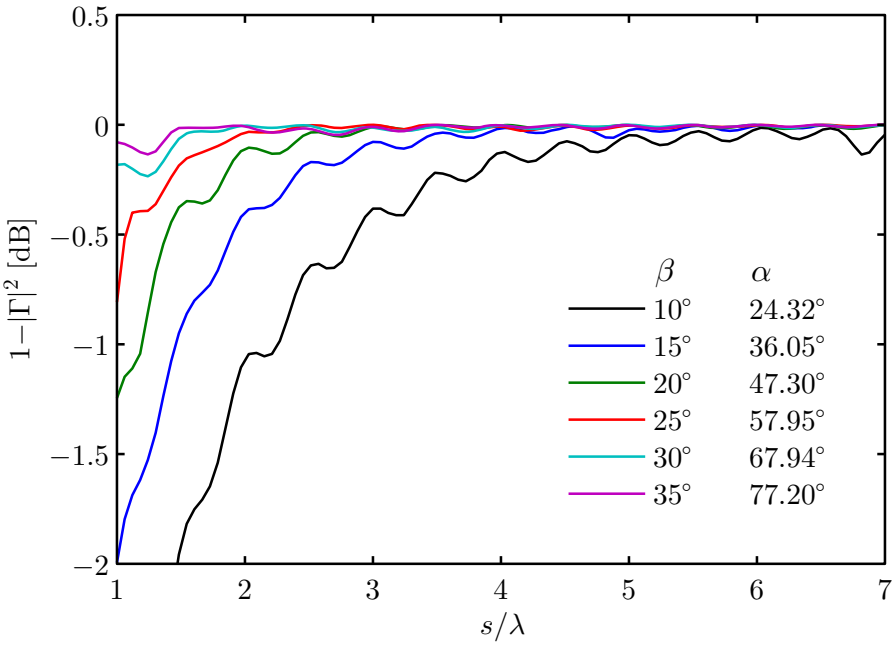


Figure A.13: Fraction of the incident power lost due to mismatch, $1 - |\Gamma|^2$, for TEM horn antennas versus electrical length. For all antennas $Z_c = 100\,\Omega$.

from the scattering parameters:

$$G = \frac{4\pi r}{\lambda} \frac{|S_{21}|}{1 - |S_{11}|^2}. \tag{A.24}$$

The gain calculated from (A.24) will be independent of the distance between the two antennas, $r$, only when the antennas are in each other's far zone. This occurs roughly when $r > 2d^2/\lambda$, where $d$ is the maximum dimension of the antennas. For the antennas used, this inequality was not satisfied with $r = 96.1\,\text{cm}$. As a result, far-zone approximations could not be used when making the numerical computations for comparison with the measurements. Instead, a full model that includes both antennas was required.

In Figure A.15 the theoretical (black line) and measured (red line) gains are shown as a function of the electrical size of the antenna $s/\lambda$. These results are for an antenna with $\alpha = 71.73°, \beta = 32°$, $s = 18\,\text{cm}$, and $Z_c = 100\,\Omega$ for the full antenna ($Z_c = 50\,\Omega$ for the half antenna). The theoretical and measured gains are seen to be in good agreement. The small differences ($< 1\,\text{dB}$) that do exist at the higher frequencies are probably due to the differences in the feed structures for the theoretical and experimental models: A parallel-plate line is used with the full antenna in the theoretical model, Figure A.7, and a coaxial

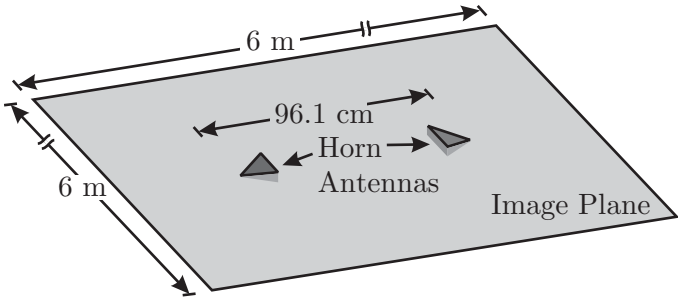


(a)

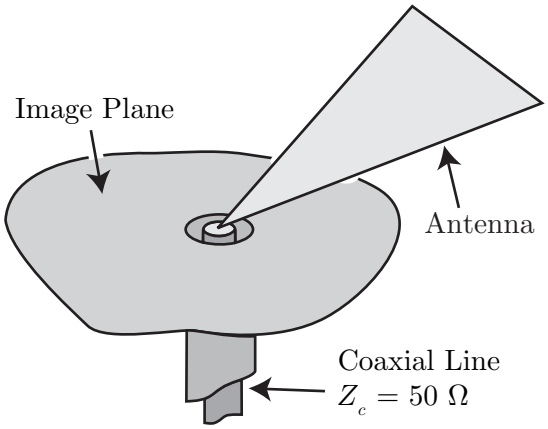


(b)

Figure A.14: (a) Schematic drawing showing the measurement system. Drawing is not to scale. (b) Detail of the feed region.

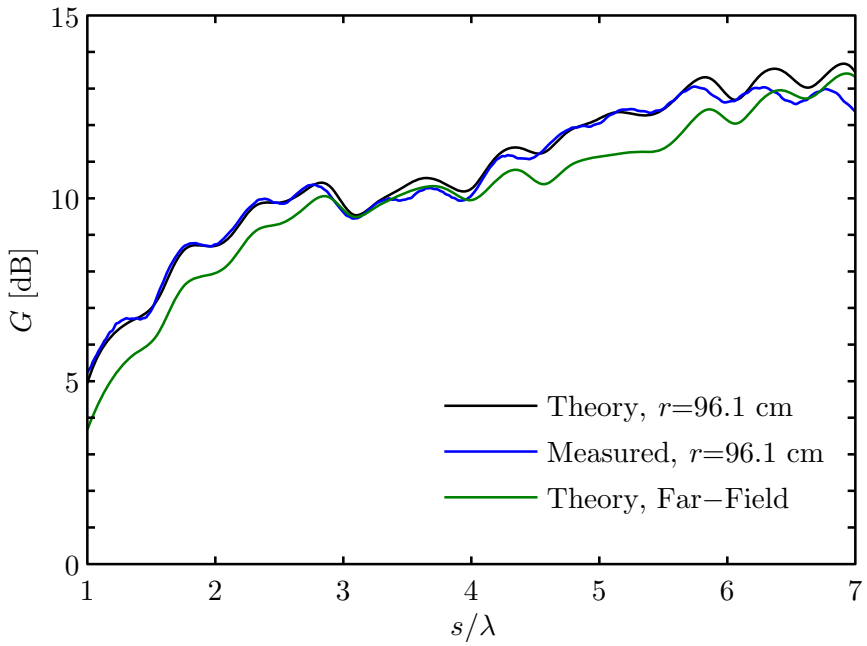


Figure A.15: Comparison of theoretical results for the gain with measurements. For this antenna, $\alpha = 71.73°$, $\beta = 32°$, $s = 18\,\text{cm}$, and $Z_c = 50\,\Omega$ (half antenna).

line is used with the half-antenna in the experimental model, Figure A.14. The theoretical far-zone gain (blue line) is also shown in Figure A.15. A comparison of this result with the gain computed at $r = 96.1\,\text{cm}$ (black line) clearly shows the necessity of using the full two-antenna model for the numerical calculations of the gain.

## *A.4 Conclusion*

In this appendix, the analytical solutions of various researchers for the characteristic impedance of the TEM horn antenna have been compared with a numerical solution. The microstrip approximation for the characteristic impedance of the horn has been shown to be in good agreement with the exact solution when the angles $\alpha$ and $\beta$ are both small.

Next, a design study was performed for the basic TEM horn antenna. In the theoretical model, care was taken to avoid the problems associated with the use of gap sources when calculating the reflection coefficient and input impedance of the antenna. All numerical calculations were made with a program based on the method of moments, and the accuracy of the numerical calculations was established with measured results for selected antennas.

In this study, the characteristic impedance for the TEM horn antenna was chosen to be

$Z_c = 100\,\Omega$, and the antenna was fed by a parallel-plate transmission line with the same characteristic impedance. The angular separation between the plates, $\beta$, was taken to be a variable parameter, and the angle of the plates, $\alpha$, was always determined so as to keep $Z_c = 100\,\Omega$. Graphs were presented for the gain and the fraction of the incident power lost due to reflection versus the electrical length of the horn with the angle $\beta$ as a parameter. Representative field patterns were also presented to show the variation in the directional characteristics of the radiation with the length and angles of the antenna. These graphs should be useful for those wishing to design a basic TEM horn antenna for a particular application.

# APPENDIX B

# CHARACTERISTIC IMPEDANCE OF A TEM HORN ANTENNA

In this appendix, the characteristic impedance of the TEM horn antenna is derived using conformal mapping. A series of transformations are performed so that the geometry is mapped onto a geometry for which the solution is known. The solution simplifies to the known solution for the bow-tie antenna when $\beta = \pi$ (in this appendix, all angles are in radians).

## *B.1 Definitions of Special Functions*

In this derivation, several special functions are used. We use the notation from [83]. First, we have the incomplete elliptic integral of the first kind,

$$F(\varphi, k) = \int_0^{\varphi} \frac{d\alpha}{\sqrt{1 - k^2 \sin^2 \alpha}}, \tag{B.1}$$

and the incomplete elliptic integral of the third kind,

$$\Pi(\varphi, n, k) = \int_0^{\varphi} \frac{d\alpha}{(1 - n \sin^2 \alpha)\sqrt{1 - k^2 \sin^2 \alpha}}. \tag{B.2}$$

The number $k$ is the modulus and $\varphi$ is the amplitude. For $\varphi = \pi/2$, the elliptic integrals are complete. In that case, we have

$$K(k) = F(\pi/2, k) \tag{B.3}$$

$$\Pi(n, k) = \Pi(\pi/2, n, k). \tag{B.4}$$

We will also use one of the Jacobian elliptic functions,

$$\mathrm{sn}(u, k) = \sin \varphi, \tag{B.5}$$

in which $u = F(\varphi, k)$. This function can be thought of as the inverse of an elliptic integral.

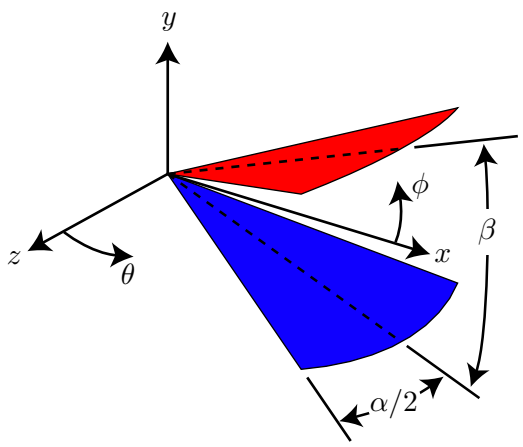


Figure B.1: Original geometry for the infinite TEM horn antenna.

## *B.2 Original Geometry*

As shown in Figure B.1, the structure consists of two perfectly conducting triangular plates held at opposite potentials. The plates are defined as:

$$0 \leq r < \infty \tag{B.6}$$

$$\frac{\pi - \alpha}{2} \leq \theta \leq \frac{\pi + \alpha}{2} \tag{B.7}$$

$$\phi = +\beta/2 \text{ (red plate)} \quad \phi = -\beta/2 \text{ (blue plate)}. \tag{B.8}$$

## *B.3 Stereographic Projection*

The original geometry is mapped onto the extended complex plane $w_1 = u_1 + iv_1$ by means of a stereographic projection [84, p. 147]:

$$w_1 = \cot\left(\frac{\theta}{2}\right) e^{j\phi}. \tag{B.9}$$

As shown in Figure B.2, the plates are mapped onto two radial line segments extending from $R^{-1}e^{\pm j\beta/2}$ to $Re^{\pm j\beta/2}$, where

$$R = \cot\left(\frac{\pi/2 - \alpha/2}{2}\right) = \sqrt{\frac{1 + \sin(\alpha/2)}{1 - \sin(\alpha/2)}}. \tag{B.10}$$

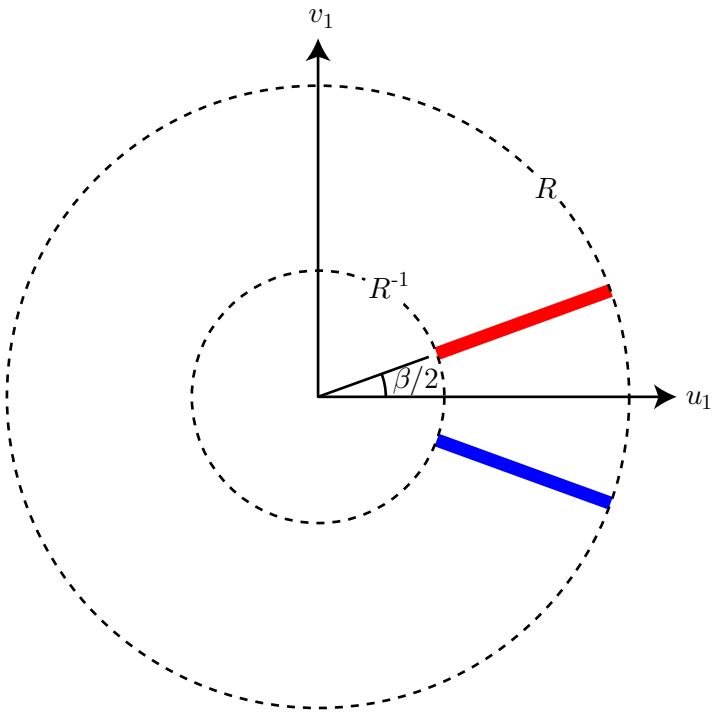


Figure B.2: Geometry after stereographic projection.

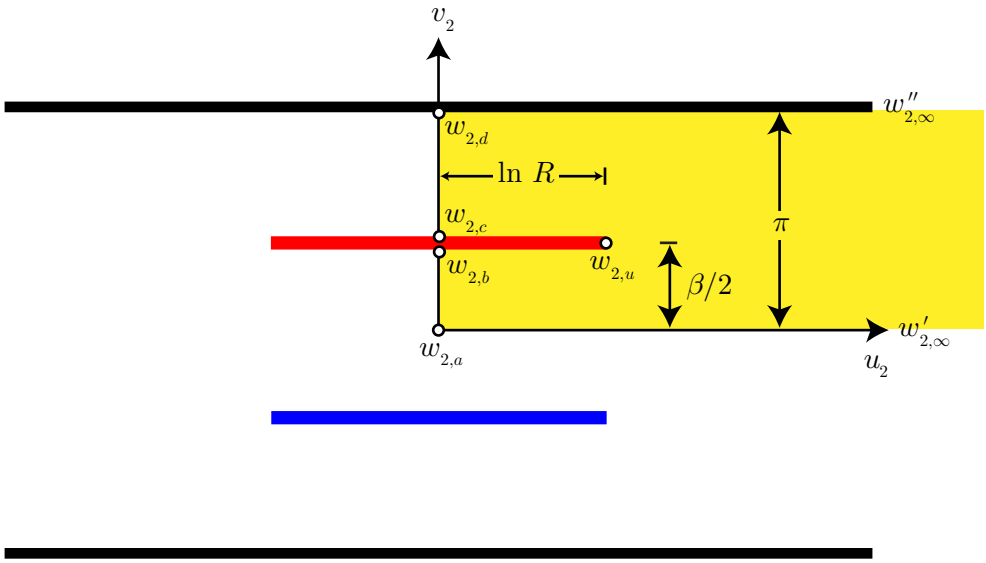


Figure B.3: Geometry after logarithm mapping.

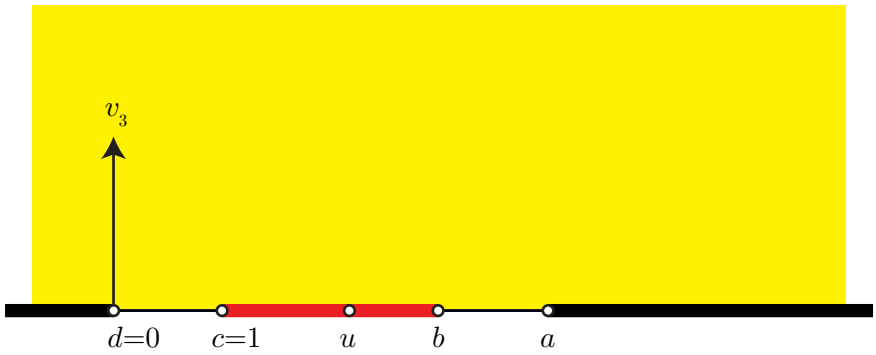


Figure B.4: Geometry after first Schwarz-Christoffel mapping.

## *B.4 Logarithm Mapping*

The entire complex plane $w_1$ is mapped onto an infinite strip in $w_2$ using a logarithm mapping:

$$w_2 = \mathrm{Log}\, w_1 = \ln|w_1| + i\,\mathrm{Arg}(w_1). \tag{B.11}$$

As shown in Figure B.3, the geometry now consists of a pair of parallel strips between two PEC surfaces. Due to electrical and geometric symmetry, only the first quadrant, shown in yellow, needs to be considered for the remainder of the derivation.

## *B.5 First Schwarz-Christoffel Mapping*

The first quadrant of $w_2$ is now mapped onto the upper half plane of $w_3$, as shown in Figure B.4. The map is a Schwarz-Christoffel transformation, but the definition is implicit; that is, the mapping function is $w_2 = f(w_3)$. The derivative of the mapping function is

$$f'(w_3) = A_2 \frac{w_3 - u}{\sqrt{(w_3 - a)(w_3 - b)(w_3 - c)(w_3 - d)}}. \tag{B.12}$$

The value of the constant $A_2$ can be determined based on the points at infinity in $w_2$:

$$A_2 = \frac{w''_{2,\infty} - w'_{2,\infty}}{j\pi} = 1. \tag{B.13}$$

It will be convenient to split the mapping derivative into two terms:

$$f'(w_3) = \sqrt{\frac{w_3 - d}{(w_3 - a)(w_3 - b)(w_3 - c)}} - \frac{u - d}{\sqrt{(w_3 - a)(w_3 - b)(w_3 - c)(w_3 - d)}}. \tag{B.14}$$

There are now five unknowns, any two of which can be arbitrary; we will choose $d = 0$ and $c = 1$. Therefore, we need three independent equations. These can be found by

integrating the mapping derivative, for example,

$$\int_b^a f'(w_3)dw_3 = \int_{f(b)}^{f(a)} dw_2 = -j\frac{\beta}{2}. \tag{B.15}$$

We will evaluate this integral over three ranges to get three independent equations. The integrations will not include poles in $w_3$. In the following, sign reversals are generally required to match the notation in [83]; each reversal results in a $j$ in front of the radical.

### B.5.1 Integration of $f'(w_3)$ from $c$ to $b$

We first integrate $f'(w_3)$ from $c$ to $b$. From Figure B.3, we know that

$$\int_{f(c)}^{f(b)} dw_2 = 0. \tag{B.16}$$

We use two sign reversals and obtain

$$\begin{aligned} 0 = -\Bigg[ & \int_c^b \sqrt{\frac{w_3 - d}{(a - w_3)(b - w_3)(w_3 - c)}} dw_3 \\ & - (u - d) \int_c^b \frac{1}{\sqrt{(a - w_3)(b - w_3)(w_3 - c)(w_3 - d)}} dw_3 \Bigg] \end{aligned} \tag{B.17}$$

Using [83, §3.167(4)] for the first integral and [83, §3.147(4)], we obtain

$$0 = \frac{2}{\sqrt{(a - c)(b - d)}} \left[ (u - d)K(k) - (c - d)\Pi(n, k) \right] \tag{B.18}$$

where $k$ and $n$ are given by

$$k = \sqrt{\frac{(b - c)(a - d)}{(a - c)(b - d)}} = \sqrt{\frac{(b - 1)(a)}{(a - 1)(b)}} \tag{B.19}$$

$$n = \frac{b - c}{b - d} = \frac{b - 1}{b} \tag{B.20}$$

It follows that

$$a = \frac{k^2}{k^2 - n} \tag{B.21}$$

$$b = \frac{1}{1 - n} \tag{B.22}$$

$$u = \frac{\Pi(n, k)}{K(k)} \tag{B.23}$$

### B.5.2 Integration of $f'(w_3)$ from $b$ to $a$

We next integrate $f'(w_3)$ from $b$ to $a$. From Figure B.3, we know that

$$\int_{f(b)}^{f(a)} dw_3 = -j\frac{\beta}{2}. \tag{B.24}$$

We use one sign reversal and obtain

$$\begin{aligned} -j\frac{\beta}{2} = -j\Bigg[\int_b^a \sqrt{\frac{w_3-d}{(a-w_3)(w_3-b)(w_3-c)}}dw_3 \\ -(u-d)\int_b^a \frac{1}{\sqrt{(a-w_3)(w_3-b)(w_3-c)(w_3-d)}}dw_3\Bigg] \end{aligned} \tag{B.25}$$

Using [83, §3.167(6)] for the first integral and [83, §3.147(6)] for the second, we obtain

$$\begin{aligned} \frac{\beta}{2} &= \frac{2}{\sqrt{(a-c)(b-d)}}\left[(b-c)\Pi\left(\frac{a-b}{a-c},k'\right)+(c-d)K(k')-(u-d)K(k')\right] \\ &= 2\sqrt{\frac{(k^2-n)(1-n)}{n}}\left[\left(\frac{n}{1-n}\right)\Pi\left(\frac{k'^2}{1-n},k'\right)+K(k')-\frac{K(k')\Pi(n,k)}{K(k)}\right] \\ &= \frac{2}{K(k)}\sqrt{\frac{k^2-n}{(n)(1-n)}}\Bigg[nK(k)\Pi\left(\frac{k'^2}{1-n},k'\right)+(1-n)K(k)K(k') \\ &\qquad +(n-1)K(k')\Pi(n,k)\Bigg] \\ &= \frac{2}{K(k)}\sqrt{\frac{k^2-n}{(n)(1-n)}}\left[\frac{\pi}{2}\sqrt{\frac{(n)(1-n)}{k^2-n}}F\left(\arcsin\frac{\sqrt{n}}{k},k\right)\right] \\ &= \frac{\pi}{K(k)}F\left(\arcsin\frac{\sqrt{n}}{k},k\right). \end{aligned} \tag{B.26}$$

We have used [85, §117.05] to eliminate the $\Pi$ functions. It follows that

$$n = k^2\,\mathrm{sn}^2\left[\frac{\beta}{2\pi}K(k),k\right]. \tag{B.27}$$

### B.5.3 Integration of $f'(w_3)$ from $c$ to $u$

We now integrate $f'(w_3)$ from $c$ to $u$. From Figure B.3, we know that

$$\int_{f(c)}^{f(u)} dw_2 = \ln R. \tag{B.28}$$

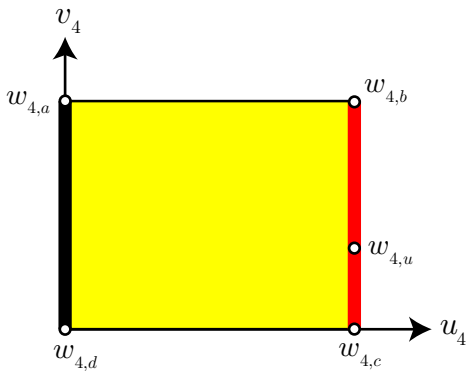


Figure B.5: Geometry after second Schwarz-Christoffel mapping.

The setup is identical to the integration from $c$ to $b$, but the elliptic integrals are now incomplete.

$$\begin{aligned}
\ln R &= -\left[\int_c^u \sqrt{\frac{w_3 - d}{(a - w_3)(b - w_3)(w_3 - c)}}\, dw_3 \right. \\
&\qquad \left. - (u - d) \int_c^u \frac{1}{\sqrt{(a - w_3)(b - w_3)(w_3 - c)(w_3 - d)}}\, dw_3 \right] \\
&= \frac{2}{\sqrt{(a - c)(b - d)}} \left[(u - d)F(\varphi, k) - (c - d)\Pi(\varphi, n, k)\right] \\
&= 2\sqrt{\frac{(k^2 - n)(1 - n)}{n}} \left[\frac{\Pi(n, k)F(\varphi, k)}{K(k)} - \Pi(\varphi, n, k)\right],
\end{aligned} \tag{B.29}$$

where $\varphi$ is given by

$$\begin{aligned}
\varphi &= \arcsin \sqrt{\frac{(b - d)(u - c)}{(b - c)(u - d)}} \\
&= \arcsin \sqrt{\frac{1}{n}\left[1 - \frac{K(k)}{\Pi(n, k)}\right]}.
\end{aligned} \tag{B.30}$$

One more conformal mapping is required to determine $k$.

### *B.6 Second Schwarz-Christoffel Mapping*

The final step is to map the upper half plane of $w_3$ onto a closed rectangle in $w_4$, as shown in Figure B.5. Once again, we use a Schwarz-Christoffel mapping; however, this mapping is explicit. The derivative of the mapping function $w_4 = g(w_3)$ is given by

$$g'(w_3) = \frac{A_4}{\sqrt{(w_3 - a)(w_3 - b)(w_3 - c)(w_3 - d)}}. \tag{B.31}$$

### B.6.1 Integration of $g'(w_3)$ from $b$ to $a$

We first integrate $g'(w_3)$ from $b$ to $a$. We use [83, §3.147(6)] and one sign reversal to obtain

$$\begin{aligned}\int_{g(b)}^{g(a)} dw_4 = w_{4,a} - w_{4,b} &= -jA_4 \int_b^a \frac{dw_3}{\sqrt{(a-w_3)(w_3-b)(w_3-c)(w_3-d)}} \\ &= -jA_4 \frac{2}{\sqrt{(a-c)(b-d)}} K(k') \\ &= -j2\sqrt{\frac{(k^2-n)(1-n)}{n}} K(k').\end{aligned} \tag{B.32}$$

### B.6.2 Integration of $g'(w_3)$ from $c$ to $b$

We next integrate $g'(w_3)$ from $c$ to $b$. We use [83, §3.147(4)] and two pole reversals to obtain

$$\begin{aligned}\int_{g(c)}^{g(b)} dw_4 = w_{4,b} - w_{4,c} &= -A_4 \int_c^b \frac{dw_3}{\sqrt{(a-w_3)(b-w_3)(w_3-c)(w_3-d)}} \\ &= -A_4 \frac{2}{\sqrt{(a-c)(b-d)}} K(k) \\ &= -2\sqrt{\frac{(k^2-n)(1-n)}{n}} K(k).\end{aligned} \tag{B.33}$$

### B.6.3 Characteristic Impedance

The characteristic impedance of the structure in $w_4$ is

$$Z_4 = \eta_o \frac{|w_{4,a} - w_{4,b}|}{|w_{4,b} - w_{4,c}|}. \tag{B.34}$$

By examining the highlighted regions in Figure B.3 and Figure B.5, we see that $Z_c = Z_4$. Therefore, we have

$$Z_c = \eta_o \frac{K(k')}{K(k)}. \tag{B.35}$$

### B.7 Final Expression

Using (B.10), (B.27), (B.29), (B.30), and (B.35), the value of $\alpha$ can be determined as a function of $Z_c$ and $\beta$.

$$Z_c = \eta_o \frac{K(k')}{K(k)} \tag{B.36}$$

$$n = k^2 \,\mathrm{sn}^2 \left[ \frac{\beta}{2\pi} K(k), k \right] \tag{B.37}$$

$$\varphi = \sin^{-1} \sqrt{\frac{1}{n} \left[ 1 - \frac{K(k)}{\Pi(n,k)} \right]} \tag{B.38}$$

$$R = \exp \left\{ 2\sqrt{\frac{(1-n)(k^2-n)}{n}} \left[ \Pi(n,k) \frac{F(\varphi,k)}{K(k)} - \Pi(\varphi,n,k) \right] \right\} \tag{B.39}$$

$$\alpha = 2 \sin^{-1} \left( \frac{R^2 - 1}{R^2 + 1} \right) \tag{B.40}$$

These are not coupled equations; each line can be computed based on values from the previous lines.

### B.8 Comparison with Bowtie Antenna

This solution should reduce to the known bowtie solution for $\beta = \pi$. For that case, we find

$$n = 1 - k' \tag{B.41}$$

$$\varphi = \sin^{-1} \sqrt{\frac{1}{1+k'}} \tag{B.42}$$

This value of $\varphi$ is a "special" value of the elliptic integrals that results in a number of simplifications. We apply these to find

$$R = \frac{1}{\sqrt{k'}} = \sqrt{\frac{1 - \sin(\alpha/2)}{1 + \sin(\alpha/2)}} \tag{B.43}$$

$$k' = \frac{1 - \sin(\alpha/2)}{1 + \sin(\alpha/2)} \tag{B.44}$$

$$Z_c = \eta_o \frac{K(k')}{K(k)} \tag{B.45}$$

This is identical to the bowtie solution [69], except that $k \to k'$.

## REFERENCES


[1] G. S. Smith, *An Introduction to Classical Electromagnetic Radiation.* Cambridge University Press, 1997.

[2] K. S. Yee, "Numerical solution of initial boundary value problems involving Maxwell's equations in isotropic media," *IEEE Transactions on Antennas and Propagation*, vol. 14, no. 3, pp. 302–307, 1966.

[3] A. Taflove and M. E. Brodwin, "Numerical solution of steady-state electromagnetic scattering problems using time-dependent Maxwell's equations," *IEEE Transactions on Microwave Theory and Techniques*, vol. 23, no. 8, pp. 623–630, 1975.

[4] B. Engquist and A. Majda, "Absorbing boundary-conditions for numerical-simulation of waves," *Mathematics of Computation*, vol. 31, no. 139, pp. 629–651, 1977.

[5] G. Mur, "Absorbing boundary-conditions for the finite-difference approximation of the time-domain electromagnetic-field equations," *IEEE Transactions on Electromagnetic Compatibility*, vol. 23, no. 4, pp. 377–382, 1981.

[6] J.-P. Berenger, "A perfectly matched layer for the absorption of electromagnetic waves," *Journal of Computational Physics*, vol. 114, no. 2, pp. 185–200, 1994.

[7] Z. S. Sacks, D. M. Kingsland, R. Lee, and J.-F. Lee, "A perfectly matched anisotropic absorber for use as an absorbing boundary condition," *IEEE Transactions on Antennas and Propagation*, vol. 43, no. 12, pp. 1460–1463, 1995.

[8] S. D. Gedney, "An anisotropic perfectly matched layer absorbing medium for the truncation of FDTD lattices," *IEEE Transactions on Antennas and Propagation*, vol. 44, no. 12, pp. 1630–1639, 1996.

[9] W. C. Chew and W. H. Weedon, "A 3D perfectly matched medium from modified Maxwell's equations with stretched coordinates," *Microwave and Optical Technology Letters*, vol. 7, no. 13, pp. 599–604, 1994.

[10] W. C. Chew, J. M. Jin, and E. Michielssen, "Complex coordinate stretching as a generalized absorbing boundary condition," *Microwave and Optical Technology Letters*, vol. 15, no. 6, pp. 363–369, 1997.

[11] F. L. Teixeira and W. C. Chew, "System derivation of anisotropic PML absorbing media in cylindrical and spherical coordinates," *IEEE Microwave and Guided Wave Letters*, vol. 7, no. 11, pp. 371–373, 1997.

[12] J. A. Roden and S. D. Gedney, "Convolutional PML (CPML): An efficient FDTD implementation of the CFS-PML for arbitrary media," *Microwave and Optical Technology Letters*, vol. 27, no. 5, pp. 334–339, 2000.

[13] D. E. Merewether, R. Fisher, and F. W. Smith, "On implementing a numeric Huygens source scheme in a finite-difference program to illuminate scattering bodies," *IEEE Transactions on Nuclear Science*, vol. 27, no. 6, pp. 1829–1833, 1980.

[14] J. B. Schneider and C. L. Wagner, "FDTD dispersion revisited: Faster-than-light propagation," *IEEE Microwave and Guided Wave Letters*, vol. 9, no. 2, pp. 54–56, 1999.

[15] J. B. Schneider and R. J. Kruhlak, "Dispersion of homogeneous and inhomogeneous waves in the Yee finite-difference time-domain grid," *IEEE Transactions on Microwave Theory and Techniques*, vol. 49, no. 2, pp. 280–287, 2001.

[16] J. B. Schneider, "Plane waves in FDTD simulations and a nearly perfect total-field/scattered-field boundary," *IEEE Transactions on Antennas and Propagation*, vol. 52, no. 12, pp. 3280–3287, 2004.

[17] A. Taflove and S. C. Hagness, *Computational Electrodynamics: The Finite-Difference Time-Domain Method*, 3rd ed. Artech House, 2005.

[18] J. G. Maloney and M. P. Kesler, "Analysis of periodic structures," in *Computational Electrodynamics: The Finite-Difference Time-Domain Method*, 3rd ed., A. Taflove and S. C. Hagness, Eds. Artech House, 2005.

[19] M. E. Veysoglu, R. T. Shin, and J. A. Kong, "A finite-difference time-domain analysis of wave scattering from periodic surfaces: Oblique incidence case," *Journal of Electromagnetic Waves and Applications*, vol. 7, pp. 1595–1607, 1993.

[20] H. Holter and H. Steyskal, "Broadband FDTD analysis of infinite phased arrays using periodic boundary conditions," *Electronics Letters*, vol. 35, no. 10, pp. 758–759, 1999.

[21] ——, "Infinite phased-array analysis using FDTD periodic boundary conditions - pulse scanning in oblique directions," *IEEE Transactions on Antennas and Propagation*, vol. 47, no. 10, pp. 1508–1514, 1999.

[22] S. Kinoshita, S. Yoshioka, and J. Miyazaki, "Physics of structural colors," *Reports on Progress in Physics*, vol. 71, no. 7, p. 076401 (30pp), 2008.

[23] P. Vukusic, J. R. Sambles, C. R. Lawrence, and R. J. Wooten, "Quantified interference and diffraction in single *Morpho* butterfly scales," *Proceedings of the Royal Society of London. Series B: Biological Sciences*, vol. 266, pp. 1403–1411, 1999.

[24] A. A. Michelson, "On metallic colouring in birds and insects," *Philosophical Magazine*, vol. 21, pp. 554–567, 1911.

[25] A. Mallock, "Note on the iridescent colours of birds and insects," *Proceedings of the Royal Society of London Series a-Containing Papers of a Mathematical and Physical Character*, vol. 85, no. 582, pp. 598–605, 1911.

[26] L. Rayleigh, "On the optical character of some brilliant animal colours," *Philosophical Magazine*, vol. 37, pp. 98–111, 1919.

[27] C. W. Mason, "Structural colors in insects. i," *Journal of Physical Chemistry*, vol. 30, no. 3, pp. 383–395, 1926.

[28] ——, "Structural colors in insects. ii," *Journal of Physical Chemistry*, vol. 31, no. 3, pp. 321–354, 1927.

[29] ——, "Structural colors in insects. iii," *Journal of Physical Chemistry*, vol. 31, no. 12, pp. 1856–1872, 1927.

[30] T. F. Anderson and A. G. Richards, "An electron microscope study of some structural colors of insects," *Journal of Applied Physics*, vol. 13, no. 12, pp. 748–758, 1942.

[31] H. Ghiradella, D. Aneshansley, T. Eisner, R. E. Silberglied, and H. E. Hinton, "Ultraviolet reflection of a male butterfly - interference color caused by thin-layer elaboration of wing scales," *Science*, vol. 178, no. 4066, pp. 1214–1217, 1972.

[32] H. Ghiradella, "Structure of iridescent lepidopteran scales - variations on several themes," *Annals of the Entomological Society of America*, vol. 77, no. 6, pp. 637–645, 1984.

[33] ——, "Light and color on the wing: Structural colors in butterflies and moths," *Applied Optics*, vol. 30, no. 24, pp. 3492–3500, 1991.

[34] ——, "Structure of butterfly scales - patterning in an insect cuticle," *Microscopy Research and Technique*, vol. 27, no. 5, pp. 429–438, 1994.

[35] ——, "Hairs, bristles, and scales," in *Microscopic Anatomy of Invertebrates*, W. H. Frederick and L. Michael, Eds. Wiley-Liss, 1998, vol. 11A.

[36] P. Vukusic, J. R. Sambles, and H. Ghiradella, "Optical classification of microstructure in butterfly wing-scales," *Photonics Science News*, vol. 6, pp. 61–68, 2000.

[37] P. K. C. Pillai, "Spectral reflection characteristics of *Morpho* butterfly wing," *Journal of the Optical Society of America*, vol. 58, no. 8, pp. 1019–1022, 1968.

[38] B. Gralak, G. Tayeb, and S. Enoch, "*Morpho* butterflies wings color modeled with lamellar grating theory," *Optics Express*, vol. 9, no. 11, pp. 567–578, 2001.

[39] S. Kinoshita, S. Yoshioka, and K. Kawagoe, "Mechanisms of structural colour in the morpho butterfly: cooperation of regularity and irregularity in an iridescent scale," *Proceedings of the Royal Society of London Series B-Biological Sciences*, vol. 269, no. 1499, pp. 1417–1421, 2002.

[40] L. Plattner, "Optical properties of the scales of *Morpho rhetenor* butterflies: theoretical and experimental investigation of the back-scattering of light in the visible spectrum," *Journal of the Royal Society Interface*, vol. 1, no. 1, pp. 49–59, 2004.

[41] S. Banerjee, J. B. Cole, and T. Yatagai, "Colour characterization of a *Morpho* butterfly wing-scale using a high accuracy nonstandard finite-difference time-domain method," *Micron*, vol. 38, no. 2, pp. 97–103, 2007.

[42] M. Abramowitz and I. Stegan, *Handbook of Mathematical Functions*. US Government Printing Office, 1964.

[43] A. Taflove, "Review of the formulation and applications of the finite-difference time-domain method for numerical modeling of electromagnetic-wave interactions with arbitrary structures," *Wave Motion*, vol. 10, no. 6, pp. 547–582, 1988.

[44] J.-P. Berenger, "Numerical reflection from FDTD-PMLs: A comparison of the split PML with the unsplit and CFS PMLs," *IEEE Transactions on Antennas and Propagation*, vol. 50, no. 3, pp. 258–265, 2002.

[45] S. D. Gedney, "Scaled CFS-PML: it is more robust, more accurate, more efficient, and simple to implement. Why aren't you using it?" in *Proceedings of the 2005 IEEE Antennas and Propagation Society International Symposium*, vol. 4B, Washington, DC, 2005, pp. 364–367.

[46] R. T. Lee and G. S. Smith, "A conceptually simple method for incorporating periodic boundary conditions into the FDTD method," *Microwave and Optical Technology Letters*, vol. 45, no. 6, pp. 472–476, 2005.

[47] E. J. Kuster, 2004, personal communication.

[48] R. T. Lee and G. S. Smith, "An alternative approach for implementing periodic boundary conditions in the FDTD method using multiple unit cells," *IEEE Transactions on Antennas and Propagation*, vol. 54, no. 2, pp. 698–705, 2006.

[49] S. D. Gedney and A. Taflove, "Perfectly matched layer absorbing boundary conditions," in *Computational Electrodynamics: The Finite-Difference Time-Domain Method*, ser. 7, T. Allen and C. H. Susan, Eds. Artech House, 2000.

[50] S. Ramo, J. R. Whinnery, and T. V. Duzer, *Fields and Waves in Communication Electronics*. Wiley, 1994.

[51] R. F. Harrington, *Time-Harmonic Electromagnetic Fields*. McGraw-Hill, 1961.

[52] C. F. Bohren and D. R. Huffman, *Absorption and Scattering of Light by Small Particles*. Wiley-VCH, 1983.

[53] ASTM International, *ASTM E 284 08: Standard Terminology of Appearance*. West Conshohocken, PA: ASTM International, 2008.

[54] R. S. Berns, *Billmeyer and Saltzman's Principles of Color Technology*, 3rd ed. Wiley, 2000.

[55] ASTM International, *ASTM E 308 06: Standard Practice for Computing the Colors of Objects by Using the CIE System*. West Conshohocken, PA: ASTM International, 2006.

[56] A. Stockman and L. T. Sharpe, "Color and vision database research laboratories, institute of opthalmology, ucl."

[57] International Electrotechnical Commission, *IEC 61966-2-1: Default RGB Colour Space - sRGB*. Geneva, Switzerland: IEC, 1999.

[58] E. Hecht and A. Zajac, *Optics*. Addison-Wesley, 1974.

[59] D. J. Brink and M. E. Lee, "Confined blue iridescence by a diffracting microstructure: an optical investigation of the cynandra opis butterfly," *Applied Optics*, vol. 38, no. 25, pp. 5282–5289, 1999.

[60] S. Kinoshita and S. Yoshioka, "Structural colors in nature: The role of regularity and irregularity in the structure," *Chemphyschem*, vol. 6, no. 8, pp. 1442–1459, 2005.

[61] R. A. Potyrailo, H. Ghiradella, A. Vertiatchikh, K. Dovidenko, J. R. Cournoyer, and E. Olson, "*Morpho* butterfly wing scales demonstrate highly selective vapour response," *Nature Photonics*, vol. 1, no. 2, pp. 123–128, 2007.

[62] S. Berthier, E. Charron, and J. Boulenguez, "Morphological structure and optical properties of the wings of *Morphidae*," *Insect Science*, vol. 13, no. 2, pp. 145–158, 2006.

[63] S. Berthier, *Iridescences: The Physical Colors of Insects*. Springer, 2007, translated by Capucine Lafait.

[64] S. Yoshioka and S. Kinoshita, "Wavelength-selective and anisotropic light-diffusing scale on the wing of the *Morpho* butterfly," *Proceedings of the Royal Society of London. Series B: Biological Sciences*, vol. 271, no. 1539, pp. 581–587, 2004.

[65] C. Lawrence, P. Vukusic, and R. Sambles, "Grazing-incidence iridescence from a butterfly wing," *Applied Optics*, vol. 41, no. 3, pp. 437–441, 2002.

[66] P. Vukusic, J. R. Sambles, C. R. Lawrence, and R. J. Wootton, "Limited-view iridescence in the butterfly *Ancyluris meliboeus*," *Proceedings of the Royal Society of London. Series B: Biological Sciences*, vol. 269, no. 1486, pp. 7–14, 2002.

[67] R. T. Lee and G. S. Smith, "On the characteristic impedance of the TEM horn antenna," *IEEE Transactions on Antennas and Propagation*, vol. 52, no. 1, pp. 315–318, 2004.

[68] ——, "A design study for the basic TEM horn antenna," *IEEE Antennas and Propagation Magazine*, vol. 46, no. 1, pp. 86–92, 2004.

[69] R. L. Carrel, "The characteristic impedance of two infinite cones of arbitrary cross section," *IRE Transactions on Antennas and Propagation*, vol. AP-6, pp. 197–201, 1958.

[70] F. C. Yang and K. S. H. Lee, "Impedance of a two-conical-plate transmission line," *Sensor and Simulation Notes*, no. 221, 1976.

[71] J. G. Maloney and G. S. Smith, "On the characteristic impedance of TEM horn antennas," in *Proc. Antennas Propagat. Society Int. Symp.*, 1995, pp. 182–185.

[72] A. P. Lambert, S. M. Booker, and P. D. Smith, "Calculation of the characteristic impedance of TEM horn antennas using the conformal mapping approach," *IEEE Transactions on Antennas and Propagation*, vol. AP-43, no. 1, pp. 47–53, 1995.

[73] M. Kanda, "The effects of resistive loading of "TEM" horns," *IEEE Transactions on Electromagnetic Compatibility*, vol. EMC-24, no. 2, pp. 245–255, 1982.

[74] K. L. Shlager, G. S. Smith, and J. G. Maloney, "Accurate analysis of TEM horn antennas for pulse radiation," *IEEE Transactions on Electromagnetic Compatibility*, vol. 38, no. 3, pp. 414–423, 1996.

[75] R. J. Wohlers, "The GWIA, an extremely wide bandwidth low-dispersion antenna," 1971.

[76] C. A. Balanis, *Antenna Theory: Analysis and Design.* Wiley, 1997.

[77] R. E. Collin, *Foundations for Microwave Engineering.* McGraw-Hill, 1992.

[78] P. D. Smith, 2002, personal communication.

[79] E. O. Hammerstad, "Equations for microstrip circuit design," in *Proc. European Microwave Conf.*, 1975, pp. 268–272.

[80] M. V. Schneider, "Microstrip lines for microwave integrated circuits," *Bell System Technical Journal*, vol. 48, no. 5, pp. 1421–1444, 1969.

[81] EM Software & Systems, "FEKO," 2003, suite 4.1.

[82] *IEEE Standard Test Procedures for Antennas.* Institute of Electrical and Electronics Engineers, 1979.

[83] I. S. Gradshteyn and I. M. Ryzhik, *Table of Integrals, Series, and Products*, 7th ed. Burlington, MA: Academic Press, 2007.

[84] T. Needham, *Visual Complex Analysis.* Oxford: Oxford University Press, 1997.

[85] P. F. Byrd and M. D. Friedman, *Handbook of Elliptic Integrals for Engineers and Scientists.* Springer-Verlag, 1971.

# VITA

Richard Todd Lee was born in Fitzgerald, Georgia, on March 3, 1979. He received the B.S.E.E. and M.S.E.C.E. degrees from the Georgia Institute of Technology in 2001 and 2003, respectively. From 1998 to 2001, he was employed as a student assistant in the Signature Technology Laboratory at the Georgia Tech Research Institute, and from 2001 to 2009 as a graduate research assistant in the School of Electrical and Computer Engineering. Upon graduation, he plans to accept a full-time position in the Signature Technology Laboratory.